Fog and Boundary Layer Clouds: Fog Visibility and Forecasting

Edited by
Ismail Gultepe

pageoph topical volumes

BIRKHÄUSER

Fog and Boundary Layer Clouds: Fog Visibility and Forecasting

Edited by
Ismail Gultepe

Birkhäuser
Basel · Boston · Berlin

Reprint from Pure and Applied Geophysics
(PAGEOPH), Volume 164 (2007) No. 6-7

Editor:
Ismail Gultepe
Cloud Physics and Severe Weather Research Section
Science and Technology Branch, Environment Canada
4905 Dufferin Street
Toronto, Ontario, M3H5T4
Canada
ismail.gultepe@ec.gc.ca

Library of Congress Control Number: 2007925898

Bibliographic information published by Die Deutsche Bibliothek:
Die Deutsche Bibliothek lists this publication in the Deutsche Nationalbibliografie; detailed bibliographic data is available in the Internet at <http://dnb.ddb.de>

ISBN 978-3-7643-8418-0 Birkhäuser Verlag AG, Basel · Boston · Berlin

ISBN 978-3-7643-8418-0
9 8 7 6 5 4 3 2 1

e-ISBN 978-3-7643-8419-7
www.birkhauser.ch

PURE AND APPLIED GEOPHYSICS
Vol. 164, No. 6-7, 2007

Contents

COST- the acronym for European **CO**operation in the field of **S**cientific and **T**echnical Research- is the oldest and widest European intergovernmental network for cooperation in research. Established by the Ministerial Conference in November 1971, COST is presently used by the scientific communities of 35 European countries to cooperate in common research projects supported by national funds.

The funds provided by COST - less than 1% of the total value of the projects - support the COST cooperation networks (COST Actions) through which, with only around €20 million per year, more than 30.000 European scientists are involved in research having a total value which exceeds €2 billion per year. This is the financial worth of the European added value which COST achieves.

A "bottom up approach" (the initiative of launching a COST Action comes from the European scientists themselves), "à la carte participation" (only countries interested in the Action participate), "equality of access" (participation is open also to the scientific communities of countries not belonging to the European Union) and "flexible structure" (easy implementation and light management of the research initiatives) are the main characteristics of COST.

As precursor of advanced multidisciplinary research COST has a very important role for the realisation of the European Research Area (ERA) anticipating and complementing the activities of the Framework Programmes, constituting a "bridge" towards the scientific communities of emerging countries, increasing the mobility of researchers across Europe and fostering the establishment of "Networks of Excellence" in many key scientific domains such as: Biomedicine and Molecular Biosciences; Food and Agriculture; Forests, their Products and Services; Materials, Physics and Nanosciences; Chemistry and Molecular Sciences and Technologies; Earth System Science and Environmental Management; Information and Communication Technologies; Transport and Urban Development; Individuals, Society, Culture and Health. It covers basic and more applied research and also addresses issues of pre-normative nature or of societal importance.

Pure appl. geophys. 164 (2007) 1115–1116
0033–4553/07/071115–2
DOI 10.1007/s00024-007-0209-4

Pure and Applied Geophysics

Fog and Boundary Layer Clouds: Introduction

This special issue of the Journal of Pure and Applied Geophysics contains 15 papers related to fog, visibility, and low clouds that focus on microphysical and conventional surface observations, satellite detection techniques, modeling aspects, and climatological and statistical methods for fog forecasting. The results presented in this special issue come from research efforts in North America and Europe, mainly from the Canadian Fog Remote Sensing And Modeling (FRAM) and European COST-722 fog/visibility related projects. COST (http://www.cost.esf.org/) is an intergovernmental European framework for international cooperation between nationally funded research activities. COST creates scientific networks and enables scientists to collaborate in a wide spectrum of activities in research and technology. COST activities are administered by the COST Office.

Fog affects human being in various ways, both from a negative point of view (hazard to aviation, land and marine transportation) and in a positive way (fog water harvesting in arid regions). Our understanding of the physics of fog remains incomplete due to the time and space scales involved in the numerous processes influencing fog formation, development, and decay (e.g. nucleation, radiative processes, surface turbulent fluxes, mesoscale circulations, etc.). Because of this complexity, the accurate forecasting/nowcasting of fog remains difficult and related issues need to be further studied in detail. We do not know accurately how basic physical processes interact to determine the timing and location of fog formation, impeding our ability to provide accurate forecasts. Presently, typical numerical forecast models lack sufficient resolution and appropriate physical parameterizations to represent fog and use a simple approach in estimating visibility that leads to uncertainty of more than 50% in many conditions. Better forecasts would help mitigate the financial losses associated to delays at airports as well as the human and financial losses due to accidents, which can be comparable to losses resulting from tornadoes.

From an analysis perspective, the modeling issue of fog needs to be further developed because surface observations are too sparsely distributed to adequately capture the spatial variability of fog, and satellite retrievals have serious limitations in the presence of mid- and high-level clouds. Although various methods were developed for fog remote sensing from satellites, they can be limited when visibility channels are not available at night and contributions from shortwave radiation affect the near infrared channels during the day time. This implies that integrated methods need to be developed. When observations are integrated with model based output, better methods for fog nowcasting/forecasting can be developed.

Careful analysis of climatological data can serve as a basis for the better understanding of the various conditions that led to fog formation in the past. Also, if

any trend occurred in the past, the fog occurrence may be predicted in the future when similar conditions occur. This defines an approach where artificial neural networks, ruled-based climatological methods, and some other statistical methods (e.g. tree approaches) can bring added-value to fog forecasting.

In this special issue, various contributions related to the above issues are included. These are the result of various COST-722 meetings and FRAM workshops, and this collection of various articles presents a cutting edge research in the field. Although the works presented here suggest that fog/low cloud visibility calculations have improved significantly, there are still issues to be resolved and it is hoped that this special issue will facilitate future works on this subject.

We wish to thank the scientific contributors to this book and members of the FRAM, and COST-722 groups, and specifically to Dr. Pavol Nejedlik who was a science officer for the Earth System Science and Environmental Domain at the COST office in Brussels. The COST is operated under the auspices of the European Science Foundation and the European Commission. We also gratefully acknowledge funding support for this work provided by the Canadian National Search and Rescue Secretariat and Environment Canada. Additional funding was also provided by the COST-722 project office. Technical support for the data collection was provided by the Cloud Physics and Severe Weather Research Section of the Science and Technology Branch, Environment Canada, Toronto, Ontario. In addition, I like to sincerely thank Prof. Renata Dmowska, Editor in chief for topical issues at Pure and Applied Geophysics, inviting our working group to prepare this special issue, handling the review process and providing invaluable advice during the preparation of this special issue. Many thanks also to Prof. Brian Mitchell for valuable suggestions during the course of this work with whom I work as an editor in Atmospheric and Ocean Sciences of the Pure and Applied Geophysics.

The editor is indebted to the reviewers who took the time and effort to carefully review the manuscripts and make suggestions for improvements. The following reviewers were involved in the review process: N. Ahmad, A. Bott, J. Bendix, T. Bergot, A. Cannon, J. Cermak, Z. Boybeyi, L. S. F. Fuente, M. Gordon, I. Gultepe, B. Hansen, P. King, S. C. Michaelides, M. Pagowski, G. Pearson, R. Tardif, A. Tokay, G. Toth, and Z. Vukovic.

I. Gultepe
Environment Canada
Dec. 15 2006

Pure appl. geophys. 164 (2007) 1117–1119
0033–4553/07/071117–3
10.1007/s00024-007-0210-y

Pure and Applied Geophysics

Obituary

This special issue on fog, low clouds and visibility is dedicated to the memory of Professor Peter Zwack, who passed away prematurely on November 8, 2005, after a courageous bout with cancer.

As a curious child, Peter was fascinated by a wide variety of weather phenomena. It is no wonder he graduated in 1966 from the renowned City College of New York with a Bachelor's Degree in Meteorology. He later went on to tackle the practical aspects of the field by working as a weather forecaster at the National Weather Service in New York City. Given his curious nature, it did not take long for Peter to reconnect with the joys of scientific discovery. He completed a Master's Degree in meteorology at New Jersey's Rutgers University in 1968 while working in the New York weather office. He then moved to Montreal to pursue a Ph.D. in radar meteorology at McGill University under the supervision of J.S. Marshall. Shortly after graduating in 1973, Peter was among the first professors hired to create the Atmospheric Sciences program at the Université du Québec à Montréal (UQAM). Part of the original mandate of the program was to provide professional training to upcoming weather forecasters hired by the Meteorological Service of Canada (MSC). At UQAM, in 1976, Peter also contributed to the creation of North America's only graduate program in Atmospheric Sciences available to French-speaking students.

Teaching and research activities geared toward the needs of the weather forecasting community would become the central themes of Peter's career. In the mid-eighties, he and a graduate student developed diagnostic equations describing in intuitive ways the mechanisms responsible for the development of large-scale weather systems and associated vertical motions in the atmosphere. The so-called "Zwack-Okossi" equations became a fixture among the practices of Environment Canada's (EC) weather forecasters and were the basis for the prototype of the DIONYSOS software, which has been developed by Peter and his students over several years. This software provides insights into the physical mechanisms influencing the vertical motions associated with synoptic weather systems and the cyclogenesis of such systems, as simulated by numerical weather prediction models. It has been implemented at operational weather centers in Canada, France and the United States.

Throughout his career, Peter had a profound desire to teach. He was renowned for his ability to illustrate difficult subjects in lucid and simple ways. Classes he taught ranged from "Introduction to Meteorology," taken as an elective by numerous students from other programs, to undergraduate and graduate-level "Synoptic Meteorology." He also taught the meteorology fundamentals to UQAM students who studied to become high school science teachers. Peter also remained

involved in the professional training world for most of his career. He was among the developers of the EUROMET project which culminated in the availability of online interactive training modules used by European weather forecasters. The EUROMET project was awarded, in 1998, the prize for best European educational software.

From the nineties onward, aviation meteorology became one of the main thrusts of Peter's efforts. He recognized that the prediction of low cloud ceilings and fog remained among the most challenging tasks performed by forecasters. Peter was instrumental in establishing the STRATUS project, which involved a wide spectrum of experts in meteorology, artificial intelligence and software engineering. The project led to the development of an expert system for the short-term forecasting of low cloud ceilings and produced a number of spin-off projects that developed software applications currently in use at EC's weather offices. These efforts were followed by Peter's involvement in a project aimed at providing improved guidance to personnel tasked with forecasting the dissipation of marine stratus in the approach zone of the San Francisco airport. Peter provided scientific leadership on the application of high-resolution one-dimensional numerical modeling to that specific problem. In 2002, the Federal Aviation Administration awarded Peter and the other members of the development team a certificate of recognition for their efforts resulting in the operational Marine Stratus Forecast System for the San Francisco International Airport.

Peter received individual honors and prizes during his career. In 1992 he was awarded the Dr. Andrew Thomson Prize from the Canadian Meteorological and Oceanography Society for his innovative contributions to the field of applied meteorology. He was also recognized in 1997 by the Association Professionelle des Météorologistes du Québec with the ''Alcide Ouellet'' prize for his contribution to the meteorology profession.

Always active in the community, Peter served as the president of the Canadian Meteorological and Oceanography Society in 1996–1997. He also served on many committees and advisory boards on a range of subjects dear to him, from artificial intelligence to the role of the private sector in meteorology. These activities underscored Peter's eagerness to collaborate with others and his constant desire to exchange ideas with members of the atmospheric science community.

Perhaps Peter's greatest achievements were outside meteorology. As a father with a son diagnosed with autism, Peter became a determined advocate for the rights of autistic people and their caretakers, and raised awareness and understanding about the disorder. He was vice-president of the Montreal Autism Society from 1990 to 1995, president of the Québec Society for Autism from 1995 to 2000, and joined the Board of Autism Society Canada in 2000. He became vice-president in 2001 and president in 2004. Throughout this period, he spearheaded numerous initiatives to better the lives of autistic children and adults alike, as well as family members providing constant care.

The passing of Peter represents a great loss not just for science, but for the autism community as well. We have lost an exceptional colleague and a good friend. He will be remembered by many colleagues and numerous students for his communicative laughter, enthusiasm, intellectual mind, and kind heart.

Robert Tardif
National Center for Atmospheric Research,
Boulder, Colorado, USA
Dec. 15 2006

Pure appl. geophys. 164 (2007) 1121–1159
0033–4553/07/071121–39
DOI 10.1007/s00024-007-0211-x

Pure and Applied Geophysics

Fog Research: A Review of Past Achievements and Future Perspectives

I. Gultepe,[1] R. Tardif,[2] S. C. Michaelides,[3] J. Cermak,[4] A. Bott,[5] J. Bendix,[4] M. D. Müller,[6] M. Pagowski,[7] B. Hansen,[1] G. Ellrod,[8] W. Jacobs,[9] G. Toth,[10] and S. G. Cober[1]

Abstract—The scientific community that includes meteorologists, physical scientists, engineers, medical doctors, biologists, and environmentalists has shown interest in a better understanding of fog for years because of its effects on, directly or indirectly, the daily life of human beings. The total economic losses associated with the impact of the presence of fog on aviation, marine and land transportation can be comparable to those of tornadoes or, in some cases, winter storms and hurricanes. The number of articles including the word "fog" in Journals of American Meteorological Society alone was found to be about 4700, indicating that there is substantial interest in this subject. In spite of this extensive body of work, our ability to accurately forecast/nowcast fog remains limited due to our incomplete understanding of the fog processes over various time and space scales. Fog processes involve droplet microphysics, aerosol chemistry, radiation, turbulence, large/small-scale dynamics, and surface conditions (e.g., partaining to the presence of ice, snow, liquid, plants, and various types of soil). This review paper summarizes past achievements related to the understanding of fog formation, development and decay, and in this respect, the analysis of observations and the development of forecasting models and remote sensing methods are discussed in detail. Finally, future perspectives for fog-related research are highlighted.

Key words: Fog review, fog observations, fog modeling, fog remote sensing, fog forecasting.

[1] Cloud Physics and Severe Weather Research Section, Meteorological Research Division, Environment Canada, Toronto, ON, Canada. E-mail: ismail.gultepe@ec.gc.ca; Stewart.cober@ec.gc.ca

[2] National Center for Atmospheric Research, Box 3000, Boulder, CO 80301, USA. E-mail: tardif@ucar.edu

[3] Meteorological Service, P.O. Box 43059, Larnaka Airport, CY 6650, Cyprus. E-mail: silas@ucy.ac.cy

[4] Laboratory for Climatology and Remote Sensing (LCRS), Department of Geography, Philipps-Universität Marburg, 35032 Marburg, Germany. E-mail: cermak@lcrs.de; bendix@lcrs.de

[5] Meteorologisches Institut Universität Bonn, Auf dem Hügel 20, D-53121 Bonn, Germany. E-mail: a.bott@uni-bonn.de

[6] Institute of Meteorology, Climatology and Remote Sensing, University of Basel, Basel, Switzerland. E-mail: mathias.mueller@unibas.ch

[7] Global Systems Division, NOAA Earth System Research Laboratory, Boulder, CO, USA. E-mail: Mariusz.Pagowski@noaa.gov

[8] NOAA/NESDIS (Retired), P.O. Box 240, Granby, CT 06035, USA. E-mail: gary.ellrod@gmail.com

[9] Deutscher Wetterdienst, Bildungs und Tagungszentrum, Am DFS-Campus 4, D-63225 Langen, Germany. E-mail: wilfried.jacobs@dwd.de

[10] Hydrology and Arctic Lab, Prairie and Northern Region, Environment Canada, Edmonton, AB, Canada. E-mail: garrym.toth@ec.gc.ca

1. Introduction

The effect of fog on human life was recognized in the early ages of mankind but its impact has significantly increased during recent decades due to increasing air, marine, and road traffic. In fact, the financial and human losses related to fog and low visibility became comparable to the losses from other weather events, e.g., tornadoes or, in some situations, even hurricanes. The purpose of this review is to summarize the earlier works on fog and to lay a basis for the articles presented in this special issue and outline perspectives for future fog research.

The earliest works on fog can be traced back to Aristotle's Meteorologica (284–322 B.C.). These were extensively referenced by NEUMANN (1989) in his study of early works on fog and weather. This paragraph is mainly based on his detailed work. In the English translation by H.D.P. Lee (1962, ARISTOTLE), a statement is given on the relationship between fog and good weather. Also, NEUMANN (1989) relates a poem by ARATUS (315–240 B.C.), which was referred to as Prognostication Through Weather Signs, in an English translation by G.R. Mair (ARATUS, 1921). The poem reads " *If a misty cloud be stretched along the base of a high hill, while the upper peaks shine clear, very bright will be the sky. Fair weather, too, shall thou have, when by sea-verge is seen a cloud low (fog) on the ground, never reaching a height, but penned there like a flat reef of rock''*. In this regard, Pliny the Elder (A.D. 23–79, PLINY, 1971), a Roman historian, admiral, scientist and author, states in his work of Natural History "……. *Mist (fog) coming down from the mountains or falling from the sky or settling in the valleys will promise fine weather.''* These works suggested that fog was recognized for use as a fair weather predictor.

The influence of fog was also felt on historical events. LINDGREN and NEUMANN (1980) describe one such event during the Crimean War, when the Russian empire faced the alliance of Britain, France, and Turkey. The allied forces landed in Crimea in September 1854. Intense fog developed early on the morning of the 5th, just when the Russian forces were launching their first major offensive. The allied forces could not realize what was occurring on the other side. It was stated that "…*for the vapors*, *fog*, *and drizzling mist* obscured the ground to such an extent as to render it impossible to see what was going on at a distance of a few yard.'' This suggests that fog was a major player in this historical event.

The formation of fog and its extent at the surface are not easy to predict. The fog formation does not always occur in calm windless conditions. In fact, the formation of fog associated with turbulent windy conditions was studied at the end of 18th century. SCOTT (1896) stated that fogs with strong winds occurred in the British Isles, and sometimes lasted a month. He also mentioned that the strong wind fogs were accompanied by rain which was frequently heavy. SCOTT (1894) showed that fog occurrence was correlated to strong winds (Beaufort scale of 6), and that there was no clear relationship between weather patterns (e.g., cyclonic or anticyclonic) and fog formation. Scott also stated that the total number of fog cases with strong wind was

estimated to be about 135 over 15 years. The role of aerosols in fog formation was recognized by MENSBRUGGHE (1892) who stated that "*aqueous vapor condenses in the air only in the presence of solid particles around which the invisible vapor becomes a liquid*." The heavy London fog on 10–11 January, 1925 followed the great fog of December 1924 (BONANCINA, 1925). During this episode, two types of fog occurred: 1) unsaturated haze without condensation and 2) fog with liquid characteristics. These fog episodes paralyzed the entire city with very low visibility values. This discussion shows that fog formation and its relation to environmental conditions were known early on but detailed field and modeling works were limited.

The importance of fog and low ceiling in weather forecasting was studied by WILLETT (1928). In his detailed work, he emphasized the importance of condensation nuclei for fog formation. He listed that dust particles with some degree of surface curvature, particles having an electric charge or ions, and hygroscopic particles were facilitating agents to droplet formation. He also proposed a classification for fog and haze based on causes and favorable synoptic conditions. Overall, fogs were classified into two groups: 1) airmass fogs and 2) frontal fogs. Subsequently, he emphasized the importance of all meteorological parameters affecting fog formation. For each group, he then sub-classified them, e.g., advection type, radiation fog, and marine fog, etc. He also summarized the works done by others such as KÖPPEN (1916, 1917), TAYLOR (1917), and GEORGII (1920).

Numerous field studies with a focus on fog and other boundary layer clouds were performed over the last few decades. Among the regions where these experiments took place are the coastal regions off the California coast in the western United States. Review articles on issues of fog that focused on West Coast marine fog and stratocumulus were presented by LEIPPER (1994) and KLOESEL (1992). Among the noteworthy experiments was the CEWCOM project (1977) which consisted of a major set of experiments off the California coast conducted during the 1972–1982 time period under the US Navy Naval Air Systems Command. These series of meso- and micro-meteorological experiments involved a land and sea network of radiosonde observations, ships, aircraft, balloons, and kites. Studies based on observations were complemented by modeling studies. An investigation of low-level stratus/fog was performed by KORACIN *et al.* (2001) using a one-dimensional (1-D) model and observations with results suggesting that radiative cooling and large-scale subsidence was an important factor for fog formation. The interactions between radiative and turbulence processes studied in detail by OLIVER *et al.* (1977; 1978) suggested that radiative cooling at fog top was an important process in the fog life cycle. Similarly, it was shown by WELCH and WIELICKI (1986) that $\sim$5C°/hour cooling occurred during a simulation of warm fog layer in which the liquid water content (LWC) reached 0.3 g m^{-3}. These results were found to be comparable with observations. Radiation fog studies using detailed surface observations were lead by MEYER *et al.* (1986), ROACH *et al.* (1976), and CHOULARTON *et al.* (1981). These authors also focused on various aspects of fog formation and its evolution by using numerical models. FUZZI *et al.*

(1992) carried out the Po Valley Fog Experiment which was a joint effort by several European research groups from five countries. The physical and chemical behavior of the multiphase fog system was studied experimentally by following the temporal evolution of the relevant chemical species in the different phases (gas, droplet, interstitial aerosol) and the evolution of micrometeorological and microphysical conditions, from the pre-fog state, through the whole fog life cycle, to the post-fog period. FUZZI *et al.* (1998) also conducted a second field project called CHEMDROP (CHEMical composition of DROPlets) that took place in the Po Valley region. Their project focused mostly on fog microphysics and chemistry as in the previous field experiment. Ice fog studies (BOWLING *et al.*, 1968; GIRARD and BLANCHET, 2001; GOTAAS and BENSON, 1965) were limited due to the difficulties of measurement ice particles at sizes less than 100 μm (GULTEPE *et al.*, 2001). However, Gotaas and Benson results showed that 10°C/day cooling was due to ice fog occurrence on January 1962. More recently, GULTEPE *et al.* (2006a) and GULTEPE and MILBRANDT (2007) conducted a field project over Eastern Canada for marine fog studies and at a site in the Ontario region for winter warm fog studies with a focus on nowcasting/forecasting issues. These projects contributed to the better understanding of fog physics, and the development of parameterizations for numerical models and remote sensing studies.

In addition to fog formation, development and decay, the artificial dissipation of fog was also studied in the early 1970s. The main objective of these works was to study how fog can be eliminated from a specific area such as over an airport or a shipping port. Because the fog droplets are found in a narrow drop size range e.g., 4–10 μm, by somehow increasing droplet size, the dissipation of fog can occur through coalescence processes. The work by HOUGHTON and RADFORD (1938) was the first to use hygroscopic particle seeding to dissipate fog droplets. JIUSTO *et al.* (1968) studied the possibility of fog dissipation by giant hygroscopic nuclei seeding and stated that the use of carefully controlled sizes and amounts of hygroscopic (NaCl) nuclei can produce significant improvements in visibility. KORNFELD and SILVERMAN (1970) and WEINSTEIN and SILVERMAN (1973) also indicated similar results and stated that if the fog droplet size distribution is known, the seeding nuclei are to be chosen carefully for dissipating the fog. These works suggested that fog dissipation seems possible but its detailed microphysics should be known. Another method used helicopters to dissipate fog on the theoretical basis of turbulent mixing of dry air into the fog layer by the helicopter's downwash (PLANK *et al.*, 1971).

The increased fog water content as dripping water, opposite to the fog dissipating idea, was used as a resource for the ecosystem hydrology and water resources. The Standard Fog Collector (SFC) was developed by SCHEMENAUER AND CERECEDA (1994) which is a 1 m^2 frame with a double layer of 40% shade cloth mesh. It is set up perpendicular to the prevailing wind direction. The collected fog water is routed from the collection trough to a large-capacity tipping bucket gage with data logger to measure the amount and frequency of precipitation. The polypropylene nets similar

to the original SFC over the coastal cliffs and desert areas transform windborne fog and mists into water. Fog catchers use a simple idea in which a fine-mesh netting is placed against the wind that carries fog droplets, so that water would condense on the filaments. At the arid stretches of coastal Chile, Peru, Ecuador, and several other countries around the world, this method was utilized to obtain water from fog droplets. Trees also serve as natural fog catchers (AZEVEDO and MORGAN, 1974); a forest growing in an arid area can provide as much water as rain into the dry soil. They suggested that fog drifting inland is caught by plant leaves, the nutrients contained in the fog as nuclei and dissolved gases become available to the plants. Some nutrients may be absorbed directly by the leaf and the rest become available to the plants via the soil as water drips to the ground.

The number of articles that includes the word "fog" in the American Meteorological Society (AMS) published journals was found to be about 4700, suggesting that there is an abundance of works on this subject. In spite of this extensive body of work, concerns related to fog forecasting/nowcasting still remain because of fog's considerable time and space variability related to interactions among various processes.

Among the reasons behind the difficulties in accurately forecasting/nowcasting fog are the difficulties in detecting fog and representing the physical processes involved. Remote sensing of fog using satellites is very useful but more spectral channels compared to the ones available are needed to improve detection algorithms (ELLROD and GULTEPE, 2007). Lately, a Moderate Resolution Imaging Spectroradiometer (MODIS) base algorithm (BENDIX *et al*., 2006) for fog detection has been developed and includes more channels in the near IR and better resolution (of about 100 m). Although various methods were developed for forecasting and nowcasting applications, the accuracy of these algorithms needs to be assessed further, especially over snow and ice surfaces. From the numerical modeling point of view, important issues are related to the horizontal (PAGOWSKI *et al*., 2004) and vertical (TARDIF, 2007) resolutions, and physical parameterizations (GULTEPE *et al*., 2007b). For instance, if the total droplet number concentration (N_d) is not obtained prognostically, it can be obtained diagnostically as a function of supersaturation or simply fixed (GULTEPE and ISAAC, 2004). It is a well known fact that visibility in fog is directly related to N_d. In the large-scale models, N_d is either not considered or is simply fixed. In most models, visibility is obtained from extinction versus LWC relationships (KUNKEL, 1984), in turn, LWC is obtained using either a simple LWC-T relationship (GULTEPE and ISAAC, 1997) or a prognostic equation (TEIXEIRA, 1999; BERGOT and GUÉDALIA, 1994; BOTT and TRAUTMANN, 2002; PAGOWSKI *et al*., 2004). Therefore, detailed three-dimensional cloud/fog models are needed to better understand issues related to fog, but they are not used extensively because of the computational cost involved in producing operational forecasts (MÜLLER *et al*., 2007; GULTEPE *et al*., 2006b). One-dimensional (1-D) models are cheaper to run and can prove to be useful in certain situations (BERGOT and GUÉDALIA, 1994; BERGOT

et al., 2005; BOTT, 1991). However, their applicability becomes limited in regions of complex and heterogeneous terrain (MÜLLER *et al.*, 2007). The applicability of the different modeling strategies for fog forecasting and various parameterizations requires extensive research.

In order to better evaluate forecasts of fog formation, development, and decay, field observations should be used for verification purposes. This can be done: 1) using carefully analyzed climatological surface data (TARDIF and RASMUSSEN, 2007), 2) *in situ* observations (GULTEPE *et al.*, 2006; GULTEPE *et al.*, 2007b), and 3) remote sensing data (CERMAK and BENDIX, 2006). Detailed studies by TARDIF and RASMUSSEN (2007), HANSEN *et al.* (2007), and HYVARINEN *et al.* (2007) suggest that the climatological data can help in developing better understanding of fog formation, forecasting methods, and organize better field programs (GULTEPE *et al.*, 2006b). In the following sections, fog definition and types, observations (including field and remote sensing observations), models, climatology and statistical methods, and concluding remarks together with discussions will be given in the context of prior achievements and future works.

2. Definition and Fog Classification

The international definition of fog consists of a collection of suspended water droplets or ice crystals near the Earth's surface that lead to a reduction of horizontal visibility below 1 km (5/8 of a statute mile) (NATIONAL OCEANIC AND ATMOSPHERIC ADMINISTRATION, 1995). If the visibility is greater than 1 km, then it is called mist (WMO, 1966). Prevailing visibility is the maximum visibility value common to sectors comprising one-half or more of the horizon circle (MANOBS, 2006). Water droplets and ice crystals, typically 5 to 50 μm in diameter (PRUPPACHER and KLETT, 1997), form as a result of supersaturation generated by cooling, moistening and/or mixing of near surface air parcels of contrasting temperatures. The presence of suspended droplets and/or crystals can render an object undistinguishable to a distant observer and thus causes poor visibility conditions. This occurs through a reduction in the brightness contrast between an object and its background by particle concentration and size-dependent scattering losses of the light propagating between the object and the observer (GAZZI *et al.*, 1997; 2001) and through the blurring effect of forward scattering of light due to the presence of the droplets/crystals (BISSONETTE, 1992).

Several approaches have been used in the classification of fog. It can be based on physical (freezing fog), thermodynamical (mixed phased fog) properties, dynamical processes (mixing and turbulence fog), chemical composition of particles (dry fog), physiographic character of the surface (valley fog), and meteorological features (frontal fog). An earlier work by PETTERSSEN (1956) suggested that fog can also be divided into three subsections: 1) Liquid fog ($T > -10°C$), 2) mixed phase fog

($-10°C > T > -30°C$), and 3) ice fog ($T < -30°C$). These fog types can occur under the various scenarios listed above. One should recognize that the criteria used in this respect do not always occur in a clear-cut fashion as implied by the classification. For example, ice fog may occur at $T = -20°C$ when excessive vapor is used by ice nuclei within a steady-state condition occurring with no mixing processes (GULTEPE *et al.*, 2007b). Usually freezing fog occurs when T gradually decreases below 0°C.

As suggested by the discussion above, fog does occur in a wide variety of conditions. These conditions can be described using various fog types. WILLETT (1928) study, later modified by BYERS (1959), established a classification describing eleven types of fog, each defined by the main physical processes responsible for their formation as well as circumstances in which these processes occur.

The most studied and therefore well-described fog types are those associated with radiative cooling over land. These can be divided among: 1) radiation fog, 2) high-inversion fog, and 3) advection-radiation fog. Radiation fog usually forms near the surface under clear skies in stagnant air in association with an anticyclone. Numerous researchers have devoted efforts to understanding the relationship between the occurrence of this type of fog with the various mechanisms known to influence the evolution of the nocturnal boundary layer. The main mechanism is radiative cooling, but the opposing influences of upward soil heat flux, as well as warming effects and moisture losses through dew deposition from turbulent mixing in the stable boundary layer largely determine the likelihood and timing of radiation fog formation (TAYLOR, 1917; LALA *et al.*, 1975; ROACH, 1976; ROACH *et al.*, 1976; BROWN and ROACH, 1976; PILIÉ *et al.*, 1975; FINDLATER, 1985; TURTON and BROWN, 1987; FITZJARRALD and LALA, 1989; BERGOT and GUÉDALIA, 1994; ROACH, 1995a; DUYNKERKE, 1999). Advection-radiation fog is a coastal phenomenon and results from the radiative cooling of moist air that has been advected over land from the ocean or from any large water body during the previous daylight hours (RYZNAR, 1977). So-called high-inversion fog usually forms in valleys within a deep moist layer capped by a strong inversion (HOLETS and SWANSON, 1981). The inversion results from prolonged radiative cooling and subsidence associated with a persistent anti-cyclone. This type of fog is common during winter in the Central Valley of California (UNDERWOOD *et al.*, 2004).

Another relatively well-studied fog type is associated with the advection of a moist airmass with contrasting temperature properties with respect to the underlying surface and is therefore referred to as advection fog. BYERS (1959) makes the distinction between sea fog, land- and sea-breeze fog, and tropical-air fog even though all are associated with advection of moist warm air over a colder water surface. Sea fog typically occurs as a result of warm marine air advection over a region affected by a cold ocean current, and thus, it is common at sea in locations where boundaries with cold ocean currents can be found, such as the Grand Banks of Newfoundland and areas over the coastal northeastern United States, in the North Pacific, off the west coast of North America and over the British Isles (LEWIS *et al.*,

2004). The frequency of this type of fog is maximized when air with a high dew point initially flows over a sea-surface with a few degrees colder (TAYLOR, 1917; FINDLATER *et al.* 1989; KLEIN and HARTMANN, 1993; ROACH, 1995b; CROFT *et al.*, 1997; CHO *et al.*, 2000). In contrast to this, PILIÉ *et al.* (1979) reported cases where marine fog patches are associated with regions having a warmer ocean surface, where buoyant mixing of the moist near surface air results in saturation of the low-level air. Adding to the complexity, TELFORD and CHAI (1993) report on the dissipation of an existing fog layer over warmer water, with a sensitivity of the fog behavior on the temperature and moisture structure above the fog layer. Once fog has formed, its evolution is largely determined by the influences of radiative cooling at fog top, subsidence, drizzle and the evolution of surface heat and moisture turbulent fluxes as the air flows over sea-surface temperature gradients (FINDLATER *et al.*, 1989). Furthermore, it has been shown that the origin and history of air masses are important factors in the observed variability in the spatial distribution of fog/stratus in the coastal zone (LEWIS *et al.*, 2003). Land- and sea-breeze fogs are purely coastal phenomena and occur when warm moist air over land is transported offshore over the cool coastal ocean, leading to fog formation. This fog may subsequently move over land under the influence of a sea-breeze circulation that sets up during the following afternoon hours. Tropical-air fog is another advection fog type and is associated with long-range transport of tropical air pole-ward along the large-scale latitudinal ocean temperature gradient leading to gradual cooling of the air mass. Advection fog has also been observed over land in winter in the central United States as warm moist air flows over the cooler (sometimes snowy) surface (FRIEDLEIN, 2004).

Another type of fog associated with advection and mixing is the so-called steam fog. It tends to be observed in the Arctic and results from cold air with a low vapor pressure being advected over a relatively warm water surface. The difference in vapor pressure between the air and the water surface leads to evaporation, and mixing of water vapor into the cold air leads to supersaturation and fog (SAUNDERS, 1964; ØKLAND and GOTAAS, 1995; GULTEPE *et al.*, 2003).

Fog may also form as a result of a cloud base lowering all the way to the surface. Some influences have been cited by various authors, mainly dealing with conditions out over the open ocean. For instance, the presence of a sufficiently shallow cloudy marine boundary layer capped by a strong inversion and a sufficiently moist subcloud layer (dew point higher than the sea-surface temperature by a few degrees) have been cited by PEAK and TAG (1989) and TAG and PEAK (1996) as important factors. Furthermore, cloud base lowering has been shown to be tied to the diurnal cycle of stratiform boundary layer clouds related to the interaction of the cloud with radiation (DUYNKERKE and HIGNETT, 1993). The coupling of the cloud layer with the subcloud layer occurs as top-down turbulent mixing is generated by the destabilization induced by the radiative cooling at cloud top. Radiatively cooled air is transported downward by the turbulent eddies, cooling the subcloud layer and thus

leading to a lowering of cloud base (OLIVER *et al.*, 1978; PILIÉ *et al.*, 1979). It has been hypothesized that this process can be aided by the moistening of the subcloud layer by the evaporation of settling cloud droplets or drizzle drops (PILIÉ *et al.*, 1979). Adding to this complex picture, KORAČIN *et al.* (2001) and LEWIS *et al.* (2003) have shown that stratus lowering can occur under the influence of persistent subsidence leading to a decrease in the depth of the marine boundary layer.

Fog forming together with precipitation, often referred to as frontal fog, is described as a common occurrence ahead of warm frontal boundaries (GEORGE, 1940a,b,c; BYERS, 1959; PETTERSSEN, 1969). Its presence has also been documented in regions of extra-tropical cyclones characterized by a transition in precipitation type (STEWART, 1992; STEWART *et al.*, 1995) presumably due to the evaporation of melting or freezing precipitation hydrometeors (DONALDSON and STEWART, 1993). BYERS (1959) further divided the precipitation fog type into three subcategories: pre-frontal, post-frontal and frontal passage fogs. Pre-frontal fog is usually associated with an approaching warm front. The textbook explanation involves the evaporation of warm rain into the stable cold air near the surface, leading to saturation and fog formation. Post-frontal fog usually occurs behind a cold front and is much like pre-frontal fog as the main mechanism is the evaporation of falling precipitation, but is less likely to be widespread as the precipitation bands associated with cold fronts occur over a smaller spatial scale. Frontal passage fogs are said to be associated with the mixing of near saturated air from the warm and cold air masses. This further separation of precipitation-induced fog into subcategories merely describes the various scenarios under which fog is observed and does little in terms of providing a comprehensive description of the physical processes involved.

Finally, upslope fog is associated with the cooling of near-surface moist air resulting from an adiabatic expansion as it is forced to higher elevations, and thus lower pressure, by topography.

This discussion confirms that fog is influenced by numerous factors, spanning multiple spatial and temporal scales. This complexity is central to the persistent difficulty associated with providing accurate fog forecasts.

3. Observations and Models

3.1. Microphysics and Nucleation Processes

Fog formation typically occurs in aerosol-laden surface air under high relative humidity conditions, ranging from undersaturated to slightly supersaturated conditions (PRUPPACHER and KLETT, 1997). Fogs are typically composed of a mixture of micron-size haze (unactivated) particles and activated droplets reaching tens of microns in size (PINNICK *et al.*, 1978; HUDSON, 1980; GERBER, 1981). Compared to convective cloud types where strong updrafts generate higher levels of

supersaturation, fog droplets are generally smaller than cloud droplets and the resulting LWC generally remain small. Most fogs have LWC ranging from 0.01 to 0.4 g m^{-3} (GULTEPE *et al.*, 2007b).

Significant variability has been observed in the droplet size distribution (DSD) in fog. For instance, KUNKEL (1982) reports various shapes in DSDs measured in advection fogs. Some DSDs were characterized by continuous decrease of droplet concentration with size which can simply be parameterized by a power law. Other DSDs were observed to be distinctly bi-modal (GULTEPE *et al.*, 2007b) while others exhibited hybrid characteristics, with the presence of a nearly constant droplet concentration for droplet size between 20 and 30 μm in diameter. Other studies have shown the development of mostly bi-modal DSDs in mature radiation fogs (PILIÉ *et al.*, 1975; ROACH *et al.*, 1976; PINNICK *et al.*, 1978; MEYER *et al.*, 1980; WENDISCH *et al.*, 1998). Processes shaping the microstructure of fog include activation and diffusion growth of droplets, droplet growth related to radiative cooling, as well as turbulent mixing and differential gravitational settling of drops of different size.

Intricate relationships exist between aerosols and fog characteristics since the activation and diffusion growth of droplets depends on the physico-chemical character of the ambient aerosols. For instance, fog is more likely to appear in an environment with large concentrations of aerosols characterized by a low activation supersaturation. Early efforts were performed by J. Aitken in 1880s (KNOTT, 1923). NEIRBURGER and WURTELE (1948) and ELDRIDGE (1966) studied aerosol characteristics and droplet nucleation related to various environmental conditions and they established a dependency between fog microstructure and the characteristics of condensation nuclei. This was later confirmed by HUDSON (1980), who found systematic differences in fog microstructure between polluted urban and cleaner maritime air masses. Fog which formed in polluted environments was characterized by DSDs for which the distinction between inactivated haze particles and activated droplets was not as straightforward as for other clouds types, whereas a clearer demarcation existed in the case of fogs forming in the cleaner maritime air. The complexity of the aerosol-fog microphysics interdependence is an important process in the understanding of fog processes. It has been shown that the occurrence of fog also has an impact on ambient aerosols (YUSKIEWICZ *et al.*, 1998) who summarized aerosol characteristics related to fog formation from measurements of particles in various size ranges (from 0.003 μm up to 47 μm) covering the ultra fine, Aitken, and accumulation modes as well as the activated fog droplets. A comparison of particle number concentrations during fog and clear air conditions suggested a 78% and 65% decrease in ultra fine and accumulation mode particles, respectively. This points out the important scavenging influence of fog.

A numerical study performed by BOTT (1991) provides further insight into the dependence of the fog's microstructure and life cycle on the properties of aerosols. He performed simulations using aerosol size distributions and properties typical of urban, rural and maritime environments and showed that aerosols have a direct

influence on the life cycle of a fog layer. In urban environments fog is characterized by the presence of absorbing aerosols and its formation is delayed by small aerosol number concentrations while higher number concentrations of aerosols yield the highest vertical extent of the fog layer and highest fog water contents. This is related to the radiative effects of absorbing particles, decreasing the incoming solar radiation at the surface and leading to an early initiation of the evening transition of the boundary layer and earlier formation of fog. The fog layer then is allowed to deepen over a longer time period and generate higher LWC under the influence of prolonged cooling at fog top.

In terms of DSD, the main difference between urban and other aerosol models has been found in droplet concentrations for the submicron-size droplets. The concentration of inactivated drops was found to be roughly an order of magnitude higher for the urban aerosols compared to the rural aerosols. Similar results were obtained for rural aerosols compared to maritime aerosols. Supersaturation within the fog was also found to be strongly dependent on aerosol properties. The higher the particle concentration, the lower supersaturation are. However, supersaturation levels have also been found to depend on dynamical processes, such as large supersaturations resulting from turbulent mixing processes (PILIÉ *et al.*, 1975; GERBER, 1991).

Significant high frequency variability in fog droplet concentration and LWC has also been reported in the literature. Observations from GARCÍA-GARCÍA *et al.* (2002) suggest that fog layers are heterogeneous in nature. Small–scale variability in fog microstructure has been observed, with regions of decreased droplet concentration corresponding to broader DSDs. Rapid temporal variations in droplet concentrations, sometimes with amplitudes corresponding to two orders of magnitude (GERBER, 1981; 1991), and LWC from near zero up to 0.5 g m^{-3} have been observed (FUZZI *et al.*, 1992). Some fluctuations are seemingly random while others are found to be quasi-periodic in nature. Random fluctuations are thought to be related to intermittent turbulent mixing events (PILIÉ *et al.*, 1975; GERBER, 1991) while some evidence points to the fact that quasi-periodic oscillations are the result of the interaction between the radiatively induced droplet growth and subsequent depletion of LWC by the enhanced gravitational settling of the larger droplets (BOTT *et al.*, 1990).

Lower frequency variations in the microphysical character of fog layers have also been tied to the various stages defining the life cycle of fog by some authors (PILIÉ *et al.*, 1975; KUNKEL, 1982). Concurrent increases in droplet concentration, mean droplet size and LWC have been observed to occur gradually during the formation stage of fog. This is followed by the mature stage, generally characterized by nearly constant mean droplet concentration and LWC, and a gradually decreasing mean droplet size. JIUSTO (1981) suggested a relationship for visibility as a function of both droplet size and LWC, showing that LWC was directly related to droplet size. The dissipation stage typically occurs as the droplet concentration, mean droplet size, and LWC all decrease.

The variability in the fog microstructure translates into a considerable variability in the reduction of visibility (extinction) induced by the presence of droplets. Numerous efforts have aimed at defining relationships between the overall characteristics of fog and associated visibility reduction. Most have focused on power-law relationships between *LWC* of the fog and its associated extinction coefficient (β) (ELDRIDGE, 1971; TOMASI and TAMPIERI, 1976; KUNKEL, 1984) as

$$\beta = a(LWC)^b, \tag{1}$$

with coefficients determined empirically. Experimental results show considerable variability, with values falling in the range of $65 \leq a \leq 178$ and $0.63 \leq b \leq 0.96$. These values include results reported in GULTEPE *et al.* (2006a) obtained in warm stratiform boundary layer clouds. Some of the variability is related to the different instruments and experimental designs as well as variability in ambient conditions (ex. polluted vs. clean air masses). MEYER *et al.* (1980) took a different approach by establishing an empirical relationship between visibility and the product of total particle concentration and mean diameter. More recently, a relationship between visibility and the product of droplet number concentration (ND) and LWC was proposed by GULTEPE *et al.* (2006a) as

$$Vis_{fi} = \frac{1.002}{(LWC \cdot N_d)^{0.6473}}$$

This approach recognizes the presence of variability in droplet sizes and its role in influencing extinction (visibility) in fog.

In spite of a considerable body of work on fog microphysics, the overall role of interactions between the various processes shaping the microstructure of fog is still not fully understood and properly parameterized. For example, the effects of radiative fluxes on droplet growth are not considered in the growth equations in many fog models. The vertical structure in fog microphysics and its representation in fog models are still not well characterized and understood. In particular, the role of turbulent mixing remains a topic of discussion. Also, the occurrence of ice fog and associated physics still include many unknowns, e.g., ice particle concentration and nucleation, and saturation with respect to ice (MEYERS *et al.*, 1992). The difficulty in obtaining reliable measurements at the small sizes, as for other mixed-phase or ice clouds, contributes to our incomplete understanding. In particular, a multi-year dataset with consistent state-of-the-art instrumentation as shown in GULTEPE *et al.* (2006b) could prove invaluable in efforts to characterize, understand and parameterize the considerable variability in fog microstructure within the various environments.

3.2. Turbulent Fluxes and Surface Conditions

Fog is a boundary layer phenomenon; therefore, its formation and evolution are strongly influenced by surface conditions that are determined by the properties and

current state of the soil and canopy (vegetation or urban) for ground fogs, or by the state of the sea surface for marine fog. Effects of the underlying surface on fogs can be direct when the surface influences the profiles of wind, temperature, humidity, and local circulations through horizontal heterogeneities, or indirect through modification of radiative properties of the atmosphere by microphysical processes and varying aerosol spectra. In this section, only the direct effects of surface conditions on fogs are considered.

Surface cooling or warming is determined by an energy balance composed of incoming and outgoing radiation and heat fluxes in the atmosphere, canopy, and soil. Radiative balance at the surface is influenced by surface albedo and emissivity. The surface interacts with the atmosphere through momentum drag and sensible and latent heat fluxes. Especially in the case of radiation fog, complexities involved in the calculation of fluxes are substantial. Fog observations have a long history and provide a basis for the development and verification of numerical fog models. Detail numerical models can be used for forecasting and, most easily in the one-dimensional form, to investigate the importance of local processes affecting fog development. SIEBERT *et al*. (1992a;b;c) considered the effects of soil and vegetation on surface fluxes. In a detailed study with a one-dimensional soil-vegetation-atmosphere model and using a comprehensive parameterization of surface characteristics, they verified modeled surface fluxes against measurements and performed a series of sensitivity experiments. The experiments demonstrated the important role of vegetation coverage in damping the diurnal temperature amplitude, the significance of soil moisture content, and minimum stomatal resistance of plants in determining the Bowen ratio.

DUYNKERKE (1991) studied the effects of local factors on radiative fogs using a one-dimensional model of soil, vegetation and the atmosphere. He noted that large resistance of the canopy can lead to differences between vegetation and the upper soil temperatures (e.g., up to 10K for grass). This difference is significant for the deposition of dew or frost on the cool canopy (dewfall). Depending on the atmospheric conditions dew can lead to drying of the surface layer that can delay or prevent fog or, adversely, to further cooling of the air and formation of fog (LALA *et al*., 1975; BROWN and ROACH, 1976; DUYNKERKE, 1991; GUÉDALIA and BERGOT, 1994). Formation of dew on vegetation can also occur through distillation when an upward flux of moisture from warm and wet soil reaches the top of the canopy and is followed by condensation on the leaves. The presence of dew can lead to fogs when the surface warms up at sunrise (TARDIF and RASMUSSEN, 2007).

Intense turbulence, which leads to intense vertical mixing, usually has a detrimental effect on radiation fogs and its intensity (though in some cases the opposite can be true, see the discussion below on the role of turbulence in fogs). The most conducive conditions to radiative fog formation occur in stable boundary layers where turbulence is generated through wind shear. Surface roughness, a length scale representing the geometry of surface elements, is a primary factor for shear

generation. Thus fogs are generally less likely to occur over rough (e.g., urban) than over smooth (e.g., field) terrain but either way the air parcel needs to be saturated. Surface processes are rather easier to parameterize for marine fogs which are usually associated with advection of warm air over colder waters and vapor condensation in the cooled surface layer. A reverse process can also occur when cool and relatively dry air is brought over warm waters leading to evaporation from the surface and vapor condensation.

Turbulence and radiative processes can have an important role in fogs characteristics that can be both constructive to their formation, or destructive leading to their dissipation. Observations as well as modeling provide sometimes contradictory answers with regard to this problem (e.g., BROWN and ROACH, 1976; ROACH *et al.*, 1976; LALA *et al.*, 1982), depending on atmospheric conditions. For example, for radiative fogs, enhanced vertical mixing in strong turbulence can lead to droplet evaporation when they mix with the drier air above. On the other hand, fog can form after dew having evaporated from the surface is carried upward with turbulence, and then condenses in the air above. Destabilization of the atmosphere via radiative cooling of stratus tops can also lead to enhanced turbulence and downward mixing of cloud droplets leading to fog as mentioned in section 2.

As of now, modeling often does not provide a clear answer to the role of turbulence since results depend on the parameterization of turbulence and radiative processes, both burdened with significant uncertainty. Development and improvement of turbulence parameterizations in stable stratifications might lead to better understanding and forecasting of fogs. Complexity of turbulence and surface parameterizations plus the required high vertical and horizontal resolutions pose a major obstacle for successful and timely fog forecasts. For this reason, surface conditions and turbulence flux parameterizations will remain a significant research area for fog research and its modeling.

3.3. Remote Sensing Applications

The first goal in the investigation of radiative processes in natural fogs was to learn about the propagation and modification of electromagnetic radiation, and then develop and optimize optical systems to measure horizontal visibility. Pioneer work by GRANATH and HULBURT (1929), HOUGHTON (1931) and STRATTON and HOUGHTON (1931) dealt with absorption and transmission of light by/through fog in solar wavelengths. In the 1960s and 1970s, several studies addressed the relationship between fog properties and broad band extinction/horizontal visibility (e.g., DICKSON and VERN HALES, 1963; ELDRIDGE, 1971). The work was done to better understand the applicability of Koschmieder's law (KOSCHMIEDER, 1924) for various drop size distributions (DSD). To address the needs of the air traffic industry, slant visibility was investigated to find relations to horizontal visibility at ground level, required to estimate the visibility along the touch down path of aircraft through

fog/very low stratus (e.g., FOITZIK, 1947; STALENHOEF, 1974). STEWARD and ESSENWANGER (1982) presented a review paper on the relation between fog properties (DSD, LWC and geometrical thickness) and extinction of electromagnetic radiation at different wavelengths for several types of fog.

The relationship between fog properties and extinction/visibility was investigated for the specific wavelengths (e.g., BARBER and LARSON, 1985) with growing importance over the development of fog detection techniques based on multispectral satellite data. Based on the insights from earlier work, the radiative transfer models for a plane-parallel fog layer, including anisotropic scattering, were developed for the shortwave region (e.g., PAHOR and GROS, 1970), and also used for the infrared region (e.g., KORB and ZDUNKOWSKI, 1970). The state-of-the-art radiative transfer models were used as a part of numerical radiation fog forecasting systems (e.g., BOTT *et al.*, 1990). HUNT (1973) presented an overview of radiative properties of the various cloud types. This publication has since become the basis of many fog-detection algorithms in satellite remote sensing.

Remote sensing of fog started with the development of fog detection techniques based on data obtained from the polar orbiting weather satellites. The detection of fog from satellite images at night was developed using observations from the Advanced Very High Resolution Radiometer (AVHRR) on board the NOAA satellite series. The potential of the delineation of fog/low stratus layers by the dual channel technique using the brightness temperature difference of the 10.8 μm and 3.7 μm bands was highlighted by the work of EYRE *et al.* (1984) and TURNER *et al.* (1986). HUNT (1973) as well as BENDIX and BACHMANN (1991) showed that this was mainly due to the reduced emissivity of clouds with small droplets in the 3.7 μm band. SAUNDERS and GRAY (1985) were able to show that clouds composed of small droplets (e.g., radiation fog) reveal a high reflectivity in the 3.7 μm spectral band. This method has since been widely used by numerous authors and on a wide range of platforms, including geostationary systems (TURNER *et al.*, 1986; ALLAM, 1987; D'ENTREMONT and THOMASON, 1987; BENDIX and BACHMANN, 1991; DERRIEN *et al.*, 1993; BENDIX, 1995a, 2002; ELLROD, 1995; LEE *et al.*, 1997; REUDENBACH and BENDIX, 1998; PUTSAY *et al.*, 2001; UNDERWOOD *et al.*, 2004; ČERMAK and BENDIX; 2007a; GULTEPE *et al.*, 2007a). These studies also suggested that accurate detection of clouds with small-droplets can be used for separation of low stratus from cloud-free regions, snow at the surface, and other cloud types.

The dual-channel technique also could be useful for fog/low stratus detection during daylight (KIDDER and WU, 1984). Because the 3.7 μm channel was not available for the first generation of geostationary systems (e.g., Meteosat MVIRI), in the past, special schemes including structural parameters (e.g., the spatial standard deviation) were used to detect fog/low stratus layers with a limited accuracy (e.g., GÜLS and BENDIX, 1996; KARLSSON, 1989). More recently, BENDIX *et al.* (2006) developed a radiative-transfer-based classification scheme for the MODIS (Moderate Resolution Imaging Spectroradiometer) instrument aboard the Terra and Aqua

satellites. In this approach, the authors derive albedo thresholds for modeled fog layers in a number of spectral channels using radiative transfer computations.

The general problems of daytime approaches using channels in the visible range are diurnal changes in illumination (solar elevation), and the separation of fog from other highly reflective surfaces (e.g., other clouds and ice surfaces). To compensate for these factors, ČERMAK and BENDIX (2007b) introduced a technique consisting of both spectral and spatial tests, allowing for a clear separation of fog/low stratus from other surfaces.

The retrieval of fog and low stratus properties is important for the characterization of the distinction between ground fog and elevated fog. Microphysical properties of fog can be retrieved based on radiative transfer parameterizations. Techniques along these lines have been presented by a number of authors (HEIDINGER and STEPHENS, 2000; MINNIS *et al.*, 1992; GULTEPE *et al.*, 2002; BENDIX, 1995a; NAUSS *et al.*, 2005a;b). In order to distinguish between ground fog and elevated low stratus layers, information on cloud base height is needed. This is obtained using cloud top height and cloud physical thickness as given in ČERMAK (2006). Cloud top height is computed using a cloud-entity-basis analysis, interpolating the marginal heights deduced from terrain and temperature lapse rates. For cloud thickness, a model of cloud liquid water distribution is fitted to liquid water path. A comparison of cloud base height and terrain height yields a decision on ground fog presence.

The dissipation of fog layers was modeled based on remote sensing data and a thermo-dynamical model developed for NOAA AVHRR by REUDENBACH and BENDIX (1998), and more recently, for Meteosat SEVIRI instrument by NAUSS *et al.* (2005a). Calculation of fog dissipation time from the satellite-based analysis techniques needs to be explored because of limited knowledge on the energy budget of a fog layer close to the Earth's surface.

The distinction of fog and low stratus at night remains a problem to be solved (BENDIX, 1995b). The daytime approach suggested by ČERMAK (2006) requires knowledge of cloud liquid water path as input for cloud base height computation. In order to adapt this method for nighttime application, a solid approach to retrieve fog microphysical properties (i.e., liquid water path) are needed. Such a technique based on optical sensors is not currently operational.

A number of approaches have been used to integrate the satellite data with SYNOP observations, model fields, and conventional surface observations (HERZEGH *et al.*, 2006). WRIGHT and THOMAS (1998) and GULTEPE *et al.* (2007) combined a forecast model output with satellite-based observations, and verified the results using surface observations. HUTCHISON *et al.* (2006), ELLROD (2002), and ELLROD and GULTEPE (2007) integrated the cloud base data from observations with satellite retrievals of cloud physical thickness to estimate low cloud base height. In general, satellite observations provide information for fog horizontal coverage and model-based data help to estimate variables such as the visibility, surface temperature and relative humidity, and fog physical thickness. In the future, increasing

accuracy of 3-D fog models can provide a better opportunity to integrate the satellite observations with other data sets.

Current and future active remote sensing instruments can provide great potential to further improve satellite retrievals of fog micro and macro physical properties. They can also be used for calibration of optical sensor algorithms. Among these instruments planned for future missions are satellite-based radars that will likely have the greatest potential by providing liquid water content profiles. Currently, a satellite based cloud radar on the NASA CloudSat satellite (STEPHENS *et al.*, 2002) and an Earth-CARE instrument on the European-Japanese satellite (INGMANN *et al.*, 2006) will likely lead to new methodologies for boundary layer cloud/fog studies.

3.4. Modeling and Forecasting

The formation, dispersion, and decay of fog are the result of complex interactions among microphysical, thermodynamical, and dynamical processes. DUYNKERKE (1991) identified the most important factors for fog formation as follows: Cooling of moist air by radiative flux divergence, mixing of heat and moisture, vegetation, horizontal and vertical wind, heat and moisture transport within soil, horizontal advection, and topographic effects; he also emphasized that atmospheric stability location, and season affect the contributions from each factor.

The presence of clouds increases the incoming longwave radiation at ground level and thus reduces the longwave radiative cooling at the surface, which has great influence on fog formation. Over a complex topography, cold air outflow and pooling, and advection over the heterogeneous landscape are also important in the forecasting of fog. Once the fog has formed, there are additional processes affecting the fog development such as longwave radiative cooling at the fog top, fog microphysics, shortwave radiation, and turbulent mixing. Owing to the complex interactions of various thermodynamic processes, in principle, an accurate 3-D model is needed for reliable fog forecasting.

The earlier work of ZDUNKOWSKI and NIELSEN (1969) included some of the listed processes above, however there was no parameterization for the sedimentation of liquid water. In addition to this, turbulence was treated by means of constant exchange coefficients. The latter were introduced by ZDUNKOWSKI and BARR (1972). A more sophisticated model was developed by BROWN and ROACH (1976), and later further refined by TURTON and BROWN (1987), including new formulations for turbulence exchange coefficients in the nocturnal boundary layer. A similar model was also used by MUSSON-GENON (1987) for the quantitative comparison between computed and observed fog characteristics. DUYNKERKE (1991) also developed a column fog model to study fog evolution and validated it using detailed measurements. A detailed cloud microphysical approach was introduced by BROWN (1980). BOTT *et al.* (1990) developed a fog model with a new two-dimensional treatment of spectral cloud microphysics. They also investigated in detail the interaction of fog

with the atmospheric radiation field. Later, BALLARD *et al.* (1991) used a 3-D numerical weather prediction model to simulate sea fog and they pointed out the importance of initial conditions and vertical resolution. GOLDING (1993) stated that the development of local nocturnal winds in complex terrain often determines the location and timing of fog formation. GUÉDALIA and BERGOT (1994) illustrated in their one-dimensional fog model the importance of advection terms and their role in fog formation and evolution. In addition to the above studies, SIEBERT *et al.* (1992a, b) and VON GLASOW and BOTT (1999) included the new modules into their fog models to simulate the influence of vegetation on the evolution of radiation fogs. In these later models, the evolution of the droplet size distribution and cloud condensation nuclei is explicitly calculated although even today such an approach is computationally very expensive. For a better understanding of the three-dimensional structure of radiation fog and its generation mechanisms, NAKANISHI (2000) applied a large-eddy simulation and found distinct flow regimes in the various stages of the fog layer's evolution. Based on these results, NAKANISHI and NIINO (2004, 2006) developed a second-order turbulence closure appropriate for fog modeling that was used for forecasting in a regional model. Other applications of 3-D models for fog forecasting include PAGOWSKI *et al.* (2004).

In addition to the one-dimensional models, single-column versions of existing 3-D models have been frequently used for the fog studies. (e.g., BRETHERTON *et al.*, 1999; DUYNKERKE *et al.*, 1999; TEIXEIRA, 1999). Recently, the 1-D models have been developed for research and operational purposes e.g., TEIXEIRA and MIRANDA (2001) who combined a set of established parameterizations with the finite-element methods for the vertical discretization. In fact, the microphysical and turbulence parameterizations for numerical weather prediction and climate models were first used as a part of the 1-D forecasting models.

The coupling of 1-D and 3-D models and their integration with observations lead to promising results for fog forecasting. BERGOT *et al.* (2005) clearly demonstrated the necessity of using surface measurements in 1-D models with a local assimilation scheme. CLARK and HOPWOOOD (2001) used a modified single column version of the UK Meteorological Office Unified Model which is driven by an operational 3-D forecasting model. Similarly, MÜLLER (2006) developed a 1-D variational assimilation scheme for surface observations and coupled two 1-D models with several operational 3-D models to produce an ensemble forecast. Currently, parameterized versions of detailed fog microphysics originating from 1-D models were incorporated into 3-D models and were able to improve visibility forecasts (MÜLLER, 2006; GULTEPE *et al.*, 2006b; GULTEPE and MILBRANDT, 2007).

Successful numerical modeling and forecasting of fog depends on the fog type that has to be predicted. Some fog events are largely driven by dynamic processes, such as advection fog and orographic fog (PEACE, 1969; WEICKMANN, 1979; MARKUS *et al.*, 1991; TJERNSTROM, 1993). The results of a study by PEACE (1969) suggested that orographic effects associated with the foothills of the Rocky Mountains tend to

broaden the frequency distribution of fog, and 20 days of heavy fog per year are located along the eastern slopes of the mountains. Obviously, the effective forecast of these fog events depends on the complexity of the underlying atmospheric models. For instance, the correct simulation of orographic fog may only be possible if the model is capable of accurately treating three-dimensional flow over a complex terrain surface, e.g., mountain-valley wind systems (TERRA *et al.*, 2004; BANTA, 1990). Certainly, an adequate cloud model must also be part of the atmospheric model in which simple bulk microphysical cloud schemes (e.g., KESSLER, 1969) have been proven to be sufficient.

If the occurrence of fog is dominated by other than dynamical processes, e.g., atmospheric radiation, turbulence, and the direct interaction between the Earth's surface and the atmosphere, then the numerical fog forecast may become a very difficult task. For instance, owing to the large heterogeneities at the Earth's surface, the fluxes of mass and heat may be highly variable in space and in time, resulting in a corresponding patchy fog. Radiation fog over a heterogeneous Earth's surface is a typical example for a fog that is very difficult to predict (MASON, 1982; BOTT *et al.*, 1990). In the following, the major uncertainties occurring in the numerical simulation of fog events are outlined.

a) Uncertainties for 1-D model simulations

In the simplest approach for the numerical simulation of fog, one-dimensional models of the atmospheric boundary layer are utilized. The basic assumption used in these models is the horizontal homogeneity of the thermodynamic variables. Thus, the evolution of fog is mainly driven by the atmospheric radiation field, turbulent mixing as well as the fluxes of moisture and heat at the Earth's surface. Other dynamic processes such as horizontal advection or large-scale subsidence are usually not considered. At first glance, one might think that in these simplified situations, where dynamical processes are considered to be less important for fog formation, the successful forecast of fog is relatively straightforward. However, the opposite is true. By comparing the numerical results of various one-dimensional models with observations (COST722 workshops), it turned out that, most of the time, the models failed to predict the fog event with reasonable agreement. There are many reasons for this deficiency and the most important are:

- The assumption of horizontal homogeneity is not valid. Certainly, disregarding horizontal gradients of thermodynamic variables in one-dimensional models results in large errors in the time evolution of fog parameters. Some authors (e.g., MUSSON-GENON, 1987; GUÉDALIA and BERGOT, 1994; TEXEIRA and MIRANDA, 2001) tried to avoid this deficiency by introducing the prognostic model equations with additional forcing terms describing horizontal advection processes. However, this treatment may be problematic since horizontal gradients in the one-dimensional models are not considered adequately; therefore, additional assumptions have to be introduced.

- Clouds are not correctly represented. Radiation fogs are characterized by a distinct cooling of the lowest atmospheric layers during the night, i.e., when the thermal emission of the ground is not balanced by the incoming solar radiation. However, the resulting radiative cooling strongly depends on the cloud cover and it increases with decreasing cloud cover. While permanent and complete cloudiness may be treated in the radiative transfer calculations with sufficient accuracy, cases with partial cloudiness cannot be adequately resolved.
- The fluxes of moisture and heat are not adequately treated in heterogeneous surface conditions. Of particular importance for the evolution of radiation fogs are the fluxes of moisture and heat at the Earth's surface. These fluxes strongly depend on the characteristics of the surface regarding vegetation, soil type, soil humidity, and soil temperature. Obviously, these soil characteristics are assumed to be horizontally homogeneous in the one-dimensional models. As a consequence of this, patterns of soil and vegetation cannot be represented adequately in the model. These heterogeneities may, however, be responsible for the patchy structure of fogs that is often observed.
- Atmospheric turbulence is not properly treated, particularly under strongly stable conditions. Although the numerical modeling of atmospheric turbulence has a long history, in many cases, the existing approaches fail to simulate turbulence sufficiently well. This holds, in particular, for situations with strong atmospheric stability, such as the temperature inversion evolving in the lowest atmospheric layers before the onset of radiation fog.

b) Uncertainties for 3-D model simulations

Fog forecasts using operational weather prediction models usually are very difficult. Owing to the relatively coarse grid resolutions in the horizontal (larger than 5 km) as well as in the vertical (grid distances of typically more than 50 m in the lowest atmospheric layers), these models cannot resolve the surface patterns with the necessary detail. As a consequence of this, operational fog forecast is usually performed by means of some proxy data. However, it might be possible to obtain a deterministic 3-D fog model by modifying existing weather prediction models in an appropriate way (MÜLLER, 2006). In these models, the horizontal and the vertical grid resolutions near the ground have been distinctly reduced. Modified grid resolutions influence significantly the parameterizations of the model physics, such as the turbulence and heat and moisture fluxes at the surface that in turn affect the fog evolution.

A comparison of several 3-D fog models has been performed during COST722. In this comparison, three fog episodes have been investigated and the model results have been compared with observations. The preliminary results of this study demonstrated that 3-D fog simulations have to cope with several problems that include:

- The grid resolution of the model must be sufficiently less than a few meters. It is very important to use fine grid resolutions in the horizontal and the vertical

directions. Particularly, the vertical grid distances of the lowest atmospheric layers must be small enough so that the time evolution of the physical processes within atmospheric boundary-layer near the ground can be resolved accurately. For example, a necessary condition for the simulation of radiation fog sometimes requires the evolution of an inversion layer at 10 m height above the surface before the fog forms.

- Horizontal heterogeneities of soil and vegetation must be adequately accounted for. The patchy structure of fog, which is often observed, is largely driven by the heterogeneities of the Earth's surface. Thus, for a realistic fog simulation, it is important to resolve the geographic distribution of soil moisture and vegetation over the resolved model grid area.
- The simulated fog episodes are rather sensitive to the model initial conditions. Usually, numerical models need some spin-up time before the numerical results may be used with confidence. The model intercomparison study during COST722 has shown that sometimes the fog formation strongly depends on the time of model initialization. For example, initializing a fog model at 00 UTC may yield completely different results compared to initializing it at 12 UTC. Also, initializing the models after the fog occurrence likely results in substantial uncertainties related to fog simulations.
- The verification of model results using observations cannot easily be done because numerical output represents a grid area with a spatial scale. On the other hand, observations represent a single point data. This especially, happens along the fog boundaries in the horizontal and vertical scales.

Based on the above-mentioned issues, the use of numerical weather prediction models for fog forecasting/nowcasting is still an issue and needs continued research. Furthermore, 3-D forecasting models for fog prediction should be developed for better forecasting of the various fog types.

3.5. Statistical Forecasting Models

Statistics have been traditionally used in Meteorology as a standard tool in tackling a variety of problems. The statistical approach in this discipline has been reviewed repeatedly (PANOFSKY and BRIER, 1958; WILKS, 1995). In this respect, efforts towards forecasting the occurrence of fog and low cloud base by using statistical or empirical techniques date back well before the widespread use of modern computer technologies, advanced statistically-based advanced computational methodologies and related software packages. A brief survey of the statistical models used in forecasting visibility is made in this section.

At first, the concept of statistical forecasting refers to the *traditional* methodologies of data fitting. In ceiling and visibility forecasting, examples with such traditional methodologies are those using a linear regression (e.g., VISLOCKY and FRITSCH, 1997) and a logistic regression (e.g., HILLIKER and FRITSCH, 1999).

However, new data driven methodologies are now available which can handle the inherent uncertainty in the analysis. The concept of statistical modeling is now-a-days more generic, in the sense that it encompasses a wider range of procedures for treating uncertainty and which have been devised as a result of modern computational methodologies. It is within this context that the term *statistical forecasting* is used in this section and some newer methodologies are reviewed briefly.

Artificial Neural Networks (ANN) are computational methodologies capable of establishing associations between the independent variables (i.e., the predictors) and the dependent variable (i.e., predictand), through the experimentation of a multitude of situations (i.e., learning data set). Information on the relationship between the predictors and the predictand is placed in a net of interacting nodes. Although ANN have been extensively used in atmospheric science (for a review see HSIEH and TANG, 1998; GARDNER and DORLING, 1998; MICHAELIDES *et al.*, 2006), their application in ceiling and visibility forecasting is rather limited. It is only very recently that a rather restricted number of researchers have adopted the use of ANN in the area of statistical ceiling and visibility forecasting (PASINI *et al.*, 2001; COSTA *et al.*, 2006; BREMNES and MICHAELIDES, 2007). A natural question arising is whether ANN have any advantages over the traditional statistical tools mentioned above. MARZBAN *et al.* (2006) compared neural network with linear and logistic regression in forecasting ceiling and low visibilities, and they concluded that the ANN approach yields superior forecast quality.

Fuzzy logic is a methodology to treat uncertainty in systems whose variables are rather qualitative, imprecise or ambiguous. Over the past few years, this methodology has been increasingly adopted as a favorable technique in a variety of environmental issues but has found limited applications in weather prediction. The appropriateness of fog occurrence for treatment with fuzzy logic has been tested with promising results (SUJITJORN *et al.*, 1994; MURTHA, 1995). More recently, PETTY *et al.* (2000) describe a fuzzy logic system for the analysis and prediction of cloud ceiling and visibility. Also HANSEN (2000) reports on the use of such a forecasting system to forecast ceiling and visibility and concludes that the fuzzy system outperforms persistence-based forecasts.

In a decision-making process, a *Decision Tree* is defined as a graphical representation of all the alternatives and the paths by which they may be reached. Decision trees are quite popular tools in many domains and can be powerful prediction tools (see ALMUALLIM *et al.*, 2001). In contrast to neural networks, decision trees represent sets of comprehensible rules. Despite the potential attractiveness of decision trees for weather prediction, there are few examples of applying them; COLQUHOUN (1987) lists a few such applications to meteorological issues. The complexity of the phenomena discussed in this paper makes the determination of ''rules'' a very difficult task. It is probably for this reason that examples of the application of decision trees in forecasting ceiling and visibility are also limited. WANTUCH (2001) presents one such successful attempt.

In terms of expressing the uncertainty which is inherent in any kind of statistical forecasting, two types of forecasting models can be generally identified as *deterministic* and *probabilistic*. *Deterministic* forecasts are statements indicating that the predictand takes some specific values without any notion on the uncertainty involved in forecasting it. In contrast, probabilistic forecasts with use of an uncertainty level are more informative, thus providing the best possible guidance for weather forecasters and other decision makers (LEYTON and FRITSCH, 2003; BREMNES and MICHAELIDES, 2007).

a) Selection of predictand and predictors

With regard to fog forecasting, it is natural to consider visibility (measured by expert observers or by appropriate instrumentation e.g., transmissometers) as the predictand. This is the most widely used predictand in low visibility/fog forecasting. Nevertheless, two early such methods used for forecasting fog formation (SAUNDERS, 1950; CRADDOCK and PRITCHARD, 1951) were designed to predict the fog-point temperature (i.e., the temperature at which radiation fog is formed by nocturnal cooling).

In the appropriateness of the statistical model to build for fog analysis, the second challenge is the selection of the appropriate informative predictors i.e., predictors which are considered to be strongly related to the predictand. In practice, there are numerous potential predictors to choose from, normally far more than would be suitable in any particular model. Although it is possible to employ all the available parameters as predictors in a statistical approach, the resultant prognostic relationship is generally less efficient. As a general *subjective* rule, concerning the choice of the predictors, it is advantageous to retain the lowest number of physically reasonable predictors, thus rendering the prognostic relationship more stable. However, the choice can be based on purely *objective* criteria. A forward stepwise screening algorithm is usually used to select the best predictor variables. In this method, potential predictors are added one at a time to the model. A predictor is retained when, combined with the predictors already selected, it contributes significantly to an additional reduction of variance; otherwise a potential predictor is considered as redundant (VISLOCKY and FRITSCH, 1995, 1997). Nevertheless, other approaches can be adopted too. ROBASKY and WILSON (2006) have recently summarized such objective steps which may be adopted in order to reach a set of predictors. These include the search for synergies within the set of potential predictors; the determination of the forecast models with the best performance by eliminating the least important predictors by a nulling process which is accomplished iteratively.

b) Statistical models versus learning and application data

Depending on a type of data used in developing and/or implementing the prognostic relationships, three approaches are recognized.

In the *Classical method*, both the building and application of the prognostic relationships use exclusively available observational data (VISLOCKY and FRITSCH, 1997). In such a forecast system the future visibility conditions are predicted through a time-lagged statistical relationship built and implemented with data derived from surface or upper level meteorological observations.

The *Perfect Prog method* is described by KLEIN *et al.* (1959). With this approach, in the development of the prognostic relationship, the predictand is related to recorded values of the predictors. In applying the Perfect Prog forecast system, however, the predictors' values are derived exclusively from a Numerical Weather Prediction (NWP) model output (assuming that the predictions are perfect, hence the name of the method).

The third approach is referred to as the *Model Output Statistics (MOS) method* and is described by GLAHN and LOWRY (1972). In this method, both in developing and implementing the statistically established forecast system, predictors are derived from the NWP model output, observations, and climatic data. BOCCHIERI *et al.* (1974) applied linear regression to both observations and output from atmospheric models as predictors in an automated system for predicting ceiling and visibility.

Bearing in mind the above description of the three methods, MOS can be considered as a procedure for optimizing the statistical forecast system's performance by post-processing NWP model output and observations. In the MOS procedure, observations (ceiling and visibility) are correlated to NWP model forecasts (e.g., predicted fields of humidity, precipitable water, vertical velocity, etc), climatic variables and observed parameters. Typically, the predictors based on observations are the most important components in short-range MOS forecasting systems (WMO, 1991). When the latest surface observation is also used as a predictor in the MOS scheme, this appears to have a strong impact on the forecasts.

3.6. Climatology of Fog

The main purposes of studying fog climatology are to better understand the nature of fog and to apply this understanding to better predict its occurrence. Surface observations at airports and climatological stations are a rich source of data for fog climatology. Long records of such observations exist for many sites in the world. Such observations are made following directions given in MANOBS (2006).

Various approaches have been used to devise fog climatologies. One of the most common approaches is the use of the mean annual number of days of fog over a geographic area (e.g., MURACA *et al.* 2001; PEACE 1969). Such analyses are useful for summary views and for visualizing locations that are relatively more prone to fog. When such analyses are stratified according to season, marked differences may be seen (HARDWICK, 1973) and this can provide insights into the seasonal dependence (or lack thereof) of specific fog regimes (TARDIF and RASMUSSEN, 2007). A problem in considering only mean annual or monthly number of days with fog is that such

analyses tend to exaggerate the actual amount of fog, because during any given number of days with fog, fog itself is typically only present for a fraction of the time. For example, PHILLIPS (1990) reported that in Halifax, Nova Scotia, there is on average 15 days with fog in June and 18 days in July. Such reports may give the impression that Halifax is foggier than it actually is: ''half the time.'' However, when the average frequency of fog is analyzed in terms of hours as in Figure 1, then, the true frequency is less than ''half the time.''

Other approaches have also been employed, such as the use of *fog events* as a basis for the identification of important climatological parameters (MEYER and LALA 1990; TARDIF and RASMUSSEN, 2007). This approach seems more intuitive since factors influencing fog formation and its subsequent evolution are not constrained by the arbitrary change from one day to the next at midnight. By focusing on conditions leading to events at one or more locations, these authors were able to ascertain the importance of certain factors involved with fog formation. The occurrence of inland radiation fog during the fall season is driven by the radiative cooling potential (length of the night) and the availability of moisture. Radiation fog has also been shown to occur in spring in coastal plains under the influence of advection inland of moist marine air during the previous afternoon. Advection fog tends to occur in the spring and summer months (as shown in Fig. 1) as this is the time of year where the occurrence of warm air flowing over the cold ocean is maximized.

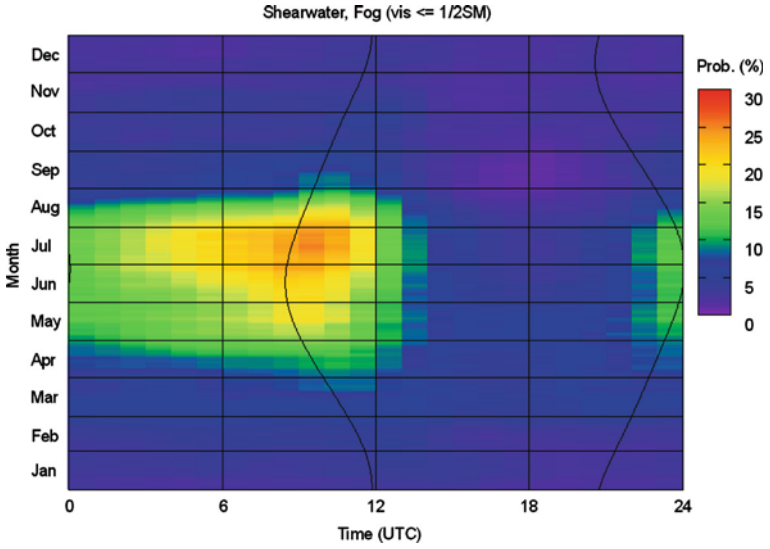

Figure 1
Seasonal-diurnal frequency of fog (visibility ≤ ½ statute mile) at Halifax, Nova Scotia (44°40′N, 63°30′W). Statistics based on complete hourly records from 1971 to 2005 inclusive. Curved gridlines correspond to time of sunrise (left) and time of sunset (right) (HANSEN *et al.*, 2007).

Apart from surface-based observations, data from polar-orbiting satellites have been successfully used by BENDIX (1994, 2002) for fog mapping and to derive the climatology of fog physical parameters for Germany and adjacent areas. Significant spatial variability was observed in microphysical properties between continental radiation fog and the coastal sea fog.

The study of interannual trends in frequency can also yield significant insights into the complex nature of fog. However, great care must be taken in extracting meaningful information from climatological time series. For instance, HANESIAK and WANG (2005) describe procedures for mitigating the effects of "artificial step changes" in long-term climatologies. Such changes are often plainly visible in time series plots of obscuration frequency, appearing as sharp discontinuities in trends and moving averages. Such changes can often be attributed to changes in instrumentation or changes in instrumented site. HANESIAK and WANG (2005), using the logistic regression technique, reported long-term trends in fog conditions in the Canadian Arctic, specifically, decreasing in the east and increasing in the southwest. FORTHUN *et al.* (2006), using simple linear regression, reported finding a variation of trends in the southeast U.S. (decreasing, flat, increasing); however, decreasing trends predominate. LADOCHY (2005) also found decreasing trends in the Los Angeles area on the West Coast of the United States and attributed them to the urbanization of the area and its associated urban heat island. Similar findings have also been reported by WITIW and BAARS (2003) for various cities in South and North America and the United Kingdom, while some cities in the United States and Asia are characterized by increasing trends. Some evidence points to increasing air pollution as a possible reason for fog increase. In many instances, decadal trends at individual sites are often quite distinct, which implies that knowledge of such trends should always be factored into any fog climatology-based forecast application.

The information extracted from fog climatologies can serve as a basis for the development of forecast decision support and guidance tools. For example, MARTIN (1972), using data from 15 airports in the U.S., comprising in excess of 340 years worth of hourly observations, showed how large amounts of climatological data can be condensed into a small amount of relevant conditional climatology information which is useful for short-term forecasting at airports. Frequencies of ceilings in various important flight categories were graphed as a field bounded by two axes: Time of year (month) and time of day (hour UTC). When the data for specific airports were thus graphed, seasonal and diurnal site-specific features in the climatology were revealed. Such seasonal-diurnal (SD) graphs were further refined to display probabilities of various ceilings given additional conditions, such as, probability of persistence of a category of ceiling at 2 hours, and probability of a ceiling category when the wind direction is from a given sector. This work was advanced for its time, however its applicability was limited mainly by two factors: 1) Low computing power meant that analyses for individual airports took a long time and had to be completed manually, and 2) forecasters still had to manually search

through numerous charts to locate specific information applicable to any current forecast situation.

In recent years, increases in computer power and improvements in data analysis methods and in graphic user interfaces have made possible a greatly increased applicability of SD analyses and graphs. FISK (2004) showed how production of such graphs could be semi-automated and how such graphs adapt well to presentation on the internet. TARDIF and RASMUSSEN (2007) use carefully prepared SD graphs to study the nature of various types of fog (types such as precipitation, radiation, advection, and cloud-base-lowering), particularly with respect to characteristic times of formation and times of dissipation of each type of fog.

Future efforts should concentrate on various aspects related to the improvement of how climatologies are put together. In particular, three complicating issues in the analysis of fog climatology from airport observations are: First, how to account for any changes in observational practices (i.e., climate data homogenization); second, how to account for any long-term changes in fog frequency (non-stationarity); and third, what to make of semi-subjective observations of simultaneous fog and precipitation (e.g., in an isolated observation of "1/2SM FG -RASN", it is difficult to know exactly how fog, rain and snow interacted to reduce the visibility to ½ statute mile). The analysis of long-term data from specialized instruments deployed at various sites characterized by distinct fog regimes would provide valuable information about such issues.

4. Discussion and Future Research

This review paper demonstrated that there have been numerous studies related to various aspects of fog. Persisting and emerging challenges, listed below, require further state-of-the-art observations and numerical modeling studies. Fog forms, develops, and dissipates as a result of complex interactions among various local microphysical, dynamical, radiative and chemical processes, boundary layer conditions, and large-scale meteorological processes, e.g., frontal systems. As a result, its definition and classification remain unclear, as evidenced by the numerous different names and classification methodologies used.

Extensive measurements of fog under various conditions are needed to better parameterize its physics, and develop accurate forecasting systems and retrieval techniques using remote sensing data. Further studies using combinations of 3-D and 1-D numerical models, remote sensing methods based on a greater number of channels on satellites (e.g., MODIS), along with the careful statistical analysis of climatological data, could further enhance our understanding of issues related to the improvement of fog nowcasting, and the changing character of fog under global warming conditions. The increased resolution and sampling rates from operational satellites such as GOES-R and METEOSAT could further improve the nowcasting of fog.

To cover the wide spectrum of processes involved in shaping the complexity of fog formation and evolution, a carefully designed high-resolution 3-D fog model is needed. The use of such a model becomes more feasible with the ever-increasing computing power made available with the new computing systems constantly being developed. However, in some situations, the less expensive 1-D models still represent a viable alternative, particularly in the context of frequently updated very short-term ensemble site-specific forecasts issued from initial conditions determined from local observations. Given the inherent uncertainty in initial conditions and inaccuracies of physical parameterizations, fog forecasting with ensembles would also provide a range of possible outcomes and thus improve fog prediction. In this respect, new research on data assimilation techniques and use of novel data sources providing better initial conditions could lead to more accurate forecasts.

Basic research is still needed with respect to the role of turbulence and interactions between the atmosphere and an underlying complex surface, particularly during the stable regime in the nocturnal boundary layer. Data from recent or upcoming field experiments, combined with results from a wide range of models (Direct Numerical Simulation, Large Eddy Simulation, high-resolution 1-D boundary layer and 3-D mesoscale models) are required. Also, fog formation in the turbulent high wind conditions should be investigated, along with fog forming large-scale systems, e.g., frontal systems.

Although there are efforts focusing on ice fog, freezing fog, and mixed-phase fog, their physical understanding is still in question because of limited measurements of particle sizes less than 100 μm and unknown nucleation processes of ice crystals in fog. In fact, ice fog and freezing fog in the northern latitudes can be one of the major hazardous conditions for transportation that include aviation, marine, and land transportation (THUMAN and ROBINSON, 1954; CHARLTON and PARK, 1984). Figure 2 is obtained using surface observations from seven northern Canadian stations. This figure shows that fog occurrence is likely related to rain, snow, or mixed phase precipitation conditions although this figure does not show joint probability distributions. Warm fog and drizzle occur at $T > -10°C$ and ice fog conditions occur at $T < -30°C$. This suggests that field observations should focus on the above T range where models should be able to accurately forecast fog related parameters, e.g., LWC, ice water content (IWC), and visibility values. This figure here also suggests that heterogeneous nucleation at $T > -40°C$ is likely the source of fog particle formations (GULTEPE and ISAAC, 1999; GULTEPE *et al.*, 2001) but ice fog microphysical properties need to be explored for its effect on aviation and transportation.

Statistical and climatological methods should be developed to support the design of future airport locations and next-generation aviation weather applications. Based on carefully crafted climatologies, better field programs can be developed for our further understanding of physical parameterizations for specific applications. For instance, current parameterizations are applied for all types of fog but averaging

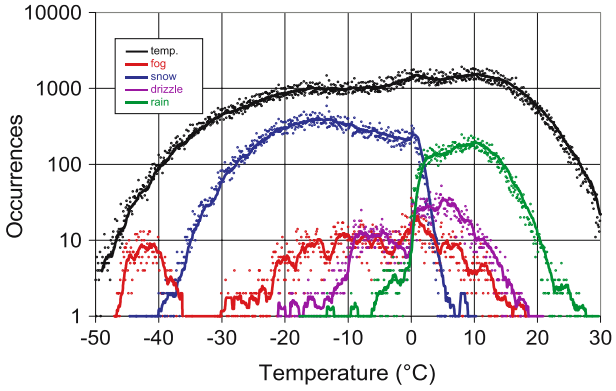

Figure 2
Occurrence of fog, drizzle, snow, rain, and temperature for seven northern Canadian airports. Points represent the number of occurrences in 0.1°C bins. Lines represent the 11-point moving averages.

scales are generally not considered (RÄISÄNEN *et al.*, 2003; GULTEPE and ISAAC, 1999). In fact, the amount (coverage and density) of fog over some scale is a strong function of the averaging scale itself GULTEPE and ISAAC (2007). Therefore the development of scale-dependent parameterizations is an important issue to consider.

Future efforts related to the issues summarized above would be extremely helpful to our better understanding of fog related processes and fog nowcasting/forecasting issues. It is our hope that the papers presented in this special issue serve as the basis for new research challenges and findings on the subject of fog.

Acknowledgments

We wish to thank the scientific contributors to this book and members of the Fog Remote Sensing and Modeling (FRAM), and COST-722 groups, and specifically Dr. Pavol Nejedlik, Scientific Secretary, COST Program—Meteorology Domain, European Science Foundation. We also gratefully acknowledge funding support for this work provided by the Canadian National Search and Rescue Secretariat and Environment Canada. Some additional funding was also provided by the European COST-722 fog initiative project office.

REFERENCES

ALLAM, R. (1987), *The detection of fog from satellites, In Satellite and Radar Imagery Interpretation*, preprints for a Workshop on Satellite and Radar Imagery Interpretation, Meteorological Office College,

Shinfield Park, Berkshire, England, 20–24 July, 1987, Darmstadt Eberstadt, West Germany: EUMETSAT, 1987, 495–505.

ALMUALLIM, H., KANEDA, S., and AKIBA, Y. (2001), *Development and applications of decision trees* [Chapter 3]. In *Expert Systems* (ed. C.T. Leondes), vol. 1, 53–77. (Elsevier).

ARATUS In *Callimachus and Lycrophon, Aratus* (W. Heinemann, London, and Harvard University Press, Cambridge, Mass. 1921), 644 pp.

ARISTOTLE *Meteorologica* (London, W. Heinemann, and Cambridge, Harvard University Press 1962).

AZEVEDO, A. and MORGAN, D.L. (1974), *Fog precipitation in coastal California forests*, Ecology *55*, 1135–1141.

BALLARD, S., GOLDING, B., and SMITH, R. (1991), *Mesoscale model experimental forecasts of the Haar of northeast Scotland*, Monthly Weather Rev. *191*, 2107–2123.

BANTA, R.M. (1990), *The role of mountain flows in making clouds*. Atmospheric Processes over Complex Terrain, Meteor. Monogr., *23*, Am. Meteor. Soc. 229–282.

BARBER, T.L. and LARSON, D.R. (1985), *Visibility related backscatter at 1.06* μm, Appl. Optics *24*, 3523–3525.

BENDIX, J. and BACHMANN, M. (1991), *Ein operationell einsetzbares Verfahren zur Nebelerkennung auf der Basis von AVHRR-Daten der NOAA-Satelliten,* Meteorologische Rundschau *43*, 169–178.

BENDIX, J. (1994), *Fog climatology of the Po Valley,* Rivista di Meteorologia Aeronautica *54, N.3-4,* 25–36.

BENDIX, J. (1995a), *A case study on the determination of fog optical depth and liquid water path using AVHRR data and relations to fog liquid water content and horizontal visibility,* Internat. J. Remote Sensing *16*, 515–530.

BENDIX, J. (1995b), *Ground fog or low level stratus: Decision-making using AVHRR data*. In Proc. 1995 Meteorol. Satellite Data Users' Conf. 385–392, Winchester, U.K.

BENDIX, J. (2002), *A satellite-based climatology of fog and low-level stratus in Germany and adjacent areas,* Atmos. Res. *64*, 3–18.

BENDIX, J., THIES, B., NAUSS, T., and ČERMAK, J. (2006), *A feasibility study of daytime fog and low stratus detection with TERRA/AQUA-MODIS over land*, Meteorol. Applications *13*, 111–125.

BERGOT, T. and GUÉDALIA, D. (1994), *Numerical forecasting of radiation fog. Part I: Numerical model and sensitivity tests,* Monthly Weather Rev. *122*, 1218–1230.

BERGOT, T., CARRER, D., NOILHAN, J., and BOUGEAULT, P. (2005), *Improved site-specific numerical prediction of fog and low clouds: A feasibility study,* Weather and Forecasting *20*, 627–646.

BISSONETTE, L.R. (1992), *Imaging through fog and rain,* Opt. Eng. *31*, 1045–1052.

BOCCHIERI, J.R., CRISCI, R.L., GLAHN, H.R., LEWIS, F., and GLOBOKAR, F.T. (1974), *Recent developments in automated prediction of ceiling and visibility*, J. Appl. Meteor. *13*, 277–288.

BONANCINA, L.C.W. (1925), *Notes on the fog of January 10th–12th, 1925,* Meteor. Mag. *60*, 7–8.

BOTT, A., SIEVERS, U., and ZDUNKOWSKI, W. (1990), *A radiation fog model with a detailed treatment of the interaction between radiative transfer and fog microphysics,* J. Atmos. Sci. *47*, 2153–2166.

BOTT, A. (1991), *On the influence of the physico-chemical properties of aerosols on the life cycle of radiation fogs,* Bound.-Layer Meteor. *56*, 1–31.

BOTT, A. and TRAUTMANN, T. (2002), *PAFOG - a new efficient forecast model of radiation fog and low-level stratiform clouds*. Atmospheric Research, *64*, 191–203.

BOWLING, S.A., OHTAKE, T., and BENSON, C.S. (1968), *Winter pressure systems and ice fog in Fairbanks, Alaska,* J. Appl. Meteor. *7*, 961–968.

BREMNES, J.B. and MICHAELIDES, S.C. (2007), *Probabilistic visibility forecasting using neural networks*, Pure Appl. Geophys. *164*, 7/8, this issue.

BRETHERTON, C.S., KRUEGER, S.K., WYANT, M.C., BECHTOLD, P., VAN MEIJGAARD, E., STEVENS, B., and TEIXEIRA, J. (1999), *A GCSS boundary layer model inter-comparison study of the first ASTEX Lagrangian experiment,* Bound. Layer Meteor. *93*, 341–380.

BROWN, R. and ROACH, W.T. (1976), *The physics of radiation fog: II - A numerical study,* Quart. J. Roy. Meteor. Soc. *102*, 335–354.

BROWN, R. (1980), *A numerical study of radiation fog with an explicit formulation of the microphysics*, Quart. J. Roy. Meteor. Soc. *106*, 781–802.

BYERS, H.R., *General Meteorology,* Third Ed., (McGraw Hill, New York 1959).

CERMAK, J. (2006), *SOFOS – A New Satellite-based Operational Fog Observation Scheme*, Ph.D. Thesis, Philipps-Universität Marburg, Germany.

CERMAK, J. and BENDIX, J. (2007a), *Dynamical nighttime fog/low stratus detection based on Meteosat SEVIRI data – a feasibility study,* Pure Appl. Geophys. *164*, 7/8, this issue.

CERMAK, J. and BENDIX, J. (2007b), *A novel approach to fog/low stratus detection using Meteosat 8 data*, Atmos. Res. in press.

CEWCOM (1977), *Cooperative experimental in West Coast oceanography and meteorology, Multi-platform marine fog study*, Bull. Am. Meteor. Soc. *58*, 1226–1227.

CHOULARTON, T.W., FULLARTON, G., LATHAM, J., MILL, C.S., SMITH, M.H., and STROMBERG, I.M. (1981), *A field study of radiation fog in Meppen, West Germany,* Quart. J. Roy. Meteor. Soc. *107*, 381–394.

CHO, Y.-K., KIM, M.-O., and KIM, B.-C. (2000), *Sea fog around the Korean Peninsula*. J. Appl. Meteor. *39*, 2473–2479.

CLARK, P.A. and HOPWOOD, W.P. (2001), *One-dimensional site-specific forecasting of radiation fog. Part 1: Model formulation and idealized sensitivity studies,* Meteor. Applications *8*, 279–286.

CHARLTON, R.B. and PARK, C. (1984), *Observations of industrial fog, cloud, and preciptation on very cold days*, Atmos. and Ocean *22*, 106–121.

COLQUHOUN, J.R. (1987), *A decision tree method for forecasting thunderstorms and tornadoes*, Weather and Forecasting *2*, 337–345.

COSTA, S.B., CARVALHO, F.O., AMORIM, R.F.C, CAMPOS, A.M.V., RIBEIRO, J.C., CARVALHO, V.N., and DOS SANTOS, D.M.B. (2006), *Fog forecast for the international airport of Maceió, Brazil using artificial neural network,* Proc. 8th ICSHMO, Foz do Iguaçu, Brazil, 24–28 April, 2006, INPE, 1741–1750.

CRADDOCK, J.M. and PRITCHARD, D.L. (1951), *Forecasting the formation of radiation fog—A preliminary approach,* Met. Res. Pap. No. 624 (Meteorological Office, United Kingdom).

CROFT, P.J., PFOST, R.L., MEDLIN J.M., and JOHNSON, G.A. (1997), *Fog forecasting for the Southern Region: A conceptual model approach,* Weather and Forecasting *12*, 545–556.

D'ENTREMONT, R. and THOMASON, L. (1987), *Interpreting meteorological satellite images using a color-composite technique,* Bull. Am. Meteor. Soc. *68*, 762–768.

DERRIEN, M., FARKI, B., HARANG, L., LEGLEAU, H., NOYALET, A., POCHIC, D., and SAIROUNI, A. (1993), *Automatic cloud detection applied to NOAA-11 / AVHRR imagery,* Remote Sensing of Environment *46*, 246–267.

DICKSON, D.R. and VERN HALES, J. (1963), *Computation of visual range in fog and low clouds,* J. Appl. Meteor. *2*, 281–285.

DONALDSON, N.R. and STEWART, R.E. (1993), *Fog induced by mixed-phase precipitation*, Atmos. Res. *29*, 9–25.

DUYNKERKE, P.G. (1991) *Radiation fog: A comparison of model simulation with detailed observations,* Monthly Weather Rev. *119*, 324–341.

DUYNKERKE, P.G. and HIGNETT, P. (1993), *Simulation of diurnal variation in a stratocumulus-capped marine boundary layer during FIRE*, Monthly Weather Rev. *121*, 3291–3300.

DUYNKERKE, P.G. (1999) *Turbulence, radiation and fog in Dutch stable boundary layers*, Bound.-Layer Meteor. *90*, 447–477.

DUYNKERKE, P.G., JONKER, P.J., CHLOND, A., VAN ZANTEN, M.C., CUXART, J., CLARK, P., SANCHEZ, E., MARTIN, G., LENDERINK, G., and TEIXEIRA, J. (1999), *Intercomparison of three- and one-dimensional model simulations and aircraft observations of stratocumulus,* Bound. Layer Meteorol. *92*, 453–487.

ELDRIDGE, R.G. (1971), *The relationship between visibility and liquid water content of fog,* J. Atmos. Sci. *28*, 1183–1186.

ELLROD, G.P. (1995), *Advances in the detection and analysis of fog at night using GOES multispectral infrared imagery*, Weather and Forecasting *10*, 606–619.

ELLROD, G.P. (2002), *Estimation of low cloud base heights at night from satellite infrared and surface temperature data*, National Weather Digest *26*, 39–44.

ELLROD, G.P. and GULTEPE, I. (2007), *Inferring low cloud base heights at night for aviation using satellite infrared and surface temperature data*, Pure Appl. Geophys. *164*, 7/8, in this issue.

EYRE, J.R., BROWNSCOMBE, J.L., and ALLAM, R.J. (1984), *Detection of fog at night using Advanced Very High Resolution Radiometer (AVHRR) imagery*, Meteor. Mag. *113*, 266–271.

FINDLATER, J. (1985), *Field investigations of radiation fog formation at outstations*, Meteor. Mag. *114*, 187–201.

FINDLATER, J., ROACH, W.T., and MCHUGH, B.C. (1989), *The Haar of North-East Scotland*, Quart. J. Roy. Meteor. Soc. *115*, 581–608.

FITZJARRALD, D.R. and LALA, G.G. (1989), *Hudson Valley Fog Environments*, J Appl. Meteor. *28*, 1303–1328.

FISK, C. (2004), *Two-way (Hour-Month) Time Section Plots as a Tool for Climatological Visualization and Summarization,* 14th Conf. Appl. Climatology, Am. Meteor. Soc. 11–15 January 2004, Seattle, Washington.

FOITZIK, L. (1947), *Theorie der Schrägsicht*. Zeitschrift für Meteorologie *6*, 161–175.

FORTHUN, G.M., JOHNSON, M.B., SCHMITZ, W.G., BLUME, J., and CALDWELL, R.J. (2006), *Trends in fog frequency and duration in the southeast United States*, Phys. Geography *27*, 206–222.

FRIEDLEIN, M.T. (2004), *Dense fog climatology. Chicago O'Hare International Airport, July 1996–April 2002*, Bull. Am. Meteor. Soc. *85*, 515–517.

FUZZI, S., FACCHINI, M.C., ORSI, G., LIND, J.A., WOBROCK, W., KESSEL, M., MASER, R., JAESCHKE, W., ENDERLE, K.H., ARENDS, B.G.,, BERNER, A., SOLLY, A., KRUISZ, C., REISCHL, G., PAHL, S., KAMINSKI, U., WINKLER, P., OGREN, J.A., NOONE, K.J., HALLBERG, A., FIERLINGER-OBERLINNINGER, H., PUXBAUM, H., MARZORATI, A., HANSSON, H.-C., WIEDENSOHLER, A., SVENNINGSSON, I.B., MARTINSSON, B.G., SCHELL, D., and GEORGII, H.W. (1992), *The Po Valley fog experiment 1989. An overview,* Tellus *44B*, 448–468.

FUZZI, S., LAJ, P., RICCI, L., ORSI, G., HEINTZENBERG, J., WENDISCH, M., YUSKIEWICZ, B., MERTES, S., ORSINI, D., SCHWANZ, M., WIEDENSOHLER, A., STRATMANN, F., BERG, O.H., SWIETLICKI, E., FRANK, G., MARTINSSON, B.G., GÜNTHER, A., DIERSSEN, J.P., SCHELL, D., JAESCHKE, W., BERNER, A., DUSEK, U., GALAMBOS, Z., KRUISZ, C., MESFIN, N.S., WOBROCK, W., ARENDS, B., and TEN B.H., (1998), *Overview of the Po Valley fog experiment 1994 (CHEMDROP)*, Contr. Atmos. Phys. *71*, 3–19.

GARCÍA-GARCÍA, F., VIRAFUENTES, U., and MONTERO-MARTINEZ, G. (2002), *Fine-scale measurements of fog-droplet concentrations: A preliminary assessment,* Atmos. Res. *64*, 179–189.

GARDNER, M.W. and DORLING, S.R. (1998), *Artificial neural networks (the multilayer perceptron)—A review of applications in the atmospheric sciences*, Atmos. Environ. *32*, 2627–2636.

GAZZI, M., VINCENTINI, V., and PESCI, C. (1997), *Dependence of a black target's apparent luminance on fog droplet size distribution,* Atmos. Environ. *31*, 3441–3447.

GAZZI, M., GEORGIADIS, T., and VINCENTINI, V. (2001), *Distant contrast measurements through fog and thick haze*, Atmos. Environ. *35*, 5143–5149.

GEORGII, W. (1920), *Die Ursachen der Nebelbildung,* Annalen der Hydrographie und Maritimen Meteorologie *48*, 207–222.

GEORGE, J.J. (1940a), *Fog: Its causes and forecasting with special reference to eastern and southern United States (1),* Bull. Am. Meteor. Soc. *21*, 135–148.

GEORGE, J.J. (1940b), *Fog: Its causes and forecasting with special reference to eastern and southern United States (1),* Bull. Am. Meteor. Soc. *21*, 261–269.

GEORGE, J.J. (1940c), *Fog: Its causes and forecasting with special reference to eastern and southern United States (1),* Bull. Am. Meteor. Soc. *21*, 285–291.

GERBER, H.E. (1981), *Microstructure of a radiation fog*, J. Atmos. Sci. *38*, 454–458.

GERBER, H. (1991), *Supersaturation and droplet spectral evolution in fog*, J. Atmos. Sci. *48*, 2569–2588.

GIRARD, E. and BLANCHET, J.-P. (2001), *Simulation of arctic diamond dust, ice fog, and thin stratus using an explicit aerosol–cloud–radiation model*, J. Atmos. Sci. *58*, 1199–1221.

GLAHN, H.R. and LOWRY, D.A. (1972), *The use of model output statistics (MOS) in objective weather forecasting,* J. Appl. Meteor. *11*, 1203–1211.

GOLDING, B.W. (1993), *A study of the influence of terrain on fog development,* Monthly Weather Rev. *121*, 2529–2541.

GOTAAS, Y. and BENSON, C.S. (1965), *The effect of suspended ice crystals on radiative cooling*, J. App. Meteor. *4*, 446–453.

GRANATH, L.P. and HULBURT, E.O. (1929), *The absorption of light by fog,* Phys. Rev. *34*, 140–144.

GUÉDALIA, D. and BERGOT, T. (1994), *Numerical forecasting of radiation fog. Part II: A comparison of model simulations with several observed fog events,* Monthly Weather Rev. *122*, 1231–1246.

GÜLS, I. and BENDIX, J. (1996), *Fog detection and fog mapping using low cost Meteosat-WEFAX transmission*, Meteor. Applications *3*, 179–187.

GULTEPE, I. and ISAAC, G.A., (1997), *Relationship between liquid water content and temperature based on aircraft observations and its applicability to GCMs*, J. Climate *10,* 446–452.

GULTEPE, I. and ISAAC, G.A. (1999), *Scale effects on averaging of cloud droplet and aerosol number concentrations: observations and models,* J. Climate *12,* 1268–1279.

GULTEPE, I., ISAAC, G.A., and COBER, S.G. (2001), *Ice crystal number concentration versus temperature for climate studies*, Inter. J. of Climatology *21*, 1281–1302.

GULTEPE, I., ISAAC, G.A., and COBER, S.G. (2002), *Cloud microphysical characteristics versus temperature for three Canadian field projects*, Annales Geophysicae *20*, 1891–1898.

GULTEPE, I., ISAAC, G., MACPHERSON, I., MARCOTTE, D., and STRAWBRIDGE, K. (2003), *Characteristics of moisture and heat fluxes over leads and polynyas, and their effect on Arctic clouds during FIRE.ACE,* Atmos. and Ocean *41*, 15–34.

GULTEPE, I. and ISAAC, G. (2004), *An analysis of cloud droplet number concentration (N_d) for climate studies: Emphasis on constant N_d,* Quart. J. Roy. Meteor. Soc. *130*, Part A, 2377–2390.

GULTEPE, I., MÜLLER, M.D., and BOYBEYI, Z. (2006a), *A new warm fog parameterization scheme for numerical weather prediction models,* J. Appl. Meteor. *45*, 1469–1480.

GULTEPE, I., COBER, S.G., KING, P., ISAAC, G., TAYLOR, P., and HANSEN, B. (2006b), *The Fog Remote Sensing and Modeling (FRAM) Field Project And Preliminary Results,* AMS 12th Cloud Physics Conference, July 9–14, 2006, Madison, Wisconsin, USA, Print in CD, P4.3.

GULTEPE, I. and MILBRANDT, J. (2007), *Microphysical observations and mesoscale model simulation of a warm fog case during FRAM project*, Pure Appl. Geophys. *164*, 7/8, this issue.

GULTEPE, I. and ISAAC, G.A. (2007), *Cloud fraction parameterization as a function of mean cloud water content and its variance using in-situ observation*, Geophys. Res. Lett., *34*, L07801, doi:10.1029/2006GL028223.

GULTEPE, I., PAGOWSKI, M., and REID, J. (2007a), *Using surface data to validate a satellite based fog detection scheme,* Weather and Forecasting, in press.

GULTEPE, I., COBER, S.G., ISAAC, G.A., HUDAK, D., KING, P., TAYLOR, P., GORDON, M., RODRIGUEZ, P., HANSEN, B., and JACOB, M. (2007b), *The fog remote sensing and modeling (FRAM) field project and preliminary results,* Bull. Am. Meteor. Soc. accepted preproposal.

HANESIAK, J.M. and WANG, X.L. (2005), *Adverse-weather trends in the Canadian Arctic*, J. Climate *18*, 3140–3156.

HANSEN, B.K. (2000), *Analog forecasting of ceiling and visibility using fuzzy sets*, 2nd Conference on Artificial Intelligence, American Meteorological Society, 1–7.

HANSEN, B., GULTEPE, I., KING, P., TOTH, G., and MOONEY, C. (2007), *Visualization of seasonal-diurnal climatology of visibility in fog and precipitation at Canadian airports,* AMS Annual Meeting, 16th Conf. Appl. Climatology, San Antonio, Texas, 14–18 January, 2007, CD.

HARDWICK, W.C. (1973), *Monthly fog frequency in the continental United States,* Monthly Weather Rev. *101*, 763–766.

HEIDINGER, A.K. and STEPHENS, G.L. (2000), *Molecular line absorption in a scattering atmosphere. Part II: Application to remote sensing in the O_2 A-band,* J. Atmos. Sci. *57*, 1615–1634.

HERZEGH, P., WIENER, G., BANKERT, R., BENJAMIN, S., BATEMAN, R., COWIE, J., HADJIMICHAEL, M., TRYHANE, M., and WEEKLEY, B. (2006), *Development of FAA National Ceiling and Visibility products: Challenges, strategies and progress*, Perprints 12th Conference on Aviation Range and Aerospace Meteorology, Am. Meteor. Soc., Atlanta, GA, 30. Jan.-2 Feb., 2006. P1.17 in CD version.

HILLIKER, J.L. and FRITSCH, J.M. (1999), A*n observations-based statistical system for warm-season hourly probabilistic forecasts of low ceiling at the San Francisco International Airpor*t, J. Appl. Meteor. *38*, 1692–1705.

HSIEH, W.W. and TANG, B. (1998), *Applying neural network models to prediction and data analysis in meteorology and oceanography*, Bull. Am. Meteor. Soc. *79*, 1855–1870.

HOLETS, S. and SWANSON, R.N. (1981), *High-inversion fog episodes in Central California,* J. Appl. Meteor. *20*, 890–899.

HOUGHTON, H.G. (1931), *The transmission of visible light through fog,* Physical Rev. *38*, 152–158.

HOUGHTON, H.G. and RADFORD, W.H. (1938), *On the local dissipation of warm fog*. Papers Phys. Ocean. Meteor. *6*, 3, 63 pp.

HUDSON, J.G. (1980), *Relationship between fog condensation nuclei and fog microstructure*, J. Atmos. Sci. *37*, 1854–1867.

HUNT, G.E. (1973), *Radiative properties of terrestrial clouds at visible and infrared thermal window wavelengths*, Quart. J. Roy. Meteor. Soc. *99*, 346–369.

HUTCHISON, K.D., PEKKER, T., and SMITH, S. (2006), *Improved retrievals of cloud boundaries from modis for use in air quality modeling,* Atmos. Environ. *40*, 5798–5806.

HYVARINEN, O., JULKUNEN, J., and NIETOSVAARA, V. (2007), *Climatological tools for low visibility forecasting,* Pure Appl. Geophys. *164*, 7/8, this issue.

INGMANN, P., WEHR, T., and E.J.M.A. GROUP (2006), *EarthCARE—A new mission providing global cloud and aerosol profiles,* Proc. 2005 EUMETSAT Meteorological Satellite Conference. EUMETSAT Publication P.46, S6–02. 426–431.

JIUSTO, J.E., PILIE, R.J., and KOCMOND, W.C. (1968), *Fog modification with giant hygroscopic nuclei,* J. Appl. Meteor. *7*, 860–869.

JIUSTO, J.E. *Fog Structure. Clouds, their Formation, Optical Properties, End Effects* (eds. P.V. Hobbs and A. Deepak) (Academic Press 1981), pp. 187–239.

KARLSSON, K.-G. (1989), *Development of an operational cloud classification model,* Internat. J. Remote Sensing *10*, 687–693.

KESSLER, E. (1969), *On the distribution and continuity of water substances in atmospheric circulations,* Meteor. Monographs, Am. Meteor. Soc. 84 pp.

KIDDER, S.Q. and WU, H.-T. (1984), *Dramatic contrast between low clouds and snow cover in daytime 3.7 μm imagery*, Monthly Weather Rev. *112*, 2345–2346.

KLEIN, S.A. and HARTMANN, D.L. (1993), *The seasonal cycle of low stratiform clouds*, J. Climate *6*, 1587–1606.

KLEIN, W.H., LEWIS, B.M., and ENGER, I. (1959), *Objective prediction of five-day mean temperatures during winter*, J. Meteorol. *16*, 672–682.

KLOESEL, K.A. (1992), *A 70-year history of marine stratocumulus cloud field experiments off the coast of California.* Bull. Am. Meteor. Soc. *73*, 1581–1585.

KNOTT, C.G., *Collected Scientific Papers of John Aitken* (Cambridge University Press 1923).

KÖPPEN, W. (1916), *Landnebel und Seenebel, Part I,* Annalen der Hydrographie und maritimen Meteorologie *44*(5), 233–257.

KÖPPEN, W. (1917), *Landnebel und Seenebel, Part II,* Annalen der Hydrographie und maritimen Meteorologie *45*(10), 401–405.

KORACIN, D., LEWIS, J., THOMPSON, W.T., DORMAN, C.E., and BUSINGER, J.A. (2001), *Transition of stratus into fog along the California Coast: Observations and modeling*, J. Atmos. Sci. *58*, 1714–1731.

KORB, G. and ZDUNKOWSKI, W. (1970), *Distribution of radiative energy in ground fog,* Tellus *22*, 309–320.

KORNFELD, B.A. and SILVERMAN, B.A. (1970), *A comparison of the warm fog clearing capabilities of some hygroscopic materials,* J. App. Meteor. *9*, 634–638.

KOSCHMIEDER, H. (1924), *Theorie der horizontalen Sichtweite*, Beiträge zur Physik der freien Atmosphäre *12*, 33–53 and 171–181.

KUNKEL, B.A. (1982), *Microphysical Properties of Fog at Otis AFB,* Environmental Research Paper 767, AFGL-TR-82-0026, Meteorology Division, Air Force Geophysics Laboratory, Hanscom AFB, Massachusetts.

KUNKEL, B.A. (1984), *Parameterization of Droplet Terminal Velocity and Extinction Coefficient in Fog Models*, J. Climate Appl. Meteor. *23*, 34–41.

LADOCHY, S. (2005), *The disappearance of dense fog in Los Angeles: Another urban impact?*, Physical Geography *26*, 177–191.

LALA, G.G., MANDEL, E., and JIUSTO, J.E. (1975), *A numerical investigation of radiation fog variables,* J. Atmos. Sci. *32*, 720–728.

LALA, G.G., JIUSTO, J.E., MEYER, M.B., and KOMFEIN, M. (1982), *Mechanisms of radiation fog formation on four consecutive nights*, Preprints, Conf. on Cloud Physics, Nov. 15–18, 1982, Chicago, IL, AMS, Boston, MA, 9–11.

LEE, T.E., TURK, F.J., and RICHARDSON, K. (1997), *Stratus and fog products using GOES-8-9 3.9-μm data,* Weather and Forecasting, *12*, 664–677.

LEIPPER, D.F. (1994), *Fog on the US West Coast: A review*, Bull. Am. Meteor. Soc. *75*, 229–240.

LEWIS, J., KORAČIN, D., RABIN, R., and BUSINGER, J. (2003), *Sea fog off the California Coast: Viewed in the context of transient weather systems,* J. Geophys. Res. *108*(D15), 4457, doi:10.1029/2002JD002833, 6-1 to 6-17.

LEWIS, J.M., KORAČIN, D., and REDMOND, K.T. (2004), *Sea fog research in the United Kingdom and United States: A historical essay including outlook*, Bull. Am. Meteor. Soc. *85*, 395–408.

LEYTON, S.M. and FRITSCH, J.M. (2003), *Short-term probabilistic forecasts of ceiling and visibility utilizing high-density surface weather observations*, Weather and Forecasting *18*, 891–202.

LINDGREN, S. and NEUMANN, J. (1980), *Great historical events that were significantly affected by the weather: 5, Some meteorological events of the Crimean War and their consequences*, Bull. Am. Meteor. Soc. *61*, 1570–1583.

MANOBS (2006), *Manual of surface weather observations, meteorological service of Canada,* environment canada. Available online at http://www.mscsmc.ec.gc.ca/msb/manuals_e.cfm. 369 pp.

MARKUS, M.J., BAILEY, B.H., STEWART, R., and SAMSON, P.J. (1991), *Low-level cloudiness in the Appalacian region,* J. Appl. Meteor. 30, 1147–1162.

MARTIN, D.E. (1972), *Climatic presentations for short-range forecasting based on event occurrence and reoccurrence profiles,* J. Appl. Meteor. *11*, 1212–1223.

MARZBAN, C., LEYTON, S.M., and COLMAN, B. (2006), *Ceiling and visibility forecasting via neural nets*, Weather and Forecasting (accepted).

MASON, J. (1982), *The physics of radiation fog,* J. Meteor. Soc. Japan *60*, 486–498.

MENSBRUGGHE, V. (1892), *The formation of fog and of clouds, translated from Ciel et Terre,* Symons's Monthly Meteor. Magazine *27*, 40–41.

MEYER, M.B., JIUSTO, J.E., and LALA, G.G. (1980), *Measurement of visual range and radiation-fog (haze) microphysics*, J. Atmos. Sci. *37*, 622–629.

MEYER, M.B. and LALA, G.G. (1986), FOG-82: *A cooperative field study of radiation fog,* Bull. Am. Meteor. Soc. *65*, 825–832.

MEYER, M.B. and LALA, G.G. (1990), *Climatological aspects of radiation fog occurrence at Albany, New York*, J. Climate *3*, 577–586.

MEYERS, M.P., DEMOTT, P.J., and COTTON, W.R. (1992), *New primary ice nucleation parameterizations in an explicit cloud model*, J. Appl. Meteor. *31*, 708–721.

MICHAELIDES, S.C., TYMVIOS, F.S., and KALOGIROU, S., *Artificial neural networks for meteorological variables pertained to energy and renewable energy applications* [Chapter 2]. In *Artificial Intelligence in Energy and Renewable Energy Systems* (ed. S. Kalogirou) (Nova Science Publishers, Inc. 2006).

MINNIS, P., HECK, P.W., YOUNG, D.F., FAIRALL, C.W., and SNIDER, J.B. (1992), *Stratocumulus cloud properties derived from simultaneous satellite and island-based instrumentation during FIRE*, J. Appl. Meteor. *31*, 317–339.

MÜLLER, M.D. (2006), *Numerical simulation of fog and radiation in complex terrain,* Ph.d. Thesis, University of Basel, Stratus 12. 103 pp.

MÜLLER, M.D., SCHMUTZ, C., and PARLOW, E. (2007), A one-dimensional ensemble forecast and assimilation system for fog prediction, Pure Appl. Geophys. *164*, 7/8 this issue.

MURACA, G., MACIVER, D.C., AULD, H., and URQUIZO, N. (2001), *The climatology of fog in Canada,* Proc. 2nd Internat. Conf. *Fog and Fog Collection*, St. John's, Newfoundland, 15–20 July, 2001.

MURTHA, J. (1995), *Applications of fuzzy logic in operational meteorology, Scientific Services and Professional Development Newsletter*, Canadian Forces Weather Service, 42–54.

MUSSON-GENON, L. (1987), *Numerical simulations of a fog event with a one-dimensional boundary layer model*, Monthly Weather Rev. *115*, 592–607.

NAKANISHI, M. (2000), *Large-eddy simulation of radiation fog,* Boundary-Layer Meteorol. *94*, 461–493.

NAKANISHI, M. and NIINO, H. (2004), *An improved Mellor-Yamada level-3 model with condensation physics: its design and verification*, Boundary-Layer Meteorol. *112*, 1–31.

NAKANISHI, M., and NIINO, H. (2006), *An improved Mellor-Yamada level-3 model: Its numerical stability and application to a regional prediction of advection fog*, Boundary-Layer Meteorol. *119*, 397–407.

National Oceanic and Atmospheric Administration (1995), *Surface weather observations and reports, Federal Meteorological Handbook No. 1*, 94 pp. [Available from Department of Commerce, NOAA, Office of the Federal Coordinator for Meteorological Services and Supporting Research, 8455 Colesville Road, Suite 1500, Silver Spring, MD, 20910.

Nauss, T., Čermak, J., Kokhanovsky, A., Reudenbach, C., and Bendix J. (2005a), *Satellite based retrieval of cloud properties and their use in rainfall retrievals and fog detection*, Photogrammetrie – Fernerkundung – Geoinformation *3*, 209–218.

Nauss, T., Kokhanovsky, A.A., Nakajima, T.Y., Reudenbach, C., and Bendix J. (2005b), *The intercomparison of selected cloud retrieval algorithms,* Atmos. Res. *78*, 46–78.

Neiburger, M. and Wurtele, M.G. (1949), *On the nature and size of particles in haze, fog, and stratus of the Los Angeles region.* Chemical Reviews, Baltimore, *44*, 321–335.

Neumann, J. (1989), *Forecasts of fine weather in the literature of classical antiquity,* Bull. Am. Meteor. Soc. *70*, 46–48.

Økland, H. and Gotaas, Y. (1995), *Modelling and prediction of steam fog,* Beitr. zur Phys. der Atmos. *68*, 121–131.

Oliver, D.A., Lewellen, W.S., and Williamson, G.G. (1978; 1977), *The Interaction between Turbulent and Radiative Transport in the Development of Fog and Low-Level Stratus,* J. Atmos. Sci. *35*, 301–316.

Peace, R.L. (1969), *Heavy-fog regions in the conterminous united states*, Monthly Weather Rev. 97, 116–123.

Pagowski, M., Gultepe, I., and King, P. (2004), *Analysis and modeling of an extremely dense fog event in southern Ontario*, J. Appl. Meteor. *43*, 3–16.

Pahor, S. and Gros, M. (1970), *Optical properties of thick fog layers,* Tellus *22*, 321–326.

Panofsky, H.A. and Brier, G.W. (1958), *Some Applications of Statistics to Meteorology,* (Pennsylvania State University, University Park, PA, 1958) 224 p.

Pasini, A., Pelino, V., and Potestà, S. (2001), *A neural network model for visibility nowcasting from surface observations: Results and sensitivity to physical input variables*, J. Geophys. Res. *106*, *D14*, 14951–14959.

Peace, R.L., Jr. (1969), *Heavy-fog regions in the conterminous United States*, Monthly Weather Rev. *97*, 116–123.

Peak, J.E. and Tag, P.M. (1989), *An expert system approach for prediction of maritime visibility obscuration*, Monthly Weather Rev. *117*, 2641–2653.

Petterssen, S., *Weather Analysis and Forecasting,* Second Edition, Vol. 2, (McGraw-Hill Publ. Inc., New York 1956) 266p.

Petterssen, S., *Introduction to Meteorology*, Third Edition, (McGraw-Hill Publ. Inc., New York 1969) 333p.

Petty, K., Carmichael, B., Wiener, G., Petty, M., and Limber, M. (2000), *A fuzzy logic system for the analysis and prediction of cloud ceiling and visibility,* Preprints Ninth Conference on Aviation, Range, and Aerospace Meteorology, Orlando, Fl., Am. Meteor. Soc. 331–333.

Philipps, D. (1990), *The Climates of Canada (a*vailable from Environment Canada, Downsview, Ontario).

Pilié, R.J., Mack, E.J., Kocmond , W.C., Rogers, C.W., and Eadie, W.J. (1975), *The life cycle of valley fog. Part I: Micrometeorological characteristics*, J. Appl. Meteor. *14*, 347–363.

Pilié, R.J., Mack, E.J., Rogers, C.W., Katz, U., and Kocmond, W.C. (1979), *The formation of marine fog and the development of fog-stratus systems along the California Coast,* J. Appl. Meteor. *18*, 1275–1286.

Pinnick, R.G., Hoihjelle, D.L., Fernandez, G., Stenmark, E.B., Lindberg, J.D., and Hoidale, G.B. (1978), *Vertical structure in atmospheric fog and haze and its effects on visible and infrared extinction*, J. Atmos. Sci. *35*, 2020–2032.

Plank, V.G., Spatola, A.A., and Hicks, J.R. (1971), *Summary results of the lewisburg fog clearing program,* J. Appl. Meteor. *10,* 763–779.

Pliny, *Natural History*, Books XVII-XIX. English translation by H. Rackham (Harvard University Press 1971).

Pruppacher, H.R. and Klett, J.D., *Microphysics of Clouds and Precipitation,* 2nd edition, (Kluwer Pub. Inc., Boston 1997) 954 p.

PUTSAY, M., KERÉNYI, J., SZENYÁN, I., SEBOK, I., NÉMETH, P., and DIÓSZEGHY, M. (2001), *Nighttime fog and low cloud detection in NOAA-16 AVHRR images and validation with ground observed SYNOP data and radar measurements,* Proceedings of the 2001 EUMETSAT Meteorological Satellite Conference, EUM P33, 365–373, EUMETSAT, Antalya, Turkey.

RÄISÄNEN, P, ISAAC, G.A., BARKER, H.W., and GULTEPE, I. (2003), *Impact of horizontal variations in effective radius on solar radiative properties of stratiform water clouds,* Quart. J. Roy. Meteor. Soc. *129*, 2135–2149.

REUDENBACH, C. and BENDIX, J. (1998), *Experiments with a straightforward model for the spatial forecast of fog/low stratus clearance based on multi-source data,* Meteor. Applications *5*, 205–216.

ROACH, W.T. (1995a), *Back to basics: Fog: Part 2 – The formation and dissipation of land fog*, Weather *50*, 7–11.

ROACH, W.T. (1995b), *Back to basics: Fog: Part 3 – The formation and dissipation of sea fog,* Weather *50*, 80–84.

ROACH, W.T. (1976), *On the effect of radiative exchange on the growth by condensation of a cloud or fog droplet*, Quart. J. Roy. Meteor. Soc. 102, 361–372.

ROACH, W.T., BROWN, R. CAUGHEY, R., GARLAND S.J., and READINGS, C.J. (1976), *The physics of radiation fog: I – A field study*, Quart. J. Roy. Meteor. Soc. *102*, 313–333.

ROBASKY, F.M. and WILSON, F.W. (2006), *Statistical forecasting of ceiling for New York City airspace based on routine surface observations,* 12th Conference on Aviation, Range, and Aerospace Meteorology, Atlanta, GA, Am. Meteor. Soc. Atlanta, GA, 30 Jan.–2 Feb., 2006.

RYZNAR, E. (1977), *Advection-radiation fog near Lake Michigan*, Atmos. Environ. *11*, 427–430.

SAUNDERS, W.E. (1950), *A method of forecasting the temperature of fog formation*, Meteor. Mag. *79*, 213–219.

SAUNDERS, P.M. (1964), *Sea smoke and steam fog*, Quart. J. Roy. Meteor. Soc. *90*, 156–165.

SAUNDERS, R.W. and GRAY, D.E. (1985), *Interesting cloud features seen by NOAA-6 3.7 micrometer images*, Meteor. Mag. *114*, 211–114.

SCHEMENAUER, R.S. and CERECEDA, P. (1994), *A proposed standard fog collector for use in high-elevation regions*, J. Appl. Meteor. *33*, 1313–1322.

SCOTT, R.H. (1894), *Fogs reported with strong winds during the 15 years 1876–90 in the British Isles,* Quart. J. Roy. Meteor. Soc. *XX*, 253–262.

SCOTT, R.H. (1896), *Notes on some of the difference between fogs, as related to the weather systems which accompany them,* submitted to the Fog Committee, Quart. J. Roy. Meteor. Soc. *XXII*, 41–65.

SIEBERT, J., SIEVERS, U., and ZDUNKOWSKI, W. (1992), *A one dimensional simulation of the interaction between land surface processes and the atmosphere,* Boundary-Layer Meteorol. *59*, 1–34.

SIEBERT, J., BOTT, A., and ZDUNKOWSKI, W. (1992a), *Influence of a vegetation-soil model on the simulation of radiation fog,* Beitr. Phys. Atmos. *65,* 93–106.

SIEBERT, J., BOTT, A., and ZDUNKOWSKI, W. (1992b), *A one-dimensional simulation of the interaction between land surface processes and the atmosphere,* Boundary-Layer Meteorol. *59*, 1–34.

STALENHOEF, A.H.C. (1974), *Slant visibility during fog related wind speed, air temperature and stability,* Archiv für Meteorologie, Bioklimatologie und Geophysik, Serie B *22*, 351–361.

STEPHENS, G.L., VANE, D.G., BOAIN, R.J., MACE, G.G., SASSEN, K., WANG, Z., ILLINGWORTH, A.J., O'CONNOR, E.J., ROSSOW, W.B., DURDEN, S.L., MILLER, S.D., AUSTIN, R.T., BENEDETTI, A., MITRESCU, C., and TEAM, T.C.S. (2002), *The Cloudsat mission and the A-Train—A new dimension of space-based observations of clouds and precipitation,* Bull. Am. Meteor. Soc. *83*, 1771–1790.

STEWART, R.E. (1992), *Precipitation types in the transition region of winter storms*, Bull. Am. Meteor. Soc. *73*, 287–296.

STEWART, R.E., YIU, D.T., CHUNG, K.K., HUDAK, D.R., LOZOWSKI, E.P., OLESKIW, M., SHEPPARD, B.E., and SZETO, K.K. (1995), *Weather conditions associated with the passage of precipitation type transition regions over Eastern Newfoundland*, Atmos.-Ocean *33*, 25–53.

STEWARD D.S. and ESSENWANGER, O.M. (1982), *A survey of fog and related optical propagation characteristics*, Rev. Geophys. Space Phys. *20*, 481–495.

STRATTON, J.A. and HOUGHTON, H.G. (1931), *A theoretical investigation of the transmission of light through fog*, Physical Rev. *38*, 159–165.

SUJITJORN, S., SOOKJARAS, P., and WAINIKORN, W. (1994), An expert system to forecast visibility in Don-Muang Air Force Base, 1994 IEEE Internat. Conf. on Systems, Man and Cybernetics (Humans, Information and Technology) (2-5 Oct., 1994), IEEE, NY, NY, USA, 2528–2531.

TAG, P.M. and PEAK, J.E. (1996), *Machine learning of maritime fog forecast rules*, J. Appl. Meteor. *35*, 714–724.

TARDIF, R. (2007), *The impact of vertical resolution in the explicit numerical forecasting of radiation fog: A case study*. Pure Appl. Geophys. *164*, 7/8, this issue.

TARDIF, R. and RASMUSSEN, R.M. (2007), *Event-based climatology and typology of fog in the New York City region*, J. Appl. Meteor., in press.

TAYLOR, G.I. (1917), *The formation of fog and mist,* Quart. J. Roy. Meteor. Soc. *43*, 241–268.

TEIXEIRA, J. (1999), *Simulation of fog with the ECMWF prognostic cloud scheme,* Quart. J. Roy. Meteor. Soc. *125*, 529–553.

TEIXEIRA, J. and MIRANDA, P.M.A. (2001), *Fog prediction at Lisbon airport using a one-dimensional boundary layer model*, Meteor. Applications *8*, 497–505.

TELFORD, J.W. and CHAI, S.K. (1993), Marine fog and its dissipation over warm water, J. Atmos. Sci. 50, 3336–3349.

TERRA, R., MECHOSO, C.H., and ARAKAWA, A. (2004), *Impact of orographically induced spatial variability in PBL stratiform clouds on climate simulations*, J. Climate *17*, 276–293.

THUMAN, W.C. and ROBINSON, E. (1954), *Studies of Alaskan ice–fog particles,* J. Atmos. Sci. *11*, 151–156.

TJERNSTROM, M. (2003), *Simulated liquid water and visibility in stratiform boundary-layer clouds over sloping terrain,* J. Appl. Meteor. *32*, 656–665.

TOMASI, C. and TAMPIERI, F. (1976), *Features of the proportionality coefficient in the relationship between visibility and liquid water content in haze and fog*, Atmosphere *14*, 61–76.

TURNER, J., ALLAM, R., and MAINE, D. (1986), *A case study of the detection of fog at night using channels 3 and 4 on the Advanced Very High Resolution Radiometer (AVHRR)*, Meteor. Mag. *115*, 285–290.

TURTON, J.D. and BROWN, R. (1987), *A comparison of a numerical model of radiation fog with detailed observations,* Quart. J. Roy. Meteor. Soc. *113*, 37–54.

UNDERWOOD, S.J., ELLROD, G.P., and KUHNERT, A.L. (2004), *A multiple-case analysis of nocturnal radiation-fog development in the central valley of California utilizing the GOES nighttime fog product,* J. Appl. Meteor. *43*, 297–311.

VISLOCKY, R.L. and FRITSCH, J.M. (1995), *Improved model output statistics forecasts through model consensus,* Bull. Am. Meteor. Soc. *76*, 1157–1164.

VISLOCKY, R.L. and FRITSCH, J.M. (1997), *An automated, observations-based system for short-term prediction of ceiling and visibility*, Weather and Forecasting *12*, 31–43.

VON GLASOW, R. and BOTT, A. (1999), Interaction of radiation fog with tall vegetation, Atmos. Environ. *33*, 1333–1346.

WANTUCH, F. (2001), *Visibility and fog forecasting based on decision tree method,* IDOJARAS *105*, 29–38.

WEICKMANN, H.K. (1979), *Tor Harold Percival Bergeron*, Bull. Am. Meteor. Soc. *60*, 406–414.

WEINSTEIN, A.I. and SILVERMAN, B.A. (1973), *A numerical analysis of some practical aspects of airborne urea seeding for warm fog dispersal at airports,* J. Appl. Meteor. *12*, 771–780.

WELCH, R.M. and WIELICKI, B.A. (1986), *The stratocumulus nature of fog,* J. Appl. Meteor. *25*, 101–111.

WENDISCH, M., MERTES, S., HEINTZENBERG, J. WIEDENSOHLER, A., SCHELL, D., WOBROCK, W., FRANK, G., MARTINSSON, B.G., Fuzzi, S., ORSI, G., KOS, G., and BERNER, A. (1998), *Drop size distribution and LWC in Po Valley Fog*, Contr. Atmos. Phys. *71*, 87–100.

WILKS, D.S., *Statistical Methods in the Atmospheric Sciences* (Academic Press 1995).

WILLETT, H.C. (1928), *Fog and haze, their causes, distribution, and forecasting*, Monthly Weather Rev. *56*, 435–468.

WITIW, M.R. and BAARS, J.A. (2003), *Long term climatological changes in fog intensity and coverage. Proc.* 14th Symp. *Global Change and Climate Variations*, Am. Meteor. Soc., Long Beach, CA.

WMO (1966), *International Meteorological Vocabulary* (World Meteorological Organization. Geneva Switzerland).

WMO (1991), *Lectures presented at the WMO training workshop on the interpretation of NWP products in terms of local weather phenomena and their verification*. Preprints, Program on Short- and Medium-Range Weather Prediction Research (World Meteorological Organization. Geneva Switzerland).

WRIGHT, B.J. and THOMAS, N. (1998), *An objective visibility analysis and very-short-range forecasting system,* Meteor. Applications *5,* 157–181.

YUSKIEWICZ, B., ORSINI, D., STRATMANN, F., WENDISCH, M., WIEDENSOHLER, A., HEJNTZENBERG, J., MARTINSSON, B.G., FRANK, G., WOBROCK, W., and SCELL, D. (1998), *Changes in submicrometer particle distributions and light scattering during haze and fog events in a highly polluted environment,* Contr. Atmos. Phys. *71*, 33–45.

ZDUNKOWSKI, W. and NIELSEN, B. (1969), *A preliminary prediction analysis of radiation fog*, Pure Appl. Geophys. *19*, 45–66.

ZDUNKOWSKI, W. and BARR, A. (1972), *A radiative-conductive model for the prediction of radiation fog,* Bound.-Layer Meteor. *3*, 152–157.

(Received November 1, 2006, accepted December 13, 2006)

Pure appl. geophys. 164 (2007) 1161–1178
0033–4553/07/071161–18
DOI 10.1007/s00024-007-0212-9

Pure and Applied Geophysics

Microphysical Observations and Mesoscale Model Simulation of a Warm Fog Case during FRAM Project

I. GULTEPE[1] and J. A. MILBRANDT[2]

Abstract—The objective of this work is to apply a new microphysical parameterization for fog visibility for potential use in numerical weather forecast simulations, and to compare the results with ground-based observations. The observations from the Fog Remote Sensing And Modeling (FRAM) field which took place during the winter of 2005 – 2006 over southern Ontario, Canada (Phase I) were used in the analysis. The liquid water content (*LWC*), droplet number concentration (N_d), and temperature (*T*) were obtained from the fog measuring device (FMD) spectra and Rosemount probe, correspondingly. The visibility (*Vis*) from a visibility meter, liquid water path from microwave radiometers (MWR), and inferred fog properties such as mean volume diameter, *LWC*, and N_d were also used in the analysis. The results showed that *Vis* is nonlinearly related to both *LWC* and N_d. Comparisons between newly derived parameterizations and the ones already in use as a function of *LWC* suggested that if models can predict the total N_d and *LWC* at each time step using a detailed microphysics parameterization, *Vis* can then be calculated for warm fog conditions. Using outputs from the Canadian Mesoscale Compressible Community (MC2) model, being tested with a new multi-moment bulk microphysical scheme, the new *Vis* parameterization resulted in more accurate *Vis* values where the correction reached up to 20 –50%.

Key words: Fog microphysics, fog parameterization, fog forecasting, fog remote sensing.

1. Introduction

Fog formation is directly related to thermodynamical, dynamical, radiative, aerosol, and microphysical processes as well as surface conditions. Extinction of light at visible ranges within the fog results in low visibilities that can affect low-level flight conditions, marine traveling, shipping, and transportation. Fog occurrence of more than 10% of time in some regions of Canada (WHIEFFEN, 2001) demands that fog nowcasting and/or forecasting models should be improved. Particularly, fog intensity, represented with visibility *(Vis)*, should be more accurately simulated to reduce the costs of fog-related accidents and delays in transportation.

[1] Cloud Physics and Severe Weather Research Section, Meteorological Research Division, Environment Canada, Toronto, ON, Canada. E-mail: ismail.gultepe@ec.gc.ca

[2] Numerical Weather Prediction Research Section, Meteorological Research Division, Environment Canada, Dorval, QC, Canada.

The earlier studies on droplet number concentration (N_d) and liquid water content (LWC) relationships showed that there is usually a large variability in N_d for a given LWC (GULTEPE *et al.*, 2001; GULTEPE and ISAAC, 2004a). The work by GULTEPE *et al.* (2006) on fog microphysics suggested that N_d can change from a few droplets per volume to 100 cm^{-3} for a fixed LWC and that visibility should be a function of both N_d and LWC. These works indicated that N_d should be considered in visibility parameterizations. Previously, BOTT and TRAUTMANN (2002), using prognostic equations, developed a model that predicted both N_d and LWC. Under saturated conditions, more cloud concentration nuclei (CCN) leads to the formation of a large number of small droplets (GULTEPE and ISAAC, 1999), resulting in slower gravitational settling of droplets and thus low visibility. As shown by the experimental relation of JIUSTO (1981), visibility is directly related to the average cloud droplet radius, which in turn is directly proportional to the LWC and inversely proportional to the total number concentration. Hence, visibility parameterizations should also include the total number concentration of droplets as an independent variable.

Fog forecasting/nowcasting cannot be successful until a better understanding of fog microphysics and the large/small-scale dynamical effects on its formation is provided.

The current parameterization for fog visibility in numerical weather prediction (NWP) models is not accurate due to the neglect of N_d in parameterizations (STOELINGA and WARNER, 1999; GULTEPE *et al.*, 2006). ELLROD (1995) stated that satellite observations based on a channel differencing method (ch2-ch4) can facilitate fog forecasting at night because SW radiation is absent. On the other hand, the daytime algorithm needs to take away the SW contribution from the ch2. GULTEPE *et al.* (2007) suggested that integration of satellite observations together with a forecasting model output can improve fog forecasting up to 30%. An integration of surface-based sensors, remote sensors and model data, as proposed by ISAAC *et al.* (2006) and GULTEPE *et al.* (2007) for airport winter weather, might help provide improved predictions/nowcasts for fog occurrence.

The visibility for fog and other microphysical elements used in forecasting models was calculated using equations given by KUNKEL (1986) and STOELINGA and WARNER (1999). The fog visibility parameterization for warm temperatures is only a function of LWC and it has been commonly used in NWP models (BENJAMIN *et al.*, 2004). GULTEPE *et al.* (2006) suggested that the Vis parameterization for fog should also include N_d; otherwise, a possible uncertainty in model results can reach up to 50%.

In the present work, the observations collected during Fog Remote Sensing And Modeling (FRAM) field project which took place during the winter of 2005–2006 at the Center for Atmospheric Research Experiment (CARE) site, Toronto, Ontario, were used in the analysis. A new parameterization scheme for warm fog visibility as a function of both LWC and N_d, suggested by GULTEPE *et al.* (2006), is used to predict Vis. The Canadian Mesoscale Compressibility Community (MC2) model (BENOIT *et al.*, 1997) is used to simulate the 4 January, 2006 fog case. The microphysics scheme

used by the model in the simulation, discussed below, predicts N_d and LWC independently, from which Vis is then obtained diagnostically. The visibility observations from ground-based instruments were then compared to the results of MC2 simulations. The new microphysical parameterizations for the settling rate and droplet terminal velocities were also developed for future applications.

2. Observations

Observations were collected during FRAM (GULTEPE *et al.*, 2006b) from 1 December, 2005 to 18 April, 2006 but the data only from 4 January, 2006, representing warm fog conditions, were used in the analysis because of availability of the complete observations. The instruments used in the data collections were the Droplet Measurement Systems (DMT) Fog Measuring Device (FMD), Vaisala ceilometer (CT25K), York University Ice Particle Counters (IPC, SAVELYEV *et al.*, 2003; BROWN and POMEROY, 1989) mounted on a 10 m tower, DRI Hot Plate, Radiometrics microwave radiometers (MWR; profiling and regular ones), radiometers (profiling and regular ones), Vaisala FD12P, and the Precipitation Occurrence Sensor System (POSS). Observations of sizes and number concentrations of liquid droplets, ice crystals, and aerosols were collected using optical probes; visibility was observed with a Vaisala FD12P; LWC, relative humidity with respect to water (RH_w), temperature (T), and liquid water path (LWP) were observed with a profiling MWR. Details on the FRAM field project and instruments used to collect data can be found in GULTEPE *et al.* (2006b).

3. Parameterization of Visibility

The extinction parameter (β_{ext}) used to get Vis was calculated from FSSP probe measurements by

$$\beta_{ext} = \sum Q_{ext} n(r) \pi r^2 dr, \tag{1}$$

where n is the number density of particles in a bin size represented by radius (r) and Q_{ext} is the Mie efficiency factor calculated from the Mie theory. For large size parameters, it can be taken to be approximately 2 (KOENING, 1971). It is converted to Vis using the following equation (STOELINGA and WARNER, 1999)

$$Vis = -\ln(0.02)/\beta_{ext}. \tag{2}$$

Using the *in situ* observations collected during Radiation and Aerosol Climate Experiment (RACE), LWC, N_d, and β_{ext} are used to obtain a relationship between Vis_{obs} and $(LWC \cdot N_d)^{-1}$ (referred to as the fog index) as

$$Vis = \frac{1}{(LWC \cdot N_d)^{0.65}}. \quad (3)$$

This fit indicates that Vis is inversely related to both LWC and $N_{d.}$. The maximum limiting LWC and N_d values used in the derivation of Eq. (3) are approximately 400 cm^{-3} and 0.5 g m^{-3}, respectively. The minimum limiting N_d and LWC values are 1 cm^{-3} and 0.005 g m^{-3}, respectively.

4. Model Description and Set-up

The simulation in this study was performed using the Canadian Mesoscale Compressible Community (MC2) model. This model is based on the fully-compressible Euler equations, solved on a Mercator projection, and is a limited-area model capable of one-way self-nesting. The model dynamics are discussed in detail in BENOIT *et al.* (1997) and THOMAS *et al.* (1998). The MC2 uses a comprehensive physics package (MAILHOT *et al.*, 1998) which includes a planetary boundary layer scheme based on turbulent kinetic energy (BENOIT *et al.*, 1989), implicit (explicit) vertical (horizontal) diffusion, and a detailed land-surface scheme (BELAIR *et al.*, 2003a,b). The solar (FOUQUART and BONNEL, 1980) and infrared (GARAND and MAILHOT, 1990) schemes in the radiation package are fully interactive with the model clouds.

The fog case simulated was that of 4 January, 2006 during which a warm front moved across the Ontario region. The model was initialized on a coarse-resolution domain (10-km grid-spacing, 301 × 301 points; not shown) using the 15-km regional analyses from the Canadian Meteorological Centre (CMC) at 00:00 UTC 4 January, 2006. Lateral boundary conditions from the CMC analyses were supplied every 6 h for a 24 h simulation. Using the output from the 10-km simulation, the model was then nested to a high-resolution domain (2-km grid-spacing, 251 × 251 points; see Fig. 5) for an 18-h simulation, starting at 06:00 UTC 4 January, 2006, 6 h after the initial time of the 10-km run. The purpose of this nesting strategy is to generate initial conditions for the 2-km simulation at higher resolution than are provided for by the regional analyses in order to reduce the model spin-up time for the 2-km run. Also, experience with the MC2 model has provided a rule-of-thumb for users, stating that jumps in model grid-spacing for nested runs should be limited to a factor of 5. Both simulations had 41 modified Gal-Chen levels (unevenly spaced) with 12 levels in the planetary boundary layer and a model lid at 30 km. The 10-km run employed the Kain-Fritsch scheme to parameterize subgrid-scale convection and a Sundqvist-type scheme to treat grid-scale condensation (see MAILHOT *et al.*, 1998).

The 2-km simulation, discussed below, used the triple-moment version of the multi-moment bulk scheme described in MILBRANDT and YAU (2005a,b) to parameterize cloud microphysical processes at saturated grid points. The scheme

partitions the liquid phase into separate categories for ''cloud''droplets (with diameters typically less than 200 microns) and ''rain''. Cloud nucleation is based on an assumed ''continental''-type aerosol spectrum which is used to prescribe the initial total number concentration of cloud droplets (N_d). Cloud water can be removed by conversion to rain, collection by rain and/or ice phase particles, or evaporation. Visibility is then diagnosed from the prognostic cloud variables (mass content and number concentration) using Eq. (3). Note that for the discussion of the model results in this paper, *LWC* refers only to the *cloud* mass content, and does not include contributions from the *rain* category.

5. Results

a) From GOES, MWR, and VAISALA Visibility Observations

The GOES fog and icing analysis suggested that some patchy low clouds were present just northwest of Toronto but the fog was not seen in the analyzed image because of mid-level clouds (Fig. 1a). Note that the red area in Fig. 1a denotes a supercooled droplet region likely occurring above the fog layer. Visibility obtained from the Vaisala FT12P, RH_w, and T between 20:00 and 22:00 UTC is shown in Figure 1b. The time-height cross section of T, RH_w, and *LWC* from the MWR TP3000 (Fig. 1c) shows that an elevated layer of stratiform cloud was just above the 1 km height above ground level. Below this cloud, RH_w was $\sim$100%. T and *LWC* at the surface were about 5°C and 0.1 g m^{-3} (Fig. 1c), respectively. For the same time period (between 20:00 and 22:00 UTC), T, RH_w, and *Vis* from the observations were approximately 5°C, 100%, and 500 m, respectively (Fig. 1b).

b) Microphysics of Fog

Measurements collected during FRAM were used in the analysis and compared to the model simulation. Relationships between *Vis* and fog microphysical parameters (e.g., *LWC*) were derived. As seen from Fig. 1a, snow was present at the surface on the 4 January, 2006 case and some precipitation as rain occurred before the fog event (Fig. 1c). Bimodal size distributions were seen in the FMD droplet spectra (Fig. 2a). A separation at about 15 μm size was likely due to the presence of drizzle size droplets; that is, droplets with diameters $>$ 15 μm. Time series of the 1-s N_d data from the FMD indicated that max N_d reached up to 100 cm^{-3} (Fig. 2b) and *Vis* corresponding to that value was about 30–500 m (Fig. 2c). It is shown that increasing N_d resulted in lower *Vis* values. Figure 2c shows the *LWC* time series for the same time period. *LWC* increased to 0.1 g m^{-3} when *Vis* was lowest (Fig. 2c) and N_d was at its maxima (Fig. 2b). These results suggest that *Vis* is a function of both *LWC* and N_d.

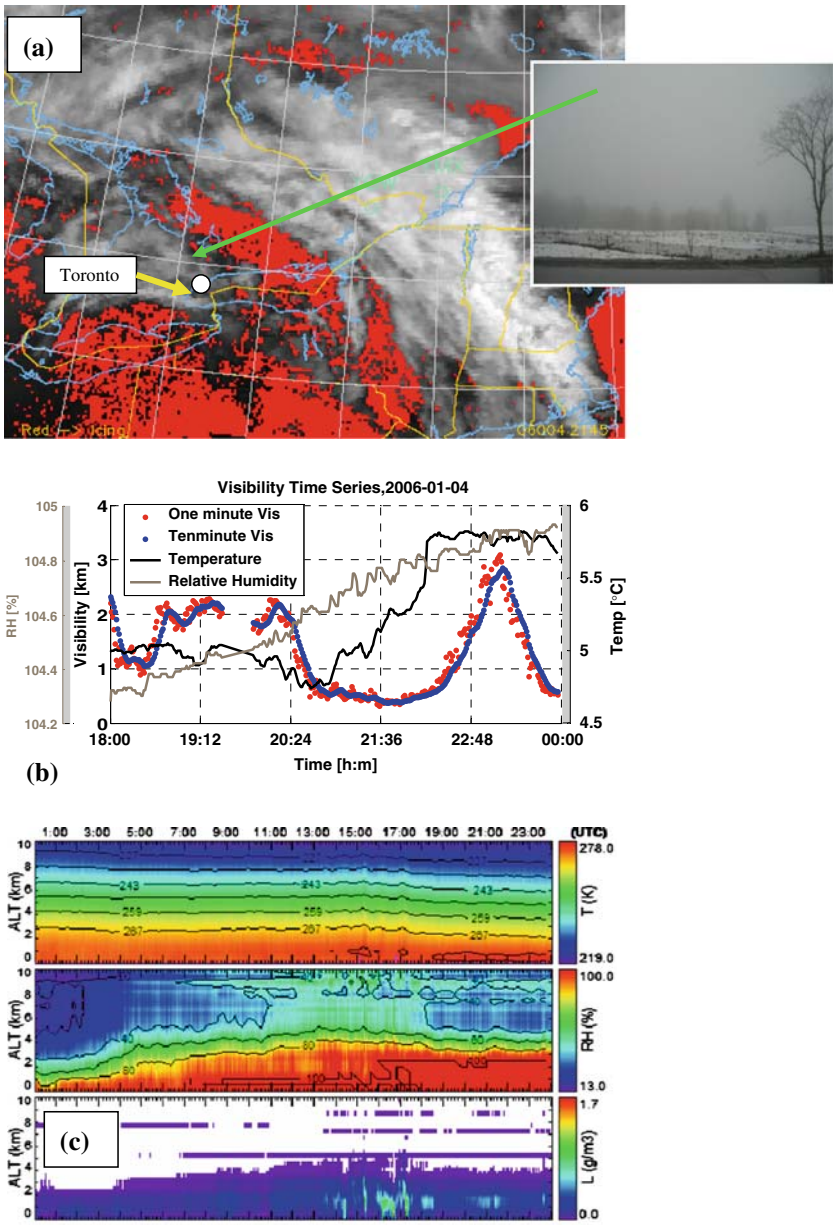

Figure 1

Particle phase analysis based on GOES satellite observations. The red color indicates liquid regions (a). The inlet picture is for the fog which occurred over the CARE site at about 10 AM on Jan. 4, 2006. The time-height views of T, RH_w, and LWC (as L) are shown in (b). The time series of visibility from VAISALA *Vis* meter, and T and RH_w from the Campbell instrument are shown in (c). The heavy fog occurrence is seen between 20:30 UTC and 22:30 UTC on Jan. 4, 2006.

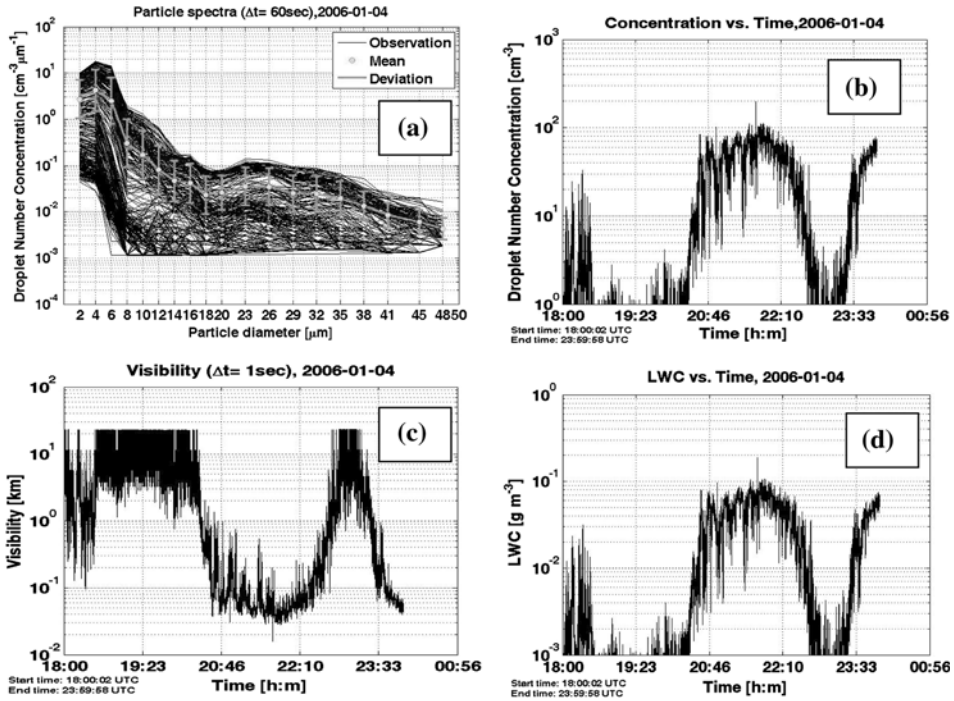

Figure 2
Shows the droplet spectra from the DMT FMD probe (a), the N_d time series calculated from the droplet spectra (b), the visibility calculated from the droplet spectra using Eqs. (1) and (2) (c), and LWC time series calculated from the droplet spectra (d). The data were collected on Jan. 4, 2006.

The FMD measurements were used to obtain relationships between Vis and N_d, LWC, and their combinations. During the analysis, it was found that LWC increases with increasing N_d (not shown) and the Vis decreases with increasing N_d (Fig. 3a) and LWC (Fig. 3b). Based on these observations, the following relationships using 1-min averages were derived (Fig. 3c) for January 4 as

$$Vis = 1.13(LWC \cdot N_d)^{-0.51}. \quad (4)$$

This relationship suggests that the parameterization given by Eq. (3) for low stratiform clouds approximately agrees with data collected at the surface. However, this result needs to be further verified for various fog types.

c) Model Simulation

The MC2 simulation results for the 4 January, 2006 case are shown in Figs. 4 to 6. Figure 4 shows that a warm and moist air advection was occurring during the fog event at 19:00 UTC where water vapor mixing ratio value was approximately

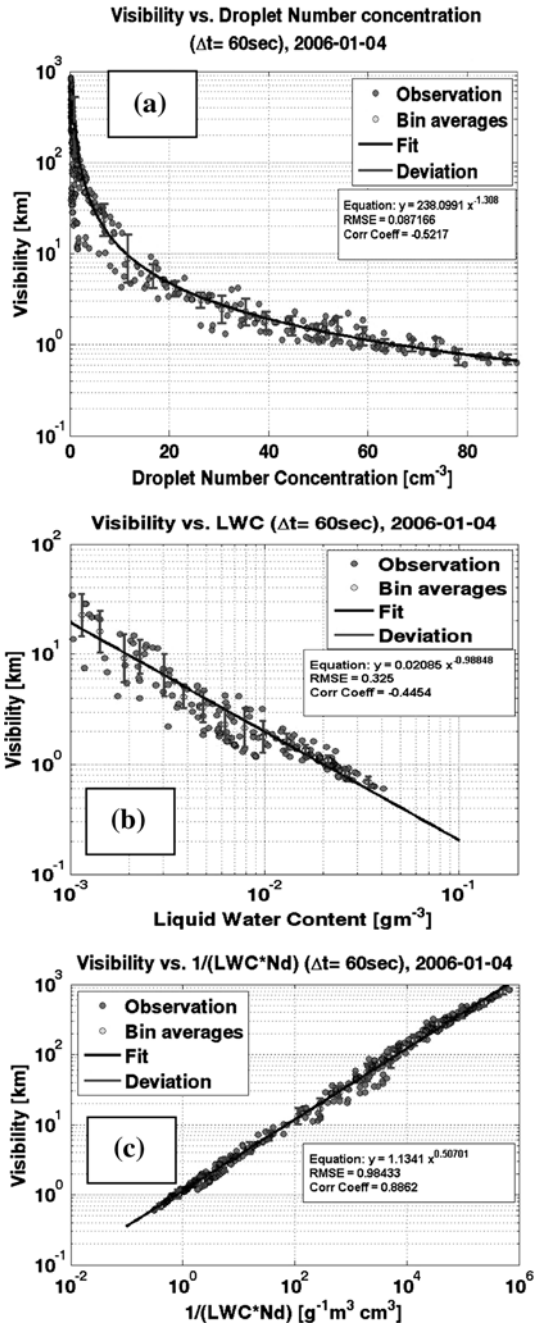

Figure 3
The visibility versus N_d, and versus LWC from the FMD measurements, and visibility as a function of both LWC and N_d is shown in (a), (b), and (c), respectively. The fits to 1-min averages are shown with solid lines.

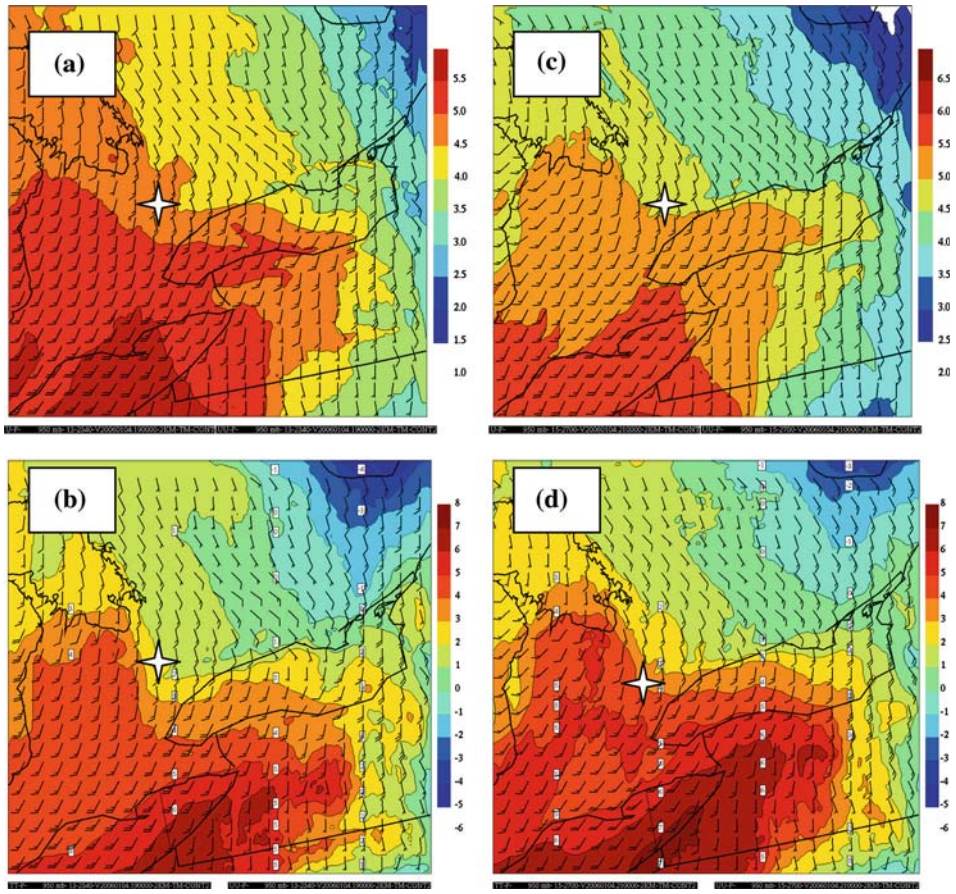

Figure 4
The vapor mixing ratio and temperature based on the 15 h forecast values obtained from the MC2 model valid at 19:00 and 21:00 UTC on Jan. 4, 2006 are given in boxes a–b and and c–d, respectively. The full barb denotes 5 m s^{-1} wind speed. The four-point star indicates the FRAM project site. Note that all figures are represented at the 950 hPa level.

5 g kg^{-1} (Figs. 4a–b). The corresponding T was approximately 3–5°C at the surface (Fig. 4b–d). The horizontal wind directions were from south and southwest and its magnitude was about 5–7 m s^{-1}. The low-level warm and moist air advection at 21:00 UTC was similar to that at 19:00 UTC. It was likely that warm and moist air moving from S and SW carried out the significant amount ofwater vapor from Lake Ontario and Lake Erie that contributed to fog formation over the cold snow surface shown in Fig. 1.

Figure 5a (19:00 UTC) shows the simulated N_d values from the model. The number concentrations were found to range from 50 to 150 cm^{-3} over the project

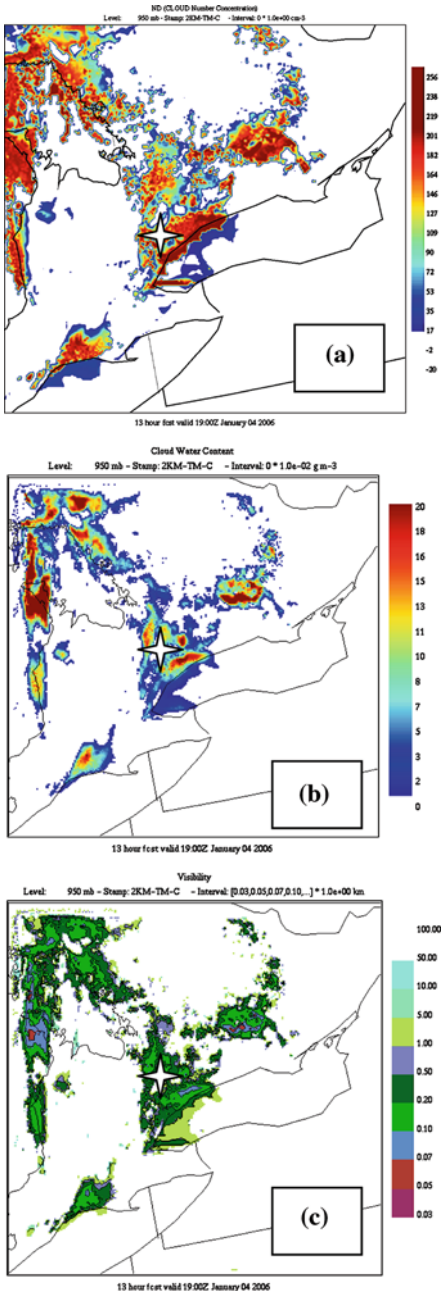

Figure 5
The droplet number concentration, *LWC*, and visibility obtained from the MC2 simulations valid at 19:00 UTC for January 4, 2006 are shown in the boxes a, b, and c, respectively. The four-point star indicates the FRAM project site.

area. Figure 5b shows the *LWC* values for 19:00 UTC, which ranged from 0.02 to 0.10 g m^{-3} over the CARE site. Note that maximum observed values of *LWC* reached 0.15 g m^{-3} at nearby areas during the fog episode (Fig. 1c). The visibility simulated by the model using the parameterization of Eq. (3), shown in Figure 5c and it ranged between 100 m and 500 m.

Later (at 21:00 UTC; Fig. 6a), the system moved to the northeast and the peak N_d values reached approximately 200 cm^{-3} in some regions. This was comparably larger than the observed number concentration of 100 cm^{-3} at CARE site (Fig. 2b). Figure 6b shows the *LWC* parameter. It changed from 0.10 to 0.30 g m^{-3} near the CARE site, indicating that fog was intensifying. Note that maximum observed values of *LWC* from the FMD instrument reached 0.1 g m^{-3} (Fig. 2d), and from the MWR radiometer it reached to about 0.4 g m^{-3} (Fig. 1c) near the CARE site. Note that rain was observed during the fog event indicated by surface precipitation measurements and this likely resulted in large MWR *LWC* values. The visibility simulated by the model using the parameterization of Eq. (3) is shown in Figure 6c and its values were between 50 and 500 m at the CARE site.

The observed extent of the low-visibility over the region based on observations was about 30–500 m (Fig. 2c) and changed quickly during the 2-h time period for the fog episode. The corresponding simulated values of *Vis* ranged from approximately 100–500 m. The lowest visibility of approximately 50 m in the NE region (Fig. 6c) was likely related to a large number of small droplets (Fig. 6a) but were not verified with observations at this location.

6. Discussions

a) Microphysics of Fog

Earlier studies suggested that visibility is indirectly related to N_d. MEYER *et al.* (1980) showed that *Vis* is a function of N_d and its relationship changes with fog intensity. The parameterizations of MEYER *et al.* (1980) for light and heavy fog are found to be comparable with the results of this study. The FMD measurements were also found useful because there was no other instrument that could make continuous measurements of fog characteristics.

Figure 7a shows the results from the Eq. (3) (GULTEPE *et al.*, 2006) and from the KUNKEL (1986) parameterization. It is ascertained that N_d can affect the *Vis* more than 50% when it is included in *Vis* parameterization. Therefore, droplet number concentration should be considered in the fog visibility parameterizations.

The fog settling rate is an important process to estimate the fog lifetime. Although it is not obtained from simulations here, we developed its parameterization that can be used for fog budget calculations and to estimate the lifetime of a fog

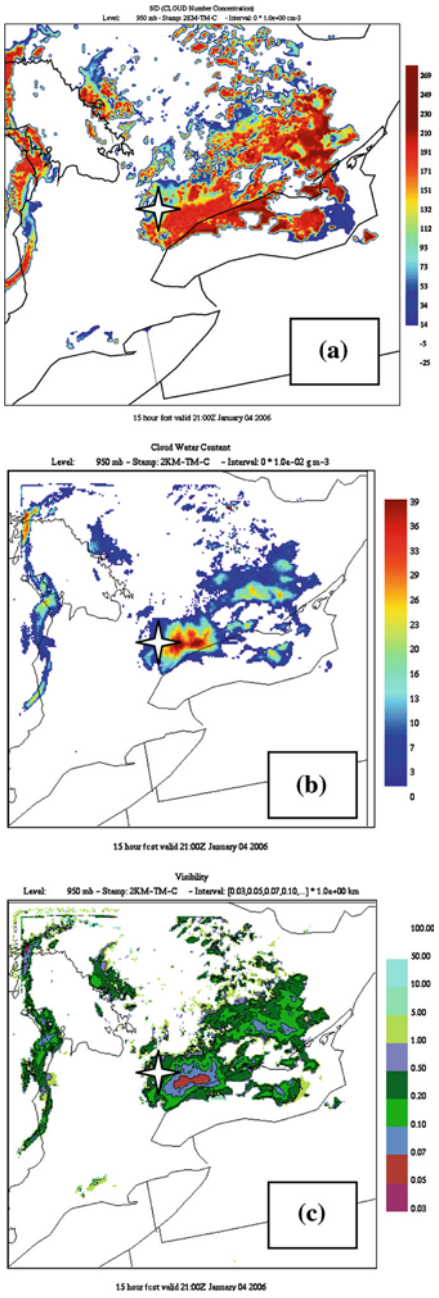

Figure 6
The droplet number concentration, *LWC*, and visibility obtained from the MC2 simulations valid at 21:00 UTC for January 4, 2006 are shown in the boxes a, b, and c, respectively. The four-point star indicates the FRAM project site.

layer. Figure 7b shows the settling rate as a function of both LWC and N_d, and its fit is obtained as

$$V_t LWC = 73138[LWC^{5/3} N_d^{(-2/3)}]^{1.1}, \tag{5}$$

where the unit for the settling rate is [g m^{-2} h^{-1}]. The V_t is the LWC weighted particle terminal velocity [cm s^{-1}] which is calculated as

$$V_t = \frac{(4/3)\rho_w \sum_{i=1}^{b} n_i r_i^3 v_i}{LWC}, \tag{6}$$

where the fog droplets terminal velocities for each size bin (KUNKEL, 1986) are calculated from

$$v_i = 1.202x10^{-2} r_i^2. \tag{7}$$

Here v_i and r_i are in the units of cm s^{-1} and μm, respectively. Using Eqs. (6) and (7), Figure 7c is generated to obtain V_t versus LWC/N_d relationship in which V_t increases rapidly with increasing $k = LWC/N_d$, then, for $k > 10^{-4}$, it almost stays constant. The equation for the fit is obtained as follows

$$V_t = -0.006\left(\frac{LWC}{N_d}\right)^{-0.61}. \tag{8}$$

When LWC and N_d are known from a detailed microphysical model, V_t can then be estimated. The fits over the scatter plots are obtained from the bin averaged values of related parameters as shown in Figures 2 and 3. The new parameterization here suggested for the droplet settling rate and weighted terminal velocities for warm fog processes could be used for model validations but an extensive analysis is required for various cloud types and environmental conditions, and this is left to a future work.

b) Model Simulations

The results suggest that the new visibility parameterization can significantly improve predictions of visibility from an NWP model, provided that the model uses a microphysics scheme which prognoses cloud mass and number concentration independently. Alternatively, GULTEPE and ISAAC (2004) suggested that N_d could be diagnostically obtained from environmental conditions such as temperature, allowing for the new *Vis* parameterization to be used in current NWP models, which use computationally cheaper single-moment cloud schemes and prognostic cloud mass only. When N_d is obtained, GULTEPE *et al.* (2006) stated that the use of new parameterization in a forecast model could improve *Vis* values up to 50%. The Rapid Update Cycle (RUC) model that is used commonly for numerical forecasting in North America, also utilizes the KUNKEL (1984) parameterization (BENJAMIN

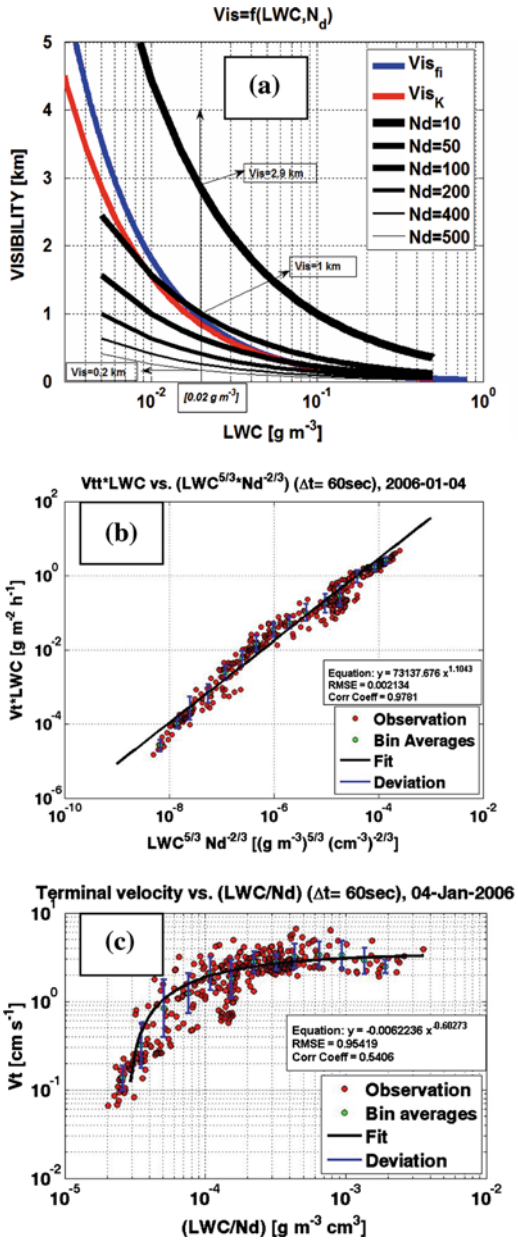

Figure 7

The relationships obtained from Eqs. (3), (5), and (8) for visibility, droplet settling rate, and weighted terminal velocity are shown in (a), (b), and (c), respectively. The fits to 1-min averages are shown with solid lines.

et al., 2004). It is suggested that if the new visibility parameterization were used in current NWP models, the fog *Vis* values would be improved significantly (up to 50%).

In the near future, the multi-moment bulk microphysics scheme of MILBRANDT and YAU (2005a,b), used in the simulation for this study, will be tested in the meso-gamma-scale limited-area version of the Canadian Global Environmental Multiscale (GEM) NWP model (COTE *et al.*, 1998), whereby the new visibility parameterization can be directly applied.

7. Conclusions

In this work, the results from the FRAM field program for a warm winter fog case study are summarized. Previous studies correlated *Vis* to *LWC* only. The present work indicated that *Vis* should be parameterized as a function of both *LWC* and N_d. GULTEPE *et al.* (2006) stated that if N_d is not included in the parameterizations for forecasting models, the predicted *Vis* values can include uncertainties more than 50%.

The settling rate of fog droplets is important for sustaining the fog presence within the boundary layer. The derived relationships can easily be used with bulk microphysical parameterization when N_d is obtained from model thermodynamical variables such as T and/or moisture.

The fog droplet spectra showed a bimodal distribution for the January 4, 2006 case. The *Vis* was almost two times less when large drizzle size drops forming the bimodal spectra were not present, indicating that preset particle spectral shape for fog modeling should be carefully chosen when bimodal spectra exist. A size that divides the spectra for fog droplets and drizzle-sized particles should be known accurately; otherwise, the calculated *Vis* can be overestimated.

Nowcasting for fog conditions needs an integration of observations and models data (e.g., ISAAC *et al.*, 2006). The present work showed that MWR, FMD, Vaisala *Vis* meter, and satellite-based algorithms are needed for a better nowcasting algorithm. A work by GULTEPE *et al.* (2007) also showed that integration of model-based parameters such as RH_w and T at the surface, together with satellite based algorithms, can improve fog forecasting up to 30%.

The following additional conclusions can be drawn as:

- The N_d ranges from a few droplets per cm^{-3} up to a few 100 cm^{-3} for a given *LWC*, which indicates that *Vis* should be parameterized as a function of both N_d and *LWC*. Otherwise, uncertainty in *Vis* can be more than 50% if *Vis* is only a function of *LWC*.
- The earlier parameterizations of visibility were developed based only on a function of *LWC* alone, and this caused the over/underestimate of the visibility depending

on environmental conditions. Thus, for improved prediction of visibility by an NWP model, the condensation scheme should be double-moment for the cloud category.

- Alternatively, if N_d is obtained as a function of environmental conditions such as T (GULTEPE and ISAAC, 2004; GULTEPE *et al.*, 1999), more accurate *Vis* predictions can be made even with current operational forecast models using single-moment cloud schemes. Visibility could thus be estimated based on a diagnostic N_d and the LWC predicted by the bulk microphysical schemes.
- Overall, the application of the MC2 model suggests that the new visibility parameterization can be used for fog forecasting in the regional forecasting models such as the Canadian GEM forecast model, the US Rapid Upper Cycle (RUC) model (BENJAMIN *et al.*, 2004), and the NCAR Weather Research and Forecasting (WRF) model CHENG and STEENBURGH (2005). Additional data set from the FRAM marine fog cases can also be used for validation of the visibility parameterizations and model verifications however, this work is left for the future.

Acknowledgements

Funding for this work was provided by the Canadian National Search and Rescue Secretariat and Environment Canada. Some additional funding was also provided by the European COST-722 fog initiative project office. Technical support for the data collection was provided by the Cloud Physics and Severe Weather Research Section of the Science and Technology Branch, Environment Canada, Toronto, Ontario. Authors were also thankful to M. Wasey and R. Reed of Environment Canada for technical support during the FRAM.

REFERENCES

BELAIR, S., CREVIER, L.-P., MAILHOT, J., Bilodeau, B., and DELAGE, Y. (2003a), *Operational implementation of the ISBA land surface scheme in the Canadian regional weather forecast model. Part I: Warm season results,* J. Hydrometeor. *4*, 352–370.

BELAIR, S., BROWN, R., MAILHOT, J., BILODEAU, B., and CREVIER, L.-P. (2003b), *Operational implementation of the ISBA land surface scheme in the Canadian regional weather forecast model. Part II: Cold season results,* J. Hydrometeor. *4*, 371–386.

BELAIR, S., MAILHOT, J., GIRARD, C., and VAILLANCOURT, P. (2005), *Boundary layer and shallow cumulus clouds in a medium-range forecast of a large-scale weather system,* Mon. Wea. Rev. *133*, 1938–1960.

BENJAMIN, S. G., DEVENYI, D., WEYGANDT, S. S., BRUNDAGE, K. J., BROWN, J. M., GRELL, G. A., KIM, D., SCHWARTZ, B. E., SMIRNOVA, T. G., SMITH, T. L., and MANIKIN, G. S. (2004), *An hourly assimilation–forecast cycle: The RUC,* Mon. Wea. Rev. *132*, 495–518.

BENOIT, R., COTE, J., and MAILHOT, J. (1989), *Inclusion of a TKE boundary layer parameterization in the Canadian regional finit-element model,* Mon. Wea. Rev. *117*, 1726–1750.

BENOIT, R., DESGAGNE, J.M., PELLERIN, P., PELLERIN, S., CHARTIER, Y., and DESJARDINS, S. (1997), *The Canadian MC2: A semi-Lagrangian, semi-implicit wideband atmospheric model suited for fine scale process studies and simulation,* Mon. Wea. Rev. *125*, 2382–2415.

BROWN T. and POMEROY J.W. (1989), *A blowing snow particle detector*. J. Cold Regions Science and Technology, *16*, 167–174.

BOTT, A. and TRAUTMANN, T. (2002), *PAFOG—A new efficient forecast model of radiation fog and low-level stratiform clouds,* Atmos. Res. *64,* 191–203.

BRENGUIER, J. L., PAWLOWSKA, H., SCHULLER, L., PREUSKER, R., FISCHER, J., and FOUQUART, Y. (2000), *Radiative properties of boundary layer clouds: Dropplet effective radius versus number concentration,* J. Atmos. Sci. *57*, 803–821.

CHENG, W. Y. Y. and STEENBURGH, W. J. (2005), *Evaluation of Surface Sensible Weather Forecasts by the WRF and the Eta Models over the Western United States,* Weather and Forecasting *20*, 812–821.

COTE, J., GRAVEL, S., METHOT, A., PATOINE, A., ROACH, M., and STANIFORTH, A. (1998), *The operational CMC-MRB Global Environmental Multiscale (GEM) model: Part I - Design considerations and formulation,* Mon. Wea. Rev. *126*, 1373–1395.

ELLROD, G. P. (1995), *Advances in the detection and analysis of fog at night using GOES multispectral infrared imagery*, Weather and Forecasting, *10*, 606–619.

FOUQUART, Y. and BONNEL, B. (1980), *Computations of solar heating of the earth's atmosphere: A new parameterization,* Contrib. Atmos. Phys. *53*, 35–62.

GARAND, L. and MAILHOT, J. (1990), *The influences of infrared radiation on numerical weather forecasts,* Preprints, Seventh Conf. on Atmospheric Radiation, San Francisco, CA, Amer. Meteor. Soc. J146–151.

GULTEPE, I., ISAAC, G. A., LEAITCH, W. R., and BANIC, C. M. (1996), *Parameterization of marine stratus microphysics based on in-situ observations: Implications for GCMs,* J. Climate *9*, 345–357.

GULTEPE, I. and ISAAC, G. A. (1999), *Scale effects on averaging of cloud droplet and aerosol number concentrations: Observations and models*, J. Climate *12*, 1268–1279.

GULTEPE, I., ISAAC, G. A., and STRAWBRIDGE, K. (2001), *Variability of cloud microphysical and optical parameters obtained from aircraft and satellite remote sensing during RACE,* Inter. J. Climate *21*, 4, 507–525.

GULTEPE, I. and ISAAC, G. A. (2004), *An analysis of cloud droplet number concentration (N_d) for climate studies: Emphasis on constant N_d.* Q. J. Royal Met. Soc. *130*, Part A, 602, 2377.

GULTEPE, I., MULLER, M. D., and BOYBEY, Z. (2006a), *A new warm fog parameterization scheme for numerical weather prediction models*, J. Appl. Meteor. *45*, 1469–1480.

GULTEPE, I, COBER, S. G., KING, P., ISAAC, G., TAYLOR, P., and HANSEN, B. (2006b), *The Fog Remote Sensing and Modeling (FRAM) Field Project And Preliminary Results*, AMS 12th Cloud Physics Conference, July 9–14, 2006, Madison, Wisconsin, USA, Print in CD, P4.3.

GULTEPE, I., PAGOWSKI, M., and REID, J. (2007), *S satellite based fog detection scheme using screen air temperature,* J. Weather and Forecasting, in press.

ISSAAC, G. A., BAILEY, M., COBER, S. G., DONALDSON, N., DRIEDGER, N., GLAZER, A., GULTEPE, I, HUDAK, D., KOROLEV, A., REID, J., RODRIGUEZ, P., STRAPP, J. W., and FABRY, F. (2006), *Airport Vicinity Icing and Snow Advisor*. AIAA 44th Aerospace Sci. Meeting and Exhibit, Reno Nevada, 9–12 January 2006, AIAA-2006-1219.

JIUSTO, J. E., *Fog structure. Clouds, Their Formation, Optical Properties, and Effects* (P. V. Hobbs and A. Deepak, eds.) (Academic Press 1981), pp. 187–239.

KOENING, L. R. (1971), *Numerical experiments pertaining to warm-fog clearing*, Mon. Wea. Rev. *9*, 227–241.

KUNKEL, B. A. (1984), *Parameterization of droplet terminal velocity and extinction coefficient in fog models*, J. Appl. Meteor. *23*, 34–41.

MAILHOT, J. and COAUTHORS, (1998), *Scientific description of RPN physics library – Version 3.6*. Recherche en prévision numérique, 188 pp. (Available online at http://collaboration.cmc.ec.gc.ca/science/rpn/physics/physics98.pdf)

MEYER, M. B., JIUSTO, J. E., and LALA, G. G. (1980), *Measurements of visual range and radiation-fog (haze) microphysics*, J. Atmos. Sci. *37*, 622–629.

MILBRANDT, J. A., and YAU, M. K. (2005a), *A multimoment bulk microphysics parameterization. Part I: Analysis of the role of the spectral shape parameter,* J. Atmos. Sci. *62*, 3051–3064.

MILBRANT, J.A. and YAU, M.K. (2005b), *A multimoment bulk microphysics parameterization. Part II: A proposed three-moment closure and scheme description*, J. Atmos. Sci. *62*, 3065–3081.

SAVELYEV, S. A., GORDON, M., HANESIAK, J., PAPAKOURIOKI, T., and TAYLOR P. A. (2006) *Blowing snow studies in CASES Canadian Arctic Shelf Exchange Study (CASES)*. Hydrological Processing, *4*, 817–827.

STOELINGA, M. T. and WARNER, T. T. (1999), *Nonhydrostatic, Mesobeta-scale model simulations of cloud ceiling and visibility for an east coast winter precipitation event*, J. Appl. Meteor. *38*, 385–404.

THOMAS, S.J., GIRARD, C., BENOIT, R., DESGAGNE, M., and PELLERIN, P. (1998), *A new adiabatic kernel for the MC2 model*, *Atmos.-Ocean 36*, 241–270.

WHIFFEN, B. (2001), *Fog: Impact on aviation and goals for meteorological prediction*. 2nd Conf. on Fog and Fog Collection, St. John's Canada, 15–20 July, 2001, 525–528.

(Received October 5, 2006, accepted November 15, 2006)
Published Online First: June 8, 2007

Pure appl. geophys. 164 (2007) 1179–1192
0033–4553/07/071179–14
DOI 10.1007/s00024-007-0213-8

Pure and Applied Geophysics

Dynamical Nighttime Fog/Low Stratus Detection Based on Meteosat SEVIRI Data: A Feasibility Study

Jan Cermak and Jörg Bendix

Abstract—Automated detection of fog and low stratus in nighttime satellite data has been implemented on the basis of numerous satellite systems in past decades. Commonly, differences in small-droplet emissivities at 11μm and 3.9μm are utilized. With Meteosat SEVIRI, however, this method cannot be applied with a fixed threshold due to instrument design: The 3.9μm band is exceptionally wide and overlaps with the 4μm CO_2 absorption band. Therefore, the emissivity difference varies with the length of the slant atmospheric column between sensor and object. To account for this effect, the new technique presented in this paper is based on the dynamical extraction of emissivity difference thresholds for different satellite viewing zenith angles. In this way, varying concentrations of CO_2 and column depths are accounted for. The new scheme is exemplified in a plausibility study and shown to provide reliable results.

Key words: Fog, low stratus, satellite retrieval, meteosat SEVIRI, CO_2 absorption, limb effect.

1. Introduction

1.1. Background

Fog and low stratus (FLS) are of great importance from several perspectives: As a modifier in the climate system (e.g., Houghton *et al.*, 2001), as an obstruction to traffic at land, sea and in the air (e.g., Pagowski *et al.*, 2004; Leigh, 1995), and as a factor with an impact on air quality (e.g., Kraus and Ebel, 1989; Bendix, 2002). Climatically, low clouds are expected to have a slight cooling effect (cf., the review by Stephens, 2005).

Reliable near-real time information on the spatio-temporal distribution of FLS can only be obtained from satellite data; station measurements lack the spatial component and the interpolation of point visibility data is impractical, due to the complex nature of spatial visibility distribution. Some approaches combine model

Laboratory for Climatology and Remote Sensing (LCRS), Philipps-Universität Marburg, Germany. E-mail: cermak@lcrs.de

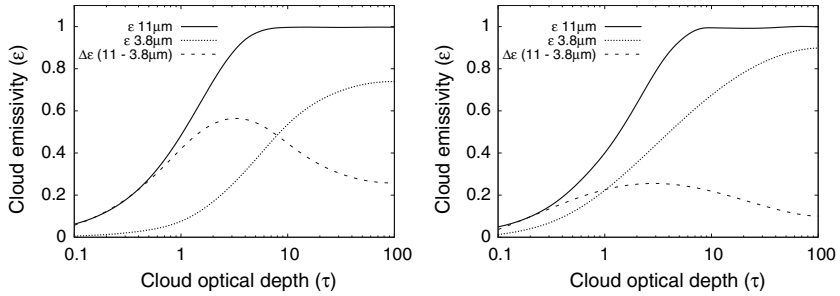

Figure 1
Emissivities as a function of droplet size and wavelength vs. cloud optical depth, after HUNT (1973). ϵ is the emissivity at wavelength λ, $\Delta\epsilon$ the difference in emissivities. The panel on the left-hand side shows the emissive behaviour for an effective droplet radius of 4 μm, the right-hand side for 10 μm.

output and satellite observations (e.g., GULTEPE *et al.*, 2007). However, model data are not always reliable and available, consequently this paper focusses on satellite data only.

Satellite-based detection of FLS has been performed on a wide range of platforms for a long time. Some of these can be applied in operational processing, i.e., they offer an objective decision on the presence of FLS, others require a pre-selection of scenes. Operational algorithms for daytime FLS detection have recently been proposed by BENDIX *et al.* (2006) (Terra MODIS) and ČERMAK and BENDIX (2006) (Meteosat SEVIRI). At night, an operationally applicable technique for the delineation of FLS has been in widespread use since it was first presented by EYRE *et al.* (1984). These authors take the difference in radiances at 10.8 and 3.7 μm as an indication of fog presence. In essence, the technique based on this principle identifies low clouds with predominantly small droplets; a combination of properties found in FLS (e.g., WMO, 1992, 1996; ROACH, 1994). The physical basis is the emissivity difference between infrared and middle infrared wavelengths as a function of cloud droplet size as presented by HUNT (1973). This relationship is shown in Figure 1 for clouds of various optical depths. It can be seen that emissivity differences between both wavelengths are considerably larger for small droplets (effective radius = 4 μm in Fig. 1) than for larger droplets (effective radius = 10 μm). This principle is used to identify small-droplet clouds in satellite imagery. Since its first application, the method has been widely used by numerous authors with NOAA AVHRR, Terra/Aqua MODIS and GOES Imager data (TURNER *et al.*, 1986; ALLAM 1987; D'ENTREMONT and THOMASON, 1987; BENDIX and BACHMANN, 1991; DERRIEN *et al.*, 1993; BENDIX, 1995; ELLROD, 1995; LEE *et al.*, 1997; REUDENBACH and BENDIX, 1998; PUTSAY *et al.*, 2001; BENDIX, 2002; UNDERWOOD *et al.*, 2004). It has been shown that this method provides accurate detection of small-droplet clouds in the studies cited, with clear separations of FLS from cloud-free regions, snow and other clouds by applying a static blackbody temperature difference threshold.

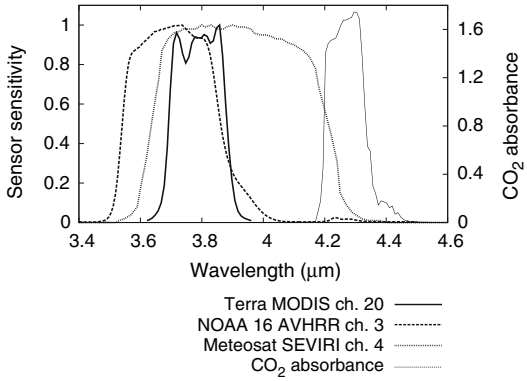

Figure 2
Response function of the SEVIRI 3.9 μm channel versus CO_2 absorbance. CO_2 data from SMITH (1982).

1.2. SEVIRI Specifics

The Spinning-Enhanced Visible and Infrared Imager (SEVIRI, AMINOU, 2002) aboard Meteosat 8 is the first European geostationary instrument to include a middle infrared band at 3.9 μm. In principle, the blackbody temperature difference method referred to above should also be applicable on this platform as well. In contrast to the systems mentioned before, however, the SEVIRI middle infrared channel has a very large spectral width and partly overlaps with the CO_2 absorption band centred around 4.2 μm. Figure 2 contrasts the spectral response function of the SEVIRI 3.9 μm channel with CO_2 absorption.

This absorptive behaviour in the middle infrared channel has a direct impact on 3.9 μm radiances measured

$$I_{3.9} = I^0_{3.9} + a_I \tag{1}$$

with $I_{3.9}$ the radiances at 3.9 μm, $I^0_{3.9}$ the same without atmospheric impact, and a_I the level of CO_2 absorption. Accordingly, the blackbody temperature is given by

$$T_{3.9} = T^0_{3.9} + a_T \tag{2}$$

with $T_{3.9}$ the blackbody temperature at 3.9 μm, $T^0_{3.9}$ the same without atmospheric impact, and a_T the level of CO_2 absorption. The blackbody temperature difference ΔT therefore is given by

$$\Delta T = T_{10.8} - T_{3.9} = T_{10.8} - (T^0_{3.9} + a_T) \tag{3}$$

with $T_{10.8}$ the blackbody temperature at 10.8 μm. The atmospheric influence a_T significantly impairs the applicability of the FLS detection approach outlined above on Meteosat SEVIRI. The effect has also been documented and addressed by the EUMETSAT Nowcasting SAF (Satellite Applications Facility) (METEO-FRANCE, 2005)

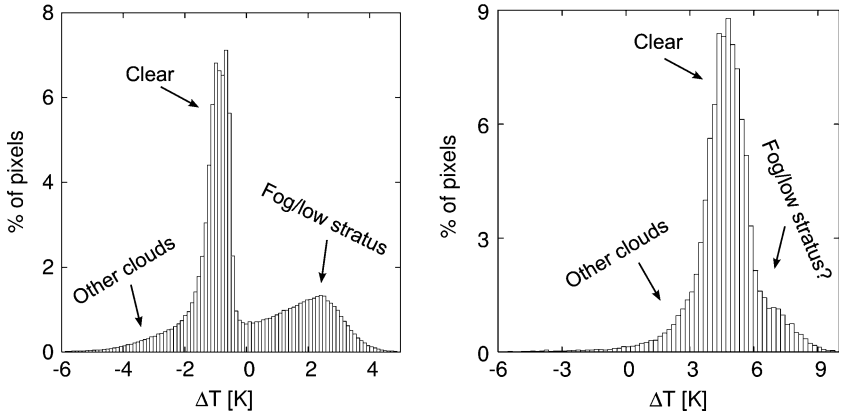

Figure 3
Blackbody temperature differences ($\Delta T = T_{10.8} - T_{3.9}$) for a MODIS scene over Central Europe, 2050 UTC, 10 February, 2006 (left-hand panel) and a subset from the corresponding SEVIRI scene (2045 UTC) for the same area.

and in the EUMETSAT MSG channel interpretation guide (KERKMANN *et al.*, 2004). These sources also report a significant effect of water vapour absorption on the infrared channel signals.

The level of CO_2 absorption (a_T) varies with the season and length of the atmospheric path. Vegetation growth is the main seasonal factor reducing the CO_2 column. This relationship is very clearly shown in products derived using the SCIAMACHY sensor by BUCHWITZ *et al.*, (2005a); in the Northern Hemisphere, CO_2 levels therefore are lowest in July (BUCHWITZ *et al.*, 2005b).

At high latitudes, "limb cooling" or "limb darkening" is a phenomenon all geostationary platforms suffer from. The blackbody temperatures measured at large satellite zenith angles (near the "limb") are reduced due to geometric (obstruction by sides of clouds) and radiometric (atmospheric extinction) effects (JOYCE *et al.*, 2001; MINNIS and KHAIYER, 2000). Therefore, the length of the slant atmospheric column between the sensor and the earth is of crucial importance from the satellite perspective. For the Meteosat SEVIRI 3.9 μm channel, the radiometric effect is especially enhanced due to the overlap with the CO_2 band. Therefore, a_T increases markedly with satellite zenith angle (θ).

2. Proposed Methodology

As outlined above, the separation of FLS from other surfaces can be founded on the blackbody temperature difference ΔT. In a sensor with two true window channels at around 11 and 3.9 μm, i.e., without CO_2 interference, a frequency distribution of

ΔT displays a distinct threshold between clear pixels and those covered by FLS as a relative minimum in the histogram. An example of this is shown in Figure 3 (left hand panel) for the MODIS sensor, for a scene centred on the European Alps.

Due to the effects referred to in the previous section, the distinction between clear pixels and pixels covered by FLS is substantially more difficult in SEVIRI imagery. On the right hand side of Figure 3, a histogram for a subset from a SEVIRI scene corresponding to the time and area of the MODIS scene is shown. Here, the total distribution as well as the clear pixel peak have considerably wider distributions than in MODIS. This can be attributed to latitudinal differences in CO_2 absorbance. The overall level of the distribution is higher, which is also an effect of CO_2 presence (see equation 3). In contrast to the corresponding MODIS histogram, no clear threshold can be seen here.

Due to these limitations, it is not possible to find a fixed threshold for FLS identification in SEVIRI scenes. As stated above, the levels of CO_2 influence vary with season and latitude. Therefore a method needs to be found that dynamically separates FLS from clear areas for each individual scene and satellite zenith angle (θ).

The new method developed to achieve a clean FLS identification consists of several steps. The procedure is outlined in Figure 4. The key hypotheses underlying the scheme are that

1. A dynamical determination of thresholds for each scene will allow for stable algorithm performance regardless of CO_2 level changes over time.
2. Local variations in CO_2 absorbance with latitude within a scene can be compensated by a satellite-zenith-angle-specific threshold determination.

The approach closely follows these hypotheses.

As a first step, the blackbody temperature difference ΔT is computed. Also, maximum and minimum satellite zenith angles $\theta_{\max}$ and $\theta_{\min}$ are determined for the particular scene. Next, the retrieval of a localised ΔT threshold value for the separation of FLS and clear pixels is attempted. This is done on the basis of zenith angles, in an iteration loop over the satellite zenith angles θ from $\theta_{\min}$ to $\theta_{\max}$.

For each zenith angle θ, the number of zenith angles θ_s present in the satellite scene so that

$$(\theta - D) \leq \theta_s \leq (\theta + D) \tag{4}$$

is counted, where D is a distance initially set to 0.5°. D is increased in steps of 0.5° until the number of pixels with θ_s meeting the above criterion reaches a predetermined minimum (5000). For a scene subset centered on Europe, D takes values between 0.5 and 1.5.

Next, all ΔT values of the pixels identified in this way are analysed for their frequency distribution. Since the path between the satellite sensor and the locations of these pixels is approximately constant, variation in the CO_2 effect is minimised, so that a distinction between different surfaces in the histogram becomes possible.

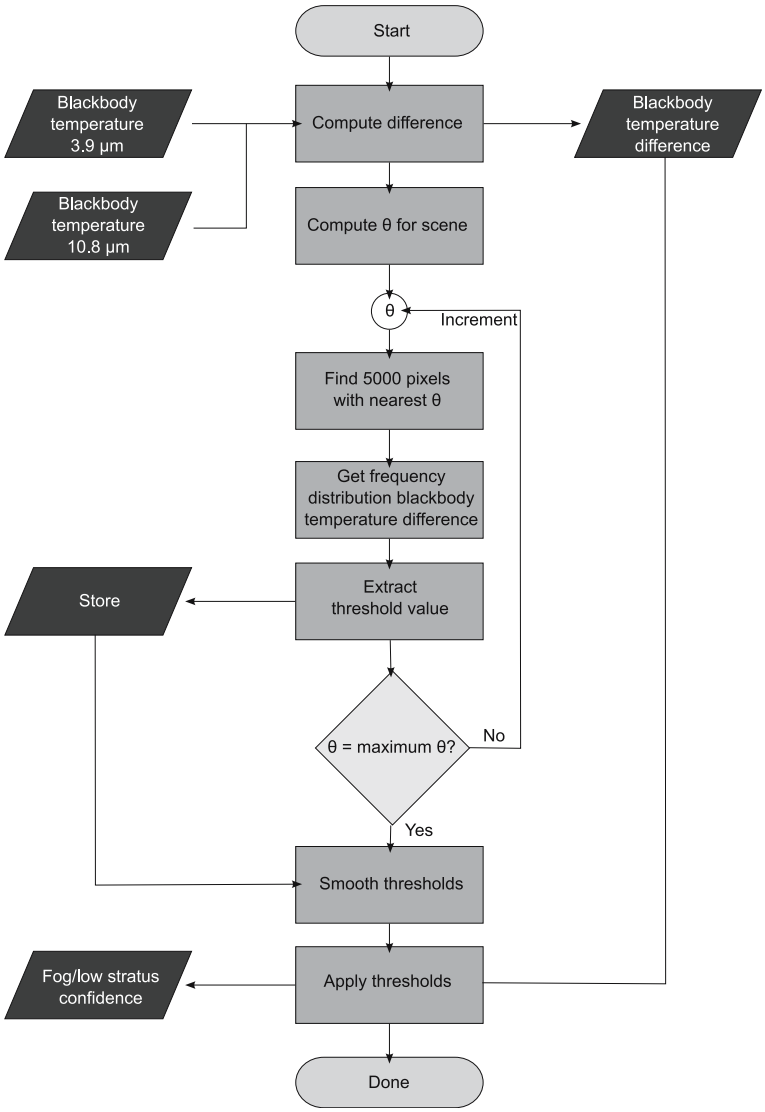

Figure 4
Overview of the new nighttime FLS detection scheme. For a detailed description see text.

Figure 5 shows two representative examples of zenith-angle-specific ΔT frequency distributions. The histogram in the left-hand panel shows a situation with distinct cloud-free and FLS peaks; the right-hand panel displays a distribution with a very low number of FLS pixels and thus without a distinct peak.

Due to the different nature of distributions shown here, different techniques for threshold identification need to be applied:

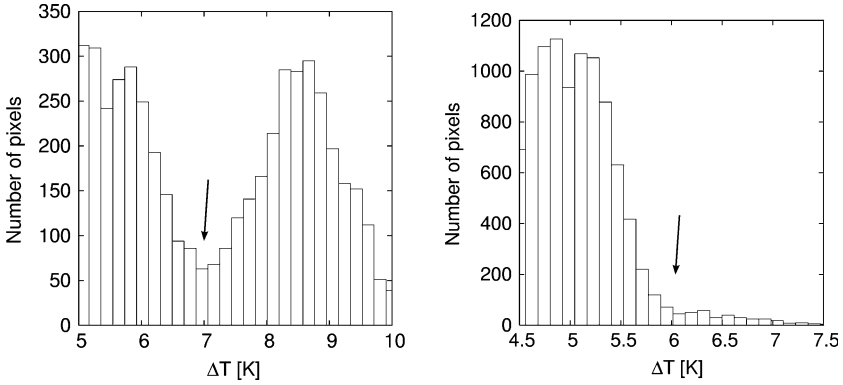

Figure 5
Histograms of the blackbody temperature differences ΔT centred around a satellite zenith angles $\theta = 69°$ (left) and $\theta = 44°$ (right), 2045 UTC, 10 February, 2006. The thresholds are indicated by arrows.

- In the case of a bimodal distribution (left panel in Fig. 5), the turning point between both peaks is extracted and used as a threshold.
- For unimodal histograms, the threshold is set to the point where the slope of the clear-sky peak drops significantly.

Both thresholds are indicated in Figure 5.

In this way, a threshold is identified for each θ present in the scene under consideration (see Fig. 4). In order to minimise the possible effect of any inaccurate thresholds, a least-squares linear regression is performed over the initial thresholds found for a scene, to derive a function relating θ and corresponding ΔT thresholds. The relationship between both parameters is shown for an exemplary scene in

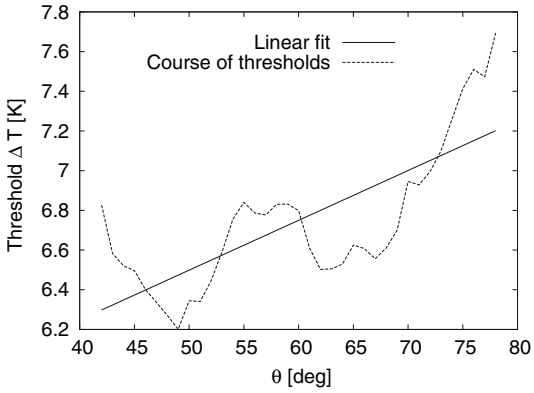

Figure 6
Satellite zenith angle θ versus FLS threshold for the SEVIRI scene 2045 UTC, 10 February, 2006.

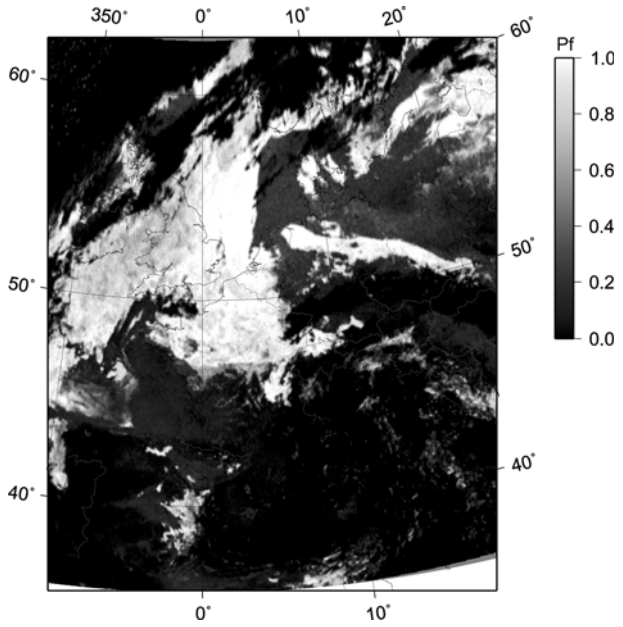

Figure 7
FLS confidence levels P_f computed with the new method for the SEVIRI scene 0400 UTC, 7 October, 2005. The corresponding infrared temperature image is shown in Figure 8.

Figure 6. The increase of the blackbody temperature difference threshold with θ is clearly visible. Oscillations in the raw thresholds extracted are mostly due to slight technical inaccuracies in the histogram interpretation technique, which can be eliminated by threshold smoothing, as shown in the figure.

Once thresholds have been determined in this way, a classification of the ΔT image is performed. The blackbody temperature difference of each pixel is compared with the appropriate interpolated threshold for θ at this location. On this basis, a FLS confidence level is obtained by

$$P_f(a) = \frac{t_{\theta(a)} - \Delta T(a) - FCR}{-2FCR} \tag{5}$$

with $P_f(a)$ the FLS confidence level at pixel a, $0 \leq P_f \leq 1$, $t_{\theta(a)}$ the threshold value at the given θ and *FCR* the FLS confidence range. The FLS confidence range is the range between the threshold and a certain clear or a certain cloudy pixel. All values in the centre of the clear peak are to be assigned a confidence level of 0, those in the centre of the cloudy peak of 1. To accommodate the average gap between the two peaks, *FCR* is set to 2 K. A value $\Delta T(a) = t_{\theta(a)}$ is thus assigned a P_f of 0.5.

An example of the FLS confidence levels P_f computed in this way is shown in Figure 7. The corresponding infrared (10.8 μm) blackbody temperatures are presented in Figure 8 for orientation.

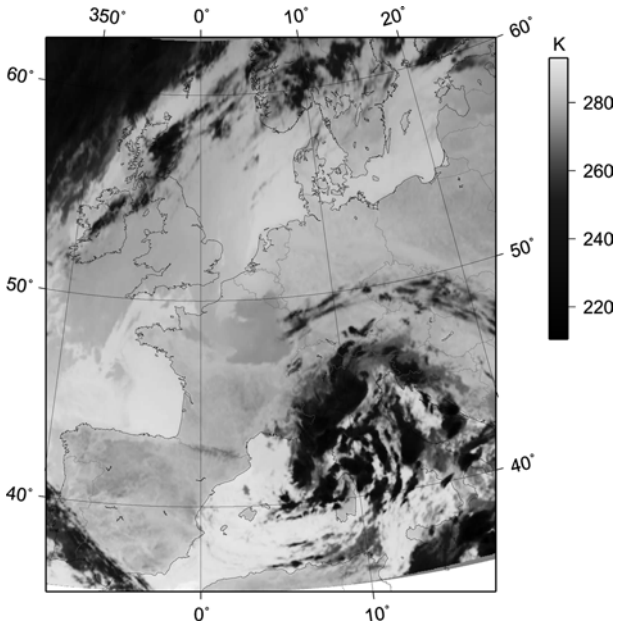

Figure 8
Blackbody temperatures in the 10.8 μm channel for the SEVIRI scene 0400 UTC, 7 October, 2005, as an orientation for Figure 7.

3. Plausibility Assessment

For validation of the new technique, a series of Meteosat SEVIRI scenes were selected and processed in the manner described above. The following criteria were applied for scene selection: a) Presence of FLS in at least some part of the scene; b) some representation of seasonal variability. The 0400 UTC scenes of the following five days were used: 18 August, 2005, 18 October, 2005, 10 December, 2005, 14 February, 2005, 24 February, 2005.

As reference data, METAR (Meteorological Aerodrome Report) data were used. METARs comprise hourly or more frequent meteorological measurements from airports worldwide. The parameter used for comparison with the satellite data is cloud height. In the METAR measurements, this represents cloud base height. A cutoff level of 2000 m was used for a low cloud decision (WMO, 1996).

A likely source of error is high-reaching clouds with low cloud bases, and low clouds 'hidden' underneath higher cloud layers. While these cases would appear as low clouds in the METAR classification, the satellite scheme would flag the corresponding pixels as non-low-cloud pixels. In order to avoid the significant bias expected from this perspective-dependent factor, these situations are explicitly excluded from the validation. In order to achieve this, all pixels on the left-hand side of the ΔT histogram (see above) are set to missing in the satellite classification.

Table 1

Contingency table. A: Correctly identified situations (hits), B: False alarms, C: Misses, D: Correct negatives

	METAR Yes	METAR No
Satellite Yes	A	B
Satellite No	C	D

Data intercomparison is based on contingency tests. The METAR classification and the satellite classification are compared in the way shown in Table 1, where 'Yes' indicates a positive observation (i.e., FLS presence) and 'No' a negative one. From the figures A, B, C and D obtained for the entire data set in this way, the probability of detection (POD), probability of false detection (PFD) and critical success index (CSI) are computed as follows:

$$POD = \frac{A}{A + C}, \tag{6}$$

$$PFD = \frac{B}{B + D}, \tag{7}$$

$$CSI = \frac{A}{A + B + C}. \tag{8}$$

All indicators are scaled from 0 to 1, with POD = 1 indicating best detection and PFD = 1 showing a situation with only misclassifications. CSI is a measure of overall classification accuracy; higher values indicate better skill. A common way of presenting POD and PFD at the same time are receiver operating characteristic (ROC) curves (WILSON and BURROWS, 2004; MARZBAN, 2004). These allow for the assessment of a method's skill with the application of varying thresholds. In the case of the present study, the FLS confidence level P_f was used as this threshold.

The ROC curve in Figure 9 shows the variation of the classification skill with changing thresholds (numbers next to the curve). The curve remains well above the random forecast skill (diagonal line) for all thresholds. The best classification (i.e., longest distance from the diagonal) is obtained for the confidence levels around 0.5. This indicates that the threshold identified in the new FLS detection approach is at the appropriate level.

At the FLS confidence level $P_f = 0.5$, POD reaches 0.47, while PFD is at 0.17. This means that while false alarms are at a low level, a good portion of the low cloud situations are missed at this P_f. This is very easily explained by the data comparison approach: The classification applied to the METAR data identifies low cloud bases only. There are very likely non-fog or non-stratiform clouds with cloud bases below 2000 m present in the scenes. A detailed treatment of this type of uncertainty is given

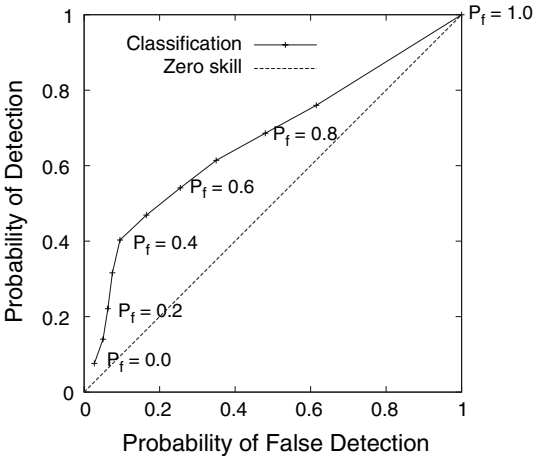

Figure 9
ROC curve for the comparison between the satellite classification and a ground-based assessment of cloud height. The confidence levels P_f used for cutoff at each step are indicated next to the curve. The diagonal line represents a hypothetical classification with no skill.

in CERMAK *et al.* (2006) and CERMAK and BENDIX (2006). In order to assess whether classification skill is really free of a regional bias, satellite zenith angle θ is plotted versus critical success index (CSI) in Figure 10. The figure clearly shows that CSI varies irregularly throughout the data set, independently of θ.

A number of uncertainties are inherent in the validation of satellite classifications with point data. Most importantly they include collocation, timing and station data accuracy. A point measurement such as a station observation is not necessarily representative for the entire area covered by the corresponding satellite pixel. Thus, not all features observed in one measurement are necessarily matched in the other. In

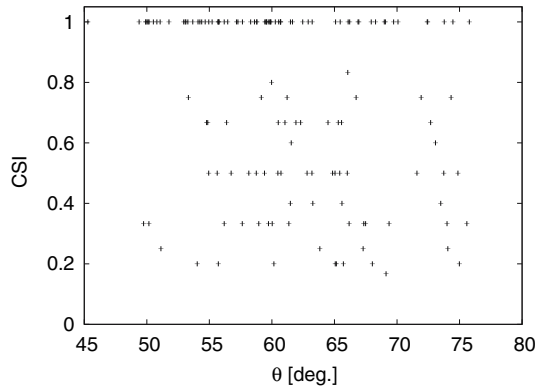

Figure 10
Satellite zenith angle θ versus critical success index CSI for the plausibility study over all scenes.

the dissipation stages of fog, small differences in the timing of observation and satellite classification may lead to diverging results without either assessment being faulty. These factors must be considered in the interpretation of the plausibility study results.

4. Conclusions and Outlook

A new technique for the detection of fog and low stratus with MSG SEVIRI data has been proposed in this paper. The plausibility tests presented in the previous section yield encouraging results despite the uncertainties involved in the validation procedure. According to the statistical evaluation, FLS is detected adequately; a regional bias was not found.

It thus appears that the newly proposed scheme is a feasible way forward to overcome the limitations of the SEVIRI sensor and exclude the seasonal and regional effects of atmospheric CO_2 absorption. In this way, with MSG SEVIRI, it should be possible to automatically identify FLS at nighttime at a high temporal resolution over Europe for the first time. The authors therefore recommend the application of a dynamic threshold as described in this paper for FLS detection with MSG SEVIRI.

The method presented here will be implemented in operational processing of SEVIRI data at the Laboratory for Climatology and Remote Sensing (LCRS) in the near future. In addition to the automated delineation of FLS areas, it would be desirable to reach a distinction between areas with ground fog (i.e., visibility impairment at the ground) and low stratiform clouds without ground contact. BENDIX *et al*. (2005) have recently presented such a scheme for daytime MODIS data. The development of a similar technique is intended for nighttime application on Meteosat SEVIRI data.

Acknowledgements

The research presented in this paper is embedded into the framework of the ESA/EUMETSAT MSG RAO PI programme (ID 141) and the ESF COST action 722 (“Short Range Forecasting Methods of Fog, Visibility and Low Clouds”). The scientific exchange with numerous colleagues within the COST action was conducive to the progress of this work.

REFERENCES

ALLAM, R. (1987), *The detection of fog from satellites*, In. Proc. Workshop on Satellite and Radar Imagery Interpretation, pp. 495–505.

AMINOU, D. M. A. (2002), *MSG's SEVIRI instrument*, ESA Bulletin *111*, 15–17.

BENDIX, J. (1995), *A case study on the determination of fog optical depth and liquid water path using AVHRR data and relations to fog liquid water content and horizontal visibility*, Internat J. Remote Sensing *16*, 515–530.

BENDIX, J. (2002), *A satellite-based climatology of fog and low-level stratus in Germany and adjacent areas*, Atmos. Res. *64*, 3–18.

BENDIX, J. and BACHMANN, M. (1991), *Ein operationell einsetzbares Verfahren zur Nebelerkennung auf der Basis von AVHRR-Daten der NOAA-Satelliten*, Meteorologische Rundschau *43*, 169–178.

BENDIX, J., THIES, B., CERMAK, J., and NAUSS, T. (2005), *Ground fog detection from space based on MODIS daytime data—A feasibility study*, Weather and Forecasting *20*, 989–1005.

BENDIX, J., THIES, B., NAUSS T., and CERMAK, J. (2006), *A feasibility study of daytime fog and low stratus detection with TERRA/AQUA-MODIS over land*, Meteor. Appl. *13*, 111–125.

BUCHWITZ, M., DE BEEK, R., BURROWS, J. P., BOVENSMANN, H., WARNEKE, T., NOTHOLT, J., MEIRINK, J. F., GOEDE, A. P. H., BERGAMASCHI, P., KÖRNER, S., HEIMANN, M., and SCHULZ, A. (2005a), *Atmospheric methane and carbon dioxide from SCIAMACHY satellite data: Initial comparison with chemistry and transport models*, Atmos. Chem. Phys. *5*, 941–962.

BUCHWITZ, M., DE BEEK, R., NOËL, S., BURROWS, J. P., BOVENSMANN, H., BREMER, H., BERGAMASCHI, P., KÖRNER, S., and HEIMANN, M. (2005b), *Carbon monoxide, methane and carbon dioxide columns retrieved from SCIAMACHY by WFM-DOAS: Year 2003 initial data set*, Atmos. Chem. Phys. *5*, 3313–3329.

CERMAK, J. and BENDIX, J. (2006), *A novel approach to fog/low stratus detection using Meteosat 8 data*, Atmos. Res. accepted.

CERMAK, J., SCHNEEBELI, M., NOWAK, D., VUILLEUMIER, L., and BENDIX, J. (2006), *Characterization of low clouds with satellite and ground-based remote sensing systems*, Meteorologische Zeitschrift *15*, 65–72.

D'ENTREMONT, R. and THOMASON, L. (1987), *Interpreting meteorological satellite images using a color-composite technique*, Bull. Am. Meteor. Soc. *68*, 762–768.

DERRIEN, M., FARKI, B., HARANG, L., LEGLEAU, H., NOYALET, A., POCHIC, D., and SAIROUNI, A. (1993), *Automatic cloud detection applied to NOAA-11/AVHRR imagery*, Remote Sensing of Environ. *46*, 246–267.

ELLROD, G. P. (1995), *Advances in the detection and analysis of fog at night using goes multispectral infrared imagery*, Weather and Forecasting *10*, 606–619.

EYRE, J. R., BROWNSCOMBE, J. L., and ALLAM, R. J. (1984), *Detection of fog at night using Advanced Very High Resolution Radiometer (AVHRR) imagery*, Meteoro. Mag. *113*, 266–271.

GULTEPE, I., PAGOWSKI, M., and REID, J. (2007), *A satellite-based fog detection scheme using screen air temperature*, Weather and Forecasting *22*, no. 3.

HOUGHTON, J. T., DING, Y., GRIGGS, D. J., NOGUER, M., VAN DER LINDEN, P. J., DAI, X., MASKEL, K., and JOHNSON, C. A. (eds.), *Climate Change 2001: The Scientific Basis* (Cambridge University Press, Cambridge, UK, 2001).

HUNT, G. E. (1973), *Radiative properties of terrestrial clouds at visible and infra-red thermal window wavelengths*, Quart. J. Roy. Meteor. Soc. *99*, 346–369.

JOYCE, R., JANOWIAK, J., and HUFFMAN, G. (2001), *Latitudinally and seasonally dependent zenith-angle corrections for geostationary satellite IR brightness temperatures*, J. Appl. Meteor. *40*, 689–703.

KERKMANN, J., ROSENFELD, D., LUTZ, H. J., PRIETO, J., and KÖNIG, M. (2004), *Applications of Meteosat Second Generation (MSG): Meteorological use of the SEVIRI IR3.9 channel*, MSG channels interpretation guide, EUMETSAT, available online at http://oiswww.eumetsat.org/WEBOPS/msg_interpretation/.

KRAUS, H. and EBEL, U. (1989), *Atmospheric boundary layer characteristics in severe smog episodes*, Meteor. Atmos. Phys. *40*, 211–224.

LEE, T. E., TURK, F. J., and RICHARDSON, K. (1997), *Stratus and fog products using GOES-8-9 3.9-μm data*, Weather and Forecasting *12*, 664–677.

LEIGH, R. J. (1995), *Economic benefits of terminal aerodrome forecasts (TAFs) for Sydney airport, Australia*, Meteor. Appl. *2*, 239–247.

MARZBAN, C. (2004), *The ROC curve and the area under it as performance measures*, Weather and Forecasting *19*, 1106–1114.

METEO-FRANCE (2005), *User manual for the PGE01-02-03 of the SAFNW/MSG: Scientific part, User manual SAF/NWC/IOP/MFL/SCI/SUM/01* , EUMETSAT SAFNWC.

MINNIS, P. and KHAIYER, M. M. (2000), *Anisotropy of land surface skin temperature derived from satellite data*, J. Appl. Meteor. *39*, 1117–1129.

PAGOWSKI, M., GULTEPE, I., and KING, P. (2004), *Analysis and modeling of an extremely dense fog event in southern Ontario*, J. Appl. Meteor. *43*, 3–16.

PUTSAY, M., KERÉNYI, J., SZENYÁN, I., SEBOK, I., NÉMETH, P., and DIÓSZEGHY, M. (2001), *Nighttime fog and low cloud detection in NOAA-16 AVHRR images and validation with ground observed SYNOP data and radar measurements*. In. Proc. 2001 EUMETSAT Meteor. Satellite Conf., EUM P33, 365–373, EUMETSAT, Antalya, Turkey.

REUDENBACH, C. and BENDIX, J. (1998), *Experiments with a straightforward model for the spatial forecast of fog/low stratus clearance based on multi-source data*, Meteor. Application. *5*, 205–216.

ROACH, W. T. (1994), *Back to basics: Fog: Part 1—Definitions and basic physics*, Weather *49*, 411–415.

SMITH, A. L., *The Coblentz Society desk book of infrared spectra*. In (Carver, C. D., ed.), *The Coblentz Society Desk Book of Infrared Spectra*, pp. 1–24 (The Coblentz Society, Kirkwood, MO, USA, 1982) 2nd edn.

STEPHENS, G. L. (2005), *Cloud feedbacks in the climate system: A critical review*, J. Climate, *18*, 237–273.

TURNER, J., ALLAM, R., and MAINE, D. (1986), *A case study of the detection of fog at night using channels 3 and 4 on the Advanced Very High Resolution Radiometer (AVHRR)*, Meteor. Mag. *115*, 285–290.

UNDERWOOD, S. J., ELLROD, G. P., and KUHNERT, A. L. (2004), *A multiple-case analysis of nocturnal radiation-fog development in the Central Valley of California utilizing the GOES nighttime fog product*, J. Appl. Meteor. *43*, 297–311.

WILSON, L. J. and BURROWS, W. R. (2004), *Spatial verification using the relative operating characteristic curve* In. Proc. 17th Conf. on Probability and Statistics in the Atmospheric Sciences, 2.8.1–2.8.6, Am. Meteor. Soc. Seattle, Washington, USA.

WMO (1992), *International Meteorological Vocabulary*, vol. 182, World Meteorological Organization (WMO), Geneva, Switzerland, 2nd edn.

WMO (1996), *Guide to meteorological instruments and methods of observation*, vol. 8, World Meteorological Organization (WMO), Geneva, Switzerland, 6th edn.

(Received May 1, 2006, accepted October 29, 2006)
Published Online First: June 8, 2007

Pure appl. geophys. 164 (2007) 1193–1205
0033–4553/07/071193–13
DOI 10.1007/s00024-007-0214-7

Pure and Applied Geophysics

Inferring Low Cloud Base Heights at Night for Aviation Using Satellite Infrared and Surface Temperature Data

GARY P. ELLROD[1] and ISMAIL GULTEPE[2]

Abstract—A nighttime image product that depicts areas of the lowest cloud base heights has been developed by combining brightness temperature data from the Geostationary Operational Environmental Satellite (GOES) Imager InfraRed (IR) bands centered at 3.9 μm and 10.7 μm, with hourly shelter temperatures from surface observing sites and offshore marine buoys. A dependent data sample showed a good correlation between the surface temperature minus IR cloud top temperature differences versus measured cloud base heights. Histogram analysis indicated that a temperature difference of less than 4-C related to a > 50% frequency of ceilings below 1000 ft above ground level, the threshold for Instrument Flight Rules (IFR). Using this result as a model, an experimental Low Cloud Base image product was developed that highlights regions of likely IFR ceilings. Validation of the Low Cloud Base product for two separate periods resulted in Probabilities of Detection of 67% and 72% and False Alarm Rates of 6% and 11%, respectively. Some regional variation observed could be related to the relative frequency of multi-layered overcast conditions. The biggest factor leading to underdetection of IFR ceilings by the GOES Low Cloud Base product is the presence of overlying clouds, including thin cirrus contamination. The GOES Low Cloud Base product shows potential for use as guidance for aviation meteorologists over both continental and marine areas.

Key words: Fog forecasting, satellite applications, aviation operations.

1. Introduction

Detection of fog and low clouds at night with meteorological satellite data can be accomplished using brightness temperature differences (BTD) between the 3.9 μm shortwave (T2) and 10.7 μm window (T4) infrared (IR) channels such as those available from the Geostationary Operational Environmental Satellite (GOES) Imagers (ELLROD, 1995; LEE *et al*., 1997), and the polar orbiting National Oceanic and Atmospheric Administration (NOAA) series (EYRE *et al.,* 1984). This derived imagery (sometimes referred to as the ''fog product'') clearly shows low-level water clouds (fog and stratus) that may often go undetected using only a single

[1] NOAA/NESDIS (Retired), P. O. Box 240. Granby, CT 06035, USA.
E-mail: gary.ellrod@gmail.com.
[2] Cloud Physics and Severe Weather Research Section, Meteorological Research Division, Environment Canada, Toronto, Ontario, Canada. E-mail: ismail.gultepe@ec.gc.ca

IR channel. Unfortunately, low clouds are only detectable if they are sufficiently thick (> 50–100 m) and not overlain by higher cloud layers. Additionally, the current nighttime low-cloud product cannot easily distinguish clouds that may result in low ceilings[1] and/or reduced surface visibilities from higher-based stratus, stratocumulus, and altostratus that do not represent significant hazards to aviation or marine interests.

The likelihood that fog is present may be assessed by means of empirical rules based on satellite image features such as: brightness, texture, growth or movement. However, these rules require some expertise and experience for proper application. A more objective, easily interpreted product that estimates the likelihood of very low ceilings and/or visibilities is desired.

Efforts to produce an experimental, enhanced GOES fog product began in 1997 with the collection of surface-based ceiling and visibility reports from Meteorological Aviation Reporting (METAR) sites in the United States, along with co-located GOES IR brightness temperature data. Analysis of the data was completed in 1999, and plans for generating an experimental prototype product for ceilings were described (ELLROD, 2000). This paper will discuss: (1) The research, (2) image processing procedures, (3) two examples of the product's capabilities, and (4) verification results.

2. Data Analysis

During the summer of 1997, cloud base ceiling heights (ft), visibilities (nm), and GOES IR cloud top temperatures (°K) were collected for a large number of cases (N = 592) of nighttime low clouds over the Continental United States (CONUS). When the GOES fog product observed low clouds (determined when $T_4 - T_2 > 2$ °K),[2] two hypotheses were tested. The first hypothesis assumed that low ceilings and visibilities were accompanied by relatively smooth appearance in the GOES fog product (consistent with stratiform clouds), resulting in a low standard deviation (more spatial coherence) of observed brightness temperatures near the surface reporting station. The second hypothesis assumed that low ceilings and visibilities were accompanied by a relatively small temperature difference between the 10.7 μm window IR cloud top temperatures (T_4) and the surface temperature (T_{sfc}) obtained from METAR data. The latter is an empirical rule that is often used to check for the presence of very low clouds. This small temperature difference results in poor discrimination of low clouds in single band IR imagery (EYRE *et al.*, 1984; BADER *et al.*, 1995). In many cases, the IR cloud top

[1] A ceiling is reported when there is 5/8 or greater cloud cover.

[2] Brightness temperatures are typically several degrees cooler in IR Channel 2 than in Channel 4 at night for opaque clouds consisting of liquid droplets, due to lower emissivity at 3.9 μm.

temperature may actually be warmer than T_{sfc} due to pronounced low-level thermal inversions. For the inter-comparisons, the cloud top temperatures used were a mean value for a 4 × 4 pixel area. This was done to minimize the effects of (1) navigational errors for the GOES, (2) instrument noise in the shortwave IR band, and (3) subpixel clear spots in the overcast.

After statistical analysis of each of these two approaches, the first was rejected due to the low correlation ($r = 0.4457$) between the standard deviation of brightness temperature to observed ceilings and visibilities. One of the complicating issues with the first approach is that instrument noise increases with colder temperatures, resulting in poor detection capability during winter and thus, a seasonal variation in reliability. The second approach ($dT = T_{sfc} - T_4$) resulted in a relatively higher correlation than the first hypothesis ($r = 0.5915$), so it was decided to utilize the GOES-surface temperature difference technique to improve the low-cloud product[3].

Evaluation of similar data for visibilities resulted in lower skill due to the complexity and large number of effects that lead to reduced visibility. The correlation coefficient between dT and visibility was only 0.3147, therefore a product that only estimates the likelihood of low ceilings has been developed and evaluated initially here.

A frequency distribution of the cloud base height data was also completed for each 1°-K interval of dT, to determine if there were any trends in the occurrence of low ceilings. The cloud base threshold selected was < 1000 ft (0.32 km) Above Ground Level (AGL), the height designated for Instrument Flight Rules (IFR) in aviation operations. In IFR conditions, pilots must be instrument qualified and file a flight plan before departure. Figure 1 shows a histogram of both IFR ceilings (solid bars) and all ceilings (open bars) versus dT. The values plotted at the top of most bars show the percentage of all ceilings that are IFR. Figure 1 indicates that as dT decreased, the likelihood of low ceilings increased, further supporting the second hypothesis. For dT of ≤3°-K, IFR ceilings accounted for more than half of all ceilings. For dT ≤1°-K, 85% of all ceilings were IFR. A cumulative frequency distribution curve (Fig. 2) shows a rapid rise in IFR ceiling occurrence at about 4°-K, increasing to ∼80% near 2°-K.

These results are consistent with an idealized vertical temperature profile of a fog bank in which there is a well-mixed sub-cloud layer (Fig. 3), with a nearly moist adiabatic (1–2°-K / 1000 ft) lapse rate, capped by a thermal inversion (FINDLATER, 1985; BROWN, 1987). The top of the fog bank is embedded in layer B, an average of 25 m above the inversion (Fig. 3). Elevated stratus can be more complex, due to the possibility of multiple cloud layers and inversions in advection situations. Assuming a single layer of stratus, the cloud base is likely to be located near the base of the

[3] During the day, this technique cannot be used due to solar reflectance in the shortwave channel.

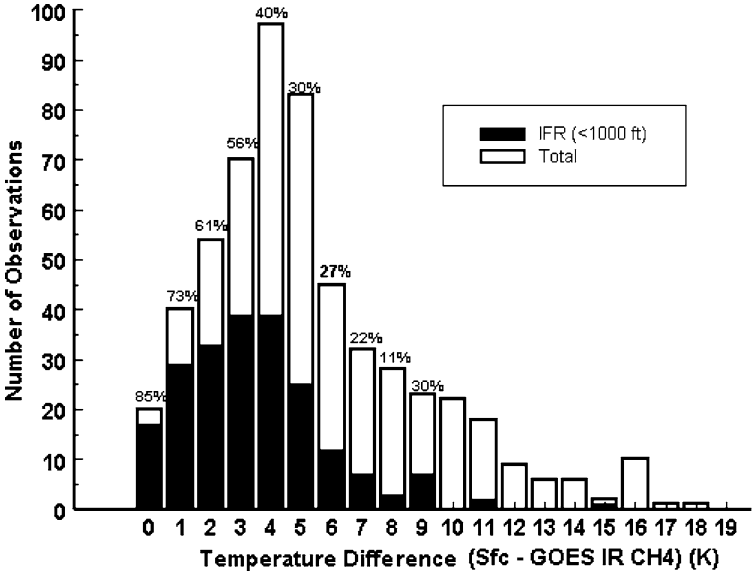

Figure 1
Frequency distribution of ceilings < 1000 ft (IFR) (solid bars) and all ceilings (open bars) plotted versus surface temperature minus CH4 IR brightness temperature difference (K). Numbers at the tops of bars represent the percentages of all ceilings that are in the IFR category.

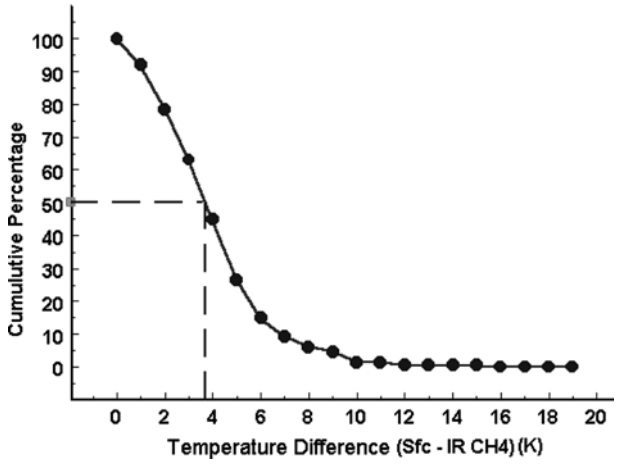

Figure 2
Cumulative frequency distribution of IFR (< 1000 ft) ceilings plotted versus surface temperature minus GOES CH4 IR brightness temperature difference (K).

inversion, with a nearly dry adiabatic lapse rate (2–3° K/1000 ft) below. Since GOES IR is observing the top of the stratus cloud, the IR temperature is often warmer than the base of the inversion, and possibly even the surface as well. The current technique

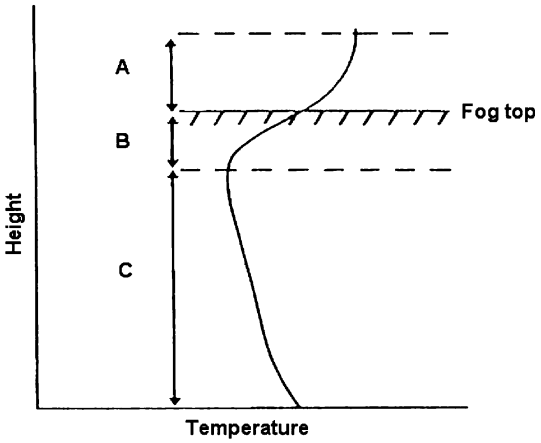

Figure 3
Idealized model of a radiation fog thermal profile described by BROWN (1987). 'A' is the dry stable layer above the fog, 'B' is the portion of the inversion containing the fog, and 'C' is the well-mixed layer formed by weak convection, with warming at the surface and radiative cooling at the top.

does not consider negative dT values (cloud top temperature $> T_{sfc}$), and sets them to zero.

3. Product Generation

Based on results described in section 2, a simple algorithm (shown by the flow diagram in Fig. 4) has been developed to show how an enhanced GOES low cloud product (hereafter referred to as the Low Cloud Base (LCB) product) may be generated to display areas of possible IFR ceilings. Details on product generation are described in ELLROD (2002). In the final image, possible IFR cloud base heights are color-coded red, while other areas of low clouds are colored green, and cirrus is shaded black or blue. Cloud-free regions are displayed as gray scale. The algorithm is generated for each pixel, so in areas where there are variable cloud conditions, or instrument noise due to cold IR temperatures, there may be difficulty in interpreting the image and matching the cloud base category with ground observations.

The LCB images are currently produced in real time for each hour at night for all CONUS regions. Six sectors are currently available: Two over the Western United States from GOES-11, and four covering the Eastern United States from GOES-12. The sectors are remapped into Lambert Conformal projection, true at 30 N and 50 N. Observed cloud ceilings (ft) at METAR sites are plotted on the image for comparison. Both single images and animated loops may be accessed at http://www.star.nesdis.noaa.gov/smcd/opdb/aviation/fog.html.

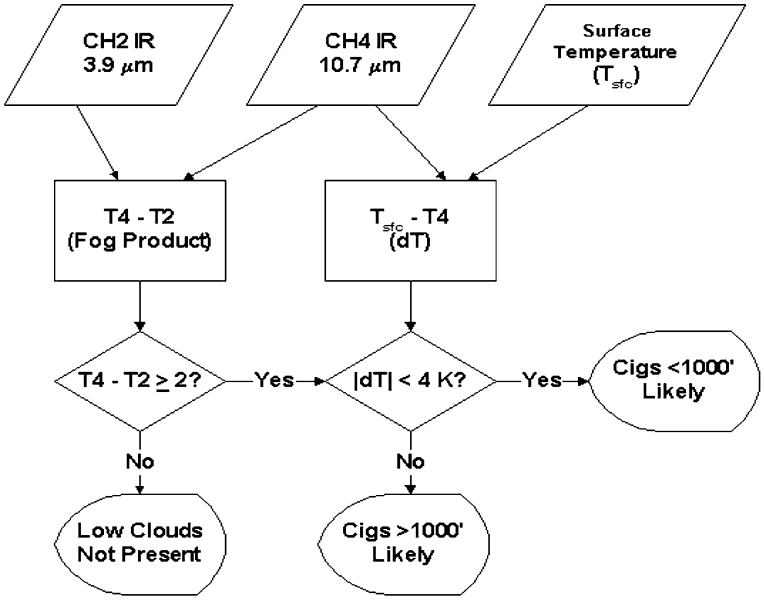

Figure 4
Flow chart showing an experimental procedure for estimating cloud base conditions at night using a GOES bi-spectral IR technique and surface temperatures from METAR sites. T_{sfc} is surface temperature, T4 is Channel 4 IR temperature, and T2 is Channel 2 IR temperature.

Certain problems associated with interpretation of the original fog images (ELLROD, 1995), such as the presence of obscuring higher cloud layers, and false signatures due to low emissivity soils such as coarse sands (SUTHERLAND, 1986) will also affect the new product. In North America, the latter effect is chiefly a problem in southwestern deserts, especially in the Gran Desierto north of the Gulf of California. Additional problems may occur in mountainous areas where METAR stations are sparse, leading to possible errors in cloud height category due to interpolation of low elevation temperature data into higher terrain.

4. Examples

a. California Coast—19 October, 2000

The first example is for the morning of 19 October, 2000 along the Pacific Coast of California. A ridge of high pressure centered from just offshore into the Pacific Northwest resulted in stable conditions near the coast, with a light northerly flow, an ideal situation for Pacific marine fog and stratus (see LEIPPER, 1994). The LCB image from GOES-10 at 1200 UTC (Fig. 5) shows extensive low cloudiness with IFR cloud bases extending from near Los Angeles (LAX) up the coast to north of San

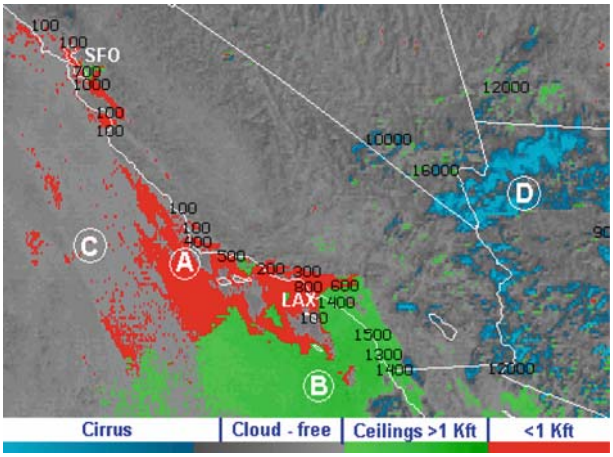

Figure 5
GOES Low Cloud Base product on 19 October, 2000 at 1200 UTC. Circled letters refer to: A) stratiform clouds with IFR cloud base heights, B) stratiform clouds with cloud bases >1000 ft, C) partially undetected stratiform clouds, and D) cirrus clouds.

Francisco (SFO) (red area A). Somewhat higher cloud bases (1000–1500 ft) were prevalent south of LAX to the Mexican border (green area B).

Conditions offshore are based on extrapolation of the coastal station and buoy temperatures. The only verification is San Clemente Island, which indicated a 100 ft ceiling, in agreement with the GOES LCB. Much of the offshore stratus is not highlighted in the low cloud products (gray portions of area C), due to smaller bi-spectral BTDs in the GOES IR data. The smaller BTD values are commonly observed with marine stratus, and are due to larger droplet sizes (LEE *et al.*, 1997). This problem can be corrected in coastal regions by assigning a lower temperature difference threshold to the cloud product, at the risk of increasing the area of false low clouds over land.

Variable cloud base heights shown near SFO are supported by a 1000 ft ceiling south of SFO. The transition from IFR to Marginal Visual Flight Rules (MVFR) cloud base heights near Los Angeles (LAX) is accurately depicted. In MVFR conditions, ceilings are ≥1000 ft but ≤3000 ft. Farther inland, the patchy blue and green areas over the Desert Southwest (D) were an indication of variable middle and high cloudiness. Overall, the GOES LCB was quite representative of actual conditions on this morning.

b. High Plains—5 March, 2001

On the morning of 5 March, 2001, a surface ridge of high pressure extended from Manitoba province southward across the northern Plains states to north central

Texas. On the west side of the ridge, a light east to southeast flow resulted in upslope conditions in the northern High Plains, leading to the formation of extensive fog and stratus. Radiational cooling under the ridge axis also resulted in some shallow fog in the James River Valley of South Dakota. The GOES-8 LCB image at 1115 UTC (Fig. 6) shows two separate areas of low clouds, one large region from northeast Montana southeastward to northeastern Kansas, and a narrow band from eastern North Dakota to central Iowa.

The LCB product correctly showed IFR ceilings over most of the northern and western parts of the larger upslope stratus region (A) west of the surface ridge axis, and ceilings ≥ 1,000 ft in southeast Nebraska and northeast Kansas (B) east of the ridge axis. The green areas in western North Dakota and west central South Dakota (C) appear to be contaminated by thin cirrus (thicker patches are shown as black and blue areas in southeast Montana), leading to slightly colder IR cloud top temperature. Valley fog in east central South Dakota (D) was poorly depicted, probably because it was very shallow. In the easternmost stratus band (E), the LCB product incorrectly showed much of this region to have IFR conditions, when ceilings were actually quite a bit higher (> 2000 ft). The speckling observed in the clear regions (F) is from instrument noise in IR band 2 caused by surface temperatures in single digits Fahrenheit.

Radiosonde data was available to help explain some of these conditions. Figure 7 shows four radiosonde profiles valid at 1200 UTC, 5 March, 2001 for Glasgow, Montana (GGW), Aberdeen, South Dakota (ABR), North Platte, Nebraska (LBF), and Topeka, Kansas (TOP). The GOES IR cloud top temperatures (T4) are indicated for GGW, LBF, and TOP. At GGW, the cloud top

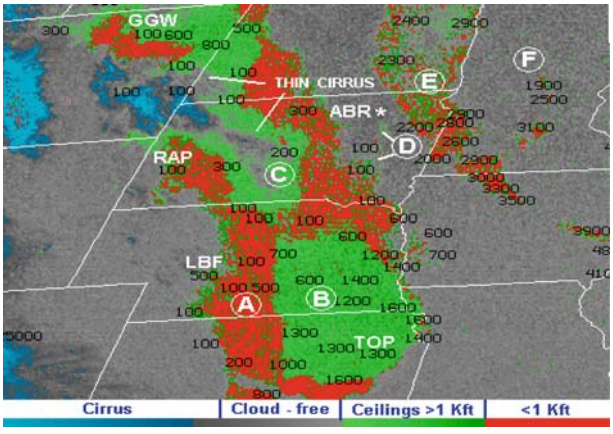

Figure 6
GOES-8 Low Cloud Base product on 5 March, 2001 at 1115 UTC. Three letter identifiers mark the locations of radiosonde plotted in Figure 7. Single letters denote cloud conditions described in text.

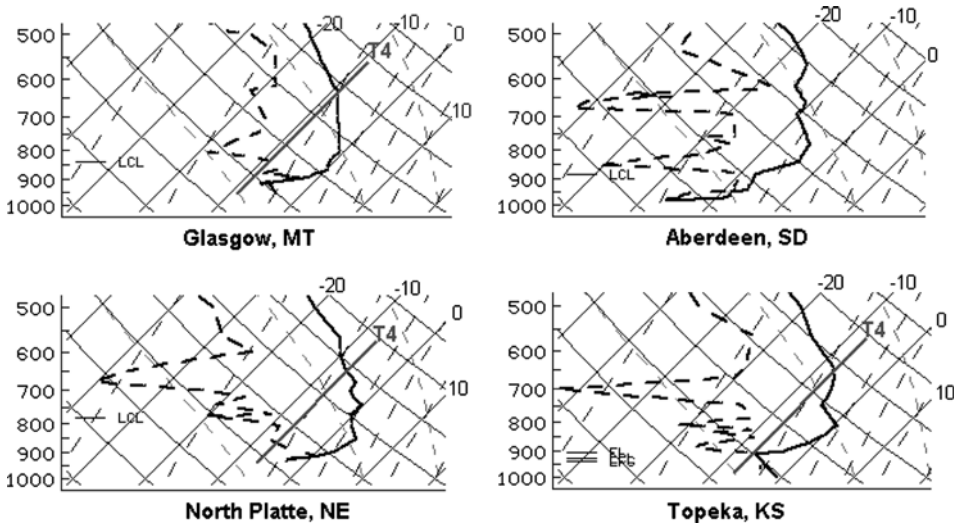

Figure 7
Radiosonde profiles for four stations shown in Figure 6, valid at 1200 UTC, 5 March, 2001. Line marked >T4′ represents the observed GOES Channel 4 IR temperature at each location.

temperature (−9.5°C) was slightly more than 4°C colder than the surface temperature (−4°C), resulting in a mis-classification of the ceiling conditions. The dT value was <4°C at LBF, although the GOES cloud top temperature is a few °C colder than indicated by the radiosonde. At TOP, sub-cloud mixing in the northerly flow was evident by the adiabatic layer, leading to an elevated cloud base. The cloud top temperature of −8°C at TOP was more than 5°C colder than the surface reading (−1°C). At ABR, sky conditions were clear, but the sounding reveals an elevated moist layer that is likely related to the higher based stratus just to the east.

5. *Verification*

Verification was completed from 30 May, 2000 to 20 August, 2000 for fog and low clouds occurring in the western and northern United States, as well as southern Canada. Since there was very little low cloud occurrence in the southeast and south central United States during this period, a separate verification was conducted for those regions from 10 January, 2001 through 26 January, 2001, slightly after the fall peak in fog formation. Nevertheless there were numerous days during this period with low clouds and foggy conditions. We did not distinguish between different types of fog (e.g., radiation, advection (including coastal), upslope, and steam fog)

during the verification. However, it is likely that the main types of fog involved in the study were advection, radiation and upslope (listed in relative order of occurrence). Many pure radiation fog events (e.g., valley fogs) and steam fogs are difficult to detect from GOES due to their small horizontal extent and low optical depth.

To accomplish the verification, the color-coded images were compared at each location where a cloud ceiling was observed at a METAR station. Only two categories were evaluated: <1000 ft (IFR), and ≥ 1000 ft. The prevailing satellite-estimated ceiling category was compared with the surface observed category. A ceiling in either category that was observed at a boundary in the satellite product was scored as a "hit." Areas where thin cirrus was suspected to be a factor were not included in the validation due to the likelihood that the cloud base height estimates were corrupted. The performance was evaluated using Probability of Detection (POD) and False Alarm Rate (FAR) (WEISS, 1977), which are defined as:

$$\mathrm{POD} = x/(x+y), \tag{1}$$

$$\mathrm{FAR} = z/(x+z), \tag{2}$$

where x is the number of correct IFR ceiling assignments as determined by GOES, y is the number of IFR events observed but not assigned, and z is the number of IFR events assigned but not observed.

Table 1 is a contingency table showing how the satellite product compared with co-located METAR ceiling observations for 1551 comparisons in the northern and western United States during May - August 2000. There was a good correlation between the satellite-estimated and observed ceilings. The POD for IFR ceilings for the entire sample was 72% and the FAR was 11%. There was a bias toward under-forecasting IFR ceilings, most likely due to the presence of multiple cloud layers. These results are similar to those obtained in Ontario, Canada using a satellite-based approach to fog detection during daytime, ignoring situations where cirrus contamination was likely (GULTEPE *et al.*, 2006).

Table 1

GOES Cloud Base Height vs. METAR height for Northern and Western United States, 30 May–20 August, 2000

Ceilings	METAR < 1 kft	METAR ≥ 1 kft	Totals	Bias
GOES < 1 kft	587	70	657	0.80
GOES ≥ 1 kft	230	664	894	1.22
GOES Totals	817	734	1551	

Table 2

GOES Cloud Base Height vs. METAR height for Southern United States, 10–26 January, 2001

Ceilings	METAR < 1 kft	METAR – ≥ 1 kft	Totals	Bias
GOES < 1 kft	261	16	277	0.72
GOES ≥ 1 kft	126	427	553	1.25
GOES Totals	387	443	830	

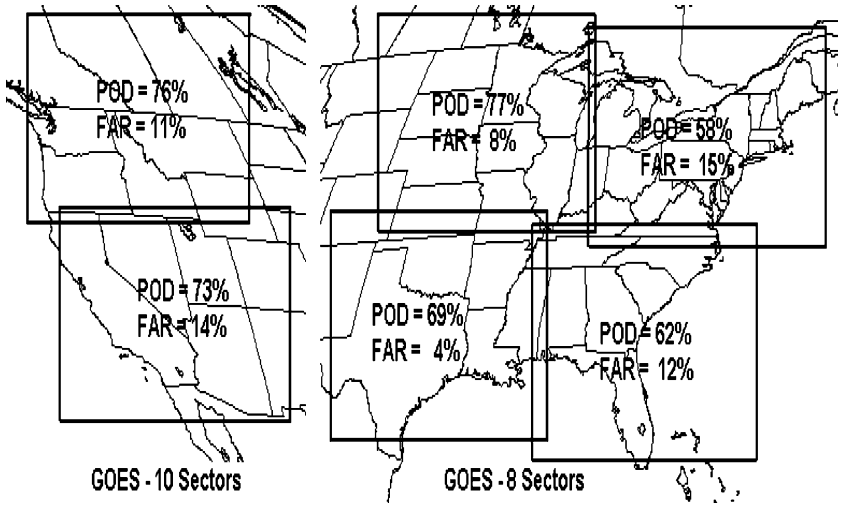

Figure 8

Verification statistics and area coverage plotted for each of six regional GOES Low Cloud Base experimental images for both GOES-8 and GOES-10. Periods during which the data were collected are described in the text. POD is the Probability of Detection, FAR is the False Alarm Rate.

Verification data for 830 comparisons during January 2001 in the southern United States are shown in Table 2. Similar results were obtained, with a POD of 67%, a FAR of 6%, and a low bias with respect to the analysis of IFR conditions. Most of these cases involved stratus and fog that developed as a result of both advection and radiation processes.

The verification data were also stratified to determine if there were any regional tendencies. Figure 8 shows the area coverage for each regional sector and the corresponding POD and FAR values. Product performance was generally best in the western and central United States, and worst in the Northeast. During the summer of 2000, there were numerous cases of multi-layered lower or middle level clouds in the Northeast due to the presence of a persistent upper level trough.

6. Summary and Conclusions

GOES bi-spectral fog and low cloud images, based on the difference of two infrared channels centered at 3.9 and 10.7 μm during night time, have been improved to show likely areas of low ceilings significant for aviation operations. The improvement is based on a method that uses surface temperatures from METAR observing stations in combination with the satellite data. If differences between the surface temperatures and GOES 10.7 μm IR cloud top brightness temperatures are ≤3° K, cloud bases below 1000 ft AGL, a criterion for Instrument Flight Rules (IFR), are likely to exist. Verification based on co-located, measured ceiling heights and GOES-derived ceiling estimates indicate that the product detects IFR conditions ~ 70% of the time, with a false alarm rate of about 10%. False alarms are most likely due to multiple cloud layers and resulting in thermal inversions. Under-detection usually occurs when thin cirrus overlies the stratus clouds. The experimentally enhanced low cloud base product has shown great potential for aviation use over both continental and oceanic areas.

Acknowledgment

The author would like to thank Ken Pryor (NOAA/NESDIS) for validating this product in the southeastern United States and Andrew Bailey (Raytheon ITSS, Landover, MD) for assistance in the processing and scheduling of the product. The work was supported in part by the GOES Improved Product Assurance Plan (GIMPAP), funded by the NESDIS Office of Systems Development.

References

Bader *et al*., (ed.), Chapter 7 (J. Gurka and R. Allam) In *Images in Weather Forecasting* (Cambridge University Press, Cambridge, United Kingdom. 1995).

Brown, R. (1987), *Observations of the structure of a deep fog*, Meteor. Mag. *116*, 329–338.

Ellrod, G. P. (1995), *Advances in the detection and analysis of fog at night using GOES multispectral infrared imagery*. Weather Forecasting *10*, 606–619.

Ellrod, G. P. (2000), *Estimation of instrument cloud base conditions at night using GOES and surface temperature data*, Preprint 9th Conf. on *Aviation, Range, and Aerospace Meteorology*, 11–15 September, 2000, Orlando, Florida, Am. Meteor. Soc., Boston, pp. 602–605.

Eyre, J. R., Brownscombe, J. L., and Allam, R. J. (1984), *Detection of fog at night using Advanced Very High Resolution Radiometer (AVHRR) imagery,* Meteor. Mag. *113*, 266–275.

Findlater, J. (1985), *Field investigations of radiation fog at outstations*. Meteor. Mag. *114*, 187–201.

Gultepe, I., Pagowski, M., and Reid, J. (2006), *A satellite-based fog detection scheme using screen air temperature*, *Weather Forecasting*, in press.

Lee, T. F., Turk, F. J., and Richardson, K. (1997), *Stratus and fog products using GOES-8–9 3.9* μm data, Weather Forecasting *12*, 664–677.

Leipper, D. F. (1994), *Fog on the U. S. West Coast: A review*, Bull. Am. Meteor. Soc. *75*, 229–240.

SUTHERLAND, R. S. (1986), *Broadband and spectral emissivities (2–18* μm) of some natural soils and vegetation, J. Atmos. Oceanic Technol. *3*, 199–202.

WEISS, S. J. (1977), *Objective verification of the severe weather outlook at the National Severe Storms Forecast Center*, Preprints, *10th Conf. on* Severe Local Storms, Omaha, Nebraska, Am. Meteor. Soc., Boston, 395–402.

(Received November 2, 2006, accepted December 11, 2006)
Published Online First: June 8, 2007

Pure appl. geophys. 164 (2007) 1207–1220
0033–4553/07/071207–14
DOI 10.1007/s00024-007-0215-6

Pure and Applied Geophysics

Analysis of Fog Probability from a Combination of Satellite and Ground Observation Data

VINCENT GUIDARD and DIANE TZANOS

Abstract—The Cloud Type product, developed by the Satellite Application Facility to support to nowcasting and very short-range forecasting (SAFNWC) of EUMETSAT and based on Météosat-8/SEVIRI, identifies cloud categories, and especially low and very low clouds which are first estimates of areas where fog is likely to occur. This cloud type is combined with precipitation information from radar data and with hourly diagnostic analyses of 2-metre relative humidity and 10-metre wind to elaborate an hourly analysis of fog probability. This analysis provides four levels of fog probability with a 3-kilometre horizontal resolution: No risk, low-level risk, medium-level risk and high-level risk. An evaluation of such fog probability analyses versus a one-year set of French hourly SYNOP reports shows encouraging results (potential of detection = 0.73 for low and medium and high-level risks), even if false alarm ratios remain high. Most of the non-detections occur at twilight and are due to satellite non-detections. Eventually, we show case studies that clearly illustrate the high potential of the method.

Key words: Fog analysis, data fusion, fog probability.

1. Introduction

Many business sectors have a pressing need in fog observation. Indeed, fog is a very dangerous phenomenon for all traffic activities, i.e., sea, air and land traffic. Apart from security concerns, each time a fog event disturbs any traffic, there is a huge economic impact, especially for air traffic.

Mandatory local needs are generally satisfied, e.g., by human observation or automatic measurement. Nevertheless, spatialized information on fog is not so often available. At least two approaches can be identified to fill this lack of information. On the one hand, visibility and fog can be processed through three-dimensional analysis and forecast models. For instance, the "Rapid Update Cycle" (RUC) is an operational regional analysis and forecast system developed by the National Center for Environmental Prediction (NCEP); a description of the RUC is given in BENJAMIN *et al.* (2004). Using an explicit scheme of the cloud microphysic describing the mixing ratios for cloud water, ice, rainwater, snow and graupel, the RUC

Météo-France/CNRM, 42 avenue G. Coriolis, 31057, Toulouse Cedex, France.
E-mail: vincent.guidard@meteo.fr

elaborates a diagnosis on visibility. Other numerical weather prediction (NWP) mesoscale models have the same approach, e.g., the French AROME (Applications of Research to Operations at Mesoscale) mesoscale project also has a prognostic cloud microphysics scheme with five condensed water species (BOUTTIER *et al.*, 2006).

On the other hand, more pragmatic approaches tend to provide only two-dimensional visibility or fog occurrence diagnoses. Data fusion is a tunable and easy method to take benefits from various kind of data. For instance, the National Ceiling and Visibility (NCV) programme of the US National Oceanic and Atmospheric Administration produces analyses of ceiling and visibility on a two-dimensional grid corresponding to the RUC's one, using METAR and TAF reports, satellite and radar data (HERZEGH *et al.*, 2003).

We consider the detection by satellite imagers of areas where fog can be expected to occur as a key point in data fusion, for our purpose. Thanks to its various SEVIRI channels, Météosat-8 enables a large amount of subsequent products with a favourable resolution in space and time. Among these products, a detection of low clouds, and more generally an identification of the cloud types, is a first step forward. Ground observations are obviously needed to discriminate between low clouds and fog.

The objective of this study is to build a simple algorithm to elaborate analyses which quantify the probability of fog occurrence, at least over France. The algorithm will use the high potential of information of Météosat-8 and of the most relevant surface variables, which are to be found among already spatialized observations as far as possible. The analyses are expected to be used by French nowcasters. The algorithm should be as robust as possible, especially to be usable both during daytime and night-time, and provide high-resolution analyses.

Input and reference data are described in Section 2, as well as the algorithm we developed. Then an extensive evaluation of the analysis of fog probability is given in Section 3, including objective evaluation and case studies. Section 4 provides concluding remarks and prospects.

2. Methodology

2.1. In situ Reference Observations

We only considered observations over land. Indeed, as very few parameters are observed over sea, we have decided to limit our study to fog occurrence over land.

SYNOP data can be used as reference observations. As a matter of fact, if the information on "present weather" is given in the report, it clearly indicates whether fog has occurred or not (except for code of present weather equals to 76, 77 or 78, see WMO Manual on Codes).

Unfortunately, present weather is not always coded in SYNOP reports, when a manned station is closed during night, for instance, and then we have to rely on measured parameters: horizontal visibility (*vv*), relative humidity (*hu*), precipitation over the last hour (*rr1*) and wind strength (*ff*). A diagnosis of fog occurrence is based on the following four criteria:

$$\begin{cases} \textbf{criterion 1}: & vv < 1000\text{m} \\ \textbf{criterion 2}: & hu \geq 90\% \\ \textbf{criterion 3}: & rr1 \leq 0.2\text{mm} \\ \textbf{criterion 4}: & ff < 7\text{m.s}^{-1} \end{cases}$$

The method to elaborate the fog diagnosis from these four criteria is given in Table 1.

Table 1

Correspondence between criteria on measured parameters and subsequent observed fog diagnosis

Conditions	Diagnosis
vv and *hu* and *rr1* and *ff* unknown	No information available
ff known and criteria 1, 2, 3 and 4 met	Fog
ff unknown and criteria 1, 2 and 3 met	Fog
Criterion 1 or 2 or 3 or 4 not met	No fog
Other possibilities	Fog is possible

2.2. Review of Input Data

2.2.1. Cloud type product

Description. In the framework of the Satellite Application Facility on support to Nowcasting and very short-range forecasting (SAFNWC) of EUMETSAT (European Organisation for the Exploitation of Meteorological Satellites), a ''Cloud Type'' product has been developed by the French Centre de Météorologie Spatiale (CMS) of Météo-France, in order to provide a detailed analysis of observed clouds (DERRIEN and LE GLÉAU, 2005). This Cloud Type product is generated from Météosat-8 SEVIRI images and the SAFNWC Cloud Mask product. Nine SEVIRI channels are used to elaborate the Cloud Type and the Cloud Mask products: 0.6 and 0.8 μm (visible), 1.6 μm (near infrared), 3.9, 7.3, 8.7, 10.8, 12.0 and 13.4 μm (infrared). The Cloud Type product is available every 15 minutes since 27 January, 2004 (during night and day) and is generated on Météosat-8 full disk, with a horizontal resolution of 3 km $\times$ 6 km over France. There are 21 cloud categories which are summarized in Table 2. For some categories, the discrimination between stratiform and cumuliform cloud is possible, but as it is not performed yet, we gathered these sub-categories.

The ''very low cloud'' category should be composed of fog, stratus and small cumulus, and the ''low cloud'' category should include stratocumulus but no fog

Table 2

Description of the Cloud Type categories (from DERRIEN *and* LE GLÉAU, *2005)*

Category id	Description
0	non-processed (no data or corrupted data)
1	Cloud-free land
2	Cloud-free sea
3	Land contaminated by snow
4	Sea contaminated by snow/ice
5–6	Very low cloud
7–8	Low cloud
9–10	Medium cloud
11–12	High opaque cloud
13–14	Very high opaque cloud
15	High semi-transparent thin cloud
16	High semi-transparent fairly thick cloud
17	High semi-transparent thick cloud
18	Semi-transparent above low or medium cloud
19	Fractional cloud (sub-pixel water cloud)
20	Undefined

occurrence. Nevertheless, very low cloud may occur under low cloud, and the limit between these two categories is not so obvious for our purpose. In this paper, we will consider five groups of categories:

- cloud-free area (categories from 1 to 4),
- very low cloud (categories 5 and 6),
- low cloud (categories 7 and 8),
- fractional cloud (category 19),
- other cloud (categories from 9 to 18).

As France is our area of interest, we performed a projection from Météosat-8 full disk domain to a polar stereographic domain of 512×512 pixels covering France with a horizontal resolution of 3 km.

Cloud classification of fog events. It has been shown that the detection of low and very low clouds is better during daytime than nighttime, and that this detection is at its worst at twilight (LE GLÉAU and DERRIEN, 2005). These results are identical for fog detection (MIZRAHI and TERRIER, *pers. comm.*). We defined nighttime as when the solar elevation is less than -3 degrees, twilight between -3 and 10 degrees, and daytime when the solar elevation is greater than 10 degrees.

In order to compare the *in situ* diagnoses of fog occurrence with the Cloud Type product, we studied the categories of cloud type under which fog occurred. In order to avoid any problem of pixel mislocation and/or discretization side effect, we deduced the cloud type category corresponding to an *in situ* diagnosis of fog

occurrence from a 3×3 pixel box centered on the observation, which covers an 81-square kilometre area. The evaluation is performed on a one-year set of hourly reports extending from 01 March, 2004 to 28 February, 2005. Over the period, 20, 698 fog occurrences are diagnosed, 59% of which occur during nighttime, 23% during daytime and 18% during twilight. The results are drawn in Figure 1.

On average, 66% of fog events occurred under ''low cloud'' or ''very low cloud'' categories, 20% occurred under higher-level cloud categories, and 14% corresponded to clear sky areas of the cloud mask. During daytime, due to the better detection of low and very low clouds, 75% of fog occurrences are linked to low or very low clouds, and only 5% correspond to clear sky areas. Meanwhile, the ''non-detection'' of fog occurrences by the cloud mask during twilight is 29%.

2.2.2. Surface analyses

In order to distinguish between fog and low or very low clouds, we needed some surface data. As the density of the ground observation network is not sufficient for our purpose (roughly 30-km horizontal resolution), we had to rely on surface analyses. Météo-France routinely produces hourly diagnostic surface analyses, named Diagpack (diagnostic package). Diagpack has been developed in the framework of the ALADIN-ARPEGE-IFS software; ARPEGE is the operational global model at Météo-France, and ALADIN is its limited area counterpart. Diagpack is based on Optimal Interpolation and is derived from CANARI (which means: analysis code necessary to ARPEGE for its initialization and observation rejection) which was the assimilation software of ARPEGE for both upper-air and

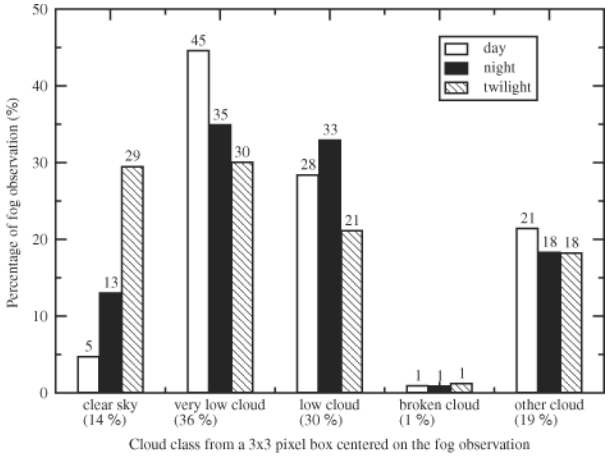

Figure 1
Distribution of observed fog occurrences according to a group of cloud type categories.

surface fields (CALAS, 1997). Note that, nowadays, ARPEGE uses a 4D-VAR assimilation scheme for upper-air fields which is described in RABIER *et al.* (1998) and CANARI is still used for surface fields. Diagpack uses the limited area spectral model ALADIN as an input, with a regular horizontal resolution of 9.5 kilometres. For an overall presentation of ALADIN, we refer to BUBNOVÁ *et al.* (1993) or RADNÓTI *et al.* (1995).

The optimal interpolation algorithm is summarized in the equation (1):

$$x^a = x^b + BH^T\left(R + HBH^T\right)^{-1}\left(y - Hx^b\right), \tag{1}$$

where x^a is the analysis, x^b is a background state (a short-range forecast of the ALADIN model in our case), y is the vector of observations, B and R are respectively the variance-covariance matrices of background errors and of observation errors, and H is the observation operator which brings a vector from the model space to the observation space. The formulation of the error covariances is univariate, that is to say that there is no crosscorrelation between the errors of 2 variables. Diagpack is specifically designed to fit the observations and cannot be used to initialize any model forecast. Diagpack outputs boundary layer fields of 2-metre temperature, 2-metre relative humidity, 10-metre zonal and meridional wind, mean sea level pressure, convective available potential energy (CAPE) and a moisture convection index.

One should note that Diagpack is sensitive to the observation network density. Indeed, due to the formulation of optimal interpolation, the fewer the observations, the closer to the ALADIN short-range forecast the analysis. Thus, in data void areas, Diagpack can no longer be considered as a spatialization of the observations.

2.3. Algorithm

First, we should identify phenomena which are incompatible with fog occurrence:

- no cloud detected by the satellite: every fog event should at least correspond to a cloudy area, except for too thin or sub-pixel fog layers that cannot be caught by the satellite;
- rainfall rate greater than 0.2 mm/h: in France, no fog is expected to occur during a rainy event; indeed, precipitation traces are possible during a fog event, as dew droplets may form on the inner side of rain gauges;
- 10-metre wind strength greater than 7 m/s: this threshold value is high enough not to reject advective fog. Nevertheless it rejects medium-level clouds hooking to mountains (identified as fog by meteorological observers according to WMO rules, i.e., horizontal visibility less than 1 km) as they do not correspond to a condensation process in the boundary layer;
- 2-metre relative humidity less than 90%: fog occurrence needs condensation which is theoretically reached for a relative humidity of 100%.

Thus these four criteria allowed to distinguish areas where fog occurrence is possible from those where the probability of fog occurrence is zero. In fog-compatible areas, we decide not to estimate the probability of fog occurrence if the cloud type category is medium cloud or higher; in other words, in fog-compatible areas, the probability of fog occurrence is quantified only under low or very low clouds. Three levels of probability were deduced from relative humidity: low-level risk for relative humidity between 90 and 95%, medium-level risk for relative humidity between 95 and 97%, and high-level risk for humidity greater than 97%. The algorithm is summarized in Figure 2. The thresholds of 95% and 97% for relative humidity were chosen subjectively from the results of an objetive study which is part of the evaluation described in section 3.1.

Thereafter, the cloud type analysis is the Cloud Type product from the SAFNWC software, 2-metre relative humidity and 10-metre wind analyses are taken from Diagpack, and the information about precipitation is inferred from radar reflectivity data within the last 5 minutes of the past hour. Examples of our analysis of fog probability are given in section 3.2.

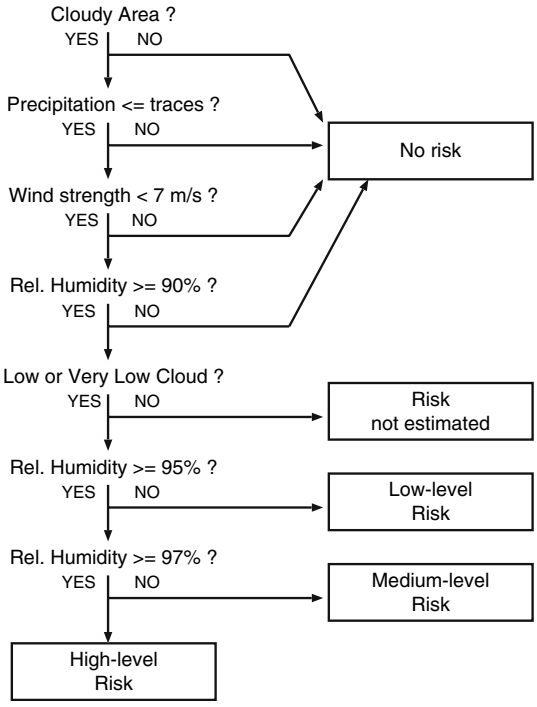

Figure 2
Algorithm of the analysis of fog probability.

3. Evaluation of the Analysis

3.1. Objective Evaluation

3.1.1. Evaluation method

The evaluation period extends from 01 March, 2004 to 28 February, 2005. The reference data are the hourly *in situ* fog diagnoses described in section 2.1. Over the period, they represent an amount of 929, 883 observations reporting either present weather information or *vv* and *hu* and *rr1* information. They divide in 2% of fog occurrences and 98% of fog non-occurrences. 42, 603 observations (i.e., 5%) correspond to a "risk not estimated" pixel; they are discarded, as it is not so obvious to include them straightforwardly in a synthetic score.

We compared our fog-occurrence hourly analyses to these reference data and filled a contingency table (cf. Table 3). We focused on scores based on this table:

- the Proportion of Correct identification: $\mathrm{PC} = \frac{h+cr}{h+fa+m+cr}$
- the Potential of Detection (POD) is the proportion of the observed fog occurrences which are well identified by our analysis: $\mathrm{POD} = \frac{h}{h+m}$;
- the Non-Detection Rate (NDR): $\mathrm{NDR} = 1 - \mathrm{POD}$;
- the False Alarm Ratio (FAR) quantifies the proportion of the fog occurrences identified as possible by our analysis which does not correspond to any observed fog event: $\mathrm{FAR} = \frac{fa}{h+fa}$;
- the frequency bias (BIAS) estimates the ratio of analyzed fog occurrences versus observed fog occurrences: $\mathrm{BIAS} = \frac{h+fa}{h+m}$.

3.1.2. Results

As the probability of fog occurrence is given on three levels, the corresponding three thresholds are to be evaluated using the above-described method. The results are gathered in Table 4 and plotted on Figure 3. The evaluation of in-between thresholds on relative humidity is added on this figure. One can note that, as the value of the threshold increases, the FAR and the POD decrease.

The threshold of 97% on relative humidity corresponds to areas of high-level risk. The threshold of 95% corresponds to areas of medium-level or high-level risk,

Table 3

Contingency table

	Likelihood of fog occurrence	No risk of fog occurrence
Fog is observed	hits (*h*)	misses (*m*)
Fog is not observed	false alarms (*fa*)	correct rejections (*cr*)

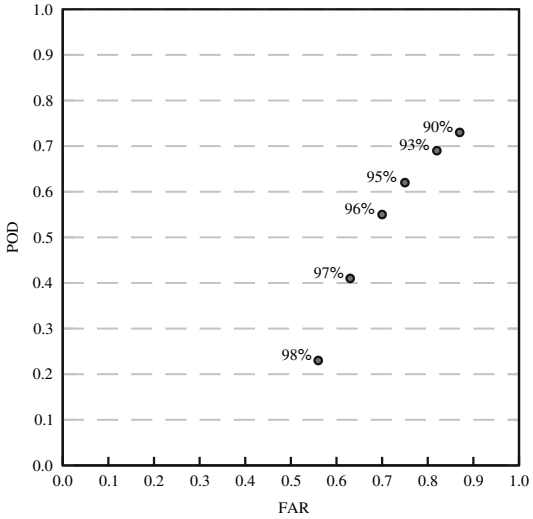

Figure 3
Potential of detection versus false alarm ratio for the scores of the algorithm with various thresholds of relative humidity versus observed fog diagnoses.

and the threshold of 90% corresponds to areas of low-level or medium-level or high-level risk.

As mentioned in Table 4, the threshold of 90% on relative humidity leads to a FAR of 87% and a frequency bias of 5.62, which indicates a high overestimation of fog occurrences. As the threshold of 90% on relative humidity corresponds to the union of areas of the three levels of risk, which is a rough estimate of areas where fog may occur, such a FAR is not penalizing. Moreover, the corresponding NDR of 27% may seem high with regard to such an overestimation. Actually 3/5 of this NDR is due to non-detections of fog events by the cloud mask. If we consider the subsample of verifying data which is under low or very low clouds, the potential of detection equals 93%, which means that there is a high potential of discrimination between lower clouds and fog.

Table 4

Results of the objective evaluation of the analyses of fog probability with respect to in situ reference observations

Relative Humidity threshold	Contingency Table				Scores			
	h(%)	m(%)	fa(%)	cr(%)	BIAS	PC(%)	POD(%)	FAR(%)
97%	0.8	1.2	1.4	96.6	1.12	97	41	63
95%	1.2	0.7	3.5	94.6	2.48	96	62	75
90%	1.4	0.5	9.4	88.7	5.62	90	73	87

The threshold of 97% on relative humidity leads to a potential of detection of 41% and to a FAR of 63%. These scores correspond to the scores for high-level risk of fog occurrence. The frequency bias equals 1.12, which means a slight overestimation of fog occurrences.

The areas which are delimited by each level of fog probability are nested: In average, areas of high-level risk are included in areas of medium-level risk which are included in areas of low-level risk. Thus, even if these objective scores are very informative, the high potential of the method is fully expressed on each hourly analysis. This is why we will show below some particular cases.

3.2. Case Studies

Typical case

The analysis valid at 12 UTC on 03 December, 2004 (cf., Fig. 4) shows a reasonable efficiency of the method. Some reference visibility data in km, which are not used in the analysis, are plotted on the same figure. Low visibilities corresponding to fog are within areas of high-level risk, i.e., there is a high potential of detection for this case. One can notice a visibility observation of 0.9 km in a "no-risk" area; this observation is located at an altitude of 1560 m, and the reduction of visibility is due to clouds hooking to the mountain, but not to a fog condensation process, which is consistent with our algorithm. The false alarms are mainly due to

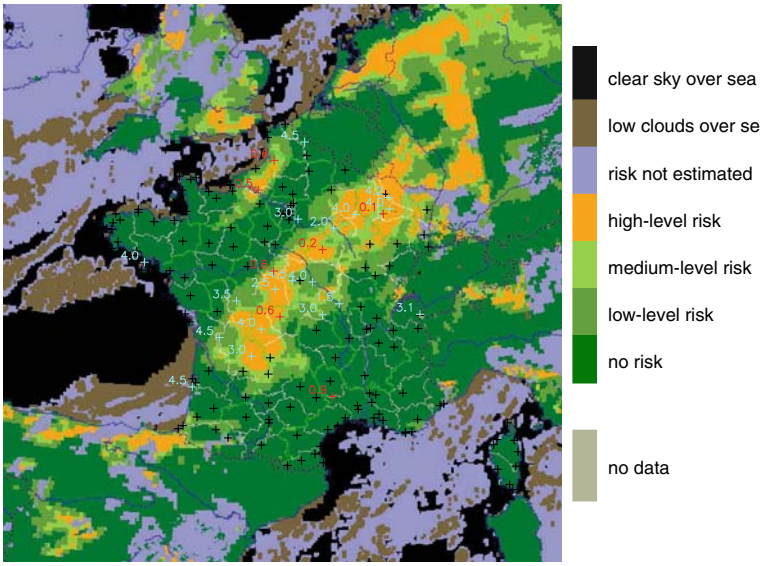

Figure 4
Analysis of fog probability valid at 12 UTC on 03 December, 2004. Plotted values are visibility (vv) observations (unit: km), drawn in red for $vv < 1$km, in cyan for $1\text{km} \leq vv < 5$km and in black (only crosses) for $vv \geq 5$km.

mist observations which is not problematic because mist and fog are due to the same physical processes.

In the northeastern part of France, two very close reference observations show very different visibility values (0.1 km and 4 km). This illustrates the high variability of the phenomenon that we try to analyze and which is missed by our algorithm.

Moreover, there is an abrupt breaking in the fog probability analysis over Germany. It is not a bug of the algorithm. It is due to the transition from the Diagpack analysis to the ALADIN forecast, as the Diagpack analysis domain is smaller than the ALADIN-France domain.

Fog occurring in river valleys

On 03 January, 2005, an anticyclonic area settles over France, which induces a cooling during night and the formation of morning fog over the southwestern part of France. Fog occurs in river valleys, with small scale patterns, which are well caught by the polar orbiting satellite NOAA-17 (cf., Fig. 5). The horizontal resolution of Météosat-8 is obviously coarser than NOAA-17's, which is clearly shown on the subsequent analysis of fog probability (cf., Fig. 6). In addition to this difference of resolution, the inference of the cloud class from a 3×3 pixel box implies that our algorithm generates wider areas of risk of fog than those actually observed (i.e., more fuzzy limits, hence a coarser description of fog patterns).

Moreover, one can notice a visibility observation of 0.3 km located on the coastal border between France and Spain which is not identified as a fog-possible area by our

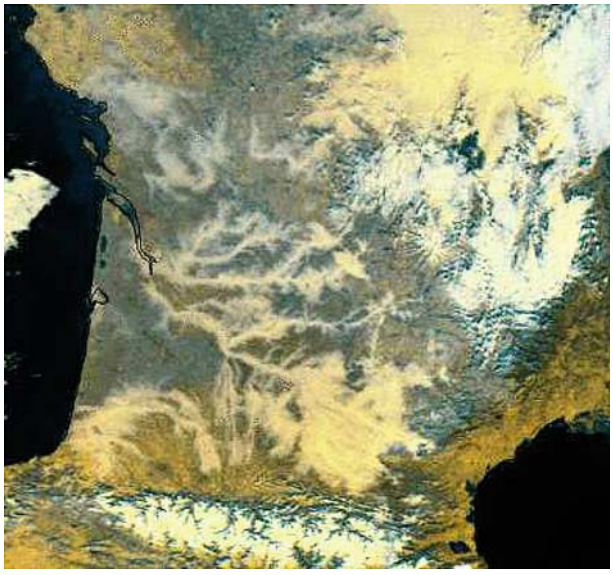

Figure 5
Multi-channel NOAA-17 image valid at 10:24 UTC on 03 January, 2005.

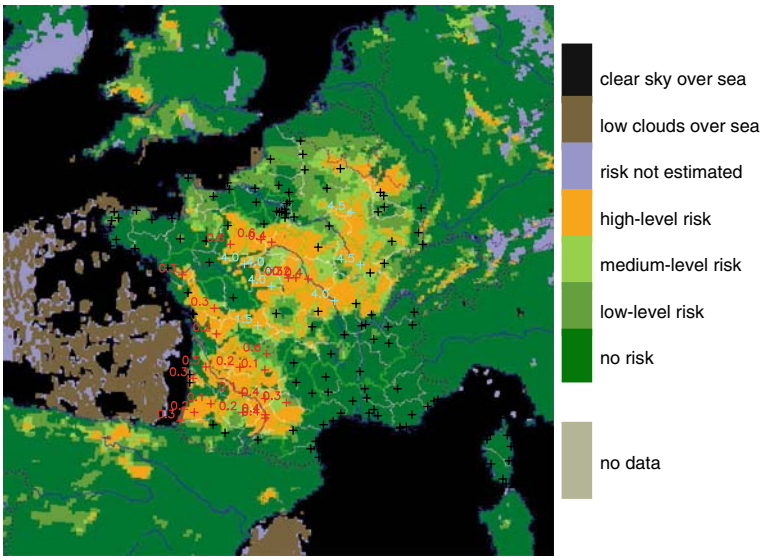

Figure 6
Analysis of fog probability valid at 10 UTC on 03 January, 2005. Plotted values are visibility (vv) observations (unit: km), drawn in red for $vv < 1$km, in cyan for $1\text{km} \leq vv < 5$km and in black (only crosses) for $vv \geq 5$km.

analysis. This non-detection is due to a non-detection by the cloud mask, probably because of the shallow optical depth of the fog layer.

4. Conclusion—Discussion

An innovative method has been elaborated to analyze the probability of fog occurrence. This analysis relies on a satellite-based Cloud Type product, on diagnostic analyses of 2-metre relative humidity and 10-metre wind, and on radar reflectivity images. In areas where fog is possible, the level of probability is set thanks to relative humidity thresholds. An objective evaluation showed encouraging results, such as a proportion of correct diagnosis equal to 97% for areas of high-level risk. The potential of detection for areas where the risk is not 0 equals 73%. The high potential of the method is clearly described thanks to case studies which have been confirmed by Météo-France nowcasters during an internal evaluation.

The non-detections during twilight are mainly due to non-detections in the Cloud Type product. Indeed, especially at dawn, the 3.9 μm channel is contaminated by visible radiation and visible channels are not usable because the visible radiation is not high enough. Thus, low and very low cloud may vanish from the cloud type product during one to maximum four slots of 15 minutes. As a consequence, 29% of

fog events are classified as clear sky during twilight versus 5 and 13% during daytime and nighttime, respectively. The CMS is working on solving this problem, and the first results seem very encouraging (DERRIEN, *pers. comm.*).

Another limit is the existence of areas where the probability of fog occurrence is not estimated. Figure 2 clearly shows that, if pixels correspond to medium or higher clouds, the probability of fog occurrence can be set to 0 using tests on precipitation rate, wind strength and relative humidity. Therefore the 20% of pixels corresponding to medium or higher cloud (1% + 19% on Fig. 1) can be split in 8% where other criteria imply a probability of fog occurrence of 0 and in 12% where the probability cannot be estimated. Even though 12% is not a high percentage, we do have to make a specific effort to elaborate a suitable algorithm for areas of medium or higher clouds.

Fog may occur thanks to specific local weather and ground conditions. The algorithm described in this article takes into account very few atmospheric parameters (four) and no soil parameter. We are naturally inclined to include parameters such as ground elevation, a description of the local topography, humidity within the first soil layers, and so on. We plan to use such extra-parameters to estimate a range of visibility in areas where fog is identified as possible by our analysis, but not to refine the actual algorithm. The distinction between the various kinds of fog (radiative fog, advective fog, etc.) may be performed, most probably in an implicit way, by choosing the parameters to estimate a range of visibility.

Acknowledgements

The authors would like to thank Françoise Taillefer and Marcel Derrien for fruitful discussions on Diagpack and on the Cloud Type product, respectively. Many thanks to Barbara Bourdelles who carefully read this article. The authors gratefully acknowledge the anonymous reviewers. Part of this study is based on a work performed during a pre-graduate stay at Météo-France/DSO, organized by the French Ecole Nationale de la Météorologie. This study has been discussed in the framework of COST722 action. The authors are grateful to COST722 for the opportunity of a special issue on fog-related topics.

REFERENCES

BENJAMIN, S. G., DÉVÉNYI, D., WEYGANDT, S. S., BRUNDAGE, K. J., BROWN, J. M., GRELL, G. A., KIM, D., SCHWARTZ, B. E., SMIRNOVA, T. G., and SMITH, T. L. (2004), *An hourly assimilation-forecast cycle: the RUC*, Mon. Wea. Rev. *132*, 495–518.

BOUTTIER, F., HELLO, G., SEITY, Y., and MALARDEL, S. (2006), *Progress of the AROME mesoscale NWP project*. In CAS/JSC WGNE "Blue Book" annual report "Research Activities in Atmospheric and Ocean Modelling" (ed. J. Côté.).

Bubnová, R., Horányi, A., and Malardel, S. (1993), *International project ARPEGE-ALADIN*. In EWGLAM Newsletter *22* (ed. I. R. M., Belgium), pp. 117–130.

Calas, C. (1997), *Apport d'une analyse à mésoéchelle pour la prévision immédiate des systèmes convectifs*. Ph.D. Thesis, Université Paul Sabatier, Available from Université Paul Sabatier, 118 route de Narbonne, 31062 Toulouse cedex, France.

Derrien, M. and Le Gléau, H. (2005), *MSG/SEVIRI cloud mask and type from SAFNWC*, Internat. J. Remote Sensing *26*(21), 4707–4732.

Herzegh, P., Benjamin, S., Rasmussen, R., Tsui, T., Wiener, G., and Zwack, P. (2003), *Development of automated analysis and forecast products for adverse ceiling and visibility conditions*. In 19th Internat. Conf. on *Interactive Information Processing Systems for Meteorology, Oceanography, and Hydrology Proceedings* (Am. Meteor. Soc.).

Le Gléau, H., and Derrien, M. (2005), *Nowcasting and very short-range forecasting SAF. Validation report for the PGE01-02-03 of the SAFNWC/MSG*, Météo-France CMS. Available from http://www.meteorologie.eu.org/safnwc.

Rabier, F., Thépaut, J.-N., and Courtier, P. (1998), *Extended assimilation and forecast experiments with a 4D-VAR system*, Quart. J. Roy. Meteor. Soc. *124*, 1861–1887.

Radnóti, G., Ajjaji, R., Bubnová, R., Caian, M., Cordoneanu, E., v. d. Emde, K., Gril, J.-D., Hoffman, J., Horányi, A., Issara, S., Ivanovici, V., Janoušek, M., Joly, A., LeMoigne, P., and Malardel, S. (1995), *The spectral limited area model ARPEGE-ALADIN*. In PWPR Report series n. 7 - WMO TD n. 699 (ed. WMO), pp. 111–118.

WMO. *Manual on Codes – International Codes* (1995, ed.), World Meteorological Organization, Volume I.1 (Annex II to WMO Technical Regulations).

(Received April 12, 2006, accepted October 30, 2006)
Published Online First: May 16, 2007

Pure appl. geophys. 164 (2007) 1221–1240
0033–4553/07/071221–20
DOI 10.1007/s00024-007-0216-5

Pure and Applied Geophysics

The Impact of Vertical Resolution in the Explicit Numerical Forecasting of Radiation Fog: A Case Study

ROBERT TARDIF

Abstract—Numerical experiments are performed with a comprehensive one-dimensional boundary layer/fog model to assess the impact of vertical resolution on explicit model forecasts of an observed fog layer. Two simulations were performed, one using a very high resolution and another with a vertical grid typical of current high-resolution mesoscale models. Both simulations were initialized with the same profiles, derived from observations from a fog field experiment. Significant differences in the onset and evolution of fog were found. The results obtained with the high-resolution simulation are in overall better agreement with available observations. The cooling rate before the appearance of fog is better represented, while the evolution of the liquid water content within the fog layer is more realistic. Fog formation is delayed in the low resolution simulation, and the water content in the fog layer shows large-amplitude oscillations. These results show that the numerical representation of key thermo-dynamical processes occurring in fog layers is significantly altered by the use of a grid with reduced vertical resolution.

Key words: Radiation fog, explicit numerical forecasting, vertical resolution.

1. Introduction

In the numerical weather prediction (NWP) literature, numerous studies have aimed at determining the influence of horizontal resolution on the representation of various weather phenomena, such as convection (WEISMAN *et al.*, 1997), sea-breeze (COLBY, 2004), and fog (PAGOWSKI *et al.*, 2004); as well as the overall accuracy of numerical weather forecasts (MASS *et al.*, 2002). Certain phenomena have limited vertical scale while exhibiting strong vertical gradients, such as the stably stratified nocturnal boundary layer, fog and other boundary layer clouds. This suggests the importance of the vertical resolution needed to accurately represent such features, as briefly discussed by BECHTOLD *et al.* (1996) for the stratocumulus-topped boundary layer.

Department of Atmospheric and Oceanic Sciences, Research Applications Laboratory, National Center for Atmospheric Research, and University of Colorado at Boulder, Box 3000, Boulder, CO 80301, U.S.A.
E-mail: tardif@ucar.edu

A greater need for accurate fine-scale very short-term forecasts of low cloud ceiling and fog at airports exists as the volume of air traffic continues to increase. For the explicit numerical forecasting of fog and low clouds, two approaches are considered. One relies on the use of three-dimensional (3-D) mesoscale models such as the Rapid Update Cycle (BENJAMIN *et al*., 2004), while another is based on the use of high vertical resolution one-dimensional (1-D) models as in CLARK and HOPWOOD (2001), BOTT and TRAUTMANN (2002) and BERGOT *et al*. (2005). Both approaches have strengths and limitations. The operational 3-D models cannot use a very high vertical resolution due to prohibitive computational cost, while 1-D models typically incorporate more sophisticated parameterizations and higher vertical resolution. However, 1-D models cannot represent the effect of spatial heterogeneities that may exist at the mesoscale as their 3-D counterpart can. Nevertheless, high-resolution 1-D models have advantages in situations characterized by the dominant role of local scale vertical exchanges of momentum, heat and moisture as in the case of radiation fog over flat terrain.

In this study, a comprehensive one-dimensional (1-D) boundary layer/fog model is used to perform numerical sensitivity experiments aimed at illustrating the impact of the vertical resolution used to generate explicit short-term forecasts of radiation fog formation and evolution. These experiments provide insights into the resolution dependence of the parameterizations of key physical processes influencing the characteristics and evolution of fog layers, such as radiative cooling, dew deposition and fog water transport by gravitational settling (ROACH, 1995). By the same token, some limitations of 3-D models related to limited vertical resolution are illustrated. For the sake of brevity, only stages corresponding to the pre-fog, formation and early evolution of the fog layer are considered. A discussion concerning fog dissipation is relegated to future efforts.

2. Description of Model and Numerical Experiments

The numerical model used to perform the sensitivity experiment is a version of the COBEL (Code de Brouillard à l'Échelle Locale) 1-D boundary layer/fog model described in BERGOT and GUÉDALIA (1994) and used at the Paris-Charles De Gaulle airport in France (BERGOT *et al*., 2005). The model was originally developed through a collaboration between the Laboratoire d'Aérologie, Université Paul Sabatier/ Centre National de la Recherche Scientifique and Météo-France/Centre National de Recherches Météorologiques. Additional modifications were implemented at the Université du Québec à Montréal and at the National Center of Atmospheric Research (NCAR). The main features of the model are a detailed parameterization of radiative transfer in the longwave part of the radiation spectrum (VEHIL *et al*., 1989), as well as a simple parameterization of shortwave (solar) radiation (FOUQUART and BONNEL, 1980). The parameterization of turbulent mixing incorporates a prognostic

equation for turbulent kinetic energy (TKE) and representations of mixing lengths (so-called TKE-ℓ scheme) suitable for unstable (BOUGEAULT and LACARRÈRE, 1989), neutral (DELAGE, 1974), stable and very stable stratification (ESTOURNEL and GUÉDALIA, 1987). The atmospheric stability is diagnosed as a function of temperature and moisture (vapor and condensed) gradients following DURRAN and KLEMP (1982). A bulk microphysical scheme incorporating a parameterization of fog droplets gravitational settling following BROWN and ROACH (1976) is used. Visibility in fog is diagnosed using the translation algorithm proposed by KUNKEL (1984). The atmospheric model is coupled with a high vertical resolution model for the evolution of soil moisture based on the two-layer model of MAHRT and PAN (1984) through a representation of soil-atmosphere interactions over bare ground. The soil moisture-dependent thermal conductivity is calculated as in PETERS-LIDARD *et al.* (1998).

Mesoscale factors influencing the state of the local boundary layer, such as the pressure gradient force (geostrophic wind), horizontal advection of temperature and moisture, local pressure tendencies and vertical motion, can all be used as input by the 1-D model. They can be estimated from careful analysis of data from networks of surface observations or from state-of-the-art three-dimensional mesoscale data assimilation/forecast systems.

In this work, COBEL simulations of the well-documented radiation fog event of November 6–7, 1988 observed during the Lille 88 field experiment are performed. A shallow layer of ground fog formed on this night roughly 100 minutes after sunset, under light wind conditions and clearing skies aloft (GUÉDALIA and BERGOT, 1994; hereafter referred to as GB94). This scenario suggests the prevailing influence of radiative cooling in the formation of fog.

Conditions observed on an 80-m tower, balloon soundings and soil sensors, before and during the dense fog event are used to specify the general conditions of the simulations and provide a basis for comparison. Two numerical simulations are performed using different grid configurations. The first configuration corresponds to the original high-resolution (HR) grid used by GB94. The grid consists of 30 levels distributed in a log-linear fashion between the surface and a height of 1400 m, with twenty-one levels below 200 m. The highest vertical resolution is close to the surface, with grid spacing gradually increasing with height, but remaining less than 30 m in the lowest 200 m of the atmosphere where fog typically occurs. The second configuration has grid spacing and level placement typical of current operational mesoscale forecast models such as the Rapid Update Cycle (BENJAMIN *et al.*, 2004). The latter configuration is referred to as the coarse or low resolution grid (LR) and has five levels below 200 m. Table 1 shows the heights of computational levels located below 250 m for the two grid configurations. In all simulations, the evolution of soil temperature and moisture is represented on a grid of five levels from a few centimeters below the surface down to a depth of 1 m. The model is integrated with a time step of 30 seconds.

Table 1

Heights (in m) of computational levels below 250 m for the two grid configurations used in the numerical sensitivity experiments

"High-resolution"	"Low resolution"
0.5	
1.7	
3.1	
4.7	
6.8	
9.3	
12.2	12.2
15.9	
20.2	
25.5	
31.9	31.9
39.6	
49.0	
60.3	
74.0	74.0
90.5	
110.5	
134.7	134.7
164.0	
199.4	
242.2	242.2

All model simulations are initialized at 1500 UTC (1600 local time) on November 6, and extend out to 0700 UTC on November 7. Thus simulations represent short-term (0–16 h) forecasts of fog formation and subsequent growth. To remain concise, the dissipation phase is not discussed here. All simulations are initialized using the same profiles, although the structure of initial profiles is somewhat degraded in the reduced resolution experiment, but still captures the main features of the boundary layer (Fig. 1). The initial wind profile is taken from the operational mesoscale model at Météo-France, in order to preserve consistency with the specified horizontal pressure force (geostrophic wind). The soil temperature profile down to 1 m is determined using measurements at the tower site, while soil moisture is chosen in order to obtain a soil thermal conductivity of 1.0 W K^{-1} m^{-1} (as in GB94) using the relationship proposed by PETERS-LIDARD *et al.* (1998).

The mesoscale forcings are specified using various sources of information such as mesoscale model output and observations from a mesonet and from the tower site. For instance, the evolution of the geostrophic wind profile was derived from operational mesoscale forecasts, while horizontal advections were deduced from regional observations. Following GB94, data from a mesonet suggested the absence of low-level temperature advection, while a slight moisture advection was specified in

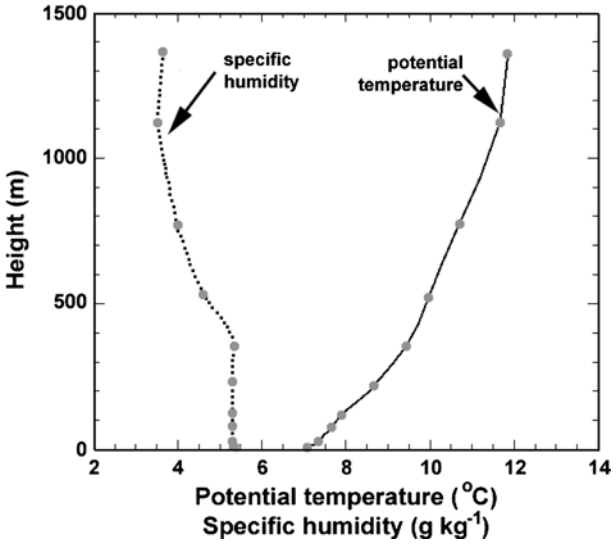

Figure 1
Initial profiles of potential temperature and specific humidity used in the numerical experiments. Profiles were derived from a radiosonde released at 1500 UTC on November 6, 1988 at the Lille site. Dots represent the data defining the initial profiles of the simulation performed with a low vertical resolution.

the lowest 250 m between 1800 UTC and 2400 UTC to improve the simulation of thermodynamical parameters. Also, an additional longwave flux is introduced at the top of the model domain to reflect the observed presence of upper level clouds. Values of this longwave flux were determined with the aid of observed downwelling longwave radiation at the top of the Lille tower (see GB94).

3. Results

Results of the numerical experiments performed with the COBEL 1-D model are discussed in this section and diagnostics of model output are examined to provide insights into the dependence of model behavior on grid resolution. The important parameters for fog forecasting are the time of onset, the depth of the mature fog and the fog intensity (minimum visibility) near the surface.

(a) Overall Model Performance

First, the temporal evolution of the near-surface visibility, as predicted by the COBEL model using the two grid configurations, is compared with measurements. Observations at the Lille tower site show that a dense fog (visibility below 1000 m) first formed at the surface at approximately 1800 UTC on November 6 and

subsequently experienced oscillations until a few minutes after 1900 UTC, at which time a period of heavy fog (visibility below 400 m) began (Fig. 2a). Once forming at the surface, the fog grew in the vertical. It first appeared at 10 m a little after 2000 UTC (Fig. 2b) and on a sustained basis from 2100 UTC onward at 20 m (Fig. 2c). The fog layer then deepened quickly to reach the 45 m level at 2130 UTC (Fig. 2d). As discussed in GB94, it is believed that the vertical growth of the fog was influenced

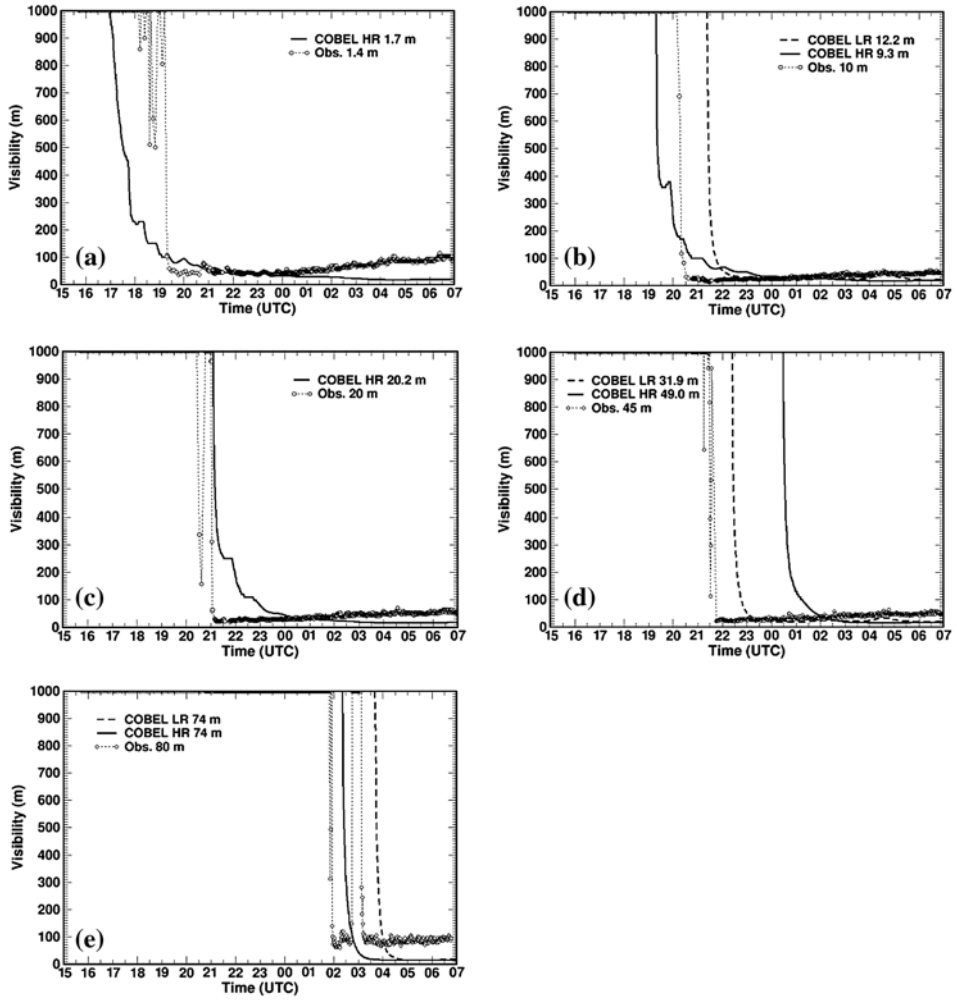

Figure 2
Temporal evolution of observed (symbols) and predicted (lines) visibility, (a) near the surface, (b) near 10 m, (c) at 20 m, (d) near 45 m and (e) near 80 m. Predictions from the COBEL model run with a high vertical resolution (solid lines) and with a coarse resolution (dashed lines) are shown.

by a slight horizontal moisture advection on that particular night. A slower growth rate occurred thereafter, with fog first reaching a height of 80 m a few minutes before 0200 UTC on November 7 (Fig. 2e).

In comparison, the predicted visibility from the HR COBEL run is first reduced below 1000 m close to the surface (1.7 m) at 1700 UTC, while dense fog first appears at 1920 UTC at 9 m and shortly after 2100 UTC at 20 m. The initiation of the dense fog near the ground surface therefore is about 45 minutes to 1 hour too early, while its onset at 20 m is well predicted. The evolution of visibility toward its minimum value is slower than observed. The combination of early fog formation and slower visibility decrease lead to a good short-term forecast of very heavy fog formation (visibilities below 100 m) adjacent to the surface (Figs. 2a and b). The rapid deepening toward the 45 m level is not well captured in the HR forecast, with the appearance of fog at that level delayed by nearly 3 hours compared to observations (Fig. 2d). However, the arrival of the fog at the upper level on the tower (80 m) is well captured, with a forecast error of the order of 30 minutes (Fig. 2e). The forecast performed with the coarse grid spacing cannot represent the ground fog phase as the fog layer is shallower than the lowest model level. Fog onset at the lowest model level (12.2 m) occurs a few minutes before 2130 UTC, 3½ hours later than the initial detection of fog at the site. However, the forecast is too late by 1¼ hours in its prediction of fog formation when compared to visibility observed at a comparable height (Fig. 2b). Interestingly, the coarse resolution forecast is more accurate in its prediction of fog onset at 45 m (Fig. 2d). However, it is again too late by about two hours in the forecast of heavy fog at 80 m (Fig. 2e). Therefore, the high-resolution forecast can be described as more accurate as far as the timing of fog onset is concerned, as well as the general deepening of the fog layer, except for the rapid growth that took place at about 2100 UTC. A general good agreement is observed between the two model simulations and observations in terms of the minimum visibility reached near the surface (below 100 m). Nevertheless, a tendency for the model to generate a fog that is too dense is observed later in the night in the two simulations. Such a tendency has been observed over multiple cases by BERGOT (2007) suggesting that this is a common problem.

Differences in the model forecasts are further illustrated in Figure 3 showing time-height contours of liquid water content (LWC) for the two simulations. The early stage of the observed growth of the fog layer (until it reached the top of the 80 m tower) is shown by the dots on the figures. As pointed out earlier, the HR forecast is more accurate in the early stage of fog development, while the LR forecast seems in better agreement with the observations with a more rapid growth of the fog layer around 2100 UTC. The HR forecast is again in better agreement with the observations with regards to the timing of the fog reaching the upper level of the tower. Also noteworthy is the fact that the LWC tends to gradually increase over time and migrate towards fog top after 0200 UTC in the HR simulation (Fig. 3a). The rate of increase of the near-surface LWC is approximately

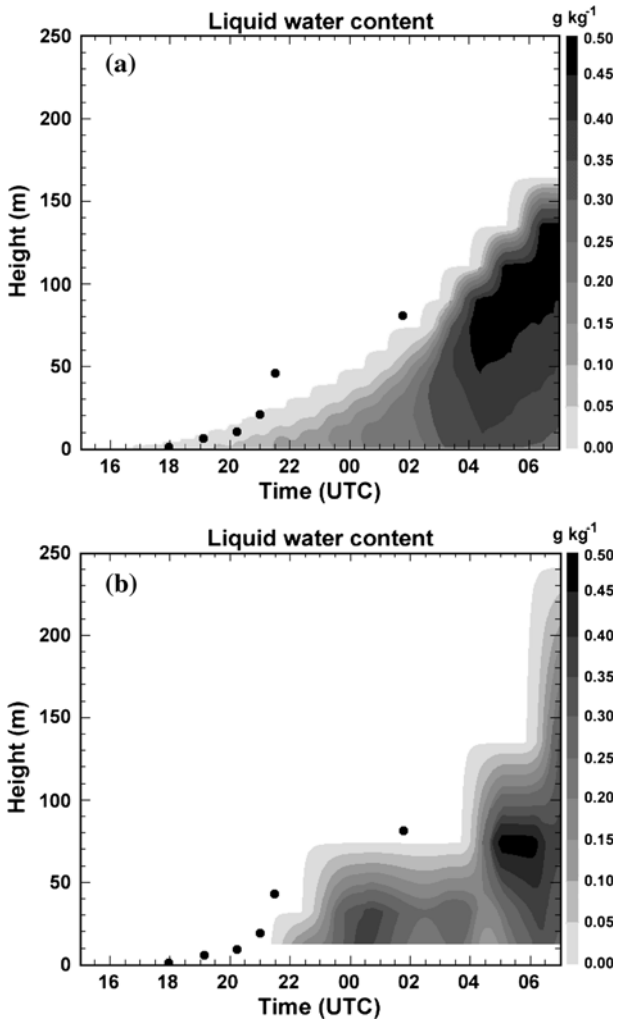

Figure 3
Time-height contour plots of fog water content simulated with (a) a high-resolution grid and (b) a coarse grid spacing (Table 1). Dots indicate the observed time at which fog top reached various heights on the tower.

0.03 g kg^{-1} h^{-1} until 0200 UTC and then 0.06 g kg^{-1} h^{-1} over the following two hours (Fig. 4a). Oscillations are observed, but have relatively small amplitudes. In contrast to this, results obtained from the LR simulation show a tendency to form regions of large LWC in the lower part of the fog early in its evolution, along with large amplitude oscillations. The initial large LWC in the run performed with the lower vertical resolution occurs after a prolonged and large rate of

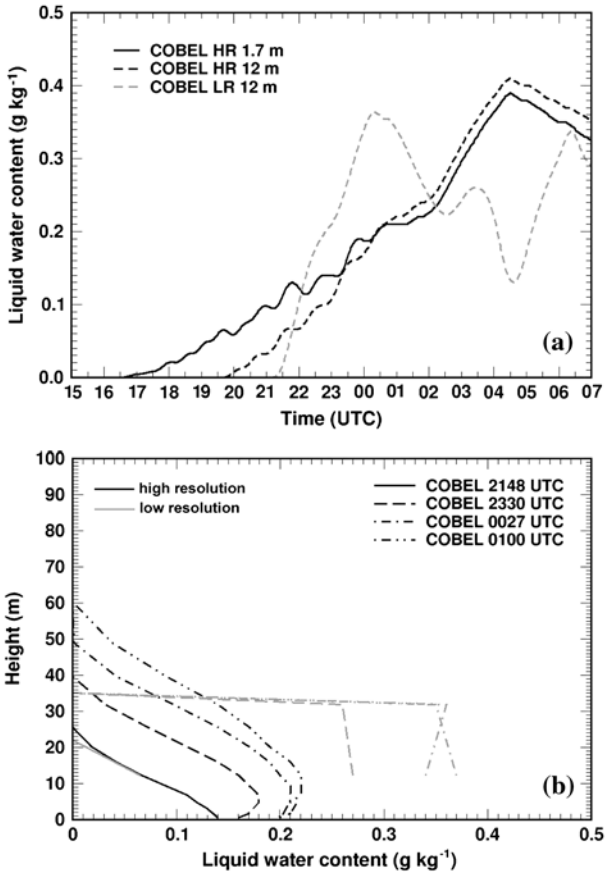

Figure 4
(a) Temporal evolution of liquid water content at the lower model levels for the two simulations performed, and (b) profiles of liquid water content at 2148 UTC (solid lines), 2330 UTC (dashed lines), 0027 UTC (dot-dashed lines) and 0100 UTC (triple dot-dashed line) for the two COBEL simulations: high (black lines) and coarse (gray lines) vertical resolutions.

increase in cloud water, (e.g., 0.15 g kg^{-1} h^{-1} during the first 3 hours of fog). This leads to drastically different LWC profiles compared to the HR run (Fig. 4b). After the initial increase, large amplitude oscillations are observed, which are not corroborated by observations.

(b) Diagnostics

As was shown in the previous section, significant differences exist between forecasts performed with different grid configurations. Deficiencies in the LR forecast are the delayed initial formation of fog near the surface, the delayed growth of the fog layer up to the upper level of the tower and the presence of large amplitude oscillations in LWC.

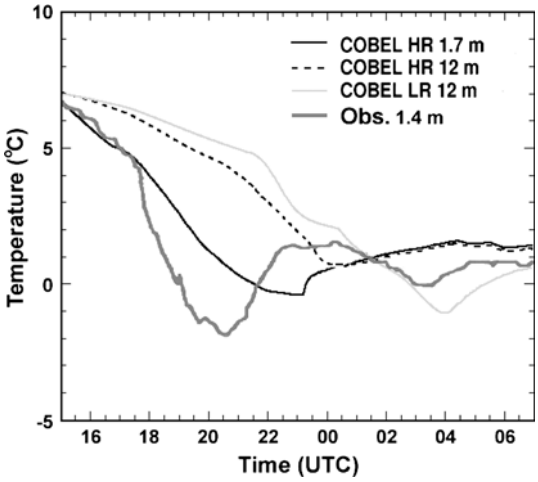

Figure 5
Evolution of the near-surface temperature for the COBEL simulation with the HR grid at 1.7 m (solid line) and at 12.2 m (dashed line); and COBEL with an LR grid (lowest model level at 12.2 m) (solid gray line). The observed temperature at 1.4 m is also shown (thick dark gray line).

On the other hand, better agreement was obtained with the LR forecast with a more rapid reduction in visibility once LWC formed and a rapid deepening of the fog layer at 2100 UTC. Reasons behind these differences are investigated in this section.

First focusing on the initial formation of fog, the evolution of the near-surface temperature is examined (Fig. 5). Observations near the surface show two periods of distinct cooling rates. A cooling rate of 1°C h^{-1} took place until about 1735 UTC, followed by two hours with a cooling rate twice as large. The increase in cooling occurred as upper clouds cleared from over the site. Fog formed during the period of enhanced cooling and became denser as cooling continued until 1930 UTC.

The HR forecast reproduces well the near-surface cooling observed during the early part of the evening. Although there is an increase in the cooling after the upper clouds cleared, the model underestimates the subsequent enhanced decrease in temperature (Fig. 5). This is likely the result of the early formation of ground fog in the simulation, thus diminishing the radiative cooling of the surface. What can be perceived as a paradox is the fog forming earlier in the simulation, even under the influence of weaker cooling than observed. This is most likely related to the evolution of the near-surface moisture. A comparison of the simulated amount of water deposited on the surface as dew in the two simulations shows small values in the HR run and none in the LR run (Fig. 6), suggesting a resolution dependency on the simulated dew flux. Small dew deposition in the HR forecast may have contributed to the premature fog onset compared to observations. Unfortunately, reliable observations of humidity are not available, preventing a conclusive evaluation of the

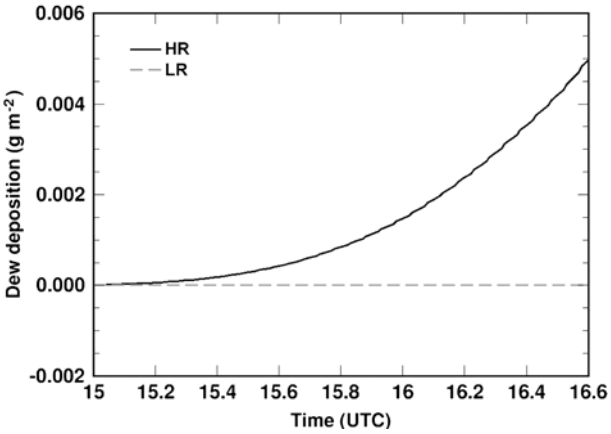

Figure 6
Temporal evolution of the cumulative mass of water deposited on the surface as dew in the COBEL simulation with the HR grid (solid line) and with the LR grid (dashed gray line), for the period before fog onset.

accuracy of the simulated dew deposition. After the minimum temperature is reached in the HR run, and a LWC of 0.14 g kg^{-1}, a period of warming is simulated as fog continues its growth. The timing and amplitude of this warming is in error compared to the observations, but still shows that the model is able to reproduce the dynamics within the foggy boundary layer.

Comparing results from the two simulations, the temperature at the lowest model level in the LR run (12 m) exhibits a significantly slower cooling than observed at the corresponding height in the HR run. For instance, the 12-m temperature in the HR run is about 0.7°C cooler than in the LR run at 2000 UTC. Furthermore, cooling continues for much longer, past the time of the initial maximum in LWC in the LR run, with a period of warming only initiated at 0400 UTC. Focusing on the early evening (pre-fog) near-surface cooling, an examination of the model-diagnosed contributions from radiative and turbulent cooling/heating rates in the surface layer (not shown) indicates the overall cooling is dominated by the divergence of radiative fluxes. Such a behavior is in agreement with results presented by HA and MAHRT (2003) for nocturnal boundary layers characterized by light winds, as is the case here. The near-surface profiles of the radiative heating rate calculated using the simulations' initial temperature and moisture profiles are shown in Figure 7. The lack of resolution of the LR grid close to the surface not only leads to an underestimation of the cooling at the lowest model level (12 m), but also to an inability at capturing the early evening maximum cooling in the air clear adjacent to the surface. Errors with such a magnitude are in agreement with the study of RÄISANEN (1996). The heating rates calculated on the LR grid only partially capture the slightly larger cooling in the 10–50 m layer, and entirely miss the fine scale

structure of the low-level cooling maximum present in the HR forecast. This can be described as the dominant factor over the lack of dew deposition in the delayed LR forecast of fog onset.

As was previously pointed out, the temporal evolution of LWC near the surface is quite different between the two COBEL forecasts. The LR forecast exhibits a large LWC near the surface which is not present in the HR simulation. On the other hand, a rapid vertical growth of the fog layer is observed in the LR simulation shortly after fog onset at the surface, providing a better agreement with observations. The equation describing the evolution of LWC (q_l) is written as

$$\frac{\partial q_l}{\partial t} = C - \frac{\partial G}{\partial z} - \frac{\partial \overline{w'q'_l}}{\partial z}, \tag{1}$$

where q_l is the liquid water mixing ratio, C is the condensation/evaporation of water, G is the sedimentation (gravitational settling) flux and $\overline{w'q'_l}$ is the turbulent flux of water. The two latter terms can be considered as transport contributions. Within COBEL, the gravitational sedimentation flux is parameterized as (BROWN and ROACH, 1976)

$$G = v_i \cdot q_l, \tag{2}$$

with v_i (sedimentation velocity) taken as a constant ($v_i = -1.6$ cm s^{-1}), and the turbulent flux is parameterized as

$$\overline{w'q'_l} = -c \cdot \ell \cdot \sqrt{e} \cdot \frac{\partial q_l}{\partial z}, \tag{3}$$

where c is a constant, ℓ is a stability dependent mixing length and e is the turbulence kinetic energy.

The individual contributions to the evolution of the near-surface LWC are evaluated from model output at various times corresponding to the period surrounding the near-surface LWC maximum in the LR Simulation (Table 2).

Table 2

Diagnosed contributions to the evolution of liquid water content from condensation/evaporation, the divergence of the sedimentation flux and the divergence of the turbulent flux. Estimates are obtained from model output at 2148 UTC, 2330 UTC, 0027 UTC and 0100 UTC in both (high and low resolution) simulations, for the level at 12.2 m

Term (g kg^{-1} h^{-1})	2148 UTC		2330 UTC		0027 UTC		0100 UTC	
	HR	LR	HR	LR	HR	LR	HR	LR
C	+0.40	+0.44	+0.40	+0.20	+0.28	0.00	+0.27	−0.48
$\frac{\partial G}{\partial z}$	−0.44	−0.23	−0.35	−0.03	−0.18	−0.07	−0.18	+0.07
$\frac{\partial \overline{w'q'_l}}{\partial z}$	+0.07	−0.06	−0.02	−0.02	−0.06	+0.06	−0.07	+0.36

Using the results of the HR simulation as a reference, it is observed that the contribution of turbulent fluxes plays a secondary role in the LWC evolution early during the fog period for this case. From the model output at 2148 UTC, a time at which the LWC at 12 m is nearly equal in both simulations but a much larger rate of increase is observed in the LR simulation (Fig. 4), results indicate that the production of water (term *C*) is similar at this time in both simulations. However, the removal of water by the gravitational settling in the LR simulation is only 52% of the value in the HR run. This shows that condensed water is transported away at a significantly slower rate in the LR simulation than in the HR simulation. The resulting excess water in the LR run then feeds back onto the radiative fluxes, leading to an enhanced radiative cooling rate at fog top, which in turn leads to an even greater production of fog water. This is illustrated in Figure 8, where a comparison of profiles of the individual contributions to the evolution of potential temperature is shown. Values were estimated at 2224 UTC, 36 minutes after the LWC at 12 m was equal in both simulations. This time also corresponds to the middle of a period of enhanced cooling in the LR simulation (Fig. 5), culminating in a LWC overestimation at 12 m by nearly a factor of two compared to the HR simulation at 0027 UTC (Fig. 4b). Figure 8 shows that by 2224 UTC, the radiative cooling is considerably larger in the LR model run (70% larger than in the HR run). Also, the turbulent downward mixing of warm air from above leads to a warming that partially counteracts the radiative cooling. Although this contribution is also larger in the LR run, its counteracting effect is not as important as in the HR run. Thus, the combined

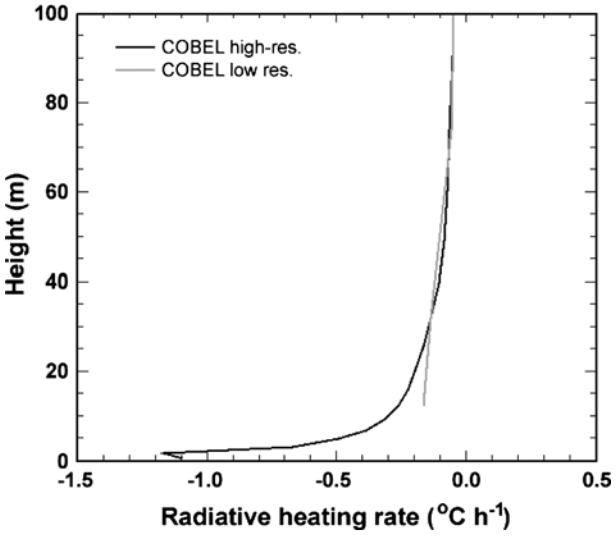

Figure 7
Profiles of radiative heating rates in the lowest 100 m, at 1500 UTC, for the two COBEL simulations: high- (black line) and low- (gray line) vertical resolutions.

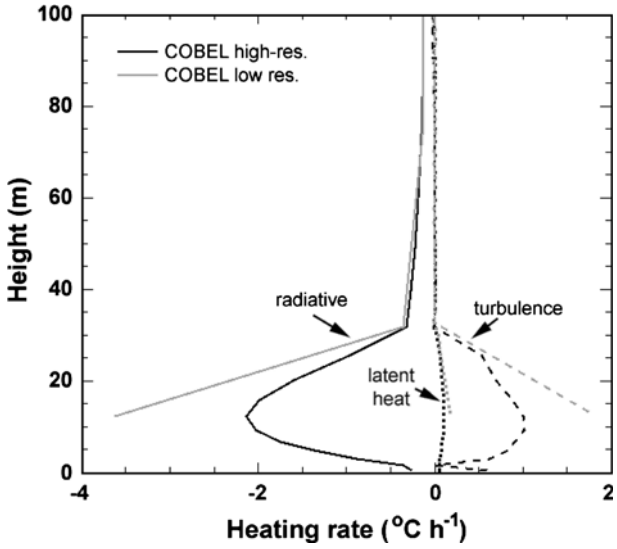

Figure 8
Profiles of contributions to the evolution of potential temperature, diagnosed in the COBEL high-resolution (black) and low-resolution (gray) simulations, at 2224 UTC. Contributions are the divergence of net radiation (solid lines), divergence of turbulent heat fluxes (dashed lines) and latent heat (dotted lines).

effects of enhanced radiative cooling and underestimated warming by turbulent fluxes lead to an overall larger cooling rate and a greater production of water. Evidence of this is provided by the larger amount of latent heat released within the fog layer in the LR run (Fig. 8). This enhanced production of fog water, combined with the underestimation of gravitational settling, leads to the maximum LWC found near the surface in the LR model simulation.

Later on in the simulations, as the LWC increases and the fog layer further develops in the vertical, the vertical gradients of LWC are significantly different in the two simulations (Fig. 4b). At 2330 UTC, fog water has appeared at the second model level in the LR simulation. The maximum in radiative cooling has increased and migrated to the top of the fog, away from the level at 12 m. This is associated with a smaller rate of water production at that level than earlier in the simulation (Table 2). A weaker LWC gradient is observed in the upper portion of the fog layer in the LR simulation (Fig. 4b). This again leads to a smaller removal rate of water by gravitational settling with a contribution corresponding to only 10% of the value diagnosed in the HR simulation. This explains the continued larger rate of increase in LWC at 12 m in the LR simulation. Later on in the LR simulation, the LWC at the lowest level begins to decrease. The model output at 0027 UTC is examined as this corresponds to the time at which the LWC decreasing trend is just beginning. The various contributions to the evolution of LWC reveal that condensation has stopped as radiative cooling at the lowest model level has vanished. The strong cooling at fog

top (now located at the second model level) has led to an increase in LWC such that the LWC gradient in the fog layer becomes small (Fig. 4b). At this time, the contributions from gravitational settling and turbulent fluxes almost offset each other (Table 2), with a slightly larger contribution by gravitational settling leading to a small decreasing rate of LWC.

Further along in both simulations, the trends in LWC have become drastically different. At 0100 UTC (10 hours into the simulations), the LWC is further increasing at a rate of about $+0.02$ g kg^{-1} h^{-1} in the HR simulations, while a decrease of about -0.05 g kg^{-1} h^{-1} is taking place in the LR simulation (Fig. 4a). The evolution of LWC in the HR simulation is again the result of a combination of condensation (through radiative cooling) and removal mainly by gravitational settling, and by turbulent fluxes to some extent (Table 2). In comparison, the decrease in LWC in the LR simulation results from the evaporation of fog water partially counter-balanced by the downward turbulent flux from the maximum LWC found above at 31.9 m (second model level). The destabilization of the fog layer by radiative cooling at fog top and warming of the skin surface by incoming longwave radiation leads to increased levels of turbulence (Fig. 9). An upward turbulent heat flux takes place at the surface, contributing to the warming at the lowest model level and hence some evaporation of fog water. However, the evaporative cooling is sufficient to lead to an overall decrease in temperature. In fact, an examination of model tendencies reveals that an overall cooling rate of -1.0°C h^{-1} is simulated at 0100 UTC, resulting from a warming contribution of $+0.47$°C h^{-1} by turbulent

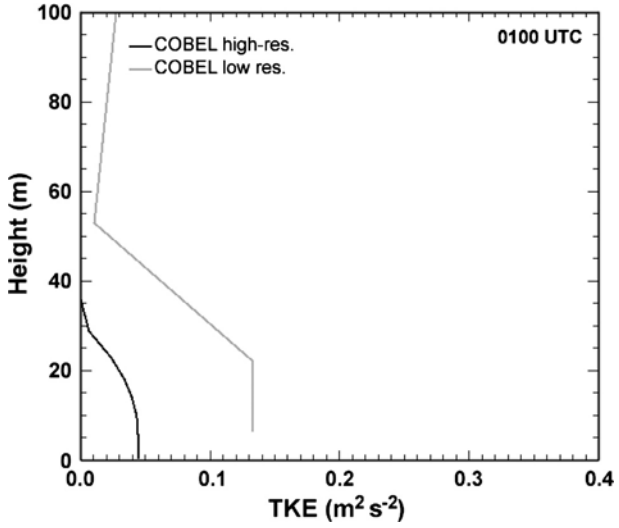

Figure 9
Comparison of vertical profiles of turbulence kinetic energy (TKE) at 0100 UTC from the high-resolution (HR) forecast (black line) and low-resolution (LR) forecast (gray line).

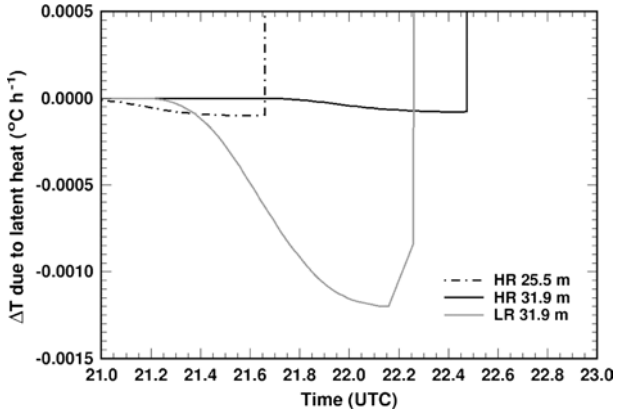

Figure 10
Comparison of the change in temperature above the fog layer from the evaporation of fog water transported upward. Results are presented from the high-resolution (HR) forecast at 32 m (black line) and low-resolution (LR) forecast at the same height (gray line). The result for the high resolution forecast at 25.5 m is also shown. Positive values indicate of condensation of water.

fluxes, cooling of $-0.27°C\ h^{-1}$ associated with radiative effects and $-1.2°C\ h^{-1}$ from evaporative cooling. This shows that variations in LWC are the result of complex interactions among radiative, turbulent and microphysical processes.

Reasons behind the rapid deepening of the fog layer shortly after 2200 UTC in the LR forecast are explored in the following. The main mechanism for upward propagation of fog in the model is the upward export of condensed water into the sub-saturated air above the fog layer by turbulent mixing, its subsequent evaporation and the resulting moistening and cooling of the clear air just above the fog. This moistening and cooling, combined with the radiative cooling, contributes to an increase in the relative humidity toward saturation in the clear air adjacent to the top of the fog layer. Therefore the upward flux of condensed water at fog top is a key mechanism. One way of tracking subtle differences in the HR and LR forecasts is to examine the diagnosed cooling associated with the evaporation of fog water transported above the fog layer by turbulent mixing. The results are compared in figure 10 at levels just above the fog for the period just before the upward growth in the LR forecast. The evaporative cooling at 32 m in the LR forecast has a significantly greater magnitude than in the HR forecast at levels just above the fog. This is indicative of a more important upward flux of water out of the fog layer in the LR forecast and the more rapid increase in relative humidity above fog top. This is partly due to the greater build-up of water at the lowest model level as previously discussed, leading to a greater gradient in the LR forecast even though model levels are located further apart. The resulting enhanced moistening of the air just above the fog contributes to the faster growth of the fog layer up to the next level once LWC formed at the lowest level. In contrast, the growth to the third level (42 m above) is

slower than the deepening of the fog layer to the same height in the HR forecast. Similar values of LWC exist in the LR simulation at the 2nd and lowest model levels, but larger grid spacing between the 2nd and 3rd levels leads to a perceived weaker vertical gradient and thus a weaker upward flux of condensed water at fog top, hence the slower growth of the fog layer.

4. Summary and Conclusions

A numerical sensitivity experiment involving the formation and early evolution of a well-documented radiation fog event was performed using the comprehensive COBEL 1-D boundary layer/fog model. Model simulations were performed with two different grid configurations; one characterized by a very high-resolution (HR) near the surface and another one with a lower resolution (LR) grid typical of those used in current mesoscale forecast models. Thus, both simulations were performed with an identical set of physical parameterizations and model numerics. Initial conditions were essentially the same, except for some degradation in resolution of the profiles used for the LR simulation. Mesoscale forcings (geostrophic wind and horizontal moisture advection) were also identical in both simulations.

The results indicate an overall better representation of the fog by the HR forecast, but also show features that are in better agreement with available observations in either the HR or LR forecasts. The HR forecast is more accurate in its representation of the initial formation of fog and the early ground fog phase. However, the rapid reduction in visibility in the observations is underestimated in the forecast. In contrast, a delayed fog onset is obtained with the forecast performed with a coarser grid, missing entirely the shallow ground fog stage. An examination of model tendencies revealed that a weaker cooling rate is responsible, related to a lack of representation of the fine-scale vertical structure and magnitude of the early evening clear-air radiative cooling in the first few meters of the atmosphere. However, once fog formed in the LR forecast, the rapid decrease in visibility toward its minimum value is more representative of observations, as well as the rapid deepening of the fog layer to 45 m that took place shortly thereafter. These features of the LR forecast are the result of a high rate of increase in LWC at the lowest model level. Diagnostics of model behavior revealed that this rapid increase in LWC results from a positive feedback between an underestimation of the gravitational settling of LWC (relative to the values in the HR forecast) and enhanced radiative cooling at fog top due to the increasing LWC. Results also suggest that the buildup of water at the lowest model level and the reasonable resolution in the lower part of the grid lead to an enhanced upward flux of water and the more rapid deepening of the fog layer to the next level, in better agreement with the observations.

The HR forecast subsequently has a more realistic increase in LWC and deepening of the fog layer, with a more realistic migration of the maximum LWC

toward the top of the fog. The evolution of the LWC in the LR forecast exhibits oscillations characterized by a significant decrease over a 2-hour period, followed by another increase, not corroborated by observations. The decrease in LWC in the LR simulation has been shown to be the result of an enhanced turbulent heat flux in the surface layer associated with the destabilization of the fog layer due to strong radiative cooling at fog top. This destabilization and heating of the lower part of the fog layer by turbulent fluxes seems to occur prematurely in the LR simulation compared to the results of the HR simulation.

It is concluded that the accurate representation of physical processes occurring during the evening transition of the atmospheric boundary layer is of critical importance to the accuracy of very short-term forecasts of fog onset. The representation of key physical processes occurring in fog layers is significantly altered by the use of a coarser vertical resolution. This suggests that adequate vertical resolution is required for the explicit representation of small-scale features found in the clear-sky nocturnal boundary layer as well as in the foggy boundary layer. As such, the profiles of radiative cooling rates and the LWC transport terms were found to be sensitive to grid resolution. This underlines the need for an appropriate vertical resolution to estimate local vertical gradients found over a few meters only for the accurate representation of mechanisms and interactions determining the evolution of the foggy boundary layer. It thus appears that the use of a local high-resolution 1-D model may be beneficial when fine details in very short-term fog forecasts are desired for a specific location, such as an airport. When high resolution is not possible due to limited computational resources, or when general forecasts are needed over a larger region and/or over longer time periods suitable representations of the subgrid-scale distribution of fog water and associated parameterizations should be developed and implemented in 3-D models. Particular attention should be devoted to the parameterization of the gravitational settling and turbulent transport of fog water, as well as on the representation of the radiative effects associated with subgrid-scale features in the clear and cloudy boundary layers.

Acknowledgments

The author would like to thank Dr. Thierry Bergot of CNRM/Météo-France and Dr. Daniel Guédalia of the Laboratoire d'Aérologie, for kindly providing the original code of the COBEL model and data from the Lille experiment. I would like to convey my deep appreciation toward Peter Zwack, who passed away recently, for the numerous opportunities he provided as my M.Sc. advisor and supervisor during the early years of my career. His mentorship has proven invaluable. Thanks also to Roy Rasmussen for his helpful review of the manuscript, as well as to two anonymous reviewers for their comments. This research is in response to requirements and funding by the Federal Aviation Administration (FAA). The views

expressed are those of the author and do not necessarily represent the official policy or position of the FAA. The National Center for Atmospheric Research is operated by the University Corporation for Atmospheric Research under the sponsorship of the National Science Foundation.

References

Bechtold, P., Krueger, S. K., Lewellen, W. S., van Meijgaard, E., Moeng, C.-H., Randall, D. A., van Ulden, A., and Wang, S. (1996), *Modeling a stratocumulus-topped PBL: Intercomparison among different one-dimensional codes and with large eddy simulation,* Bull. Am. Meteor. Soc. *77*(9), 2033–2042.

Benjamin, S. G., Grell, G. A., Brown, J. M., and Smirnova, T. G. (2004), *Mesoscale weather prediction with the RUC Hybrid Isentropic–Terrain-Following Coordinate Model,* Mon. Wea. Rev. *132*, 473–494.

Bergot, T. and Guédalia, D. (1994), *Numerical forecasting of radiation fog. Part I: Numerical model and sensitivity tests,* Mon. Wea. Rev. *122*, 1218–1230.

Bergot, T., Carrer, D., Noilhan, J., and Bougeault, P. (2005), *Improved site-specific numerical prediction of fog and low clouds: A feasibility study,* Wea. Forecasting *20*, 627–646.

Bergot, T. (2007), *Quality assessment of the Cobel-Isba numerical forecast system of fog and low clouds,* Pure Appl. Geophys. *164*, 6/7, this issue.

Bott, A. and Trautmann, T. (2002), *PAFOG – A new efficient forecast model of radiation fog and low-level stratiform clouds,* Atmos. Res. *64*, 191–203.

Bougeault, P. and Lacarrère, P. (1989), *Parameterization of orography-induced turbulence in a meso-beta scale model.* Mon. Wea. Rev. *117*, 1872–1890.

Brown, R. and Roach, W. T. (1976), *The physics of radiation fog: Part II - A numerical study,* Quart. J. Roy. Meteor. Soc. *102*, 335–354.

Clark, P. A. and Hopwood, W. P. (2001), *One-dimensional site-specific forecasting of radiation fog. Part I: Model formulation and idealized sensitivity studies,* Meteor. Appl. *8*, 279–286.

Colby, F. P. (2004), *Simulation of the New England sea breeze: The effect of grid spacing,* Wea. Forecasting *19*, 277–285.

Delage, Y. (1974), *A numerical study of the nocturnal boundary layer,* Quart. J. Roy. Meteor. Soc. *100*, 351–364.

Durran, D. and Klemp, J. B. (1982), *On the effects of moisture on the Brunt-Väisälä frequency*, J. Atmos. Sci. *39*, 2152–2158.

Estournel, C. and Guédalia, D. (1987), *A new parameterization of eddy diffusivities for nocturnal boundary layer modeling,* Bound.-Layer Meteor. *39*, 191–203.

Fouquart, Y. and Bonnel, B. (1980), *Computations of solar heating of the earth's atmosphere: A new parameterization,* Beit. zur Phys. der Atmosphäre *53*, 35–62.

Guédalia, D. and Bergot, T. (1994), *Numerical forecasting of radiation fog. Part II: A comparison of numerical simulation with several observed fog events,* Mon. Wea. Rev. *122*, 1231–1246.

Ha, K.-J. and Mahrt, L. (2003), *Radiative and turbulent fluxes in the nocturnal boundary layer,* Tellus *55A*, 317–327.

Kunkel, B. A. (1984), *Parameterization of droplet terminal velocity and extinction coefficient in fog models,* J. Climate Appl. Meteor. *23*, 34–41.

Mahrt, L. and Pan, H.-L. (1984), *A two-layer model of soil hydrology,* Bound.-Layer Meteor. *29*, 1–20.

Mass, C. F., Ovens, D., Westrick, K., and Colle, B. A. (2002), *Does increasing horizontal resolution produce more skillful forecasts?* Bull. Am. Meteor. Soc. *83*, 407–430.

Pagowski, M., Gultepe, I., and King, P. (2004), *Analysis and modeling of an extremely dense fog event in Southern Ontario,* J. Appl. Meteor. *43*, 3–16.

Peters-Lidard, C. D., Blackburn, E., Liang, X., and Wood, E. F. (1998), *The effect of soil thermal conductivity parameterization on surface energy fluxes and temperatures,* J. Atmos. Sci. *55*, 1209–1224.

Räisanen, P. (1996), *The effect of vertical resolution on clear-sky radiation calculations: Test with two schemes.* Tellus *48A*, 403–423.

ROACH, W. (1995), *Back to basics: Fog: Part 2 – The formation and dissipation of land fog,* Weather *50*, 7–11.
VEHIL, R., MONNERIS, J. GUÉDALIA, D., and SARTHOU, P. (1989), *Study of the radiative effects (long-wave and short-wave) within a fog layer,* Atmos. Res. *23*, 179–194.
WEISMAN, M. L., SKAMAROCK, W. C., and KLEMP, J. B. (1997), *The resolution dependence of explicitly modeled convective systems,* Mon. Wea. Rev. *125*, 527–548.

(Received April 17, 2006, accepted November 1, 2006)
Published Online First: June 8, 2007

Pure appl. geophys. 164 (2007) 1241–1264
0033–4553/07/071241–24
DOI 10.1007/s00024-007-0217-4

Pure and Applied Geophysics

A One-dimensional Ensemble Forecast and Assimilation System for Fog Prediction

M. D. Müller,[1] C. Schmutz,[2] and E. Parlow[1]

Abstract—A probabilistic fog forecast system was designed based on two high resolution numerical 1-D models called COBEL and PAFOG. The 1-D models are coupled to several 3-D numerical weather prediction models and thus are able to consider the effects of advection. To deal with the large uncertainty inherent to fog forecasts, a whole ensemble of 1-D runs is computed using the two different numerical models and a set of different initial conditions in combination with distinct boundary conditions. Initial conditions are obtained from variational data assimilation, which optimally combines observations with a first guess taken from operational 3-D models. The design of the ensemble scheme computes members that should fairly well represent the uncertainty of the current meteorological regime. Verification for an entire fog season reveals the importance of advection in complex terrain. The skill of 1-D fog forecasts is significantly improved if advection is considered. Thus the probabilistic forecast system has the potential to support the forecaster and therefore to provide more accurate fog forecasts.

Key words: Fog, one-dimensional, ensemble prediction, assimilation, model coupling, advection, verification.

1. Introduction

Reductions in visibility have an important impact on the capacity of an airport. Different initiatives by the International Civil Aviation Organization (ICAO) and also by Eurocontrol endeavor to address this problem. In Europe the Meteorological support for Air Traffic Management Group (METATMG) has, as one of its tasks, to study the possibilities to improve visibility and runway visual range (RVR) forecasts (METATMG, 2005). A large industry project (SESAR) under the lead of Eurocontrol intends to increase the air traffic capacity in Europe in the coming years by factors on different levels (EUROCONTROL, 2006), meteorology along with visibility forecast is one of the subtasks of the project. Imperfect visibility

[1] Institute of Meteorology, Climatology & Remote Sensing, University of Basel, Klingelbergstr. 27, Basel, Switzerland. E-mail: mathias.mueller@unibas.ch

[2] Eidgenössisches Departement des Innern EDI, Bundesamt für Meteorologie und Klimatologie MeteoSchweiz, CH-8058, Zürich-Flughafen, Schweiz.

forecast always has an adverse impact on capacity regulated airports. It results in an overload when actual capacity is lower than expected, and in a capacity loss when conditions and the actual capacity are better than expected. In 2003 Swiss International Airlines estimated the accumulated delay due to one hour of erroneous visibility forecast in the morning for Zürich airport to 1400 minutes throughout the day (Werner Suhner, Swiss Int. Airlines, pers. comm., 2003).

Fog and visibility forecasts are provided in the Terminal Area Forecast (TAF) code for the so-called terminal area (airport). It is current practice to provide point forecast for such locations and the two main approaches are based either on statistical methods or on numerical models. Statistical approaches combine long records of site-specific observations with forecast variables generally provided by numerical weather prediction. A human forecast is, to a large extent, based on experience, and thus a subjective system of pattern recognition and climatological knowledge. For this work the focus lies on the second approach, using dedicated models for fog prediction without the need for long statistical training records.

The formation and dispersion of fog is the result of a complex interaction between thermodynamic and dynamical processes. DUYNKERKE (1990) identified the most important factors for fog formation to be:

- cooling of moist air by radiative flux divergence,
- mixing of heat and moisture,
- vegetation,
- horizontal and vertical wind,
- heat and moisture transport in soil,
- advection,
- topographic effects,

where atmospheric conditions, location and season decide upon the relative importance of each factor. The presence of clouds increases the incoming longwave radiation at ground level and thus reduces the longwave radiative cooling at the surface, which has great influence on fog formation. Therefore a good cloud forecast, computed by a 3-D model, is also needed. In complex topography cold air outflow and pooling as well as advection in the heterogeneous landscape become very important. Once the fog has formed there are further influences:

- longwave radiative cooling at fog top,
- fog microphysics,
- shortwave radiation.

Starting with the work of ZDUNKOWSKI and NIELSEN (1969) some of the above listed processes were included in fog models. In this early model there was no parameterization for the sedimentation of liquid water nor turbulence exchange coefficients. The latter were introduced by ZDUNKOWSKI and BARR (1972). An even more sophisticated model was developed by BROWN and ROACH (1976) and further

refined by TURTON and BROWN (1987), including new formulations for turbulence exchange coefficients in the nocturnal boundary layer. A similar model was also used by MUSSON-GENON (1987) for his quantitative comparison between computed and observed fog evolution. Very detailed microphysics was introduced by BROWN (1980) and further refined in a new model by BOTT *et al.* (1990), who also introduced a sophisticated treatment of radiation. BERGOT and GUÉDALIA (1994b) illustrated the importance of advection terms and their role in fog formation and evolution. BALLARD *et al.* (1991) used a numerical weather prediction model to simulate sea fog and pointed out the importance of initial conditions and vertical resolution. GOLDING (1993) found that the development of local nocturnal winds in complex terrain often determines the location and timing of fog formation. SIEBERT *et al.* (1992a), SIEBERT *et al.* (1992b) and VON GLASOW and BOTT (1999) finally added a module to resolve small and tall vegetation on a high resolution grid. In these later models, the evolution of the droplet size distribution and cloud condensation nuclei is explicitly resolved, but even today such an approach is computationally very expensive. Currently parameterized versions of the detailed 1-D fog microphysics models are incorporated in 3-D models and are able to improve visibility forecasts (GULTEPE *et al.*, 2006; GULTEPE and MILBRANDT, 2007).

In this work an ensemble forecast system based on numerical prediction models is developed and tested. 1-D models are coupled to 3-D models so that they also can be used for advection fog and valley fog situations and are thus suitable for an operational forecasting system.

2. Site-specific Characteristics and Available Data

Zürich airport (432 m a.s.l.) is located in a small basin north of the City of Zürich, Switzerland. It is surrounded by hills with an average altitude of 500 m to 600 m a.s.l. Some higher hills are between 700 m and 850 m a.s.l. In the past the airport area used to be a moorland with marsh. Fog often forms in the area of the airport. Table 3 reveals that the season with the highest occurrence of fog is between September and March. SCHMUTZ *et al.* (2004) also show that the highest frequency of low visibility (here defined to be < 800 m) during the day is observed between 5 a.m. and 10 a.m. local time from December to February.

A broad spectrum of observations, listed in Table 1, is available at the airport. Furthermore a virtual profile can be constructed from standard height observations made by stations located on nearby hilltops (Table 2). For high accuracy of data assimilation it is best to directly measure profiles of temperature and humidity up to a height of approximately 2 km, which is the upper boundary of the models. This can be easily achieved with a radiosonde. However at an airport this is not allowed for safety reasons and operating costs are also very high. Remote sensing techniques could be used as a surrogate but they are in general less accurate and rather costly.

Table 1

Available observations at and in the vicinity of the Zürich airport

Parameter
visibility (spatially aggregated)
precipitation rate
precipitation type
soil temperature (−0.05, −0.1,−0.2,−1.0 m)
soil moisture (−0.01, −0.02, −0.1, −0.25, −0.6, −0.98 m)
"surface" temperature (0.02 m)
temperature (0.5 m)
temperature (all heights of virtual profile)
temperature profile (MTP−5)
wind profile
humidity (all heights of virtual profile)
u−wind (all heights of virtual profile)
v−wind (all heights of virtual profile)
cloud base
cloud cover
longwave radiation LW↓
longwave radiation LW↑
shortwave radiation SW↓
Radiosonde from Payerne (150 km away)

For temperature it was possible to use an MTP-5 microwave profiler (KADYGROV and PICK, 1998) but nothing comparable was available for humidity. In order to obtain entire profiles of temperature and humidity, an assimilation scheme is necessary to initialize the forecast models.

3. The Ensemble Forecast System

Fog forecasting is a threshold problem, namely a small difference in temperature and/or humidity determines if condensation occurs and thus fog forms or not. Keeping in mind the difficulties of providing good temperature and humidity

Table 2

Statistics of temperature deviations between the MTP−5 and the stations of the virtual temperature profile. Height in m above sea level (m a.s.l.), also indicated is the number of 10 min intervals with positive or negative temperature deviation from the MTP−5 profile

Station	Height (m a.s.l.)	RMS (K)	Mean (K)	negative	positive
Zürich airport	432	0	0	0	
Bühlhof	520	0.77	0.44	586	2745
Gubrist	640	0.79	0.28	955	2453
Zürichberg	730	0.90	0.37	922	2486
Lägeren	870	1.21	−0.56	2137	1194

Table 3

Monthly frequencies (%) of low visibility (vis) as observed between 1993 and 2002 at Zürich airport. (SCHMUTZ et al. 2004)

	vis <800 m	vis <1500 m
Jan.	6.0	8.8
Feb.	2.5	4.1
Mar.	1.4	2.2
Apr.	0.9	1.2
May.	1.0	1.2
Jun.	0.4	0.6
Jul.	0.4	0.6
Aug.	0.9	1.3
Sep.	4.0	4.9
Oct.	7.2	8.7
Nov.	5.4	7.6
Dec.	3.5	5.2

forecasts and the dependence of theses forecasts on initial conditions, a deterministic forecast incorporates rather large uncertainties. This problem can be addressed with ensemble forecasting, which not necessarily provides a more accurate forecast for all conditions although it can provide a likelihood of fog occurrence and thus also inform about the predictability of a particular situation.

The developed ensemble forecast system consists of an assimilation system to generate a set of initial conditions based on prior forecasts and current observations, two distinct 1-D forecast models and a post-processor.

Data Assimilation Strategy

An important part of every ensemble forecast is the derivation of a set of initial conditions representative of the current uncertainty of the initial state.

The process of data assimilation optimally combines observations with a first guess or background estimate. In this case data have to be assimilated by a 1-D model, and it seems natural to use a previous forecast of that model as background state. There are however several reasons for using the 3-D model forecasts, having resolutions between 2 and 7 km, as a first guess. In 1-D it is not possible to simulate horizontal gradients which are responsible for advection and wind so that the 1-D model cannot simulate its own background state needed in the data assimilation process. Basically the 1-D model is unaware of changes in temperature, humidity and wind caused by advection so that large errors develop over time. Since the 1-D model is operated at a location where observed humidity and wind is based on measurements taken only a few meters above ground, the assimilation process cannot correct the background state in most parts of the vertical profile. Another big problem is the limited vertical extent of the 1-D model, which currently simulates the lowest 2000 m of the atmosphere. Thus mid-and high-altitude clouds and their effects on radiative

fluxes are not within the domain of the 1-D models. To simulate the background state with a 1-D model it would thus be necessary to run it in an "assimilation mode" which incorporates information about advection and radiative fluxes from 3-D models. Unfortunately, due to post-processing time constraints and large data amounts, a 3-D model output is only available with very limited temporal resolution of 1 hour or even worse. The accuracy of tendencies derived from these temporally heavily discretized data is rather limited (DUNLOP and CLARK 1997). To overcome these problems related to the strong dependence of the 1-D assimilation model on 3-D data, vertical columns of the 3-D models are used directly as background terms in the assimilation process. A problem is that close to the surface the 3-D profiles are less detailed than the 1-D forecasts, due to a coarser vertical resolution. However, considering the whole profile, the surface layer contains only slight energy and the high resolution 1-D model adjusts the surface layer profiles in a relatively short time. Also the assimilation will correct a suboptimal surface layer background from the 3-D model, using all the observations. Due to large error variances and abundant observations close to the ground, the assimilation normally gives little weight to the background in the surface layer. Another important point is the fact that a 3-D model is able to do skillful forecasts for several days, where the most recent one is not necessarily the best and the skill of surface variables such as temperature, pressure and wind is generally similar within the first 48 hours as can be seen e.g., in BERNARDET *et al.* (2005) or LIN *et al.* (2005). Thus, several forecasts initialized in the past, but valid at the same time, can be used as first guess for the generation of ensemble members.

We therefore decided to base our initial conditions on available forecasts computed from different 3-D models. Currently the aLMo (STEPPELER *et al.*, 2003) of MeteoSwiss, running at 7 km resolution, as well as the semi-operational forecasts with the Nonhydrostatic Mesoscale Model (NMM) (JANJIC *et al.*, 2001; JANJIC, 2003) at resolutions of 22, 4 and 2 km from the University of Basel are available for the study area of Zürich airport. The different 3-D models driven by distinct global assimilations, with varying resolutions as well as different initialization times produce a spread in forecast fields which are used as initial conditions by the 1-D models. This spread is dependent on the current weather situation.

Certainly four different forecasts from four different models do not produce a large set of initial conditions. To increase the number of 3-D forecasts, all the runs valid at the same time but initialized at different times are used. This can be done since the most recent run does not have to be the most skillful. Of course this is not true for runs that are several days old and initial conditions are not taken if they are older than two days. It has to be noted that other models could be easily included if available. This procedure is summarized in Figure 1. Note that an individual assimilation is computed from every 3-D run using the corresponding error covariance matrix **B**, as derived in the next section. The number of members is finally doubled by using two different numerical 1-D models to integrate all initial conditions.

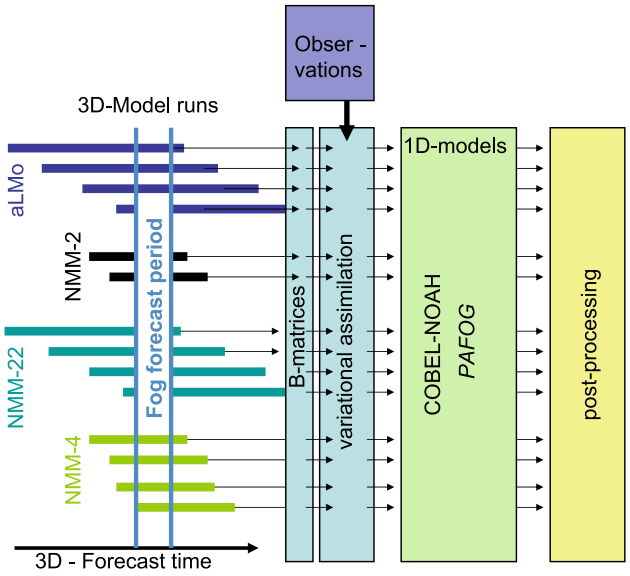

Figure 1
Schematic of the 1-D ensemble prediction system. Every 3-D run provides initial conditions that are used as a background for an individual variational assimilation. Since the 3-D models also provide boundary conditions, a 3-D run has to cover the entire 1-D fog forecast period.

Data Assimilation System

Data assimilation combines observations and a dynamic model by using specified statistical error properties of observations and of the numerical model in order to give each information source the proper weight. Under the assumption that errors can be modeled by a Gaussian unbiased distribution, and thus entirely specified by a covariance matrix, variational assimilation becomes the problem of minimizing the cost function (1) (KALNAY, 2003).

$$J(\vec{x}) = \frac{1}{2}(\vec{x} - \vec{x_b})^T \mathbf{B}^{-1}(\vec{x} - \vec{x_b}) + \frac{1}{2}(\vec{y} - \mathbf{H}\vec{x})^T \mathbf{R}^{-1}(\vec{y} - \mathbf{H}\vec{x}). \quad (1)$$

Here the following notation proposed by IDE *et al.* (1997), is used:
$\vec{x}$ model state (dimension n),
$\vec{x_t}$ true model state (dimension n),
$\vec{x_b}$ background model state (dimension n),
$\vec{y}$ vector of observations (dimension p),
$\mathbf{H}$ linearized observation operator (from dimension n to p),
$\mathbf{B}$ covariance matrix of background errors $(\vec{x_b} - \vec{x_t})$ (dimension $n \times n$),
$\mathbf{R}$ covariance matrix of observation errors $(\vec{y} - \mathbf{H}\vec{x_t})$ (dimension $p \times p$).

In order to solve the assimilation problem it is necessary to precondition **B** and reduce the number of elements, which is done by the so-called control variable transform.

$$\mathbf{U}^T\mathbf{B}^{-1}\mathbf{U} = \mathbf{I}. \tag{2}$$

It is thus necessary to transform the model variables (actually perturbations) $\vec{x}'$ into control variables $\vec{v}'$, the so called T-Transform and *vice versa* using the so called U-Transform:

$$\vec{x}' = \mathbf{U}\vec{v}', \tag{3}$$

$$\vec{v}' = \mathbf{T}\vec{x}'. \tag{4}$$

By doing so the cost function to be evaluated becomes

$$J(\vec{v}') = \frac{1}{2}(\vec{v}'^T\vec{v}') + \frac{1}{2}(\vec{y}' - \mathbf{HU}\vec{v}')^T R^{-1}(\vec{y}' - \mathbf{HU}\vec{v}'). \tag{5}$$

During the minimization process, the cost function and the gradient of (5), as derived by BOUTTIER and COURTIER (1999) and transformed into the incremental form in $\vec{v}'$-space (6), have to be evaluated during every step of the minimization.

$$\nabla_{\vec{v}'}J(\vec{v}') = \vec{v}' - \mathbf{U}^T\mathbf{H}^T\mathbf{R}^{-1}(\vec{y}' - \mathbf{HU}\vec{v}'). \tag{6}$$

In the current implementation, the Broyden-Fletcher-Goldfarb-Shanno variant of the Davidon-Fletcher-Powell method, as described in PRESS *et al.* (1988), is used to compute the minimization of the cost function with the help of its gradient.

The quality of the assimilation relies on an accurate estimation of **B**. This is a difficult task since it cannot be observed directly and hence has to be estimated in a statistical sense. Here, the "NMC" or NCEP Method (PARRISH and DERBER, 1992) is used which is independent of measurements.

$$\mathbf{B} \approx \alpha\frac{1}{n}\sum_{i=1}^{n}\Big((\vec{x_f}(t_1) - \vec{x_f}(t_0))(\vec{x_f}(t_1) - \vec{x_f}(t_0))^T\Big), \tag{7}$$

where $\vec{x_f}$ represents the forecast state vector and α is an empirical scaling factor. As can be seen in (7) **B** is estimated as the average over n differences between two short-range model forecasts verifying at the same time. Normally $t_1 = 48$ h, $t_0 = 24$ h and about 50 different forecasts representative for the season are used.

The estimates of **B** obtained for different 3-D models using the NMC-Method (7) and corresponding correlations are shown in Figure 2. The statistics are based on the vertical profiles of the 3-D models from October 2004 to February 2005. In Figure 2, it is evident that variances are largest close to the surface, where a small change in e.g., predicted cloud cover results in a large temperature difference. This means that in this region, the background term will have relatively little influence compared to the observations. Fortunately most observations are available close to the surface

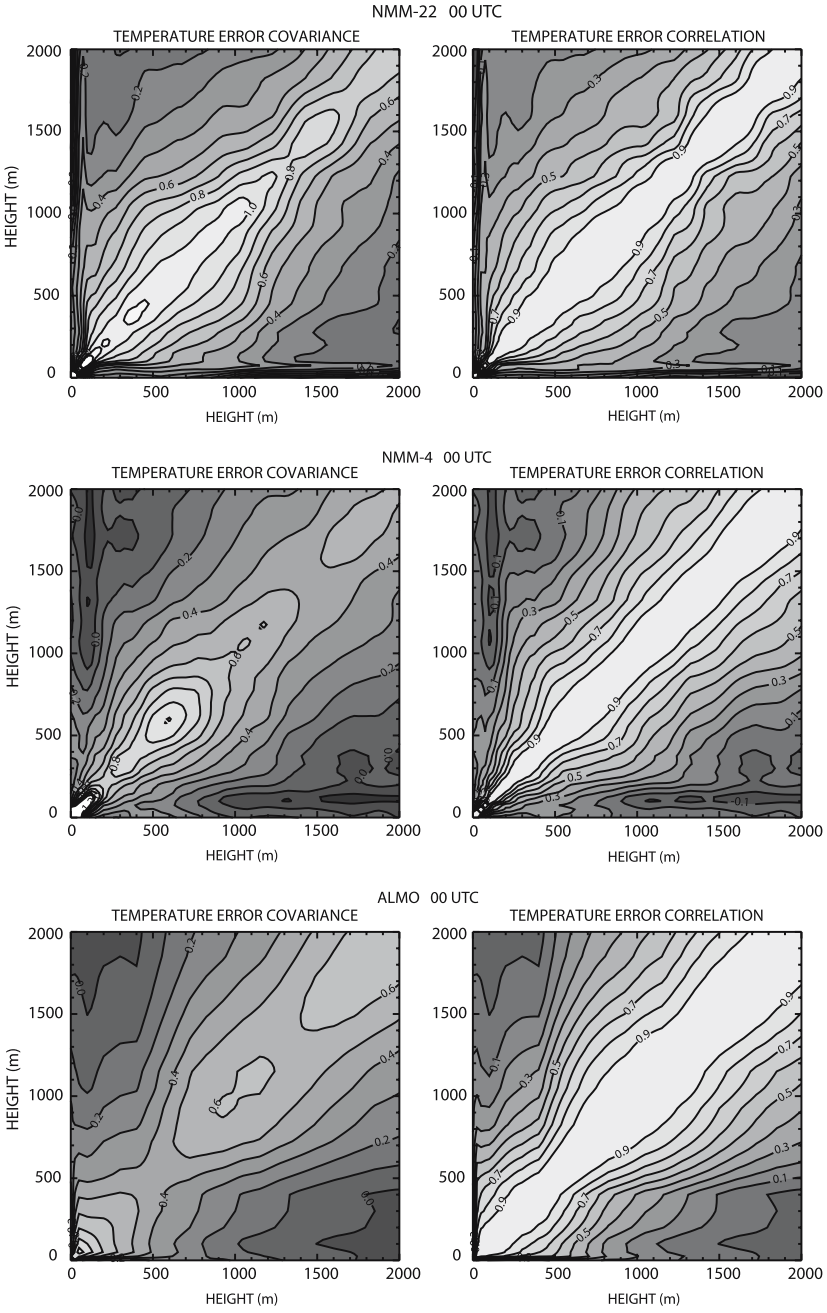

Figure 2
Temperature error covariance and error correlation matrices for the winter season 2004/2005 at 00 UTC for 3 different 3-D models.

and an unreliable forecast for that layer does not pose a problem for data assimilation. For the two resolutions of NMM, a second maximum can be found around 500 m above ground which is not present in the aLMo. The correlations between vertical layers generally increase from ground level to the region of maximum variance. In the aLMo the vertical layers are less independent of each other than in the NMM, which means that the spread and smoothing of information during the assimilation process is larger. Note that the structure of the error covariance is different throughout the day due to the diurnal evolution of the boundary layer, which was also analyzed by HACKER and SNYDER (2005).

Similar to the background error covariance matrix, **R** specifies errors of the observational system. The error is mainly caused by representativeness problems of the observation in model space and only secondly on instrumental characteristic. In contrast to **B**, correlations are assumed to be zero. Concerning the assimilation at Zürich airport, the most difficult part of **R** is assessing representativeness of radiosonde data recorded in Payerne. Because the latter is about 150 km away from Zürich, the lower part of the sounding is expected to be rather unrepresentative. To quantify the similarity between the two locations, model profiles from high resolution numerical weather prediction were analyzed. According to the amount of resolved topography, it is believed that the NMM model run at 2 km resolution is able to capture most spatial differences between Payerne and Zürich. Thus, for the time from October 2004 to March 2005, correlations for humidity as well as temperature, were computed for all vertical layers, respectively. The result is shown in Figure 3 for radiosonde ascent time of 1200 UTC.

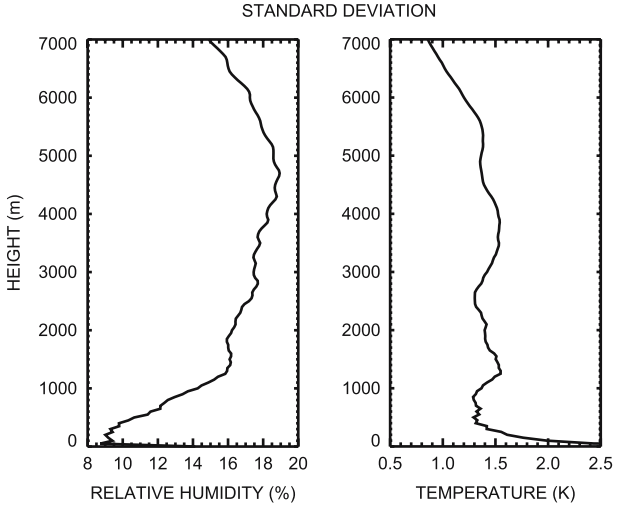

Figure 3
Standard deviations from the observational error covariance matrix **R** of the radiosonde in Payerne.

The virtual profile of temperature and humidity is problematic in that all observations are taken in close proximity to the ground instead of several hundred meters above ground, so that they are especially error-prone under calm conditions when they reflect more the local surface layer conditions than the free atmosphere. To quantify the errors of the virtual profile, mean and root-mean-squares deviations of the virtual profile from the MTP-5 profile at the corresponding height were computed at a temporal resolution of 10 minutes. MTP-5 data were linearly interpolated to the height above sea level where the station measurements took place. Considered are the statistics for each day of the MTP-5 observation period from 26 October, 2004 until 11 April, 2005. In Table 2 the RMS and mean deviations for the whole observation period are listed. Also indicated is the number of ground-based observations with negative or positive deviations from the MTP-5. As can be seen, the virtual profile deviates more as altitude increases. Also the number of cases where the stations measured lower temperatures than the MTP-5 increases with altitude, which shows the important role of radiative cooling of the surface. Thus the stations located at the surface can only provide an estimate of the thermodynamic state of the free atmosphere at that height, nonetheless there is still useful information which can be exploited by data assimilation.

Boundary Conditions

The specification of boundary conditions is used to extend the applicability of the 1-D model to more heterogeneous environments and different synoptic situations. Especially in complex terrain, advection plays an important role and is present even under synoptically calm situations in the form of cold air drainage flows. Advection of a as defined by (8) is specified as an external tendency. It is computed using centered finite differences (9) about the point of interest (i, j), which requires four additional vertical columns from the 3-D model.

$$\frac{\partial a}{\partial t} = -\vec{v}\,\vec{\nabla} a, \tag{8}$$

$$\frac{\Delta a_{i,j}}{\Delta t} = -u_{i,j}\,\frac{a_{i+1,j} - a_{i-1,j}}{2\Delta x} - v_{i,j}\,\frac{a_{i,j+1} - a_{i,j-1}}{2\Delta y}. \tag{9}$$

Another possibility in deriving advection is the use of a total tendency, rather than pure advection. Therefore, the total hourly change of humidity and temperature in the profile of the 3-D model is computed. Of course this change is not solely caused by advection but by all processes, like turbulent mixing, radiative cooling or phase changes. The dominating process depends on the actual situation, but the fog modeling system, which has to produce daily forecasts, needs to be evaluated and tested for all situations in order to be of operational use. This method is beneficial in that it requires only one column of 3-D model data at the point of interest and no neighboring columns. Furthermore temporal discretization errors in the case of

dominating advection are minimized since advection was computed internally by the 3-D model for every time step. Temporal discretization is a problem (DUNLOP and CLARK, 1997) when advection is computed using (9), since operational model output is available only on an hourly basis and not every time step.

Besides advection of temperature and humidity, radiation is another important boundary condition. It is significantly modified by clouds. Due to the limited vertical extent of the 1-D model, some clouds are above the model domain. However the effect of higher clouds can be included using the downward radiation computed by a 3-D model at the top boundary height of the 1-D model. If the radiation at a certain height is not available from the 3-D model, it can be quantified using a radiation model and predicted cloud cover for medium and high clouds. Note that the radiation model does not have to be extremely sophisticated and computationally expensive, since the cloud forecast from the 3-D model can only provide an estimate. In this study, the radiation was computed using predicted cloud cover of medium and high clouds and the radiation code of the PAFOG model.

The advection term, which represents the boundary conditions for the 1-D forecast, is difficult to determine and only a crude estimate of reality. It is thus reasonable to further increase the number of ensemble members with different temporal boundary conditions. This means that the same initial conditions in combination with different external forcings during the time integration are used. In the current implementation, the number of members is tripled. The same initial conditions are used in combination with no advection, the total tendency and the mesoscale advection. Currently, initial conditions and boundary conditions are taken from the same 3-D forecast run. It is however possible to further increase the number of ensemble members by mixing initial and boundary conditions derived from different 3-D runs.

Numerical 1-D Models

The ensemble system uses two numerical 1-D models for fog prediction, namely, COBEL-NOAH and PAFOG.

The COBEL model (Couche Brouillard Eau Liquide) was originally derived from the 1-D model of the nocturnal boundary layer, developed by the Laboratoire d'Aérologie of the Paul Sabatier University in Toulouse (ESTOURNEL, 1988). It has been used to predict fog events over the past years at Paris Charles de Gaulle airport (BERGOT *et al.*, 2005), a site in very flat topography. A detailed description of the model together with some case studies is given in BERGOT and GUÉDALIA (1994a,b). However major modifications were made to the model (MÜELLER, 2006). It was coupled to the NOAH land surface model (NOAH-LSM) using an explicit flux coupling. The NOAH-LSM has a long heritage and originated from MAHRT and PAN (1984), MAHRT and EK (1984) and PAN and MAHRT (1987). Since then several major improvements were made (CHEN *et al.*, 1997; EK *et al.*, 2003) and it is currently used in the NCEP realtime Land Data Assimilation System. In our version of

COBEL, which we call COBEL-NOAH, the LSM computes the energy balance of the canopy layer and the evolution of temperature and humidity in the soil. Furthermore a parameterization of precipitation by KESSLER (1969) which considers autoconversion, accretion, evaporation of rain and computations of mean fall speeds was implemented into COBEL-NOAH.

The other model used in the ensemble system is the 1-D model for PArameterized FOG (PAFOG) and was derived from the detailed spectral microphysical model MIFOG (BOTT *et al.*, 1990, 1989). PAFOG consists of four modules, namely the dynamic module, the microphysical module, the radiation code, and a module for low vegetation. The main difference to COBEL-NOAH is the considerably more detailed, but still parameterized, cloud microphysics module that allows to compute the total droplet number concentration. It is therefore possible to realistically compute droplet size-dependent sedimentation and supersaturation controlling condensation and evaporation. No major changes to the 1-D model PAFOG were done, so that an up-to-date description of the model can be found in BOTT and TRAUTMANN (2002) and references mentioned therein.

Post-processing

Post-processing finally aggregates the individual forecast members and computes probabilities of liquid water occurrence as well as mean values of predicted variables. Furthermore graphical output is generated for every individual member as well as for aggregated information. Figure 4 gives an example of an ensemble forecast for the fog event during the night of 14–15 October, 2005. As can be seen in the upper left panel, the cooling during the night is predicted rather well, but because the modeled fog disappears around 0800 UTC the temperature rises too fast in the morning. Note how the temperature forecasts from different members slowly diverge. The probability for a liquid water content above 0.01 g kg^{-1} is over 70% and indeed fog formed that night. The timing however was not perfect according to the visibility observations shown in the lower right panel.

4. Results

Method of Verification

The verification is carried out using fog events, which are defined based on threshold values for observed visibility and modeled liquid water content. In terms of observations, the aggregated visibility estimate derived from the different instruments installed around the runways is used. In that way an area is probed rather than a single point, which is more reliable. By definition the visibility has to be below 1000 m for fog, but in the verification other thresholds are also used to account for uncertainty in the observations and representativeness, since observed visibility at the

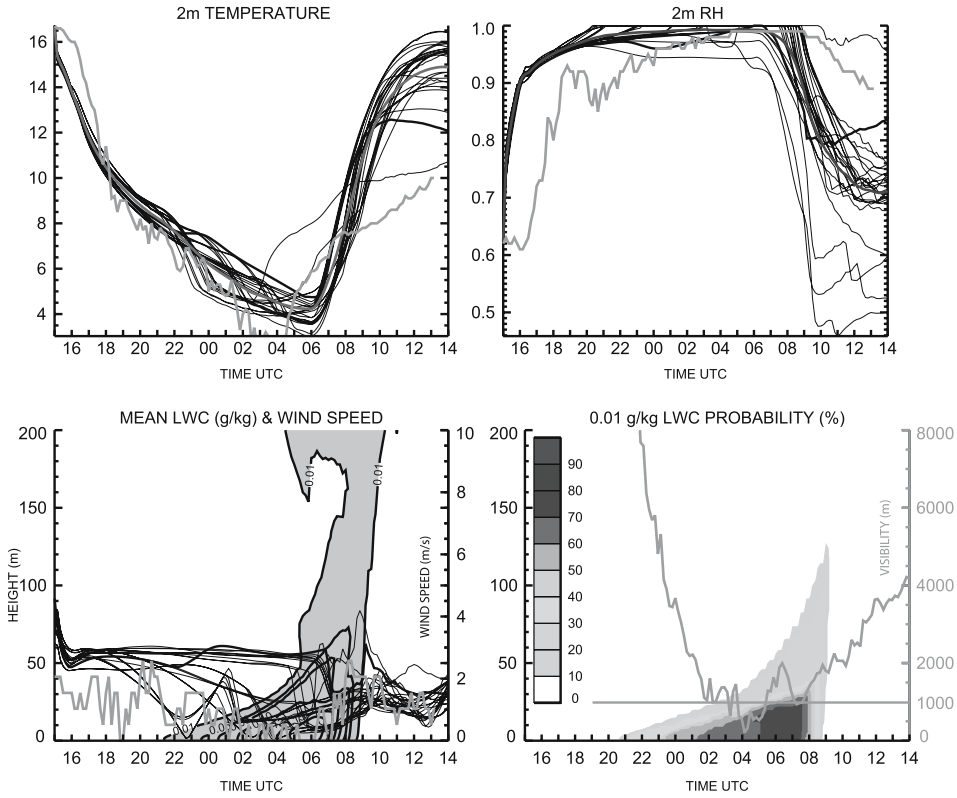

Figure 4
1-D ensemble prediction of the fog event from 14–15 October, 2005. The first two panels show computed temperature and humidity at 2 m height for each member (thin lines), the ensemble mean (white line) as well as the corresponding observations (thick gray line). In the lower left panel the ensemble mean liquid water content is contoured together with observed (thick gray line) and modeled wind speed. The last panel indicates the probability that a liquid water content of 0.01 g kg^{-1} is exceeded.

different runways of the airport often disagree due to the patchiness/inhomogeneity of fog as well as due to observational difficulties. From the model output, visibility and liquid water content can be analyzed. But visibility itself is not a prognostic variable and is derived using statistical relations that include liquid water content and eventually also the droplet number concentration. For the purpose of verification, a fog event is classified based on the presence of liquid water, rather than low visibility. This is because visibility might be wrongly derived from the prognostic variables and thus introduce another source of error. For fog the modeled liquid water content has to exceed 0.01 g kg^{-1}, which is a clear signal in the model output for the presence of liquid water. Note that higher thresholds also were used but resulted in worse verification scores.

For all results presented next, the verification period begins on 1 November, 2004 and ends on 30 April, 2005. Verification addresses the importance of advection and

uncertainties in the humidity assimilation, the impact of different initialization times as well as effects of the driving 3-D model. For every initialization time an ensemble consists of around 30 members, depending on the availability of output from semi-operational 3-D models, and over 50,000 runs were done in total, so that the statistical significance of this verification should be fulfilled. All verification is done on a temporally aggregated resolution of one hour in the time window from 03-11 UTC. This time window is of great importance for an airport and also the time of likely fog occurrence. Fog is classified as such, when the modeled liquid water content threshold is exceeded or the observed visibility lies below the threshold value for at least 10 min.

For the verification of probabilistic forecasts it is necessary to first transform the probability forecast into a set of binary yes/no forecasts using a whole sequence of probability threshold in the range 0 to 1. An event is forecast if the specified probability threshold is exceeded. The *relative operating characteristic* (ROC) is obtained by plotting the hit rate versus the false alarm rate for each possible decision probability threshold. The ROC distinguishes between the decision threshold and the intrinsic discrimination capacity of the forecast system. Low probability thresholds result in both, high hit rates but also high false alarm rates. These points of the ROC are located in the upper right corner of the ROC diagram. A forecast model with perfect discrimination has a ROC curve that rises from (0/0) along the hit rate axis, whereas the diagonal indicates no skill. A popular overall skill measure is the area under the ROC, typically denoted A_z, which would be unity for a perfect system and 0.5 for a no skill system. For values of A_z smaller than 0.5 the corresponding ROC curve lies below the diagonal, indicating the same level of discrimination ability as if it was symmetrically above the diagonal but wrongly calibrated in this case.

Importance of Advection

Advection might be insignificant in flat terrain, but will be important in a location such as Zürich airport. As there are some problems in estimating the amount of advection, two methods were proposed in section 3 and the results are indeed very different. Nevertheless we also want to look at what happens if advection is not considered at all. In Figure 5 ROC curves are given for different thresholds of observed visibility. It is evident that inclusion of advection significantly improves the forecast, if it is derived with (8), using gradients and wind. The other way of estimating advection as the total rate of change in the 3-D column did generally not improve the performance, which means that local processes in the column overshadow advection. Especially the relatively coarse vertical resolution of the 3-D model does not allow an accurate simulation of these local processes. However all possible inaccuracies are transferred into the 1-D model when the total rate of change is used to determine advection.

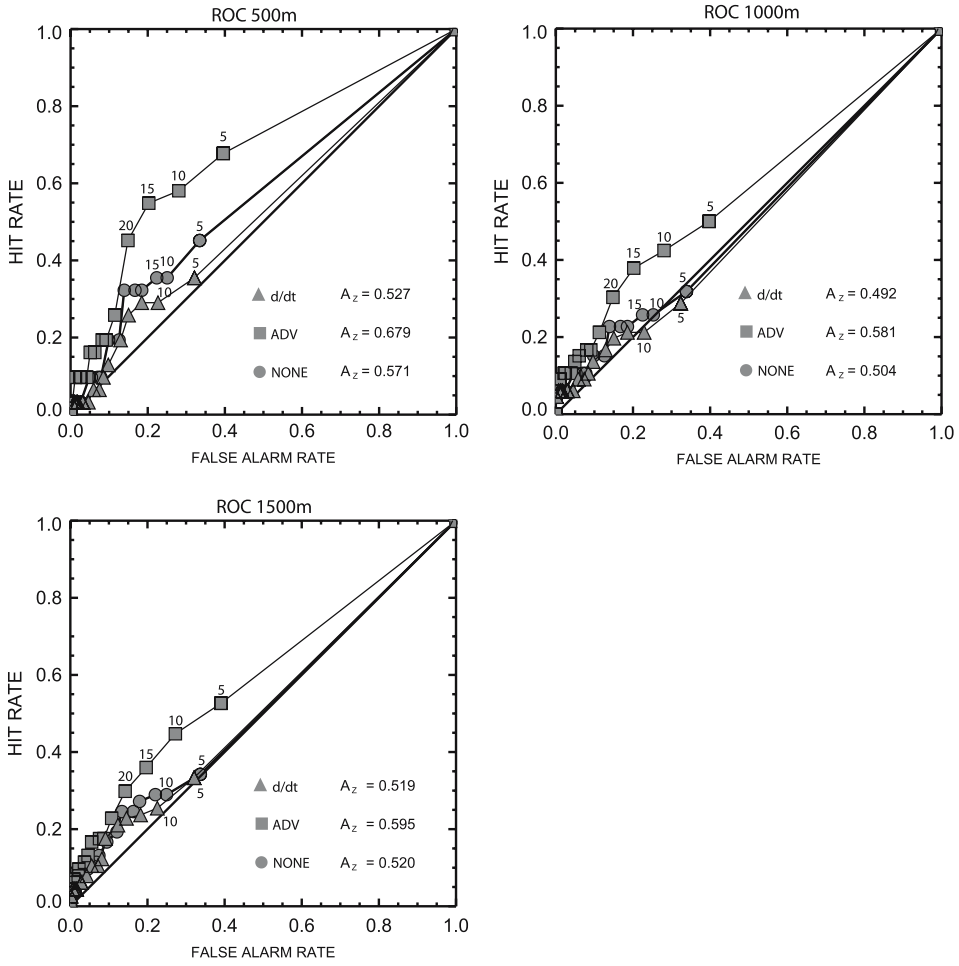

Figure 5
ROC for fog occurrence in the 1-D ensemble for different types of computed advection; ADV = pure advection, d/dt = total rate of change in profile, CONTROL = no advection. Visibilities below 500 m, 1000 m and 1500 m were used as observational thresholds of an observed fog event, respectively. Numbers above the symbols indicate the ensemble forecast probability in percent that has to be exceeded in order to be classified as a modeled fog event. A_z indicates the area under the ROC.

Different Initialization Times

After an initial spin-up time, the forecast skill of a model decreases with increasing forecast length. Thus the later we initialize, but not beyond the spin-up time, the better our forecast should be for a given time window. However, it has to be considered that for example radiosonde data are only available at 0000 and 1200 UTC and that the model also needs some spin-up. Furthermore if there is already liquid water present at

model start, it cannot be properly initialized due to the lack of liquid water content measurements.

In Figure 6 the ROC curves corresponding to different initialization times are shown. For the observations a visibility threshold of 1000 m is used and the advection is as outlined in the previous section. Obviously the 1500 UTC initialization has the highest skill. Starting at 1500 UTC, the model is able to spin-up and simulate the entire night with the cooling of the surface layer. Also the planetary boundary layer is generally well mixed, producing simple profiles of temperature and humidity. The latter allows for a more accurate initialization since the virtual profile is quite representative at that time. Radiosonde data after all do not seem to be very useful, primarily because they are available either too early (1200 UTC) or too late (0000 UTC). But again the importance of advection has to be pointed out, because basically at all times the members considering advection reach higher skill scores.

According to the ROC, a low forecast probability of about 15% has some skill. Even though the hit rate is only about 60% , the false alarm rate is significantly lower at 30%. This does not seem very convincing, but since low visibilities are very difficult to forecast in the daily operations, such a performance might potentially provide valuable hints for the synoptic forecaster about the most likely time of fog formation and dissipation.

Humidity Profile

Even though data assimilation gives a good estimate of the temperature profile, the thermodynamic state of the atmosphere is not accurately defined without a reasonable humidity profile. But the latter causes some trouble, because the assimilation simply does not have a reliable data source to work on. Therefore the effects on forecast quality related to the uncertainties in the humidity profile were examined by deriving the whole set of ensemble members again, but this time with 10% increased and decreased relative humidity profiles, respectively. This test does not intend to find the best humidity threshold but to detect a possible bias in the assimilation. By doing so each humidity class still has the same number of about 30 ensemble members. Note that the relative humidity was not allowed to exceeded 99%, to avoid an artificial creation of fog at the beginning. The result is summarized in Figure 7, where every panel represents a different visibility threshold used in the classification of observed fog events. If observed visibility has to be below 500 m to be considered as a fog event, there is not much difference between the control run and the two deviations, but as soon as the threshold, and thus also the number of events, is increased, a more humid profile yields better forecasts. This indicates that the assimilation is often too dry as can be seen by higher A_z for the increased humidity forecasts.

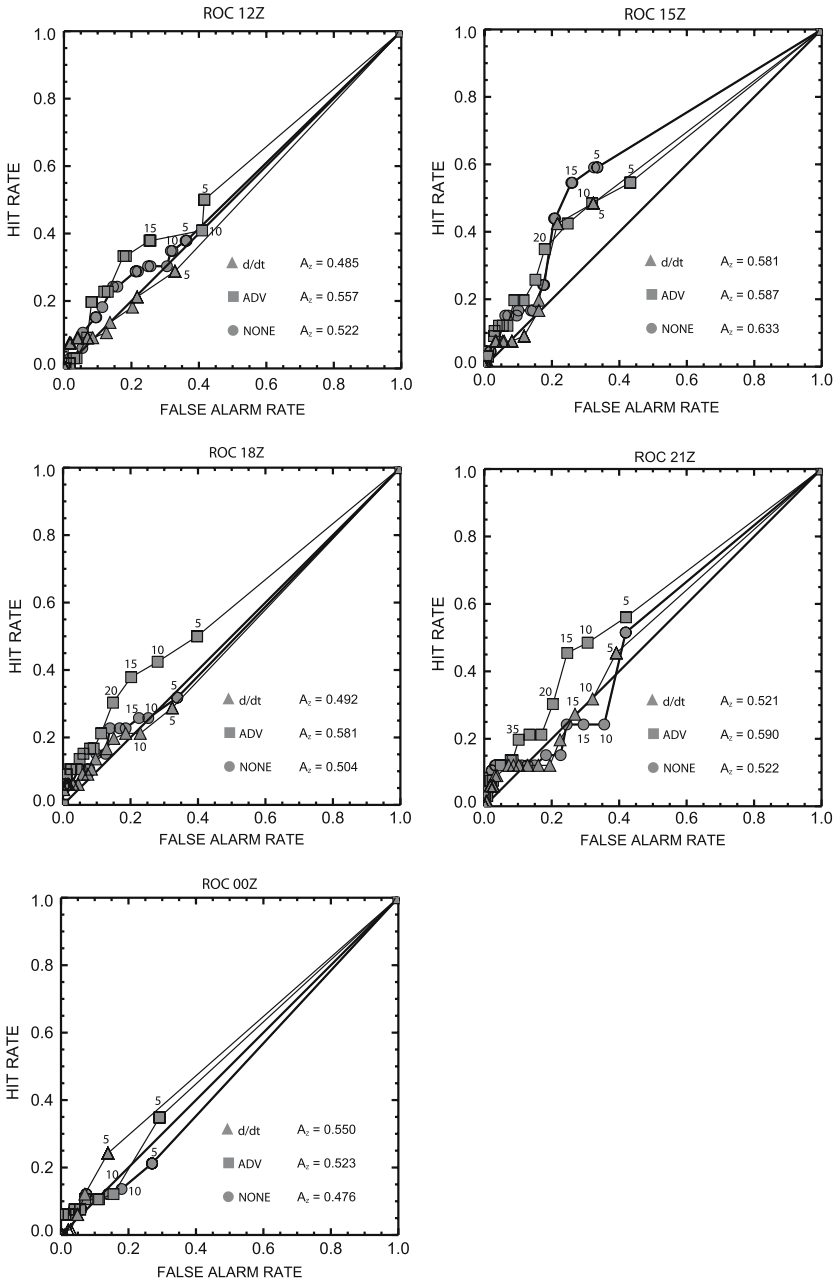

Figure 6

ROC for fog occurrence in the 1-D ensemble for different types of computed advection and initialization times. Numbers above the symbols indicate the ensemble forecast probability in percent that has to be exceeded in order to be classified as a modeled fog event. The observational visibility threshold for a fog event was 1000 m. A_z indicates the area under the ROC.

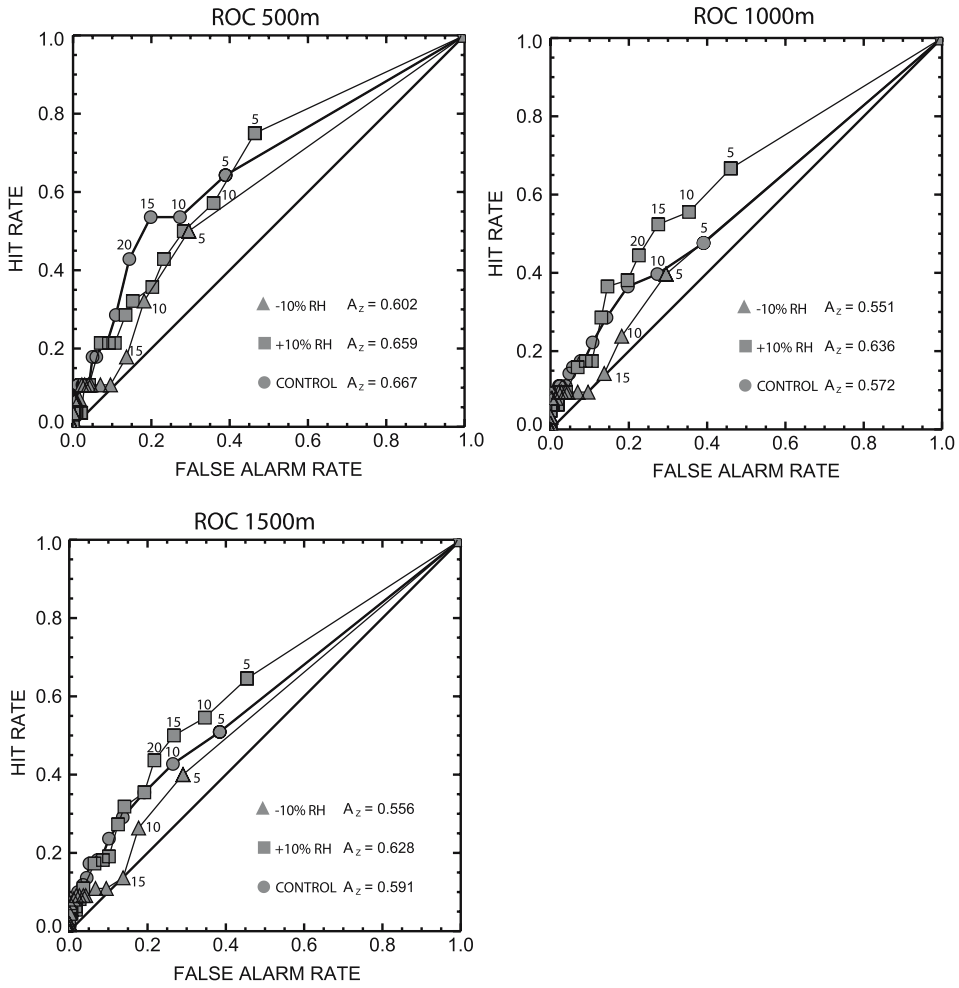

Figure 7
ROC for fog occurrence in the 1-D ensemble for initializations with different relative humidity profiles. Visibilities below 500 m, 1000 m and 1500 m were used as observational thresholds of an observed fog event, respectively. Numbers above the symbols indicate the ensemble forecast probability in percent that has to be exceeded in order to be classified as a modeled fog event. The observational visibility threshold for a fog event was 1000 m. A_z indicates the area under the ROC.

Verification of PAFOG and the Multi-model Ensemble

For maximum comparability PAFOG is verified the same way as COBEL-NOAH. The verification scores are shown in Figure 8 for different initialization times. For comparison purposes the ROC curves of COBEL-NOAH are also shown. Furthermore the ROC of the multi-model ensemble consisting of COBEL-NOAH and PAFOG was computed. From the COBEL-NOAH ensemble only the members

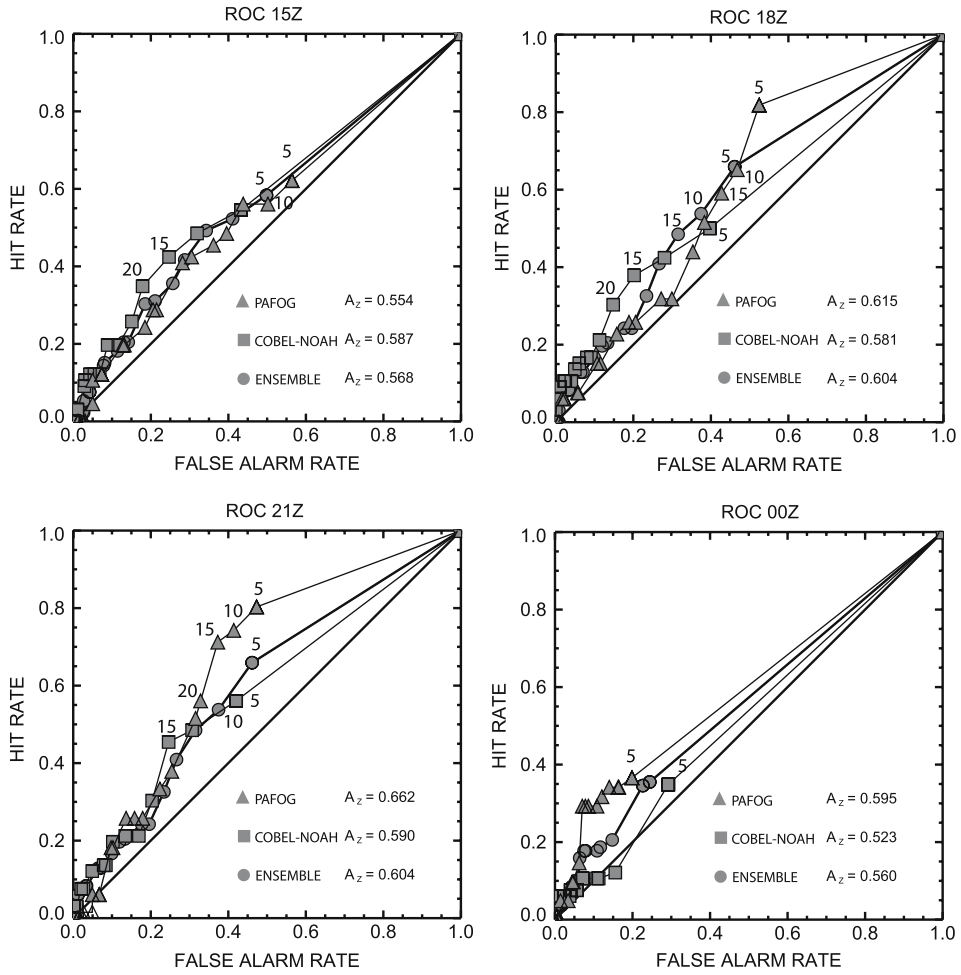

Figure 8
ROC for fog occurrence in the 1-D ensemble for PAFOG, COBEL-NOAH and the multi-model ensemble at different initialization times. A visibility of 1000 m was used as observational thresholds of an observed fog event. Numbers above the symbols indicate the ensemble forecast probability in percent that has to be exceeded in order to be classified as a modeled fog event. Verification was done on an hourly basis between 03-11 UTC from 1 November, 2004 until 30 April, 2005 at Zürich airport. A_z indicates the area under the ROC.

with advection (ADV) are considered, since they are the most skillful according to Figure 5. If we now look at the skill score A_z of PAFOG we notice that unlike COBEL-NOAH the skill increases with later initialization time. However for the 00 UTC initialization all models have less skill, because at that time fog has already formed in most cases. Note that an existing fog layer cannot be properly initialized due to the lack of observations. The ROC reveals that the low forecast probabilities

have the most skill and higher probabilities are not very useful for forecasting. Especially the 2100 UTC initialization has a remarkable discrimination between hit and false alarm rates when forecast probabilities between 5 and 15% are used.

Interestingly the multi-model ensemble is not that different from each individual model. In fact it is rarely better than any individual model and most of the time either COBEL-NOAH or PAFOG reach a higher level of discrimination. Therefore the ensemble system should not just provide the results from the multi-model ensemble but also the individual model ensembles. Especially because PAFOG outperforms COBEL-NOAH with later initialization time, a forecaster can give more weight to PAFOG for late model initializations.

5. Conclusions

The numerical simulation of fog is still a very difficult task. The reason is the need for an almost perfect prediction of boundary layer temperature, humidity and wind together with a detailed treatment of cloud microphysics. Small errors in temperature or humidity can have a dramatic effect if the air is close to saturation. Even though there are situations with better predictability, such as days with high relative humidity at the beginning of the night, clear sky and only weak wind, the exact onset and dissipation times are still difficult to obtain from numerical simulations.

Ensemble forecasting is very helpful to deal with the large quantity of uncertainties. In this study an ensemble member does not just have distinct initial conditions but also distinct boundary conditions to account for the uncertainty in advection tendencies. The variability within the ensemble members should reflect the current atmospheric uncertainty, which can be achieved by computing a separate assimilation for every member using different background estimates from different 3-D models but the same observations. To further increase the ensemble size, since the number of running operational 3-D models is limited, forecast runs valid at the same time but initialized at different times are also included. If such a series of succeeding 3-D forecasts has little variation for the initialization time of the fog model, the atmosphere is likely to be in a state of good predictability. Especially if this behavior is present in models from different operational centers.

With few observations available, variational assimilation must give considerable weight to the background derived from 3-D models. For the humidity assimilation, observational data are scarce and of poor quality, leaving considerable uncertainty in the assimilated profiles. Experiments showed that artificially increasing the humidity improves the fog forecast skill. Therefore a humidity ensemble might be helpful for operational purpose.

The same initial and boundary conditions were used by a simple (COBEL-NOAH) and by a detailed microphysics model (PAFOG). The forecast skill of the ensemble system was assessed separately for both ensembles. The COBEL-NOAH ensemble

initialized at 1800 UTC is able to increase the discrimination up to a hit rate of 60% with a false alarm rate of 30% if advection is considered or for the PAFOG ensemble, the 2100 UTC initialization achieves a hit rate of 80% with a false alarm rate of 45%. Overall the benefit of the detailed microphysics is not evident at the moment if the models are run for an entire season rather than well-defined case studies. It has to be noted that these forecasts are purely machine based. If the model results were interpreted by a human forecaster, better skills could be achieved.

The potential of a 1-D model in complex terrain is however limited by the effects resulting from spatial heterogeneity, namely advection of temperature, humidity and wind and the resulting accumulation of cold air in valleys and basins. Furthermore the radiation flux above the model domain has to be supplied to include the effects of higher clouds. If 1-D models are coupled to 3-D models it is possible to obtain estimates of these non-local effects which can be expressed as lateral and upper boundary conditions. As verification results indicate, advection should be derived using neighboring columns of the 3-D model, rather than the total change in a single column. A 1-D fog forecast is very sensitive to the forecast quality of the driving 3-D model but the benefits of the coupling are seen to be significant.

A 1-D model coupled to a 3-D model requires only a fraction of the computing power needed for a full 3-D fog simulation. Therefore it is possible to compute a probabilistic forecast for the next 18 h at a high temporal frequency, e.g., every hour on a simple workstation. Despite the large differences in computational time, preliminary results with the authors 3-D fog model, based on NMM and PAFOG, indicate that the coupled 1-D ensemble seems to be better than a full 3-D forecast in relatively simple terrain, whereas for complex terrain a single 3-D forecast can be better than the 1-D ensemble.

Acknowledgements

The authors want to express their gratitude to MeteoSwiss for providing observational data and aLMo predictions. The comments and suggestions made by anonymous reviewers lead to a significant improvement of the manuscript. This work was funded by the Swiss Federal Office for Education and Science (Grant C03.0024) and COST-722.

References

Ballard, S., Golding, B., and Smith, R. (1991), *Mesoscale model experimental forecasts of the Haar of northeast Scotland*, Mon. Wea. Rev. *191*, 2107–2123.

Bergot, T., Carrer, D., Noilhan, J., and Bougeault, P. (2005), *Improved site-specific numerical prediction of fog and low clouds*, Weather Forecast *20*, 627–646.

BERGOT, T. and GUÉDALIA, D. (1994a), *Numerical forecasting of radiation fog. part I: Numerical model and sensitivity tests*, Mon. Wea. Rev. *122*, 1218–1230.

BERGOT, T. and GUÉDALIA, D. (1994b), *Numerical forecasting of radiation fog. part II: A comparison of model simulations with several observed fog events*, Mon. Wea. Rev. *122*, 1231–1246.

BERNARDET, L. R., BOGENSCHUTZ, P., SNOOK, J., and LOUGHE, A. (2005), *WRF forecast over the southeast United States: Does a larger domain lead to better results?* In 'Preprints of the 6th WRF/15th MM5 users' workshop', *2.10*, National Center for Atmospheric Research, Boulder, Co.

BOTT, A., SIEVERS, U., and ZDUNKOWSKI, W. (1990), *A radiation fog model with a detailed treatment of the interaction between radiative transfer and fog microphysics*, J. Atmos. Sci. *47*, 2153–2166.

BOTT, A. and TRAUTMANN, T. (2002), *PAFOG - A new efficient forecast model of radiation fog and low-level stratiform clouds*, Atmos. Res. *64*, 191–203.

BOTT, A., TRAUTMANN, T., and ZDUNKOWSKI, W. (1989), *A numerical model of the cloud topped planetary boundary layer: Radiation, turbulence and spectral microphysics in a marine stratus*, Quart. J. Roy. Meteor. Soc. *122*, 635–667.

BOUTTIER, F. and COURTIER, P. (1999), *Data assimilation concepts and methods*, Technical report, European Center for Medium Range Weather Forecast ECMWF.

BROWN, R. (1980), *A numerical study of radiation fog with an explicit formulation of the microphysics*, Quart. J. Roy. Meteor. Soc. *106*, 781–802.

BROWN, R. and ROACH, W. T. (1976), *The physics of radiation fog. part II: A numerical study*, Quart. J. Roy. Meteor. Soc. *102*, 335–354.

CHEN, F., JANJIC, Z., and MITCHELL, K. (1997), *Impact of atmospheric surfacelayer parameterization in the new landsurface scheme of the NCEP mesoscale Eta model*, Boundary-Layer Meteor. *85*, 391–421.

DUNLOP, C. and CLARK, P. (1997), *Forcing the single column UM from the mesoscale model*, Technical Report 255, UK MetOffice.

DUYNKERKE, P. G. (1991), *Radiation fog: A comparison of model simulation with detailed observations*, Mon. Wea. Rev. *119*, 324–341.

EK, M. B., MITCHELL, K. E., LIN, Y., ROGERS, E., GRUNMANN, P., KOREN, V., GAYNO, G., and TARPLEY, J. D. (2003), *Implementation of NOAH land surface model advances in the National Centers for Environmental Prediction operational mesoscale Eta model*, J. Geophys. Res. *108*, doi:10.1029/2002JD003296.

ESTOURNEL, C. (1988), *Etude de la phase nocturne de la couche limite atmospherique*, These doctorat d'etat *1361*, Université Paul Sabatier, Toulouse, France.

EUROCONTROL (2006), *SESAR project site*, Internet: www.eurocontrol.int.

GOLDING, B. W. (1993), *A study of the influence of terrain on fog development*, Mon. Wea. Rev. *121*, 2529–2541.

GULTEPE, I. and MILBRANDT, J. A. (2007), *Microphysical observations and mesoscale model simulation of a warm fog case during FRAM project*, Pure Appl. Geophys. *164*, 6/7, this issue.

GULTEPE, I., MÜLLER, M. D., and BOYBEYI, Z. (2006), *A new visibility parameterization for warm-fog applications in numerical weather prediction models*, J. Appl. Meteor. Climat. *45*(11), 1469–1480.

HACKER, J. P. and SNYDER, C. (2005), *Ensemble kalman filter assimilation of fixed screen-height observations in a parameterized PBL*, Mon. Wea. Rev. *133*, 3260–3275.

IDE, K., COURTIER, P., GHIL, M., and LORENC, A. C. (1997), *Unified notation for data assimilation: Operational, sequential and variational*, J. Meteorol. Soc. Japan *75*(1B), 181–189.

JANJIC, Z. I. (2003), *A nonhydrostatic model based on a new approach*, Meteor. Atmos. Phys. *82*, 271–285.

JANJIC, Z. I., GERRITY, J. P., and NICKOVIC, S. (2001), *An alternative approach to nonhydrostatic modeling*, Mon. Wea. Rev. *129*, 1164–1178.

KADYGROV, E. N. and PICK, D. R. (1998), *The potential for temperature retrieval from an angular-scanning single channel microwave radiometer and some comparisons with in-situ observations*, Meteor. Appl. *5*, 393–404.

KALNAY, E., *Atmospheric Modeling, Data Assimilation and Predictability* (Cambridge University Press, Cambridge 2003).

KESSLER, E. (1969), *On the distribution and continuity of water substance in atmospheric circulations*, Meteor. Monog. *10*(32), 84.

LIN, Y., COLLE, B. A., and NOVAK, D. R. (2005), *Comparison of the real-time MM5 and WRF over northeastern United States*. In 'Preprints of the 6th WRF/15th MM5 users' workshop', 3.5, National Center for Atmospheric Research, Boulder, Co.

MAHRT, L. and EK, M. (1984), *The influence of atmospheric stability on potential evaporation*, J. Clim. Appl. Meteorol. *23*, 222–234.

MAHRT, L. and PAN, H.-L. (1984), *A two-layer model of soil hydrology*, Bound.-Layer Meteor. *29*, 1–20.

METATMG (2005), *Terms of References of the METATMG*, ICAO METG, Paris.

MÜLLER, M. D. (2006), *Numerical simulation of fog and radiation in complex terrain*, Ph.d. Thesis, stratus 12, University of Basel.

MUSSON-GENON, L. (1987), *Numerical simulations of a fog event with a one-dimensional boundary layer model*, Mon. Wea. Rev. *115*, 592–607.

PAN, H.-L. and MAHRT, L. (1987), *Interaction between soil hydrology and boundary-layer development*, Bound.-Layer Meteor. *38*, 185–202.

PARRISH, D. F. and DERBER, J. C. (1992), *The national meteorological center's spectral statistical-interpolation analysis system*, Mon. Wea. Rev. *120*, 1747–1763.

PRESS, W. H., FLANNERY, B. P., TEUKOLSKY, S. A., and VETTERLING, W. T., *Numerical Recipes in C: The Art of Scientific Computing* (Cambridge University Press, New York, 1998).

SCHMUTZ, C., SCHMUKI, D., and ROHLING, S. (2004), *Aeronautical climatological information Zürich LSZH*, Arbeitsbericht 201, MeteoSwiss.

SIEBERT, J., BOTT, A., and ZDUNKOWSKI, W. (1992a), *Influence of a vegetation-soil model on the simulation of radiation fog*, Beitr. Phys. Atmos. *65*, 93–106.

SIEBERT, J., BOTT, A., and ZDUNKOWSKI, W. (1992b), *A one-dimensional simulation of the interaction between land surface processes and the atmosphere*, Boundary - Layer Meteor. *59*, 1–34.

STEPPELER, J., DOMS, G., SCHÄTTLER, U., BITZER, H. W., DAMRATH, A. G., and GREGORIC, G. (2003), *Meso gamma scale forecasts by the nonhydrostatic models lm*, Meteor. Atmos. Phys. *82*, 75–96.

TURTON, J. D. and BROWN, R. (1987), *A comparison of a numerical model of radiation fog with detailed observations*, Quart. J. Roy. Meteor. Soc. *113*, 37–54.

VON GLASOW, R. and BOTT, A. (1999), *Interaction of radiation fog with tall vegetation*, Atmos. Environ. *33*, 1333–1346.

ZDUNKOWSKI, W. and BARR, A. (1972), *A radiative-conductive model for the prediction of radiation fog*, Bound.-Layer Meteor. *3*, 152–157.

ZDUNKOWSKI, W. and NIELSEN, B. (1969), *A preliminary prediction analysis of radiation fog*, Pure Appl. Geophys. *19*, 45–66.

(Received April 18, 2006, accepted October 25, 2006)
Published Online First: June 8, 2007

Pure appl. geophys. 164 (2007) 1265–1282
0033–4553/07/071265–18
DOI 10.1007/s00024-007-0218-3

Pure and Applied Geophysics

Quality Assessment of the Cobel-Isba Numerical Forecast System of Fog and Low Clouds

THIERRY BERGOT

Abstract—Short-term forecasting of fog is a difficult issue which can have a large societal impact. Fog appears in the surface boundary layer and is driven by the interactions between land surface and the lower layers of the atmosphere. These interactions are still not well parameterized in current operational NWP models, and a new methodology based on local observations, an adaptive assimilation scheme and a local numerical model is tested.The proposed numerical forecast method of foggy conditions has been run during three years at Paris-CdG international airport. This test over a long-time period allows an in-depth evaluation of the forecast quality.This study demonstrates that detailed 1-D models, including detailed physical parameterizations and high vertical resolution, can reasonably represent the major features of the life cycle of fog (onset, development and dissipation) up to +6 h. The error on the forecast onset and burn-off time is typically 1 h. The major weakness of the methodology is related to the evolution of low clouds (stratus lowering). Even if the occurrence of fog is well forecasted, the value of the horizontal visibility is only crudely forecasted. Improvements in the microphysical parameterization and in the translation algorithm converting NWP prognostic variables into a corresponding horizontal visibility seems necessary to accurately forecast the value of the visibility.

Key words: Numerical prediction, fog, short term forecast.

1. Introduction

Air-traffic safety and operational efficiency depend heavily upon accurate and timely forecasts of fog and low clouds. Adverse visibility conditions can strongly reduce the efficiency of terminal area traffic flow. For example, at Paris - Charles de Gaulle international airport (Paris-CdG), the landings and departures are reduced by a factor of 2 in foggy conditions (so called *Low Visibility Procedures* (LVP), defined by Air Traffic Control authorities (ATC) and corresponding to visibility < 600 m or ceiling < 200 ft -about 60 m). The occurrence of poor visibility conditions restricting the flow of air traffic in major airport terminals is one of the main causes of aircraft delays. Accurate anticipation of the onset and cessation of LVP conditions allows for air-traffic managers to effectively regulate traffic and to optimize the use of airport capacity.

GAME-CRNM (Météo-France, CNRS) Centre National de Recherches Météorologiques, 42, avenue G. Coriolis, F-31057, Toulouse cedex, France. E-mail: Thierry.Bergot@meteo.fr

Land surface and boundary layer processes play a fundamental role in the life cycle of a fog layer. These effects are still not well parameterized in current operational numerical weather prediction (NWP) models. Moreover, horizontal and vertical resolution of the current NWP models are larger than the corresponding characteristic fog scales (TARDIF, 2007). Consequently, fog and low clouds that are predominantly driven by local influences are poorly forecast by current NWP models. Single-column models are able to overcome these deficiencies, despite the poor estimate of horizontal heterogeneities. Several 1-D models have been used to study fog layers (e.g., MUSSON-GENON, 1986; DUYNKERKE, 1991; BERGOT and GUÉDALIA, 1994). Moreover, 1-D models are currently used in real time to forecast fog at the local scale (CLARK, 2002, 2006; TERRADELLAS and CANO, 2003; TERRADELLAS *et al.*, 2005; HERZEGH *et al.*, 2003). These feasibility studies have demonstrated the capabilities of local numerical models for short-term forecasting. Moreover, it is obvious that an important component for success is the capacity to initialize at their best, the local numerical model using specific observations and a local adaptive assimilation scheme (BERGOT *et al.*, 2005). The methodology tested in this article is based on Cobel-Isba numerical prediction system operationally used at Paris-CdG airport to forecast LVP conditions.

The objective of the work presented here is to evaluate the performance of the Cobel-Isba numerical prediction system used at Paris-CdG airport over a period of three years. This evaluation aims to better identify the strengths and weaknesses of the system, and facilitate an optimal use of Cobel-Isba forecast products. A brief description of the numerical method, including local assimilation and Cobel-Isba numerical model, is presented in section 2. The quality of the forecast of LVP conditions at Paris-CdG is detailed in section 3. Finally, recommendations and the limitation of this kind of local numerical modelling are outlined in section 4.

2. Numerical Forecast System

a. Cobel-Isba Numerical Model

The atmospheric model used in this study is the high resolution 1-D Cobel (Code de Brouillard à l'échelle locale) model. This column model was developed in collaboration between the Laboratoire d'Aérologie (Université Paul Sabatier/ C.N.R.S., France), Université du Québec a Montréal (U.Q.A.M., Canada) and Centre National de Recherches Météorologiques (GAME-CNRM/CNRS, France). A detailed description can be found in BERGOT (1993), BERGOT and GUÉDALIA (1994), and only a brief description will be given hereafter.

The model equations are classically derived from the Boussinesq hypothesis, under the assumption of horizontal homogeneity. However, spatial heterogeneities are treated as an external mesoscale forcing and are evaluated from the Météo-France operational NWP model Aladin (model grid box of about 10 km). These mesoscale

forcings (horizontal advection of temperature, horizontal advection of water vapor, vertical velocity, geostrophic wind and cloud cover), varying with time and height, are used to modify the thermodynamic evolution of the boundary layer.

The Cobel model equations are solved on a high resolution vertical grid: Near the surface, typical region for fog and very low clouds (i.e., below 200 m), numerical computations are made on 20 vertical levels (the first level is at 50 cm). The main characteristics of the physical package used in the Cobel model are described below. It includes a parameterization of boundary layer turbulent mixing, an explicit cloud scheme and parameterizations of longwave and shortwave radiation transfer.

The Cobel model is coupled with the multi-layer surface: vegetation-atmosphere transfer scheme, ISBA—Interactions Soil Biosphere Atmosphere—(NOILHAN and PLANTON, 1989; BOONE, 2000; BOONE *et al.*, 1999). The ISBA surface scheme describes the interactions between the land surface and the overlying atmosphere. In this study, seven soil layers are used to represent a soil column of 2 m in depth. The thickness of the first soil layer is 0.5 cm and the thickness is of 2.5 cm for the second soil layer.

1) Turbulence scheme

The turbulent exchanges inside the boundary layer are treated using a 1.5-order turbulence closure scheme. The turbulent fluxes are parameterized using a predictive equation for the turbulent kinetic energy (TKE) and the mixing length is a function of the stability of the atmosphere. For stable stratification, the mixing length is a function of the Richardson number, following ESTOURNEL and GUÉDALIA (1987). For unstable stratification, the mixing length follows BOUGEAULT and LACARRERE (1989).

2) Microphysics

The cloud liquid water content q_l is computed as a prognostic variable, and the size distribution of the droplets is not considered. The parameterization of the gravitational settling flux of cloud droplets is related to the liquid water content by way of a settling velocity, v_i (BROWN and ROACH, 1976). A constant value of $v_i = 1.6$ cm s^{-1}, derived from observations of fog droplet size distributions, is used in this study.

Following KUNKEL (1984), the visibility is deduced from the liquid water content

$$\text{visibility } (m) = \frac{3.9}{144.7(\rho q_l)^{0.88}}. \tag{1}$$

3) Radiation

The longwave radiation parameterization is a high resolution spectral scheme that computes the longwave radiation fluxes at every model level for 232 spectral intervals between 4 μm and 100 μm (VEHIL *et al.*, 1989). The radiative effect of the droplets is calculated inside the atmospheric window by relating linearly the longwave optical depth to the liquid water content.

The shortwave radiation is computed following the mono-spectral scheme of FOUQUART and BONNEL (1980). The effect of cloud droplets is parameterized by computing the shortwave optical thickness which is related to the liquid water content. The single scattering albedo of fog and low cloud is related to the optical thickness.

b. Assimilation Scheme

Accurate short-term forecasting of local conditions, including low ceiling and poor visibility, strongly depends on the accuracy of the initial conditions. Specific measurements have been obtained at Paris-CdG since December 2002 in order to improve the description of the surface boundary layer. These specific measurements can be summarized by

- a 30-m meteorological tower collecting observations of temperature and humidity at 1 m, 2 m, 5 m, 10 m and 30 m;
- the divergence of the radiation fluxes estimated following shortwave and longwave radiation fluxes measured at the ground level and at 45 m;
- soil temperature and soil moisture measured at −5 cm, −10 cm, −20 cm, −30 cm and −50 cm in depth.

The assimilation procedures associated with Cobel-Isba and used to construct the initial conditions are as follows:

- to estimate the atmospheric vertical profile of temperature and humidity in a 1-D-Var framework;
- if low clouds or fog are detected, adjustments of the atmospheric profiles are introduced to take into account the presence of clouds;
- to estimate the vertical profiles of temperature and water content within the soil.

A detailed description and validation of this local assimilation scheme can be found in BERGOT *et al.* (2005), and only a brief description will be given hereafter.

1) Assimilation of atmospheric profiles: 1-D-Var

The estimation of the initial profiles uses a variational assimilation approach. Observational errors are assumed to be uncorrelated. The error statistics are imposed arbitrarily but allow the initial profile to be very close to the observations near the surface, and to get closer to the 3-D NWP forecast above the boundary layer (see BERGOT *et al.*, 2005 for details).

2) Assimilation of fog and low clouds layer

The following procedure is used to modify the initial profile of temperature and humidity when fog or low clouds are detected. The main goal is to accurately represent the atmospheric boundary layer structure inside the fog layer.

It is now well known that mature fog is a well-mixed atmospheric layer as a consequence of the profile of radiative divergence. Consequently, the atmospheric profiles inside the fog or low cloud layer are adjusted following the hypothesis that total water content (liquid and vapor) is constant, that the temperature follows a moist adiabatic profile, and that the atmosphere is saturated. Above the fog or low cloud layer, the atmospheric profiles from the 1-D-Var system are not modified.

The fog depth is determined using an iterative method with the goal of minimizing the model error on radiation flux divergence. If the fog or low clouds layer is above the upper level of measurement (about 25% of studied cases), the vertical gradient between the two levels of radiative measurements is about zero, and the methodology previously presented will not be applicable. In this case, the fog depth is determined by minimizing the error on the shortwave radiation at the ground during the day or by minimizing the error on longwave radiation at the ground during the night.

3) Assimilation of soil profiles

The temperature and moisture profiles are linearly interpolated from *in situ* measurements.

3. Forecast Quality

The Cobel-Isba numerical prediction system has been run for three years, every 3 h at 00UTC, 03UTC, 06UTC, 09UTC, 12UTC, 15UTC, 18UTC and 21UTC (local time = UTC +1 during the winter season). The forecast has been performed up to +12 h. The occurrence of LVP conditions is defined every 30 minutes for both observations and forecasts. An observed or forecast LVP event was considered when the ceiling was less than 200 ft (about 60 m) or the visibility less than 600 m. The Cobel-Isba forecasts are matched against observations. Overall verification statistics are calculated based on binary LVP / no-LVP categories. The statistics produced are based on the hit ratio (HR) and false alarm rate (FAR). If a is the number of observed and forecast events, b the number of *not* observed and forecast events, and c the number of observed and *not* forecast events, these scores are determined by:

$$\mathrm{HR} = \frac{a}{a+c},$$

$$\mathrm{FAR} = \frac{b}{a+b}. \tag{2}$$

a. Verification Statistics

The frequency distribution histogram of LVP conditions along a diurnal time scale is plotted in Figure 1a for observations and in Figure 1b for all Cobel-Isba

forecasts (including all forecasted time and all runs). The relative distribution of LVP conditions is globally well forecasted by the Cobel-Isba model, with a maximum of occurrence at the end of the night and a minimum during the afternoon. However, some difference appears at the beginning of the night and at the end of the night. Between 03UTC and 06UTC, the Cobel-Isba model over-forecasts the occurrence of LVP conditions, with a maximum of 7.45% at 06UTC instead of 6.98% for observations. The sharp decrease of LVP conditions observed between 08UTC (7.45%) and 09UTC (5.43%) is slightly delayed for the Cobel-Isba forecasts between 09UTC (6.53%) and 10UTC (4.68%). At the beginning of the night, between 17UTC and 20UTC, the Cobel-Isba model under-forecasts the occurrence of LVP condi-

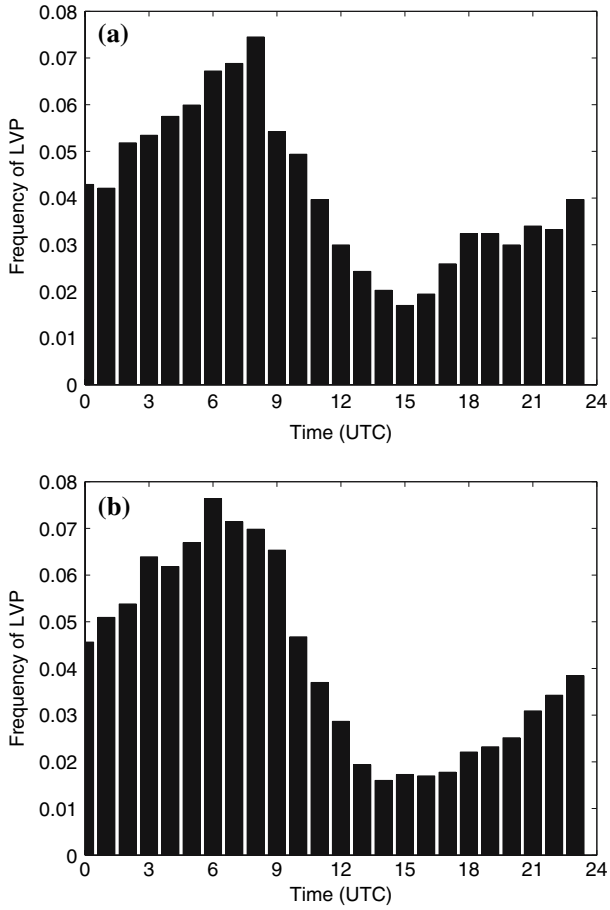

Figure 1
Frequency distribution histogram of the occurence of LVP conditions as a function of daytime for observation (a), Cobel-Isba forecasts (b).

tions. For example, at 18UTC, the observed occurrence is 3.21% and the forecasted occurrence is 2.21%.

Figure 2 shows the time evolution of the hit ratio (HR) and false alarm rate (FAR) for the Cobel-Isba forecasts up to +12 h. During the first 3 h of simulation the evolution is marked, FAR sharply increases and reaches 0.55 while HR decreases and reaches 0.60. HR is larger than FAR until +4 h forecast time. Afterwards, FAR increases very slowly to reach 0.67 for +12 h forecast while HR decreases to reach 0.32 for +12 h forecast. To examine the dependence of the forecast skill as a function of the initialization time, the statistics are presented for the various initialization times: Table 1 for +1 h forecast, Table 2 for +2 h forecast and Table 3 for +6 h forecast. The worst forecasts occur when the model is initialized during the daytime (typically 12UTC). During daytime, the local impact of observations in the surface boundary layer lasts only a few minutes since 3-D turbulence and mesoscale advections are expected to play a predominant role. However, the number of LVP events is small during this time period. The best results are obtained when the model is initialized at 03UTC, 06UTC and 21UTC. At the end of the night, an accurate initialization of fog and low clouds is crucial to forecast the evolution of the atmosphere close to the surface (e.g., BERGOT *et al.*, 2005). The score of the Cobel-Isba forecasts at sunrise demonstrates the quality of the initialization scheme including the specific observations. The decrease of the forecasts quality with forecast time is weaker for initialization times at the beginning of the night (typically 21UTC). For example, HR is typically 10% higher for simulations initialized at 21UTC and the FAR has the same behavior (Fig. 3). Consequently, predictions

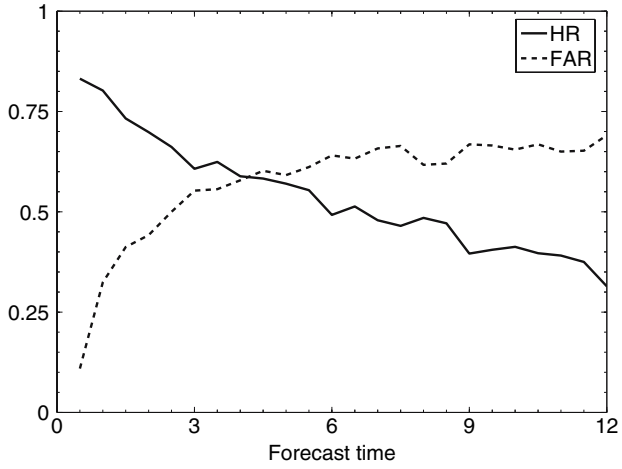

Figure 2
Cobel-Isba forecast of LVP conditions (all forecasts). Hit ratio (solid line) and false alarm rate (dashed line).

Table 1

Verification statistics of Cobel-Isba forecasts of LVP conditions for each initilization time at +1 h

	r00	r03	r06	r09	r12	r15	r18	r21	all
Good forecast	15	29	35	19	9	9	16	18	150
No detection	6	6	5	7	5	2	2	4	37
False alarm	19	9	12	10	3	5	5	9	72
HR	0.71	0.82	0.87	0.73	0.64	0.81	0.88	0.81	0.80
FAR	0.55	0.23	0.25	0.34	0.25	0.35	0.23	0.33	0.32

Table 2

Same as Table 1 at +3 h

	r00	r03	r06	r09	r12	r15	r18	r21	all
Good forecast	23	28	17	7	1	12	13	18	119
No detection	7	11	16	12	9	8	5	9	77
False alarm	29	27	27	14	7	9	16	18	147
HR	0.76	0.71	0.51	0.36	0.10	0.60	0.72	0.66	0.60
FAR	0.55	0.49	0.61	0.66	0.87	0.42	0.55	0.50	0.55

Table 3

Same as Table 1 at +6 h

	r00	r03	r06	r09	r12	r15	r18	r21	all
Good forecast	22	18	5	2	7	8	15	19	96
No detection	16	17	12	7	13	10	12	12	99
False alarm	27	28	17	9	4	14	28	34	171
HR	0.57	0.51	0.29	0.22	0.35	0.44	0.55	0.61	0.49
FAR	0.62	0.60	0.77	0.91	0.36	0.63	0.65	0.64	0.64

initialized at the beginning of the night could be successfully used to evaluate potential LVP occurrences during the night.

b. Accuracy on the Ceiling and Visibility Forecast

The LVP conditions are defined by ATC with two conditions: visibility less than 600 m or ceiling lower than 200 ft. Therefore, the quality of the Cobel-Isba forecast has also been evaluated for each of these individual conditions.

The frequency distribution histogram for observations and for the Cobel-Isba forecasts is plotted in Figure 4 for visibility lower than 600 m and in Figure 5 for ceiling lower than 200 ft. The distribution of the occurrence of visibility lower than 600 m is well forecasted by the Cobel-Isba model except for small differences between

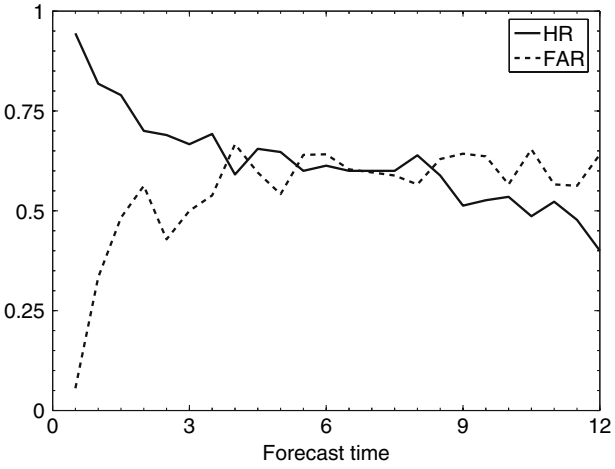

Figure 3
Same as Figure 2 for Cobel-Isba forecasts initialized at 21UTC.

08UTC and 10UTC. Cobel-Isba forecasts a slightly faster burn-off of fog at the beginning of the day (forecasted occurrence of 6.52% at 09UTC and 3.48% at 10UTC instead of observed occurrence of 5.65% at 09UTC and 3.77% at 10UTC). However, Figure 4 shows that the fog events are fairly well forecast by the Cobel-Isba model. The main differences between the Cobel-Isba forecast and observation appear more clearly on the low cloud cases (Fig. 5). The main weaknesses of the Cobel-Isba LVP forecasts previously shown in Figure 1 are observed again for low ceiling: over-forecast of low ceiling at the end of the night and under-forecast of low ceiling at the beginning of the night. This result indicates that the major weaknesses of the Cobel-Isba forecast are related to low clouds. This behavior has been previously determined by BERGOT *et al.* (2005) and seems to be a consequence of inaccurate mesoscale advections which are important to forecast low clouds (e.g., DRIEDONKS and DUYNKERKE, 1989).

NWP models, like Cobel-Isba, do not forecast horizontal visibility directly. Consequently, translation algorithms are required to compute visibility from prognostic variables. In Cobel-Isba, the visibility is deduced from the liquid water content alone following KUNKEL (1984). The observed visibility is compared to the forecasted visibility in Figure 6. The Cobel-Isba forecasts show a very rapid variation of the horizontal visibility, with visibility lower than 200 m for the majority of fog events. In contrast, the observed visibility is more scattered and the visibility occurences lower than 200 m are small. This result demonstrates a tendency for the model to forecast a too dense fog and this problem points out inaccuracies in the microphysical parameterization and the crude quality of the diagnosed visibility. Currently, only the occurrence of fog can be forecast accurately by Cobel-Isba, and

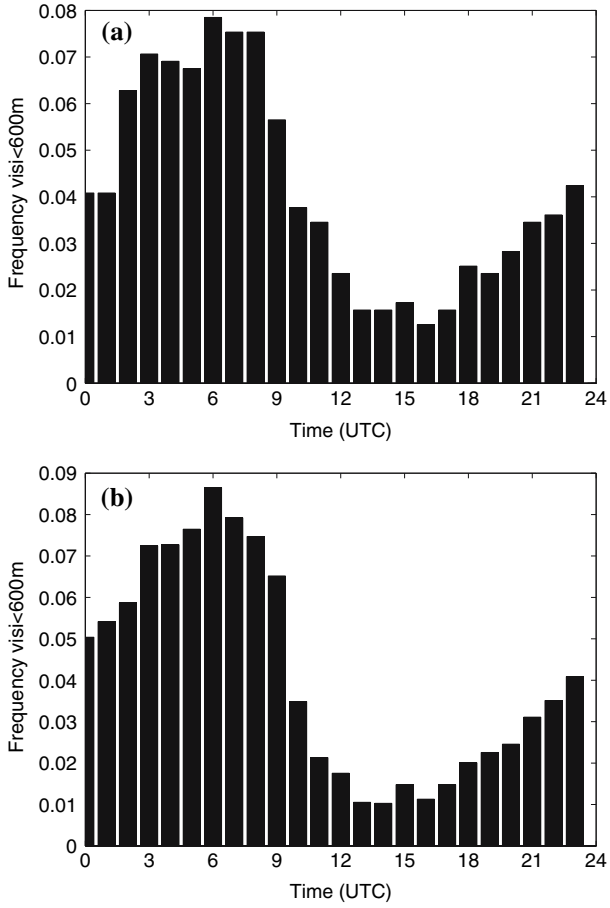

Figure 4
Frequency distribution histogram of visibility lower than 600 m as a function of daytime for observation (a), and Cobel-Isba forecasts (b).

not the value of the horizontal visibility inside the fog layer. An improved microphysical scheme and an improved translation algorithm seems to be required for accurately forecasting horizontal visibility. The histograms of low cloud ceiling plotted in Figure 7 show that the frequency of very low clouds (ceiling lower than 100 m) is quite well forecast. However, the presence of a ceiling lower than 500 m is overestimated. The rapid temporal variation of low clouds seems also not well forecast.

c. Accuracy of the Prediction of Onset and Burn-off Time

The anticipation of the beginning and end of LVP conditions is strategic for Air Traffic Control. Forecasting the beginning and the end time of LVP conditions is

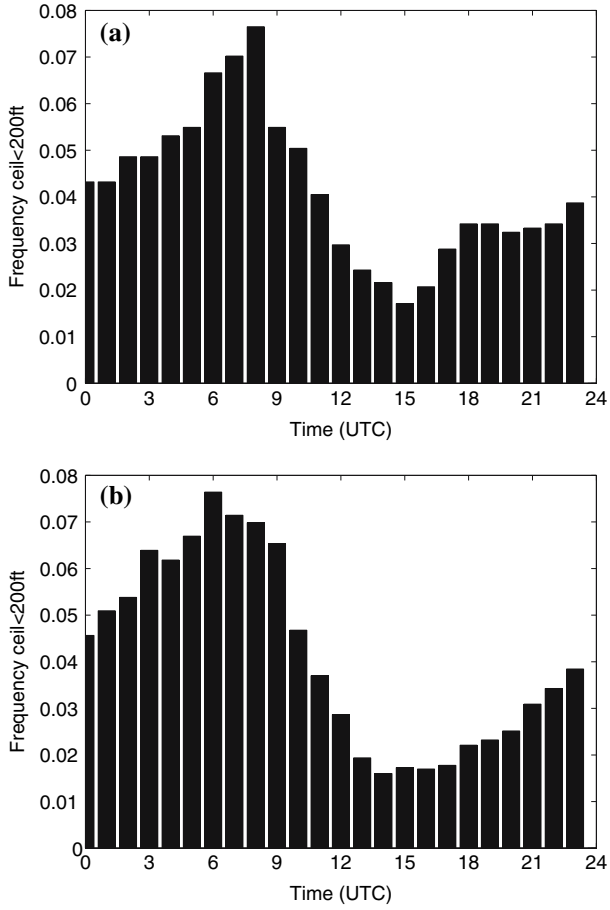

Figure 5
Same as Figure 4 for ceiling lower than 200 ft.

therefore identified as a priority. The error of forecast onset time is plotted in Figure 8, for forecast time up to +12 h. The error of onset time is unbiased, and the mean absolute error is about 1 h. The distribution of the onset error is relatively sharp: 55% of onset error time is less than 30 minutes and 63% is less than 1 hour. The error of the forecast end of LVP conditions is plotted in Figure 9. The error of burn-off time follows a bi-modal distribution, with two maxima at +1 h and −1 h error. The distribution is weakly biased (too late forecast of the end of LVP conditions of about 20 minutes), with a mean absolute error of about 1 hour 20 minutes. 27% of burn-off time error is less than 30 minutes, and 63% is less than 1 hour. The specific reason for this bi-modal distribution is unknown at this time, and unfortunately a more in-depth investigation is beyond the scope of this work.

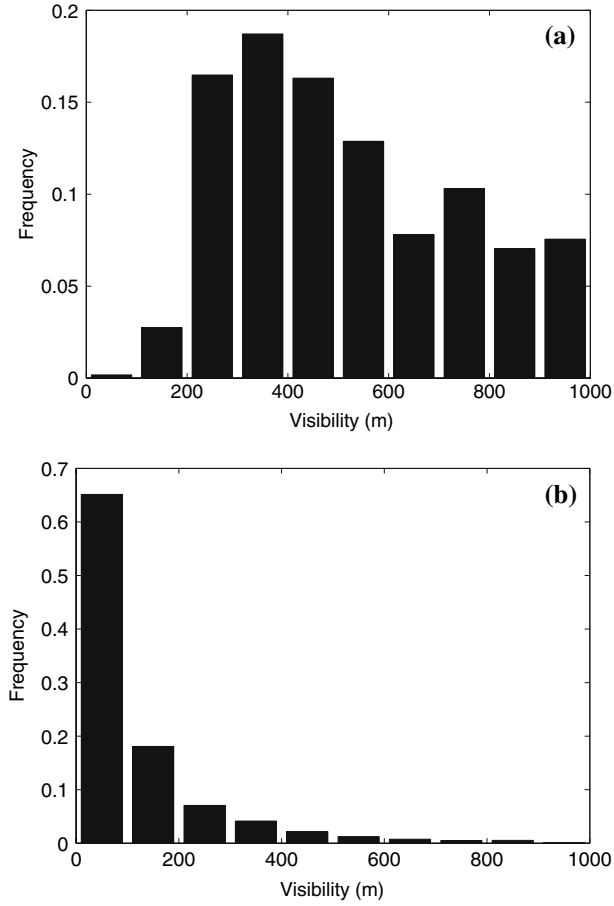

Figure 6
Frequency distribution histogram of the observed visibility (a), and forecast visibility (b).

The influence of aerosols (indirect effects and semi-direct radiative effects) on the burn-off time is suspected. The comparison between observations and the Cobel-Isba forecasts shows that the model has some skill in predicting LVP conditions for both onset and dissipation, with a typical error of 1 hour.

d. Influence of Meteorological Parameters

A systematic identification of the conditions that lead to forecast errors (no detection or false alarm) could be helpful for the operational use of the numerical LVP forecast at terminal airports. However, given the number of events, it is difficult to study each event and to draw conclusions. In order to simplify the identification of the errors, the number of well-forecast LVP events, the number of no detection and

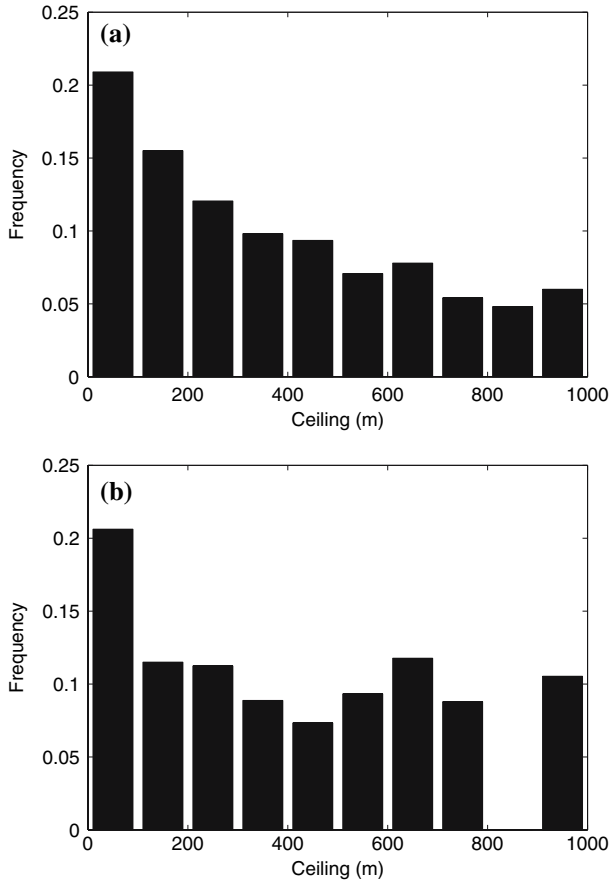

Figure 7
Same as Figure 6 for ceiling.

the number of false alarms have been classified as a function of the wind intensity, the wind direction and the surface pressure.

The Cobel-Isba forecasts of LVP conditions are more accurate for winds lower than 3 ms^{-1} (Fig. 10). An increase in the number of both no detection and false alarm is observed for wind between 3 ms^{-1} and 6 ms^{-1}. The lower winds mainly correspond to events dominated by local mechanisms, while mesoscale advections are more important for stronger winds. Consequently, the use of 1-D models is more fruitful in meteorological conditions with weak wind.

The dependence of the LVP forecast as a function of the wind direction is plotted in Figure 11. The forecasts are best for southeasterly wind, which mainly correspond to anticyclonic conditions. The false alarms are numerous for wind directions

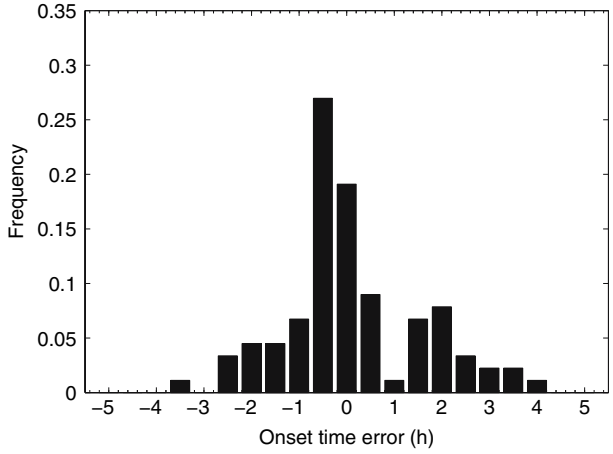

Figure 8
Frequency distribution histogram of the error on onset time (the LVP conditions at initial time are not taken into account). Positive values correspond to forecast of LVP onset that is too early.

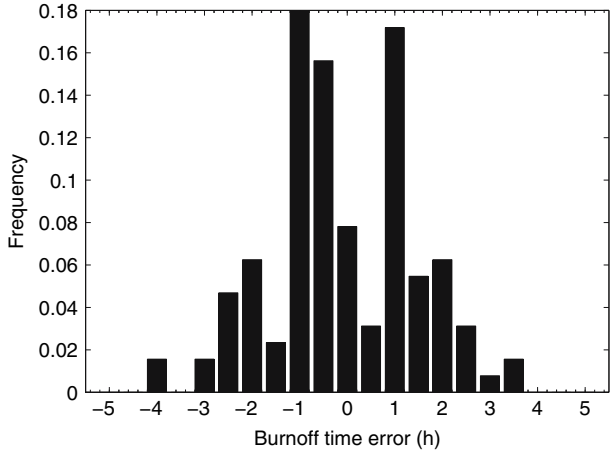

Figure 9
Frequency distribution histogram of the error on the end of LVP conditions. Positive values correspond to forecast of LVP burnoff that is too early.

between northwest and southwest. These directions mainly correspond to pre- or post-frontal conditions. In these meteorological situations, the mesoscale advections seem to prevent the occurrence of LVP conditions, and this effect seems poorly forecast by the Cobel-Isba model.

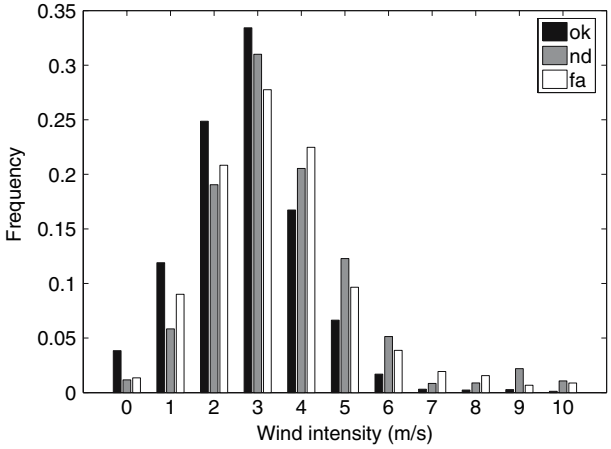

Figure 10
Frequency distribution histogram as a function of the wind intensity: Well forecast LVP events in black, no detection in gray and false alarm in white.

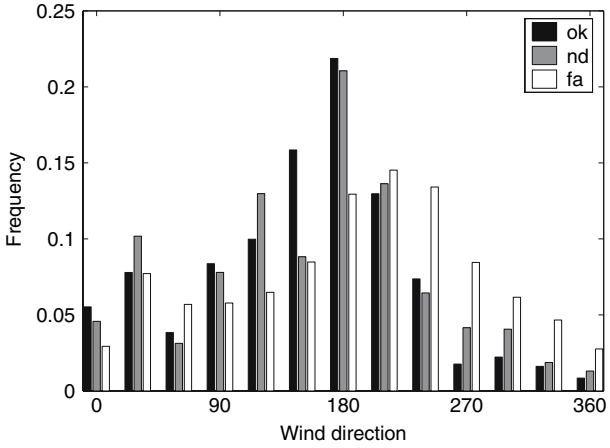

Figure 11
Same as Figure 10 for the wind direction.

The quality of the LVP forecast as a function of surface pressure is plotted in Figure 12. This figure confirms that LVP conditions in an anticyclonic situation are quite well forecast. conversely, when the surface pressure is lower than 1000 hPa, the number of errors (both no detection and false alarm) is relatively higher.

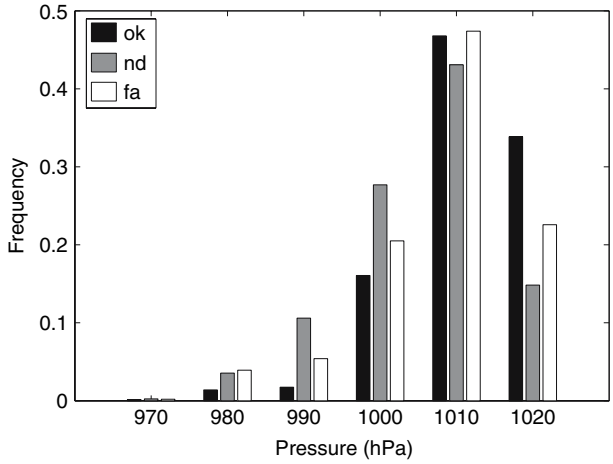

Figure 12
Same as Figure 10 for the surface pressure.

4. Conclusions

A local numerical method has been applied during three years to forecast fog and low clouds at Paris-CdG international airport. This numerical forecasting method is based on dedicated observations within the surface boundary layer, an adaptive assimilation scheme and the Cobel-Isba numerical model. This work provides a review of the performance of the Cobel-Isba numerical prediction system.

This study shows that the Cobel-Isba forecast of fog and low clouds is useful up to +6 h. During this forecast time, the false alarm rate is lower than the detection rate. The best results are obtained for 03UTC, 06UTC and 21UTC initialization times. The good results at the end of the night demonstrate the quality of the adaptive assimilation scheme associated with Cobel-Isba. The good quality of forecasts initialized at the beginning of the night demonstrates the quality of the Cobel-Isba numerical model to simulate the evolution of the nocturnal boundary layer. The major forecast weakness concerns the evolution of low clouds (stratus lowering). This result is confirmed by the study of the meteorological condition associated with errors. It seems that the low clouds are mainly driven by mesoscale flows and that the influence of the local conditions is weak. Therefore, it seems very difficult to accurately forecast the life cycle of low clouds with 1-D models.

This study has also evaluated the accuracy of the forecasts of the onset and end of fog events. For 63% of cases, the forecast errors on the onset or end of fog events are less than 1 h. This fact is very important because accurate anticipation of onset and cessation of foggy conditions provides the opportunity for Air Traffic Control to better regulate air traffic. Even if the occurrence of fog is well forecasted, the results

are not as encouraging for the forecast of the visibility in fog layers. This study reveals that the forecast visibility has a bias toward lower visibility than observed in fog. One way to improve the forecast of visibility would be to tune the translation algorithm and to improve the microphysics parameterization scheme.

These results are however very encouraging and show the usefulness of a forecast method based on a detailed local numerical model to forecast meteorological conditions at terminal airports. Given these encouraging results, the Cobel-Isba numerical forecast system is now integrated in the operational forecast system at Paris-CdG to provide a decision guidance tool.

The identification and understanding of the Cobel-Isba errors behavior open up the opportunity to reduce the impact of these errors on air traffic control. This could be accomplished through a systematic identification of the conditions that lead to these errors and then to indicate a weak predictability of these cases to end users. This work provides a basis for an optimal exploitation of the local numerical prediction system. Another way to estimate the predictability is to build an ensemble local prediction system. This research is described in ROQUELAURE and BERGOT (2007).

Acknowledgments

I would like to address many posthumous thanks to Peter Zwack for all the work performed on the Cobel model during numerous years, for his friendly help and for numerous discussions on the applications of the Cobel model. Many thanks to Robert Tardif for useful dicussions and for his comments on an early version of this manuscript.

REFERENCES

BERGOT, T. (1993), *Modélisation du brouillard à l'aide d'un mod Fle 1D forcé par des champs mésoéchelle: Application à la prévision,* Ph.D. Thesis, Université Paul Sabatier, Toulouse, France, *1546*, 192 pp.

BERGOT, T. and GUÉDALIA D. (1994), *Numerical forecasting of radiation fog. Part I : Numerical model and sensitivity tests*, Mon. Wea. Rev. *122*, 1218–1230.

BERGOT, T., CARRER, D., NOILHAN, J., and BOUGEAULT, P. (2005), *Improved site-specific numerical predictin of fog and low clouds: A feasibility study*, Weather and Forecasting *20*, 627–646.

BOONE, A.A., Calvet, J.C., and Noilhan J. (1999) *The inclusion of a third soil layer in a land surface scheme using the force-restore method.* J. Appl. Meteor., *38*, 1611–1630.

BOONE, A.A. (2000), *Modélisation des processus hydrologiques dans le schéma de surface ISBA: Inclusion d'un réservoir hydrologique, du gel et modélisation de la neige,* Ph.D. Thesis, Université Paul Sabatier, Toulouse, France, 252 pp.

BOUGEAULT, P. and LACARRERE, P. (1989), *Parameterization of orography-induced turbulence in a meso-scale model,* Mon. Wea. Rev. *117*, 1872–1890.

BROWN, R. and ROACH, W.T. (1976), *The physics of radiation fog. Part II: A numerical study,* Quart. J. Roy. Meteorol. Soc. *102*, 335–354.

CLARK, D.A. (2002), *The 2001 demonstration of automated cloud forecast guidance products for San-Francisco international airport,* Proc. 10th Conf. on Aviation, Range, and Aerospace Meteorology, AMS.

CLARK, D.A. (2006), *Terminal ceiling and visibility product development for northeast airports*, Proc. 14th Conf. on Aviation, Range, and Aerospace Meteorology, AMS.

DRIEDONKS, A.G.M. and DUYNKERKE, P.G. (1989), *Current problem in the strato-cumulus topped atmospheric boundary layer*, Bound. Layer Meteor. *46*, 275–303.

DUYNKERKE, P.G. (1991), *Radiation fog: A comparison of model simulation with detailed observations*, Mon. Wea. Rev. *119*, 324–341.

ESTOURNEL, C. and GUEDALIA, D. (1987), *A new parameterization of eddy diffusivities for nocturnal boundary layer modeling*, Bound. Layer. Meteor. *39*, 191–203.

FOUQUART Y. and BONNEL, B. (1980), *Computations of solar heating of the Earth's atmosphere: A new parameterization*, Beitr. Phys. Atmosph. *53*, 35–62.

GULTEPE, I. (2005), *A new warm fog microphysical parameterization developed using aircraft observations*, Proc. COST722 Workshop on "short-range Forecasting Methods of Fog, Visibility and Low Clouds," ESF, 46–57.

HERZEGH, P.H., BENJAMIN, S.G., RASMUSSEN, R., TSUI, T., WIENER, G., and ZWACK, P. (2003), *Development of automated analysis and forecast products for adverse ceiling and visibility conditions,* Proc. 19th Internat Conf. on Interactive Information and Processing Systems for Meteorology, Oceanography and Hydrology, AMS, 8–13 Feb., Long-Beach, California, U.S.A.

KUNKEL, B. (1984), *Parametrization of droplet terminal velocity and extinction coefficient in fog model*, J. Appl. Meteor. *23*, 34–41.

MUSSON-GENON, L. (1986), *Numerical simulation of a fog event with a one-dimensional boundary layer model*, Mon. Wea. Rev. *115*, 592–607.

NOILHAN J. and PLANTON, S. (1989), *A simple parameterization of land surface processes for meteorological models*, Mon. Wea. Rev. *117*, 536–549.

ROQUELAURE, S. and BERGOT, T. (2007), *Seasonal sensitivity on COBEL-ISBA local forecast system for fog and low clouds*, Pure. Appl. Geophys. *164*, 6/7, (this issue).

TARDIF, R. (2007), *The impact of vertical resolution in explicit numerical forecasting of radiation fog: A case study*, Pure Appl. Geophys. *164*, 6/7, (this issue).

TERRADELLAS, E. and Cano, D. (2003), *Implementation of a one-dimensional model for local forecasts at Madrid airport,* Proc. EGS-AGU-EGU Joint Assembly, ESF.

TERRADELLAS, E. and GLOWACKA, A., CANO, D. (2005), *The use of measured temperatures in the initialisation of 1-D model developed for fog forecast,* Proc. COST722 workshop on "Short-range Forecasting Methods of Fog, Visibility and Low Clouds," ESF, 58–62.

VEHIL, R., MONNERIS, J., GUEDALIA, D. and SARTHOU P. (1989), *Study of radiative effects (longwave and shortwave) whithin a fog layer,* Atmos. Res. *23*, 179–194.

(Received March 23, 2006, accepted August 5, 2006)
Published Online First: June 8, 2007

Pure appl. geophys. 164 (2007) 1283–1301
0033–4553/07/071283–19
DOI 10.1007/s00024-007-0219-2

Pure and Applied Geophysics

Seasonal Sensitivity on COBEL-ISBA Local Forecast System for Fog and Low Clouds

STEVIE ROQUELAURE and THIERRY BERGOT

Abstract—Skillful low visibility forecasts are essential for air-traffic managers to effectively regulate traffic and to optimize air-traffic control at international airports. For this purpose, the COBEL-ISBA local numerical forecast system has been implemented at Paris CDG international airport. This local approach is robust owing to the assimilation of detailed local observations. However, even with dedicated observations and initialization, uncertainties remain in both initial conditions and mesoscale forcings. The goal of the research presented here is to address the sensitivity of COBEL-ISBA forecast to initial conditions and mesoscale forcings during the winter season 2002–2003. The main sources of uncertainty of COBEL-ISBA input parameters have been estimated and the evaluation of parameter uncertainty on the forecasts has been studied. A budget strategy is applied during the winter season to quantify COBEL-ISBA sensitivity. This study is the first step toward building a local ensemble prediction system based on COBEL-ISBA. The conclusions of this work point out the potential for COBEL-ISBA ensemble forecasting and quantify sources of uncertainty that lead to dispersion.

Key words: Local numerical forecast system, fog and low clouds, seasonal sensitivity, initial conditions and mesoscale forcings uncertainties, forecast dispersion, local ensemble prediction system.

1. Introduction

Accurate prediction of fog and low clouds is one of the main issues related to improving air-traffic management and safety. At Paris Charles de Gaulle (CdG) international airport, adverse ceiling and visibility conditions (visibility under 600 m and ceiling below 60 m) lead to the application of Low Visibility Procedures (LVP). Under these conditions, the airport take-off/landing efficiency is reduced by a factor of 2, causing aircraft delays. In this context, accurate short-term forecasts of LVP conditions are considered to be a priority by airport authorities.

Unfortunately, current operational Numerical Weather Prediction (NWP) models are not able to provide detailed information due to their lack of both vertical and horizontal resolutions with respect to the typical length scale of fog. However, owing to higher vertical resolution and more detailed physics than 3D

Météo-France, Centre National de Recherches Météorologiques, CNRM/GMME, 42 Av Coriolis, F-31057 Toulouse Cedex, France. E-mail: stevie.roquelaure@cnrm.meteo.fr

NWPs, one-dimensional modeling is an attractive alternative (e.g., MUSSON-GENON, 1986; DUYNKERKE, 1991; BERGOT and GUÉDALIA, 1994). This 1-D approach to forecast the fog and low cloud life cycle is currently used operationally at San Francisco airport (CLARK, 2002) and at CdG airport (BERGOT *et al*., 2005). The same kind of strategy is tested in the northeast corridor within the framework of the US Federal Aviation Administration ceiling and visibility project (HERZEGH *et al*., 2002).

The numerical prediction method used at CdG (see BERGOT, *this issue* for more details) includes:

- Specific observations from a 30 m meteorological tower (atmospheric temperature and humidity, shortwave and longwave radiation fluxes) and soil measurements;
- the mesoscale forcings (mesoscale advection, geostrophic wind and cloud cover) are evaluated from the Météo-France operational NWP model Aladin (see http://www.cnrm.meteo.fr/aladin/);
- a local assimilation scheme is used to construct initial conditions, based on a 1-D-var assimilation scheme together with a fog and low cloud specific initialization;
- the 1-D high resolution COBEL-COde de Brouillard à l'Echelle Locale (Local scale fog code) atmospheric model (BERGOT, 1993; BERGOT and GUÉDALIA, 1994) coupled with the multilayer surface-vegetation-atmosphere transfer scheme ISBA-Interaction Soil Biosphere Atmosphere (BOONE *et al*., 2000; BOONE, 2000).

BERGOT (*this issue*) documented the conditions when the local approach should be useful. However, a finer understanding of the limits of predictability for the specific case of fog and low clouds also needs to be performed. Which is the main goal of the current study. Under the hypothesis of a "perfect model", the uncertainty of forecasts made with the Cobel-Isba numerical system arises from uncertainty caused by two distinct sources of errors, namely, from errors in the specification of the initial conditions, as well as errors in the specification of the mesoscale forcings. Here the focus is on very short-term forecasts and attention is restricted to a perfect model situation. The influence of model errors will be studied in future work. This is the first step toward building a local 1-D Ensemble Prediction System (L-EPS) based on the COBEL-ISBA model.

In the first stage, the input uncertainties have been evaluated following the spatial and temporal variability of input data. The methodology and the uncertainties regarding input parameters will be discussed in section 2. In the second stage, the impact of input uncertainties for COBEL-ISBA LVP forecasts is examined. A key aspect of this study is to assess the input uncertainty impacts on the LVP forecast in order to evaluate the dispersion of Cobel-Isba forecasts, and also to obtain insights on how to build an efficient L-EPS. Usually, 1-D studies focus on selected cases and do not give a global overview of input uncertainty impacts. Here, the problem is examined from a seasonal point of view by running the local prediction system for the winter season 2002–2003 with a three-hour data assimilation frequency. This approach permits the evaluation of the overall impact of the main input uncertainties for the

prediction of foggy conditions at CdG. In section 3, these results are summarized by focusing on the forecast scores during the winter for both initial condition and mesoscale forcing uncertainties. And finally, section 4 concludes with a discussion on how these results could be used to build a local ensemble prediction system.

2. Estimation of Uncertainties for Input Parameters

2.1. Mesoscale Forcing Uncertainties

2.1.1. Methodology

The mesoscale forcing is provided by the operational NWP model Aladin (http://www.cnrm.meteo.fr/aladin/). Three different forcing terms are evaluated: horizontal advections, geostrophic wind and cloud cover. Aladin has a 10 km horizontal resolution. However, even with this resolution unresolved scales or errors in the mesoscale initial conditions induce noticeable variability at the grid point and in the neighborhood of the study zone in time, revealing the model uncertainty (ROQUELAURE, 2004). Unfortunately, it is not possible to accurately define the uncertainties of the mesoscale forcing terms, for example by comparing with measurements. To overcome this difficulty, it is necessary to evaluate the uncertainties from the Aladin forecasts only.

The mesoscale forcing uncertainty computation is then based on the hypothesis that uncertainty is correlated with the variability of the NWP model. The model variability is assessed in both space and time. The spatial variability is evaluated by comparing the forecast over an area of 3×3 grid points. This area is representative of homogeneous surface conditions around the study area. Moreover, it is not possible to extend this homogeneous area due to the presence of urbanized areas in the south-west (Paris). The temporal variability is evaluated by comparing four Aladin runs (0, 6, 12 and 18 UTC) for the same verification time. This choice allows the comparison of short-term forecasts only. At the end of this process, the variability in both space and time is used to estimate the shape of the distribution of uncertainties.

2.1.2. Horizontal advection

The temperature and humidity advection are computed over 9 grid points using the spatio-temporal approach for uncertainty computation. Figures 1a and 1b show, respectively, the temperature and humidity advection uncertainty distributions on winter season 2002–2003 for the Aladin vertical levels below 1 km within the boundary layer. Both temperature and humidity advection distributions have a "V" symmetrical shape, which indicates a linear growth of the uncertainty along with the rise of the mean advection value. However, notice that for small advection intensities in terms of the absolute value (lower 0.1 $C.h^{-1}$ for temperature advection and lower than 0.05 $g.kg^{-1}.h^{-1}$ for humidity advection), the mean advections have the same

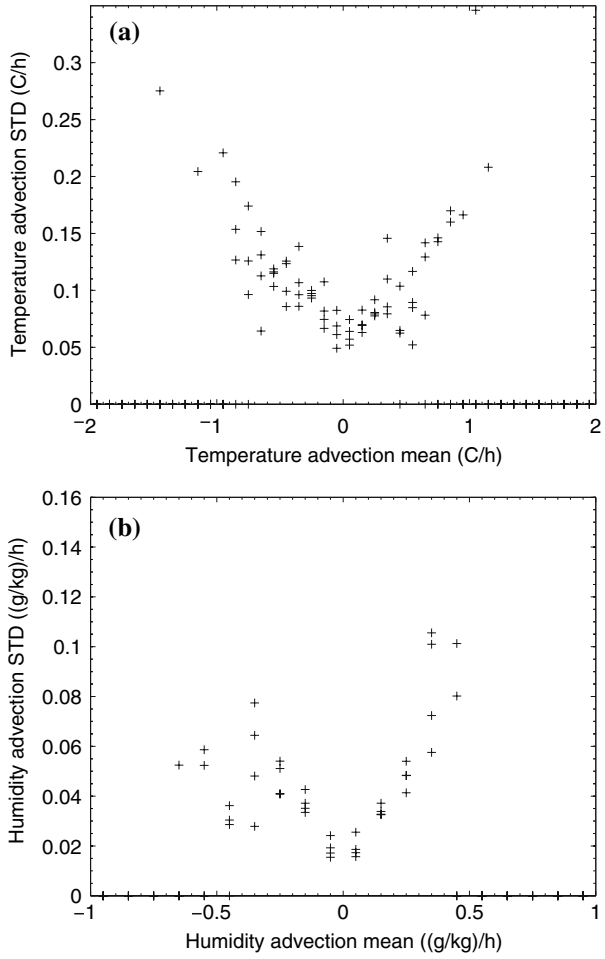

Figure 1
Aladin temperature (a) and humidity (b) advection uncertainty distributions for vertical levels below 1 km.

magnitude as the uncertainty. In radiative fog events frequently observed in CdG, the magnitude of the advections is relatively small (a fog event associated with weak winds). In these situations, advection uncertainty is as important as the mean advection. For conditions representative of higher advection values, the order of magnitude of the uncertainty increases weakly as the advection mean values increase. For temperature advection values over 0.2 $C.h^{-1}$ and humidity advection values over 0.05 $g.kg^{-1}.h^{-1}$, uncertainty is less than 40% of the advection.

2.1.3. Geostrophic wind

The geostrophic wind is computed from the horizontal pressure gradient and it is computed over a 100 × 100 km^2 area (see BERGOT *et al.*, 2005 for more details).

Figure 2 presents the geostrophic wind uncertainty as a function of the mean geostrophic wind for the winter season 2002–2003 and for vertical levels below 1 km. The evolution of the geostrophic mean wind uncertainty is almost linear for wind speeds below 15 m/s. In the case of fog, wind strength is generally below 6 m/s and even below 2 m/s in case of radiative fog, and the wind uncertainty is about 1 m/s.

2.1.4. Cloud cover

Current NWP models do not accurately forecast thin clouds or boundary layer clouds (e.g., stratocumulus). However, the appearance and the life cycle of a fog layer is very sensitive to the presence of cloud cover. Unfortunately, the spatial and temporal variation of the Aladin cloud cover are very small and it is not possible to estimate the cloud cover uncertainty by using the previously mentioned method (the cloud cover uncertainty mainly comes from approximations made in physical parameterization schemes). Two extreme hypotheses have been tested: a clear sky hypothesis and a persistence hypothesis. The persistence hypothesis is based on the assumption that the observed cloud cover is maintained during the 12 hours of the simulation, while the clear sky hypothesis assures that the sky remains clear during this period. An intermediate situation is also possible, by using the Aladin cloud cover forecasts. These three simulation cycles have been performed to quantify the cloud cover impact. Comparisons between 2 m downward longwave observations and COBEL-ISBA radiative fluxes using the clear sky hypothesis reveal a significant bias and standard deviation of the downward longwave fluxes (bias $= -16.6$ W/m^2, and std $= 25$ W/m^2). The Aladin and persistence cycles have a weaker bias for the 2 m longwave radiative fluxes (the bias for Aladin cycle $= -6.4$ W/m^2, and the bias

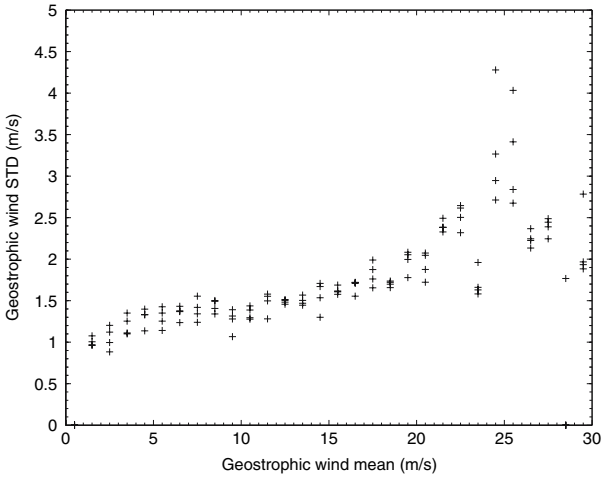

Figure 2
Aladin geostrophic wind uncertainty distribution for vertical levels below 1 km.

for persistence cycle = −2.3 W/m^2) in addition to a lower standard deviation (std for Aladin cycle = 19.8 W/m^2 and std for persistence cycle = 14.3 W/m^2).

2.2. Initial Condition Uncertainties

Initial conditions must be specified for both atmosphere and soil. Soil temperature and moisture profiles are estimated from on-site observations. The COBEL-ISBA analysis is based upon local observations, a guess field (which is the previous COBEL-ISBA forecast) and forecast profiles from NWP model Aladin. The 1-D variational assimilation scheme makes use of all this information to produce the best analysis possible. Through the 1-D variational assimilation process, observations are prevailing in the surface boundary layer. Above the surface boundary layer, as no observations are available, the COBEL guess issued from the previous forecast and the Aladin profile are combined. For more information on COBEL-ISBA data assimilation system, see BERGOT *et al.* (2005).

2.2.1. Atmospheric temperature and humidity profiles

Observations are the main information used to compute the atmospheric profiles in the surface boundary layer through the variational assimilation. Consequently, the low level temperature and humidity uncertainties are well represented by measurement uncertainties for both the temperature and the humidity. These measurement uncertainties are estimated at 0.2 degree Celcius for temperature and 0.2 g.kg^{-1} for humidity (see MARZOUKI, 2005). For the upper part of the boundary layer, the analysis follows the COBEL guess and the Aladin profiles. In practice, in order to compute uncertainties for upper atmospheric layers, we used the spatio-temporal method described in section 2.1.1. The estimated uncertainties are 0.6 degree Celcius for temperature and 0.5 g.kg^{-1} for humidity. A smooth linear interpolation is applied between the surface boundary layer where the measurement uncertainties prevail and the upper part of the boundary layer where Aladin uncertainties dominate.

2.2.2. Fog and stratus initialization

The fog/stratus initialization of COBEL-ISBA is based on an iterative method (BERGOT *et al.*, 2005). The depth of the cloud layer is determined by minimizing the radiation flux divergence between 2 m and 45 m (the two levels of radiative measurements). If the fog or low clouds are above the upper level of the radiative measurements (45 m), the fog depth is estimated by minimizing the errors of the radiative fluxes at the ground. CARRER (2003) has shown that the uncertainty is on the order of +/− 1 Cobel grid point for very low clouds (cloud top below 45 m). On the other hand, for events with higher cloud tops, uncertainty is more significant and diagnostics done by CARRER (2003) reveal that the uncertainty is on the order of +/− 2 Cobel grid points.

The liquid water content (LWC) uncertainty impact on LVP forecasts is addressed when fog (or stratus) is detected and initialized. Studies by MEYER *et al.* (1986) and WALMSLEY *et al.* (1999) have shown that LWC in fog ranges between 0.08 and 0.5 g.kg^{-1}. Here the goal is to analyze the impact of the small change of LWC in the cloud initialization. A 0.05 g.kg^{-1} liquid water uncertainty is then added (or removed) to the cloud reference liquid water content.

2.2.3. Soil temperature and moisture initialization

Soil temperature and moisture uncertainties are estimated from the accuracy of the measurements. Observed soil temperature and humidity variability during the winter are used to estimate soil vertical profile uncertainties for temperature and humidity. The maximum variability observed at each level is used as an estimate of uncertainty. Soil temperature uncertainty is constant at 0.1 degree Celcius up to −30 cm, and increases linearly up to 1 degree Celcius close to the surface. Soil humidity uncertainty is also constant up to −30 cm at 0.01 g.kg^{-1}, and increases linearly up to 0.025 g.kg^{-1} near the surface.

3. Forecast Sensitivity

3.1. Statistics Used to Perform Diagnostics

Numerous COBEL-ISBA simulations have been performed continuously for the winter season 2002–2003 for each perturbed configuration. A sensitivity study is conducted by comparing three different cycles (in a perturbed cycle, only the studied parameter is perturbed): the reference cycle (non perturbed), the cycle "+" (perturbed by adding the uncertainty), the cycle "−" (perturbed by subtracting the uncertainty).

The main statistical tools used to examine the quality of LVP forecasts (and the dispersion between perturbed cycles) are the Hit Rate (HR) and the False Alarm Rate (FAR). If a is the number of observed and forecasted events, b is the number of not observed and forecasted events, and c is the number of observed and not forecasted events, HR and FAR are defined by equations (1) and (2):

$$\mathrm{HR} = \frac{a}{a+c}, \tag{1}$$

$$\mathrm{FAR} = \frac{b}{a+b}. \tag{2}$$

The difference between the perturbed cycles scores (HR and FAR) is used. Uncertainty quantification is made by determining dispersion on LVP scores between the two perturbed cycles.

$$\mathrm{Dispersion} = \|S_{perturbed\_cycle+} - S_{perturbed\_cycle-}\| \tag{3}$$

where S can either represent HR or FAR at a particular forecast time during the 12 h simulation.

This study is designed to analyze initial conditions (IC) and mesoscale uncertainty impacts on the LVP forecast. However, uncertainty also has an indirect impact on thermodynamic parameters such as heat and humidity. Consequently, a heat and humidity budget strategy is applied to COBEL profiles to look at this question. IC and mesoscale perturbations act upon the 3-hour run needed to produce a guess field for the next assimilation. As a consequence, COBEL initial profiles are influenced by perturbations through the computation of the guess field (Fig. 3). Comparing the perturbed and the reference cycle budgets for each run during the winter season is an efficient way to quantify heat (or humidity) changes. Equation (4) gives the computation of the fraction R of heat (or humidity) gain (or loss) in the guess profiles due to uncertainty at time t for a perturbed cycle:

$$R = \frac{Q_{perturbed} - Q_{reference}}{Q_{reference}}, \tag{4}$$

where Q can either represent the heat or the humidity column balance. Subscripts refer to either the reference cycle or a perturbed cycle at time t. The mean and standard deviation of the R are computed in order to quantify the mean uncertainty impact and the variability of this impact on the winter period. Both scores are important in this context because sensitivity can be revealed by the variability of R coefficient and also by the mean value.

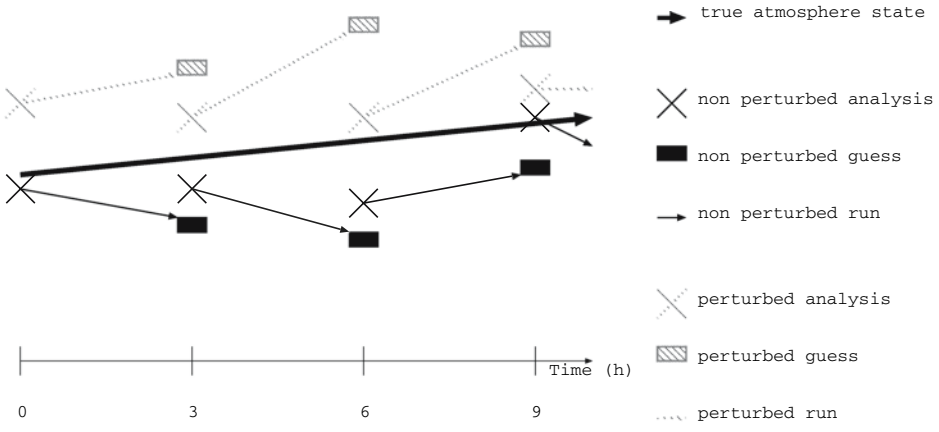

Figure 3
Schematic representation of perturbed cycles.

3.2. Forecast Sensitivity to Initial Conditions

The goal of this section is to evaluate the impact of initial condition uncertainties on LVP forecasts. The reference cycle and the perturbed cycles are done with the clear sky hypothesis (without cloud cover) and without advection.

3.2.1. Forecast sensitivity to atmospheric profiles uncertainties

The uncertainty previously estimated has been applied to the COBEL atmospheric profiles at the initial time. Tables 1 and 2 show that temperature uncertainty causes more dispersion for the LVP scores than humidity uncertainty. For humidity, dispersion is weak and almost constant during the runs (under 3%) for both HR and FAR, whereas dispersion reaches 15.5% for HR and 8% for FAR for the temperature at 9 h. The budget strategy results (Table 3) reveal that the atmospheric temperature uncertainty has an impact on both temperature and humidity in the guess atmospheric profile. For the warmer cycle, the mean heat change is 0.28% (std = 0.08%) and the mean humidity is 0.48% (std = 1.57%). This double impact can explain the higher dispersion made by temperature uncertainty. Actually, atmospheric humidity uncertainty has minimal impact on the heat balance. For example, mean impact of the moister cycle for the winter is very low (mean = −0.001% and std = 0.02%).

Figure 5 shows that the reference cycle scores (HR and FAR) do not necessarily lie between the perturbed cycles scores. Dispersion is asymmetric from the reference cycle. The colder cycle leads to similar scores as the reference cycle, but the warmer cycle gives better scores for both HR and FAR. This result suggests that there might be a cold bias in the atmospheric boundary layer profiles from the Aladin NWP model. The better results for both scores at most forecast times may be explained by the cold bias correction induced by the warm uncertainty applied for the atmospheric temperature profile.

Table 1

Hit Rate (HR) dispersion for perturbed cycles. Values of dispersion over 10% are in bold

$\|HR_{perturbed\_cycle+} - HR_{perturbed\_cycle-}\|$ (%)	Forecast time (hour)				
	1	3	6	9	12
Atmospheric temperature (initial condition)	0.0	2.3	9.4	**15.5**	2.4
Atmospheric humidity (initial condition)	2.9	2.3	2.4	0.0	2.4
Clouds depth (initial condition)	**17.6**	**23.2**	**28.9**	**24.3**	**19.5**
Clouds liquid water (initial condition)	**11.7**	**16.2**	4.6	**12.1**	9.7
Soil temperature (initial condition)	**20.5**	4.6	4.6	9.7	7.3
Soil moisture (initial condition)	8.7	0.0	2.4	2.5	0.0
Geostrophic wind (mesoscale forcing)	5.8	9.2	7.0	4.8	4.7
Cloud cover (mesoscale forcing)	5.9	2.3	4.7	4.8	7.3
Temperature advection (mesoscale forcing)	0.0	6.9	7.1	2.5	2.4
Humidity advection (mesoscale forcing)	**14.6**	**23.2**	**26.1**	**36.4**	**16.9**

Table 2

False Alarm Rate (FAR) dispersion for perturbed cycles. Values of dispersion over 10% are in bold

$\|(FAR_{perturbed\_cycle+} - FAR_{perturbed\_cycle-}\|$ (%)	Forecast time (hour)				
	1	3	6	9	12
Atmospheric temperature (initial condition)	3.3	1.4	6.4	8.0	0.5
Atmospheric humidity (initial condition)	1.9	0.1	0.7	2.9	0.2
Clouds depth (initial condition)	**23.9**	**14.4**	4.0	7.6	8.0
Clouds liquid water (initial condition)	6.2	2.4	1.7	4.9	3.4
Soil temperature (initial condition)	3.9	9.0	6.9	3.4	0.0
Soil moisture (initial condition)	0.4	0.0	1.4	1.3	0.4
Geostrophic wind (mesoscale forcing)	4.2	8.8	9.9	**13.5**	**11.0**
Cloud cover (mesoscale forcing)	7.7	4.9	5.2	5.9	4.3
Temperature advection (mesoscale forcing)	9.8	**10.3**	**10.3**	**13.5**	**14.1**
Humidity advection (mesoscale forcing)	7.7	**10.6**	9.1	7.4	**15.6**

Table 3

Heat and humidity mean changes in the atmospheric guess profile for the initial conditions cycle. Values over 0.2% for mean heat and mean humidity are in bold. Values over 0.1% and over 1% are in bold for the std of heat and the std of humidity, respectively

$\overline{R} = \overline{(Q_{perturbed} - Q_{reference})/Q_{reference}}$	Heat (%)		Humidity (%)	
	mean on cycle	std	mean on cycle	std
Temperature "+" (warmer)	**0.28**	0.08	**0.48**	**1.57**
Temperature "−" (colder)	−0.004	0.01	−0.009	0.38
Humidity "+" (moister)	0.001	0.02	**0.24**	0.50
Humidity "−" (drier)	−0.001	0.01	**−0.28**	0.49
Clouds depth "+" (deeper clouds)	−0.052	**0.136**	−0.18	**1.90**
Clouds depth "−" (thinner clouds)	0.021	0.071	**0.22**	**1.14**
Clouds liquid water "+" (heavier clouds)	0.008	0.068	0.15	**1.50**
Clouds liquid water "−" (lighter clouds)	−0.008	0.067	−0.009	**1.64**
Soil temperature "+" (warmer)	0.006	0.024	0.18	0.57
Soil temperature "−" (colder)	−0.005	0.031	**−0.23**	0.63
Soil humidity "+" (moister)	−0.001	0.018	0.02	0.56
Soil humidity "−" (drier)	0.004	0.024	−0.09	0.58

3.2.2. Forecast sensitivity to the low cloud initialization

For cloud initialization, perturbed cycles produce deeper or thiner clouds than the reference cycle. The first three simulation hours needed to compute the guess field are crucial. With different cloud properties, the vertical structure of the boundary layer could greatly change (Fig. 4). These changes are significant and evaluated with the budget strategy. Variability of the winter for humidity balance in the guess atmospheric profiles is high (1.9% for deeper clouds and 1.14% for thinner clouds). The heat balance variability is also significant (std = 0.136% for deeper clouds and

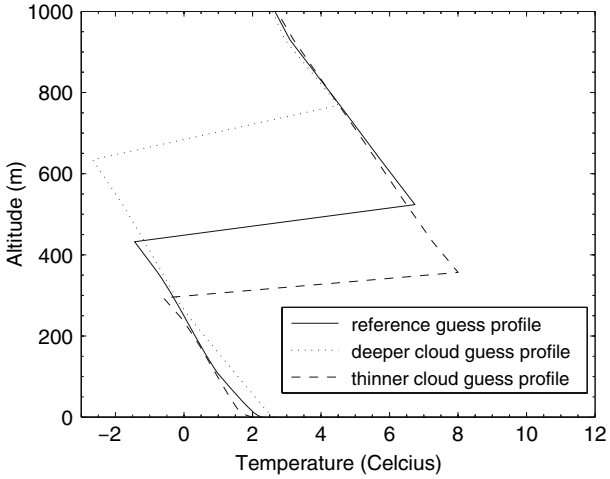

Figure 4
Guess used for the 12Z run of December 12th, 2002: The reference cycle (stratus initialised at 9Z, 90–430 m), deeper cloud cycle (stratus initialized at 9Z, 90–630 m) and thinner cloud cycle (stratus initialized at 9Z, 90–290 m).

0.071% for thinner clouds). As a consequence, the LVP score dispersion induced by the cloud depth uncertainty is significant (from 17.6% at 1 h to 28.9% at 6 h) for HR and (from 4% at 6 h to 23.9% at 1 h) for FAR.

Liquid water content (LWC) uncertainty leads indirectly to the same effects as for the fog/stratus depth initialization, by modifying the liquid water path. However, dispersion in that case is less significant than dispersion generated by a cloud depth uncertainty. Dispersion is below 17% for HR and below 7% for FAR.

3.2.3. Forecast sensitivity to soil profile uncertainties

Soil temperature uncertainty generates more LVP score dispersion than soil moisture uncertainty. Once again, the budget strategy (Table 3) shows that soil temperature uncertainty acts on both atmospheric thermodynamic parameters, whereas the soil moisture uncertainty acts essentially on the humidity balance. As a consequence, dispersion is over 4.5% for HR between perturbed soil temperature cycles. The dispersion is maximum at the beginning of the simulation (about 20%). For soil moisture perturbed cycles, the dispersion is under 3% for HR except for the beginning of the simulation, where dispersion is 8.7%. For FAR, the dispersion is under 2% between the perturbed soil moisture cycles, and between 0 to 9% for the perturbed soil temperature cycles.

3.3. Forecast Sensitivity to Mesoscale Forcings

1-D modeling allows a description of meteorological phenomenon at the local scale. Nevertheless, the mesoscale acts upon the local scale through the dynamical

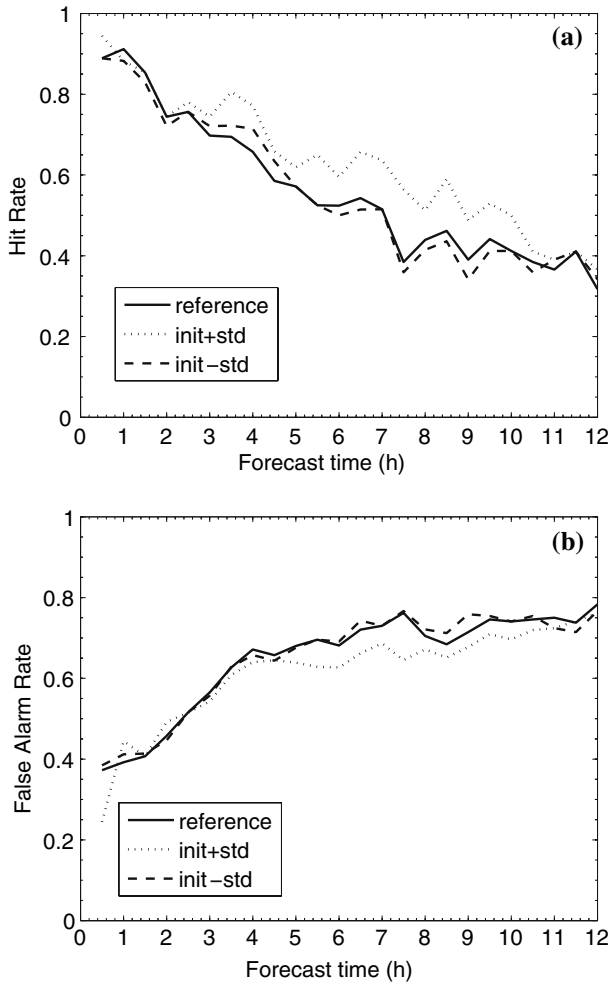

Figure 5
Hit rate (a) and false alarm rate (b) comparison for LVP forecast for the reference cycle, the perturbed atmospheric temperature cycles for winter season 2002–2003.

evolution of the atmosphere, and it is important to consider this interaction for fog and low cloud prediction. TURTON and BROWN (1987) and later BERGOT (1993) or BERGOT and GUÉDALIA (1994) have shown the importance of advection phenomenon in fog formation and evolution.

3.3.1. Forecast sensitivity to cloud cover

The impact of cloud cover is evaluated for three different cycles: the Aladin cloud cover cycle, which takes into account the cloud forcing based on Aladin forecasts, the

observed cloud cover persistence (constant cloud forcing during a COBEL run), and the clear sky cycle. Dispersion on LVP scores between cloud cover perturbed cycles is almost constant, around 5% for all forecast times for both HR and FAR. The budget strategy also reveals an important indirect impact on analyses through the guess field (Table 4). Variability for heat and humidity balances is high with values around 2.5% for humidity and 0.1% for heat balance with respect to both Aladin and the persistence cycles.

3.3.2. Forecast sensitivity to geostrophic wind

Geostrophic wind acts indirectly on the turbulence. The budget strategy shows that geostrophic wind uncertainties influence both heat and humidity balances during the computation of the guess field. The heat and humidity balance variability is moderate and is around 0.035% and 0.6% for the two perturbed cycles. Dispersion for HR is over 4.7%, and a higher spread is observed at 3 h and 6 h with values of 9.2 and 7%. Dispersion for FAR increases slowly during the 12 hours of simulation, beginning at 4.2% and ending close to 13%.

3.3.3. Forecast sensitivity to horizontal advection

First, it is of interest to note that advection forecasted by Aladin NWP models generally bring warmer and dryer air into the column compared to the cycle without advection (Figs. 6a and 6b). The budget strategy confirms a warm (mean = 0.05% and std = 0.32%) and dry (mean = −1.85% and std = 10.68%) mean advection effect during the winter (Table 4). Advection has a clear impact on the heat and humidity balances. Figure 7 shows the balances for each guess field and analysis during the winter. Variability is higher for the atmospheric profiles from the guess fields (10.68% for humidity and 0.32% for heat) than those from analyses for both thermodynamic variables because analyses are forced by observations in the assimilation process. The consequence of the dry and warm contribution of the advection is that the reference advection cycle damages the detection of LVP (HR) compared to the reference cycle (Fig. 8).

Temperature and humidity advection uncertainty impacts on LVP forecasts have been analyzed by separately perturbing temperature advection and humidity advection :

- The reference advection cycle (non perturbed),
- "AT + STD" by convention is a **colder advection** (perturbation of the temperature advection STD, without perturbation of the humidity advection (AQ)),
- "AT-STD" by convention is a **warmer advection** (perturbation of the temperature advection STD, without perturbation of the humidity advection (AQ)),
- "AQ + STD" by convention is a **drier advection** (perturbation of the humidity advection STD, without perturbation of the temperature advection (AT)),

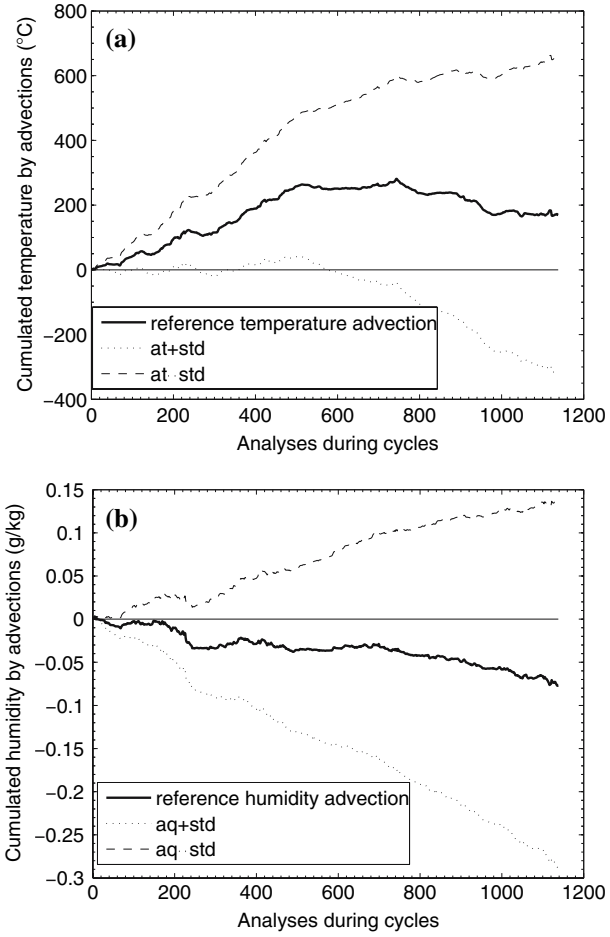

Figure 6
Cumulated (a) heat and (b) humidity during the winter season 2002–2003 for the advection cycles. Heat and humidity values are only computed from temperature and humidity advection inputs for COBEL.

- "AQ-STD" by convention is a **moister advection** (perturbation of the humidity advection STD, without perturbation of the temperature advection (AT)).

Figure 8a shows that the LVP score dispersion between temperature advection cycles is low during the first hours of the simulation. The HR spread becomes more important between 3 h and 9 h (7.1% at 6 h). Table 2 shows that the FAR dispersion is close to 10%, and it is almost constant during the 12 hours of simulation.

Both perturbed temperature advection cycles improve the HR score after two hours. The warmer cycle improves the score of the reference advection cycle, and the results become comparable to the reference cycle (without advection). This improvement, which is induced by warmer advection, pleads also in favor of a cold

Table 4

Same as Table 3 for mesoscale forcing cycles

$\overline{R} = \overline{(Q_{perturbed} - Q_{reference})/Q_{reference}}$	Heat (%)		Humidity (%)	
	mean on cycle	std	mean on cycle	std
Geostrophic wind "+" (stronger)	−0.005	0.038	0.05	0.63
Geostrophic wind "−" (lighter)	0.003	0.033	−0.17	0.77
Aladin cloud cover	0.022	**0.114**	**−0.28**	**2.53**
Observed cloud cover persistence	−0.009	0.077	**−0.93**	**2.45**
Advections without STD	0.051	**0.328**	**−1.85**	**10.68**
Temperature advection "+" (colder)	−0.14	0.05	**−0.23**	**1.02**
Temperature advection "−" (warmer)	0.14	0.05	**0.20**	0.94
Humidity advection "+" (drier)	−0.022	0.034	**−5.26**	**3.10**
Humidity advection "−" (moister)	0.025	0.054	**5.22**	**3.21**

bias in the Aladin profiles within the boundary layer (i.e., warmer atmospheric temperature uncertainty).

Figure 8b shows that dispersion between perturbed humidity advection cycles is very significant. Dispersion is low at the beginning of the simulation and increases significantly with time (14.6% at 1 h and 36.4% at 9 h for HR). On FAR, dispersion is close to 10% during the 12 hours of simulation. Compared to the reference advection cycle, asymmetry is observed between the dry and the moist cycles.

4. Summary and Perspectives

The prediction of low visibility conditions at airports is a challenge for forecasters. Previous studies have shown the potential of the COBEL-ISBA local numerical prediction system to fulfill this very specific need. The use of dedicated local observations and a local assimilation scheme to accurately initialize the COBEL-ISBA model has been conducive to improvements in fog and low cloud prediction (see BERGOT, *this issue*). However, despite these improvements, it is necessary to quantify the forecast quality. One way is to estimate the uncertainties with respect to the input parameters, such as initial conditions and mesoscale forcings, and to evaluate the impact of these uncertainties on fog and low cloud forecasts.

In this study, uncertainty distributions for both sources of error have been evaluated. Firstly, for mesoscale forcings, uncertainty has been estimated under the hypothesis that uncertainty is correlated with the "intrinsic" spatial and temporal variability of the Aladin NWP model. In conditions corresponding to fog and low clouds, it was found that the advection uncertainty is as important as the mean advection. Secondly, uncertainty of the initial conditions (IC) has been evaluated from observation errors. Owing to local observations, uncertainty of the IC is small, except in the case of low cloud initialization.

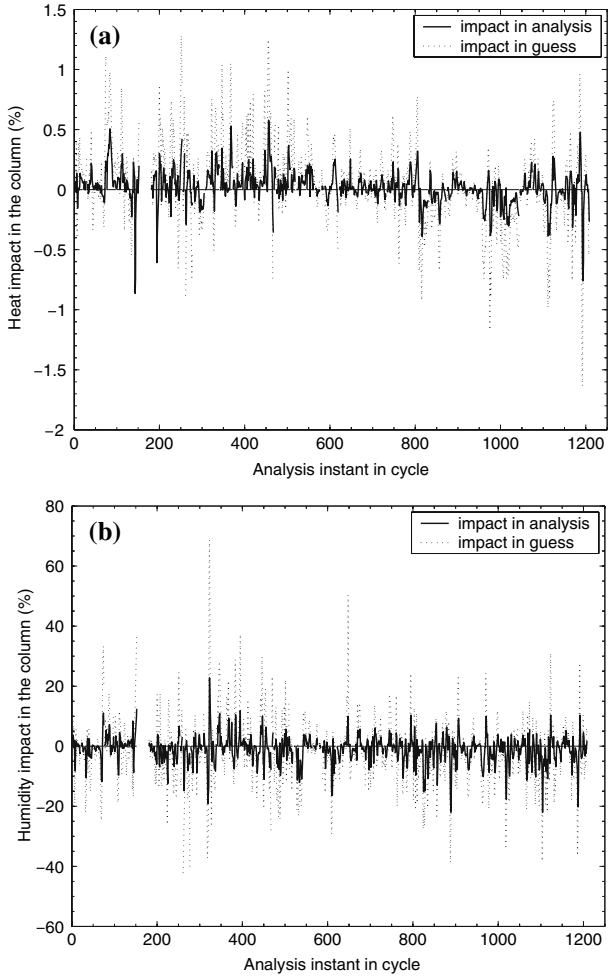

Figure 7
Advection contribution in heat (a) and humidity (b) balances for analysis and guess during the reference advection cycle for the winter season 2002–2003.

The impact of these incertainties for Cobel-Isba forecasts has been evaluated during a winter season. The study has shown the dependency between forecast time and dispersion (Fig. 9). IC uncertainties disperse during the first hours of the simulation (0 to 6 h), whereas the dispersion created by mesoscale forcing becomes more important in the second half of the simulation (6 to 12 h). The cloud radiative effect on dispersion is felt throughout the forecast period, as well as low cloud initialization. The heat and humidity budget analysis applied on the guess field has increased the understanding of the uncertainty influence on the COBEL-ISBA local forecast scheme. This strategy has permitted the quantification of the impact of perturbations on the variational data assimilation scheme. Perturbations grow

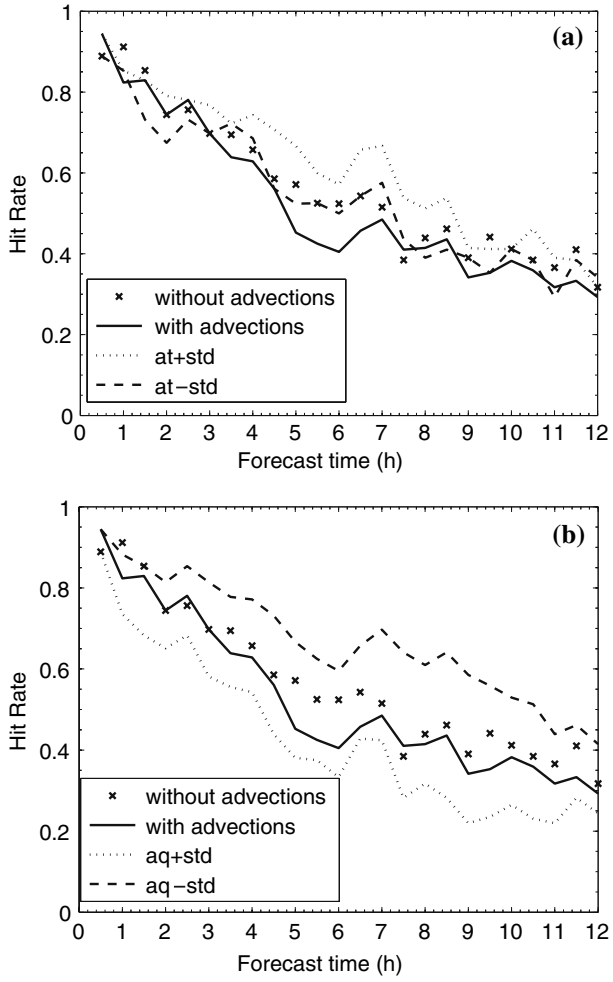

Figure 8
Hit rate for advection cycles for the winter season 2002–2003 (a). Hit rate comparisons of humidity advection cycles (b) for the winter season 2002–2003.

during the cycle and ''feed'' analyses through the assimination process. Each cycle evolves independently according to his perturbation.

One of the major avantages of a local approach (1-D) for short-term forecasts of fog and low clouds is that runs are ''inexpensive''. Within the perspective of a Local Ensemble Prediction System (L-EPS), this computational facility is highly advantageous in terms of computational time in an operational environment, and the freedom in the choice of the number of ensemble members is also a benefit. The study brings out interesting points for building a L-EPS, and they are listed below:

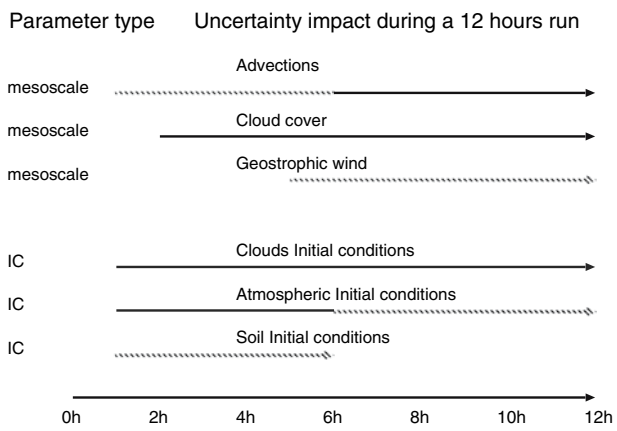

Figure 9
Summary of the uncertainty impact on fog and low cloud forecasts. For each parameter, the straight part of the arrows indicates when the dispersion is higher, the dashed part when dispersion is weaker during the 12 hour run.

- Construction of a L-EPS should take into consideration that dispersion is higher for mesoscale forcings compared to the IC. The sampling/calibration should be carefully done in order to balance both sources of uncertainty;
- construction of a L-EPS should also consider the dependency between run forecast time and dispersion. Sampling and calibration have to be carefully done for each forecast time;
- in this study the shape of uncertainty distribution has been evaluated, but not the magnitude. Consequently, a degree of freedom remains. This could be helpful to calibrate the dispersion of L-EPS;
- dissymetry (e.g., advection, atmospheric temperature profile) between perturbed cycles has been observed. Sampling/calibration have to be properly thought;
- a bias in the upper level of the atmospheric temperature profiles seems to affect the Cobel-Isba forecasts. The effect of this bias on the L-EPS should be studied in detail;
- perturbations could affect the forecasts through the assimilation system. Consequently, each member of L-EPS needs to have its own assimilation scheme.

All these points offer a starting point for building a L-EPS based on a COBEL-ISBA local numerical system. The COBEL-ISBA behavior has been determined during this study and results are encouraging.

References

Bergot, T. (1993), *Modélisation du brouillard à l'aide d'un modèle 1D forcé par des champs mésoéchelle: Application à la prévision*, Ph.D. Thesis - Université Paul Sabatier, Toulouse, France *1546*, 192 pp. (available at CNRM, Meteo-France).

Bergot, T. and Guédalia, D. (1994), *Numerical forecasting of radiation fog. Part I: Numerical model and sensitivity tests*, Mon. Wea. Rev. *122*, 1218–1230.

BERGOT, T., CARRER, D., NOILHAN, J., and BOUGEAULT, P. (2005), *Improved site-specific numerical prediction of fog and low clouds: A feasibility study*, Wea. Forecasting *20*, 627–646.

BOONE, A., MASSON, V., MEYERS, T., and NOILHAN, J. (2000), *The influence of the inclusion of soil freezing on simulations by a soil-vegetation-atmosphere transfer scheme*, J. Appl. Meteor. *9*, 1544–1569.

BOONE, A. (2000), *Modélisation des processus hydrologiques dans le schéma de surface ISBA: inclusion d'un réservoir hydrologique, du gel et la modélisation de la neige*, Ph.D. Thesis - Université Paul Sabatier, Toulouse, France.

BROWN, R. and ROACH, W.T. (1976), *The physics of radiation fog. Part II: A numerical study*, Quart. J. Meteor. Soc. *102*, 335–354.

CARRER, D. (2003), *Etude d'un système de prévision numérique locale des faibles visibilités sur Roissy. Final engineer formation repport n°860, ENM (Ecole Nationale de la Météorologie)* (available at Meteo-France/ENM, 42 Av Coriolis, F31057 Toulouse Cedex, France).

CLARK, D.A. (2002), *The 2001 demonstration of automated cloud forecast guidance products for San Francisco International airport*, 10th Conf. Aviation, Range and Aerospace Meteorology, AMS, Portland OR, May 13–16.

DUYNKERKE, P.G. (1991), *Radiation fog: A comparison of model simulation with detailed observations*, Mon. Wea. Rev. *119*, 324–341.

HERZEGH, P., PETTY, K., BENJAMIN, S., RASSMUSSEN, R., TSUI, T., WIENER, G., and ZWACK, P. (2002), *Development of automated national ceiling and visibility products: Scientific and pratical challenges, research strategies, and first steps*, 10th Conf. Aviation, Range, and Aerospace Meteorology, Am. Meteor. Soc.

JIUSTO, J.E. and LALA, G. (1983), *Radiation fog fields programs. Recents studies,* ASRC-SUNY Publication *117*, 67 pp.

KALNAY, E. (2003), *Atmospheric Modeling, Data Assimilation and Predictability* (Cambridge University Press, UK) 341 p.

MARZOUKI, H. (2005), *Impact d'un système d'assimilation dans un système de prévision numérique local des brouillards et des nuages bas, Final engineer formation report 1005, ENM (Ecole Nationale de la Météorologie)* (available at Meteo-France/ENM, 42 Av Coriolis, F31057 Toulouse, cedex, France).

MEYER, M.B., LALA, G.G., and JIUSTO, J.E. (1986), *Fog-82, A cooperative field study of radiation fog*, Bull. Am. Meteor. Soc. *67*, 825–832.

MUSSON-GUENON, L. (1987), *Numerical simulations of fog event with a one-dimensional boundary layer model*, Mon. Wea. Rev. *115*, 592–607.

ROQUELAURE, S. (2004), *Couplage du modèle COBEL avec le modèle de mésoéchelle RUC: advections horizontales de température et d'humidité*, M. Sc. Thesis - UQAM, Montréal, Canada, 113 pp.

TURTON, J.D. and BROWN, R. (1987), *A comparison of a numerical model of radiation fog with detailed observations*, Quart. J. Roy. Meteor. Soc. *113*, 37–54.

WALMSLEY, J., BURROWS, W.R., and SCHEMEAUER, R.S. (1999), *The use of routine weather observations to calculate liquid water content in summer high elevation fog*, J. Appl. Meteor. *38*, 369–384.

(Received April 11, 2006, accepted October 31, 2006)
Published Online First: May 16, 2007

Pure appl. geophys. 164 (2007) 1303–1325
0033–4553/07/071303–23
DOI 10.1007/s00024-007-0220-9

Pure and Applied Geophysics

Can Sea Fog be Inferred from Operational GEM Forecast Fields?

Lorenzo De La Fuente,[1] Yves Delage,[2] Serge Desjardins,[3] Allan MacAfee,[3] Garry Pearson,[3] and Harold Ritchie[1,2]

Abstract—Three cases of widespread sea fog in Lunenburg Bay, Nova Scotia were used to evaluate the suitability of operational regional GEM forecast fields for inferring advection fog occurrences. Verification scores suggest that the objective analyses contain significant departures from observations that will affect model accuracy, given the sensitivity of fog condensation microphysics. Dew point depression (ES) scores show larger differences compared to temperature, with both influenced by surface characteristics. For objective analyses and GEM forecasts ES < 2 C seems to match fog satellite images better than the physical threshold ES ≤ 0 C. In addition the GEM forecasts show a general tendency towards drier conditions near the surface, therefore reconfiguring GEM to better represent condensation in the boundary layer is proposed.

Key words: Sea fog forecasting, Atlantic Canada, GEM.

1. Introduction

Climatological studies in Canada (Muraca *et al.*, 2001) indicate an overall decrease in fog occurrences, consistent with the trends observed in the United States (Weber and Buckley, 2004). Despite these trends and improved vehicle safety, annual averages of fatal highway accidents involving fog are 54 for Canada and 700 for the United States (Whiffen *et al.*, 2003). Inaccurate fog forecasts cost US aviation up to $875 million in additional operational costs annually (Riordan and Hansen 2002).

In meteorological practice fog is observed when the visibility, or the distance at which a reference object cannot be distinguished from its background, falls below 1 km. It is specifically associated with near-surface layers containing water droplets averaging 10–20 μm in diameter, in concentrations up to 1 g/m^3 (Roach, 1994). Fog droplet condensation may be caused by decreasing the temperature to the dew point,

[1] Department of Oceanography, Dalhousie University, Halifax, NS, Canada.
E-mail: hal.ritchie@ec.gc.ca
[2] Meteorological Research Division, Atmospheric and Technology Directorate, Environment Canada, Dorval, QC, Canada.
[3] Meteorological Service of Canada, Dartmouth, NS, Canada.

increasing water vapor pressure until saturation or a combination of the two. In Atlantic Canada, advection of sea fog accounts for most fog observations at inland stations (ENVIRONMENT CANADA, 1995). The most common mechanism for sea-fog formation is warm moist air moving over colder water. After the lowest layers cool by conduction and accumulate water vapor evaporating from the sea surface, turbulent mixing with cooler dryer air above initiates a convective process sustained by latent heat release from droplet condensation (TELFORD and CHAI, 1993). It is theorized that saturation and droplet condensation first occur at the inversion height then proceed towards the surface, suggesting a cloud formed initially would develop downwards to create a fog bank (TELFORD and CHAI, 1993).

While sea fog in Atlantic Canada was investigated as early as 1917 by G.I. Taylor as noted in a review (LEWIS *et al.*, 2004), surprisingly little has been published recently beyond a technical report from Environment Canada (OSBORNE, 1976) and a case-based reasoning study conducted at Halifax Airport (RIORDAN and HANSEN, 2000). Other investigators have employed mesoscale numerical weather prediction models for sea fog, but most deal with US West Coast fogs as discussed in a review paper (LEIPPER, 1994). New studies have simulated California coastal fog using the Naval Research Laboratory Coupled Ocean/Atmosphere Mesoscale Prediction System and National Center for Atmospheric Research fifth generation Mesocale Model (GEISZLER *et al.*, 2000), however, these applications do not appear to use standard operational forecasts the way this study intends to do.

This investigation is part of the Marine Environmental Prediction System-Lunenburg Bay (MEPS-Bay) project described in (RITCHIE *et al.*, 2004).

2. Methodology

2.1. Area Description

The weather stations are grouped into geographical areas to simplify the analysis and identify advective trends, with locations shown in Figure 1. The Bay of Fundy area includes St. John (YSJ) and Grand Manan (XGM) in New Brunswick and Yarmouth (YQI) in Nova Scotia. The Nova Scotia area includes Lunenburg Bay (XLB), Shearwater (YAW), and Sydney (YQY). The West Atlantic area includes Sable Island (WSA) in Nova Scotia, Port Aux Basques (WZB) and St. John's (YYT) in Newfoundland. With the exception of the automatic stations XGM, XLB, and WZB these are all manned stations that report visibility and fog occurrences. Stations YQI and WSA are also upper-air stations with daily radiosonde profiles available at 0000 and 1200 UTC. It is unfortunate that during all our case studies no relevant ship reports were available in the area of interest, nor was humidity data available from the automatic weather buoys. The common analysis domain is 900 km by 900 km at 15 km resolution, centered at XLB (44.36N, 64.3W).

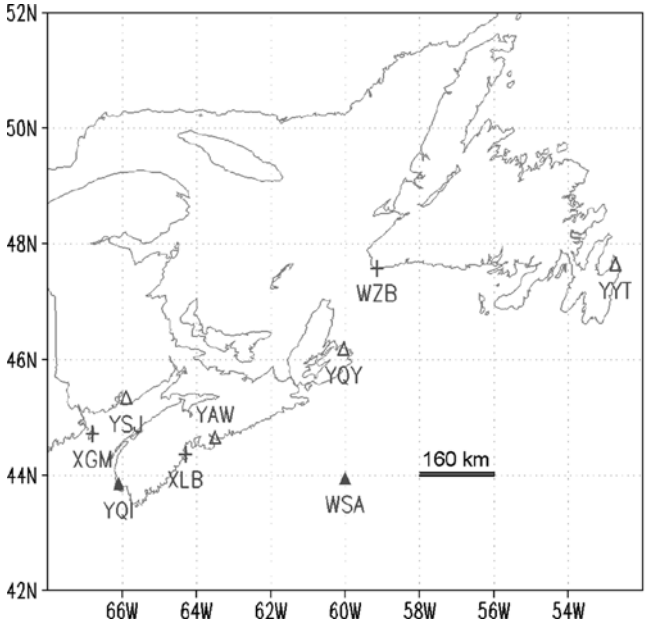

Figure 1
Atlantic Canada weather stations: Outline triangles are manned surface stations, solid triangles are manned surface and upper air stations, plus signs are automatic surface stations.

With the exception of sea breeze circulations, no localized wind regimes appear to have been documented (ENVIRONMENT CANADA, 1995).

2.2. GEM Model Background

The Global Environment Multiscale (GEM) model has a variable-resolution capability such that it is possible to use either a uniform-resolution latitude and longitude mesh, or a variable-resolution one that uses a rotated coordinate system with a high-resolution sub-domain that can be located over any portion of the globe. GEM uses horizontal variable resolution, cell-integrated, finite-element discretization reducing to staggered finite-differences discretization at uniform resolution in spherical geometry. Other features include hydrostatic-pressure-type hybrid vertical coordinates, and a semi-implicit semi-Lagrangian time discretization scheme which removes the overly-restrictive time step limitation imposed by the use of a more conventional Eulerian scheme.

Parameterizations used include a full physics package containing convective, several large-scale condensation, microphysical, turbulent kinetic energy planetary boundary layer, surface and solar and infrared radiation schemes (CÔTE *et al.*, 1998).

The regional objective analyses (henceforth OA) and the regional GEM forecasts, both at 25 km resolution in 2003 but increased to 15 km since May 2004, were

obtained from the Canadian Meteorological Centre (CMC) online archive. The OA are data assimilation products combining source data and GEM simulation results while the forecasts are deterministic outputs from the GEM model. The horizontal domain covers all of Canada and parts of the United States, while the vertical extent for 58 levels of eta model-level data ranges from about 50 m above the surface for eta 1.0 to about 30 km for eta 0.0. The OA are available daily at 0000, 0600, 1200, and 1800 UTC, while the forecasts are initiated at 0000 and 1200 UTC. This study uses the GEM forecasts initiated at T_0 = 0000 UTC, and comparisons with satellite images and the OA will be done using the forecasts at T_0 + 12 h = 1200 UTC and T_0 + 18 h = 1800 UTC. Fog is not explicitly represented in the OA or the forecasts, and must therefore be identified in terms of moisture variables like dew point TD (C), dew point spread ES (C), relative humidity HR (%), specific humidity HU (kg/kg), cloud liquid water QN (kg/kg) and total liquid and solid condensate QC (kg/kg) in the context of air temperature TT (C) and sea-surface temperature TM (C).

In the GEM physics package the near-surface moisture at eta 1.0 is computed diagnostically from upper levels using Monin-Obukhov surface layer theory, which does not take condensation into account. Although the physics package includes a condensation scheme ("Moistke") for boundary layer clouds, this scheme is not designed to represent fog (i.e., cloud based on the surface) when used in this diagnostic manner (MAILHOT, 2006, pers. comm.). This might contribute to a GEM forecast tendency toward less humid conditions near the surface and thus underprediction of condensation.

2.3. OA and Forecast Verification Scores

The difference between the observations, OA and forecasts may be quantified using verification scores. Mean Bias (MB) and Root-Mean-Squares (RMS) are scores commonly used in atmospheric sciences, and are defined in STULL (2000) as

$$\text{Mean Bias} = \left(\overline{F - V}\right) = 1/n \sum_{k=1}^{n} (F - V)_k, \tag{1}$$

where $\overline{F - V}$ is the spatial average over n data points for test data set F and reference data set V, and

$$\text{Root-Mean-Squares} = \sqrt{\left(\overline{F - V}\right)^2}. \tag{2}$$

For each case study these verification scores were calculated in three phases. First, 1-D profiles of TT and ES from the OA were compared to observations to assess the data-related vertical differences, where set F would be the OA and set V refers to the observations. To ensure robust scores based on a sufficient sample size across all case studies, data at the mandatory pressure levels of 1000, 925, 850, 700, 500, 400, 300,

200, 150, and 100 mb were selected. While data from higher altitudes are unlikely to directly affect surface phenomena, GEM forecasts are initiated using data on similar levels, so this comparison remains relevant. This first phase essentially establishes the differences between observations and the 'numerical reality' resulting from data assimilation.

Next, 1-D profiles of TT and ES from the GEM forecast were compared to the OA to assess the model-related vertical differences, where set *V* would be the OA and set *F* refers to the GEM forecast. To ensure robust scores based on a sufficient sample size across all case studies, data at the eta levels of 1.0, 0.995, 0.985, 0.9733, 0.9606, 0.9467, 0.9316, 0.9151, 0.8973, and 0.8571 were selected. Given the higher vertical resolution of eta level data near the surface and the boundary-layer nature of sea fog, the selected levels focus the comparison to within the lowest 2000 m most relevant for fog forecasts. This next phase evaluates the vertical differences between 'numerical reality' and the GEM operational forecast, at a vertical resolution finer than the mandatory pressure levels within the boundary layer.

For the first two phases, differences were also determined for pressure and eta levels within the 2000 m boundary layer. While these are unlikely to be statistically robust due to the low number of data points, they are estimates of the range of deviations from observations within the layer.

Last, 2-D fields of TT and ES from the GEM forecast were compared to the OA to assess the model-related horizontal differences near the surface, where set V would be the OA and set F refers to the GEM forecast. Similarly, this last phase evaluates the horizontal differences between 'numerical reality' and the GEM operational forecast. To ensure consistent scores across all case studies, data at eta level 1.0 for all grid points in the 15 km resolution 900 by 900 km domain were selected.

3. Results and Discussion

3.1. Case Study 1: 04–07 July, 2003

3.1.1. Synoptic weather summary

The period from 0000 UTC 04 July, 2003 to 1200 UTC 06 July, 2003 was characterized by a light to moderate southwesterly flow of moist air over the eastern seaboard of the U.S. and the Canadian Maritimes. The synoptic pattern persisted throughout with a gradually building high-pressure system east of Bermuda extending to the northeast, and a series of weak low pressure systems in an east-west trough over northeastern Canada. During this time, sea-surface temperatures south of Nova Scotia were approximately 13 to 17 C and around 12 C in the Bay of Fundy. Air temperatures in the boundary layer were 16 to 18 C south of Nova Scotia with similar dew point values in the moist air resulting in an extensive area of marine fog.

3.1.2. Station time series

Figure 2 shows visibility time series for the three geographical areas, where the observations in local time have been adjusted to UTC. In the Bay of Fundy area fog events occur from 0200–0700 UTC on 04 July, a longer event from 1700–0900 UTC 04–05 July and the last from 2100–0300 UTC 05–06 July at YQI, YSJ and XGM. For the Nova Scotia area the XLB plot is relative humidity which varies inversely as visibility, and indicates fog from 1900–0500 UTC 04–05 July at XLB and YAW. For the West Atlantic area there is almost continuous fog from 1800–0100 UTC 04–07 July at WSA and WZB. Note that WZB and YYT are on Newfoundland time, which is 0.5 h ahead of all other stations in the time series figures.

3.1.3. Horizontal fog distribution from satellite images and OA

High Resolution Picture Transmission (HRPT) images from the National Oceanic and Atmospheric Administration polar orbiting satellites are used to identify likely occurrences of sea fog from the 0.6 μm visible channel by applying standard satellite image interpretive techniques (COMET, 2006). The centers of inferred low cloud/fog banks are indicated by '*F*' in the remapped images.

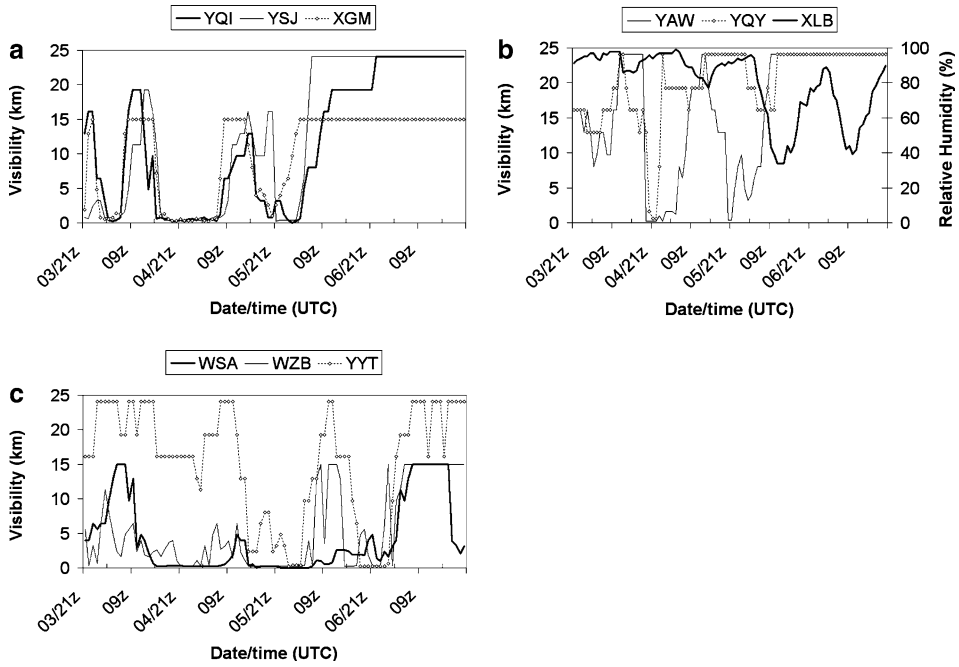

Figure 2
Time series data 04–07 July, 2003: (a) Bay of Fundy, (b) Nova Scotia with XLB in HR%, (c) West Atlantic with WZB and YYT + 0.5 h.

The selection of 05 July, 2003 for detailed study follows from the criterion that fog banks be identified clearly from satellite images unobscured by higher level clouds. Figure 3a shows what appears to be a fog bank oriented southeast to northwest, terminating at southern Nova Scotia. A bank of low cloud, judging from the brightness in the visible image, appears to the north along the same orientation. Also shown is the 1800 UTC OA of ES at eta 1.0 and 0.995 in Figure 3b, compared to the 1800 UTC GEM forecast of ES at eta 0.995, corresponding to a height about 50 m above the surface in Figure 3c. It must be noted that the archived eta-level GEM operational forecast data from the CMC archive had 25 km resolution and used a different storage format in 2003, and do not include the eta levels above the surface. Therefore height-dependent fog/moisture depth contours as shown for the following case studies are not available, although the ES contours at eta

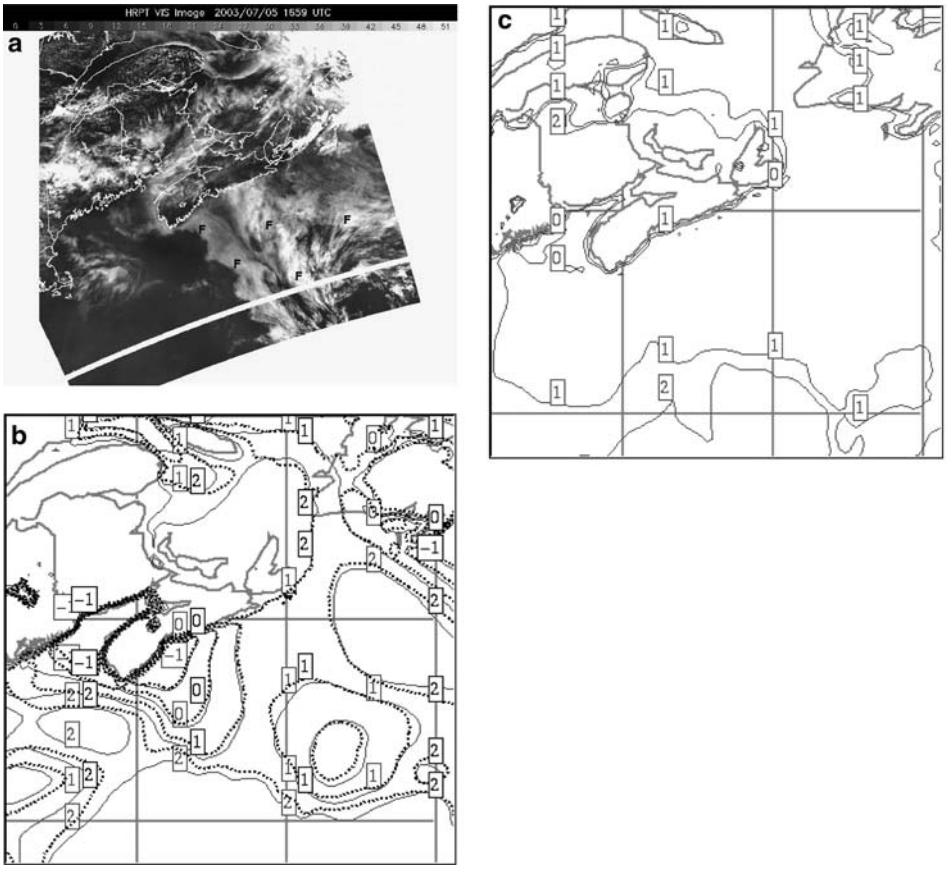

Figure 3
05 July, 2003: (a) 1659 UTC HRPT 0.6 μm visible image, (b) 1800 UTC ES at eta 1.0 (dotted lines) and 0.995 (solid lines) from OA, (c) ES at eta 1.0 from GEM T_0 + 18 h forecast.

0.995 correspond directly to the lowest fog/moisture category in the later figures. The GEM forecast does not capture the variable near-saturation ES fields in the West Atlantic shown by the OA, however neither data set completely represents the fog bank inferred from the satellite images. Also, while the physical threshold for fog occurs when ES ≤ 0 C the contours show improved agreement with satellite images when using a threshold of ES < 2.0 C.

3.1.4. Vertical fog structure from radiosonde observations and OA

Figure 4 shows a comparison between radiosonde observations and the OA for TT and TD at the mandatory pressure levels for YQI and WSA, and more detailed TT and TD profiles in the lowest 2000 m. While verification scores are calculated for ES, the profiles show TD, where ES ≤ TT - TD. Observations suggest the lowest layers up to 200 m are saturated at both locations, and remain fairly humid within the lowest 1500 m. This is consistent with prerequisite conditions for fog, and coincides with low visibilities observed in Figure 2 at 1200 UTC on 05 July.

Relative to the observations the OA plots indicate that TT is consistent with observations while ES displays significant variation with height, showing more

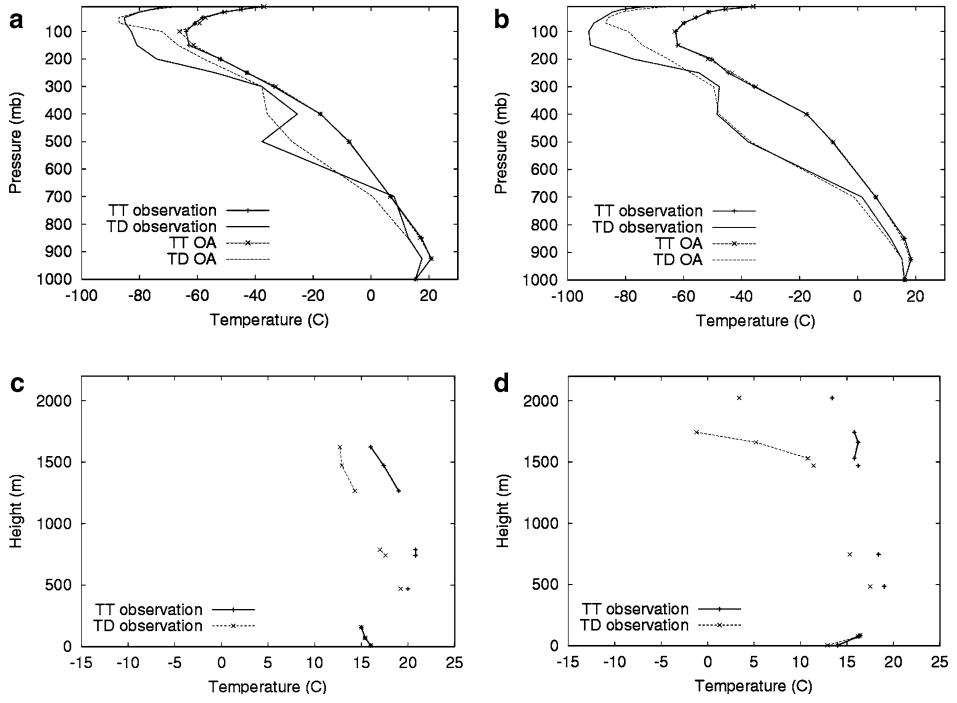

Figure 4
OA versus radiosonde data 1200 UTC 05 July, 2003: (a) YQI, (b) WSA, (c) YQI lower troposphere (d) WSA lower troposphere.

Table 1

1200 UTC OA versus radiosonde data: 1000–100 mb full atmosphere scores [1000–850 mb boundary layer scores in brackets]

Date	ES MB (C)	ES RMS (C)	TT MB (C)	TT RMS (C)
YQI				
04 July 2003	1.36 [0.34]	4.49 [0.56]	−0.31 [0.03]	0.72 [0.5]
05 July 2003	2.28 [0.04]	7.63 [0.2]	−0.22 [0.13]	0.92 [0.29]
06 July 2003	4.2 [0.75]	8.14 [1.39]	−0.21 [0.15]	0.73 [0.29]
07 July 2003	0.98 [−0.24]	5.11 [0.48]	−0.39 [−0.28]	0.8 [0.66]
Average	2.21 [0.22]	6.34 [0.68]	−0.28 [0.01]	0.79 [0.44]
WSA				
04 July 2003	−1.53 [−1.28]	7.47 [2.19]	−0.28 [0.32]	0.96 [0.57]
05 July 2003	3.66 [−0.15]	7.24 [0.35]	0.04 [0.3]	0.6 [0.43]
06 July 2003	4.11 [−0.04]	7.18 [0.56]	−0.35 [−0.8]	0.97 [1.01]
07 July 2003	2.42 [0.25]	5.5 [0.46]	−0.18 [0.43]	0.64 [0.44]
Average	2.17 [−0.3]	6.87 [0.89]	−0.2 [0.06]	0.79 [0.61]

variation at higher altitude and somewhat more variation at YQI than WSA. It is not surprising that the more conservative parameter TT varies much less than ES, but physics of fog formation require a high degree of precision to determine when and how much water vapor condenses into fog. Therefore, obtaining accurate ES values is as important as TT in numerical simulations involving fog.

In Table 1 the MB at YQI and WSA indicate that OA ES is generally drier than observed ES, while being cooler for TT. The RMS scores between observed and OA fields for TT and ES confirm the larger difference of OA ES compared to measured ES. Note that these scores are for the atmosphere from 1000–100 mb and thus include variations at high altitudes which may be less relevant to surface phenomena. While scores calculated only from the 1000, 925 and 850 mb levels may not be statistically robust they indicate the differences of TT and ES in the boundary layer, and are shown in the table and in the text in brackets. While this case shows consistently higher scores from 1000–100 mb compared to the boundary layer only, this is not always true for the other cases. The daily ES variability is typical for all cases, but for brevity the remaining scores will be averaged over the 4-day duration of each case study.

3.1.5. Comparison and discussion of GEM forecast versus OA

As shown in Table 2, the MB for horizontal fields at eta level 1.0 indicate GEM forecast TT and ES are generally cooler and smaller than the OA to a comparable extent, but ES RMS differences are almost double that for TT. Note that these scores are for the entire 900 by 900 km domain, and thus include horizontal variations too distant to affect Lunenburg Bay. Combined with the previous discussion this suggests

Table 2

GEM forecast at T_0 + 18 h versus OA at 1800 UTC: 2-D fields at eta level 1.0

Date	ES MB (C)	ES RMS (C)	TT MB (C)	TT RMS (C)
04 July 2003	0.51	2.42	0.03	1.71
05 July 2003	−0.95	3.79	−0.9	2.32
06 July 2003	−2.12	3.52	−1.09	1.55
07 July 2003	−1.03	2.42	−1.26	1.54
Average	−0.9	3.04	−0.81	1.78

that near the surface there are three-dimensional systematic differences between observations and OA for TT and ES, introducing errors to the initial conditions from the OA and therefore affecting forecast quality.

3.2. Case Study 2: 29 June–02 July, 2004

3.2.1. Synoptic weather summary

During the study period from 28 June to 01 July, 2004 there was a generally light south to southwest synoptic-scale wind flow over Nova Scotia and waters to the south. On 29 June a trough of low pressure tracked across Nova Scotia bringing a period of mid- and upper-level cloudiness with a few light showers over Nova Scotia. A weak low formed from the trough to the south of Nova Scotia late on 29 June. There were light winds associated with this weather feature. On 30 June and 01 July the weak southwest flow returned. Over Nova Scotia, coastal seabreezes were prevalent with afternoon cumulus cloudiness observed inland (FOGARTY, 2004, pers. Comm.).

3.2.2. Station time series

In the Bay of Fundy area Figure 5 indicates a number of isolated fog episodes becoming more widespread 2100–0200 UTC 30 June-1 July, and 1900–0400 UTC 1–2 July at YQI and YSJ. With XLB again showing relative humidity, the Nova Scotia area indicates widespread fog 1800–0300 UTC 30 June-1 July and 2100–0700 UTC 1–2 July at XLB, YAW and YQY. In spite of the distance between stations in the West Atlantic area which suggests isolated patches, widespread fog is indicated 1500–0400 UTC 30 June-1 July and 2100–1200 UTC 1–2 July at WSA, WZB and YYT.

3.2.3. Horizontal fog distribution from satellite images and OA

Obscuration from higher clouds was minimal on 30 June 2004 over XLB, so this date was selected for investigation. The visible image in Figure 6a suggests low cloud or fog along the southeast coast of Nova Scotia extending well into the west Atlantic, including Sable Island and Newfoundland. Areas where ES ≤ 2 C in the CMC OA

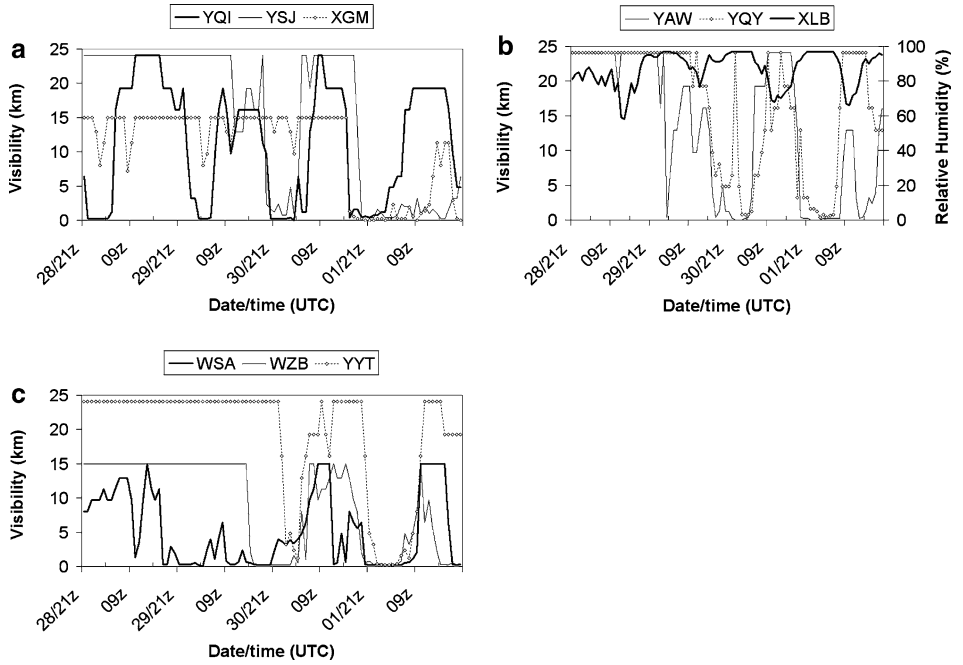

Figure 5
Time series data 29 June-02 July, 2004: (a) Bay of Fundy, (b) Nova Scotia with XLB in HR%, (c) West Atlantic with WSA + 0.5 h.

field are shown in Figure 6b as 1 when at eta level 0.995 only, while a continuous layer from eta 0.995–0.985 is shown as 2, 0.995–0.9733 as 3, 0.995–0.9606 as 4 and 0.995–0.9467 as 5. Eta 1.0–0.9467 are the lowest six levels of the OA and GEM forecast corresponding to the surface layer up to about 500 m. These form a perimeter around west and southeast Nova Scotia with an extension to the south, but not extending as far out into the Atlantic. Similar features occur in the GEM forecast in Figure 6c, except that the extension into the Atlantic and south of Nova Scotia is more extensive than the satellite images suggest. Note that 'ES depth contour' 1 corresponds directly to ES at eta level 0.995 in Figure 3.

3.2.4. Vertical fog structure from radiosonde observations and OA

Vertical profile comparisons of TT and TD between radiosonde observations and the OA are shown in Figure 7. The averaged TT MB is 0.03 C [−0.06 C] at YQI and 0.23 C [0.28 C] at WSA, while for ES it is 0.73 C [-0.31 C] at YQI and 1.5 C [−0.26 C] at WSA. Thus for TT and ES at both locations, OA values are generally warmer and moister than observed values, with the vertical profiles suggesting more variation at higher altitudes. The averaged RMS score indicates significantly larger differences between OA and observations for ES, being 3.14 C [1.0 C] at YQI and

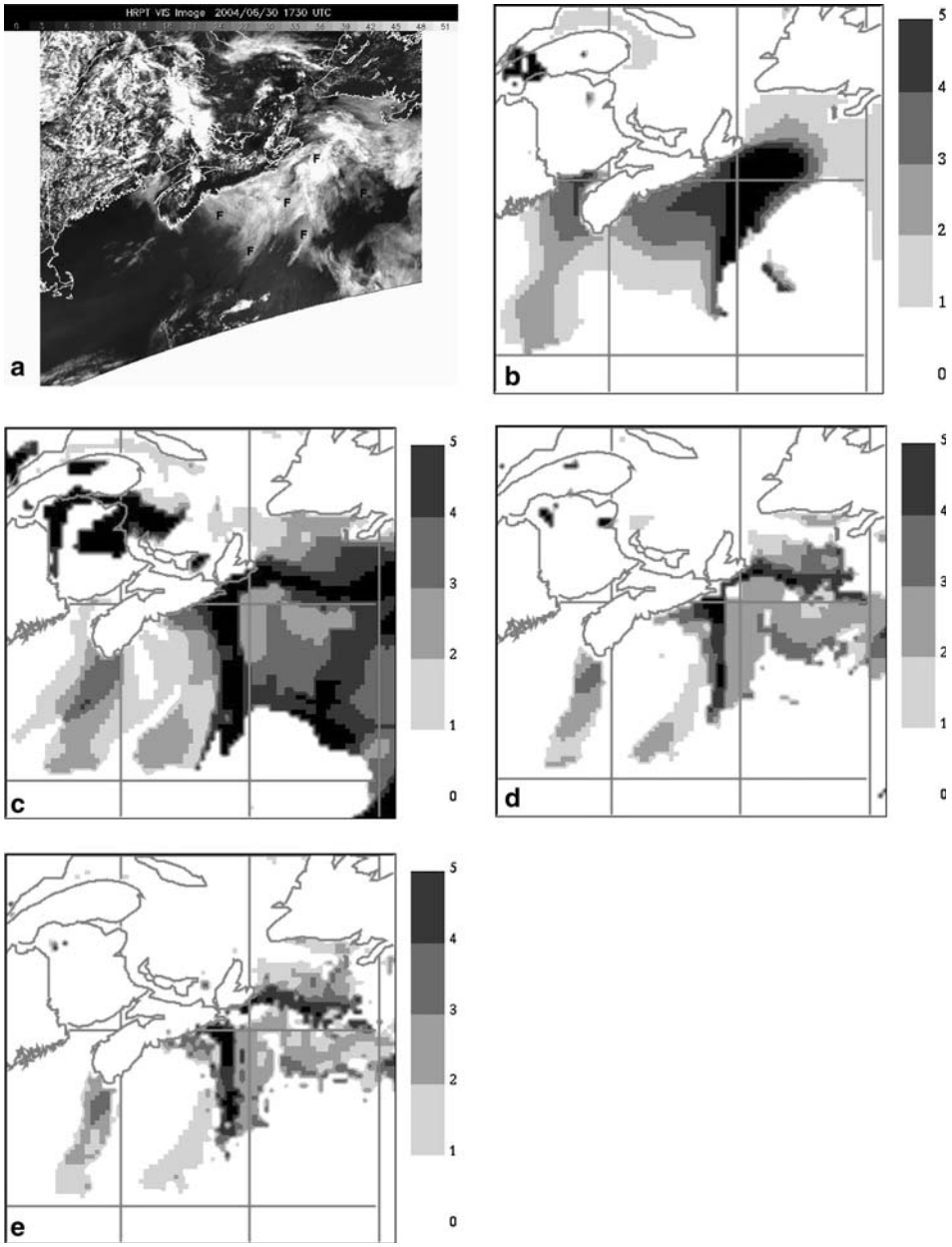

Figure 6
30 June, 2004: (a) 1730 UTC HRPT 0.6 μm visible image, (b) 1800 UTC OA moisture depth for ES $<$ 2 C where 1 is eta 0.995, 2 is eta 0.995–0.985, 3 is eta 0.995–0.9733, 4 is eta 0.995–0.9606 and 5 is eta 0.995–0.9467, (c) GEM T_0 + 18 h forecast moisture depth same as (b), (d) GEM T_0 + 18 h forecast moisture depth for ES $<$ 0.5 C, same levels as (b), (e) GEM T_0 + 18 h forecast moisture depth for QC $>$ 0 kg/kg, same levels as (b).

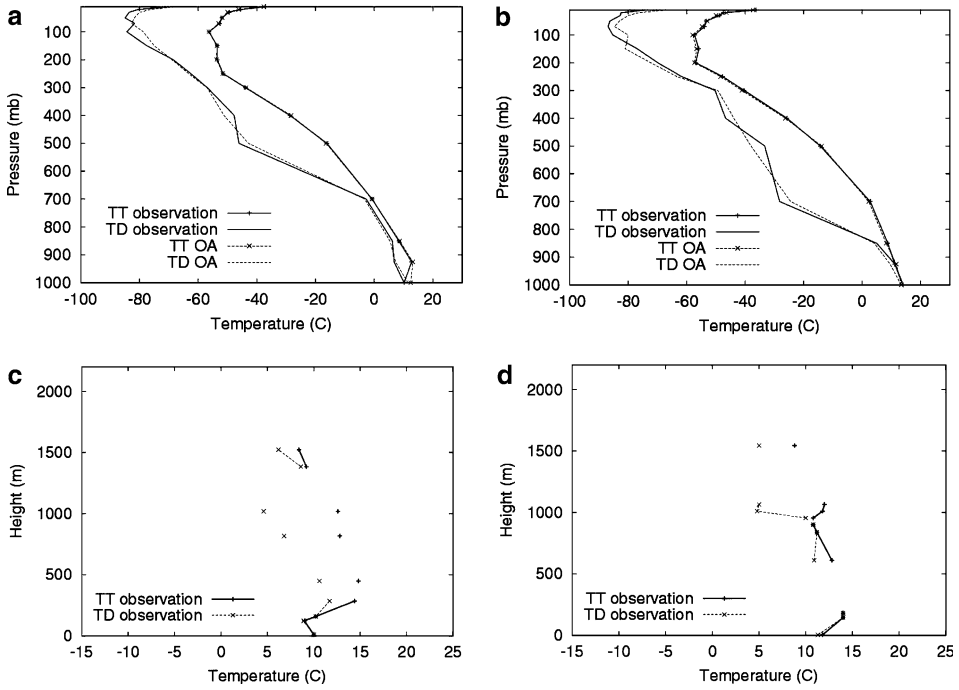

Figure 7
OA versus radiosonde data 1200 UTC 30 June, 2004: (a) YQI, (b) WSA, (c) YQI lower troposphere (d) WSA lower troposphere.

4.06 C [1.2 C] at WSA while for TT they are 0.66 C [0.73 C] at YQI and 0.89 C [0.48 C] at WSA. As in the previous case, scores calculated for 1000, 925 and 850 mb in the boundary layer only are shown in brackets. Radiosonde observations in the lowest 200 m indicate saturated conditions at YQI and WSA, with WSA showing humid to saturated conditions up to 1000 m. While the saturated conditions at WSA are consistent with fog observed in Figure 5, the observed visibility at YQI does not indicate that fog occurred at 1200 UTC on the second day.

3.2.5. Comparison and discussion of GEM forecast versus OA

Since fog is a boundary layer phenomenon, the following comparisons have been vertically truncated at eta level 0.84 to focus on GEM forecast and atmospheric OA fields in the lowest 1000 meters. There are important points to note in Figure 8. First, the CMC OA allows unrealistic negative dew point spreads as shown by crossing TT and TD profiles. Second, significant deviations of the GEM forecast from the OA may be observed in the lowest levels where fog would be expected to form. Third, saturated conditions in the OA up to eta 0.99 at YQI and eta 0.97 at WSA and XLB are not well represented by the GEM forecast, and in fact saturation at WSA is

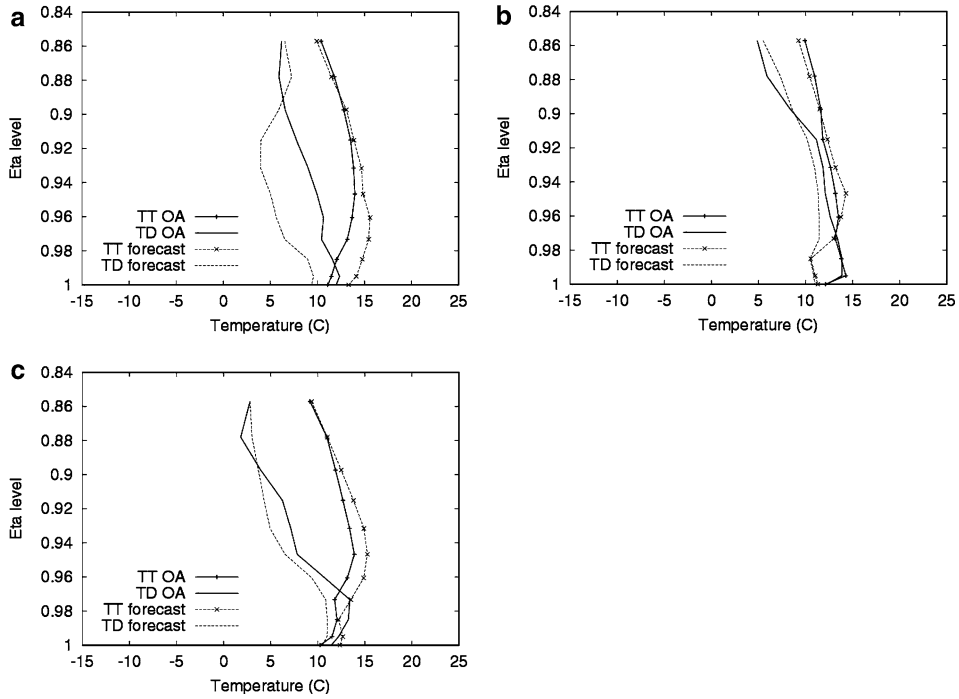

Figure 8
GEM forecast at T_0 + 12 h versus OA at 1200 UTC 30 June, 2004: (a) YQI, (b) WSA, (c) XLB.

modelled by GEM only because TT and TD are both significantly lower than in the OA.

Table 3 shows typical verification scores comparing OA and GEM forecasts in the vicinity of XLB. The TT MB suggests GEM forecasts are warmer than the OA except at WSA, which may be due to its surface boundary representation in the land-sea mask as an ocean grid point having a smaller diurnal temperature range. In half of the cases a positive ES MB suggests the vertically averaged humidity is less, and implies that the GEM forecast which does not reach saturation is less able to represent fog. Variation between individual days of the RMS scores for TT and ES are within a factor of three, but differences are largest between TT and ES rather than between individual locations or days. Both tendencies are also shown by the time-averaged scores.

For the horizontal fields at eta level 1.0, the averaged MB of −0.96 C for TT suggests OA values generally cooler than the GEM forecast values, but drier for ES at 0.11 C. The averaged RMS of 1.68 C for TT indicates higher horizontal than vertical differences between OA and GEM forecast value, but the opposite for ES with 2.32 C. Figures 6d and 6e shows vertically integrated moisture depths where QC $>$ 0.0 kg/kg implies the presence of condensate with the associated visibility effects.

Table 3

GEM forecast at T_0+12 h versus OA at 1200 UTC

Date	ES MB (C)	ES RMS (C)	TT MB (C)	TT RMS (C)
YQI				
29 June 2004	−1.51	2.58	−0.18	0.81
30 June 2004	3.9	4.83	1.21	1.65
01 July 2004	−0.35	1.62	0.44	0.58
02 July 2004	1.13	3.29	−0.58	0.83
Average	0.79	3.06	0.22	0.97
WSA				
29 June 2004	−3.87	4.59	−1.0	1.18
30 June 2004	0.43	1.31	−0.58	1.49
01 July 2004	−1.0	2.31	−1.74	2.33
02 July 2004	−1.11	2.16	0.17	0.72
Average	−1.39	2.59	−0.79	1.43
XLB				
29 June 2004	−0.64	1.17	−0.03	0.43
30 June 2004	2.23	2.72	1.06	1.26
01 July 2004	1.34	2.11	0.83	0.95
02 July 2004	1.41	3.33	−0.85	0.99
Average	1.09	2.33	0.25	0.91

This correlates GEM forecast QC with clouds and fog in satellite images while matching reasonably well with ES ≤ 0.5 C. Neither plot represents the fog bank in Figure 6a as well as the OA where ES ≤ 2.0 C, although both show some improvement over the GEM forecast where ES ≤ 2.0 C.

3.3. Case Study 3: 04–07 October, 2005

3.3.1. Synoptic weather summary

On 0000 UTC 04 October, 2005 a high pressure system located 300 km south of Nova Scotia continued to track slowly eastward. The high pressure region had a northeast-southwest ridge which was responsible for an increasing southerly flow of moist air over Canadian Maritime regions. The southerly flow continued through 06 October as the high moved eastward, resulting in an extensive area of marine fog. By 06 October, a frontal system which had developed in Ontario and Quebec was continuing southward through the Gulf of St. Lawrence in an east-west orientation. Temperatures over marine regions throughout the period were 17–20 C.

3.3.2. Station time series

The visibility time series in Figure 9 suggest sea fog with more spatial differences than the previous cases. In the Bay of Fundy area, YQI shows almost continuous fog

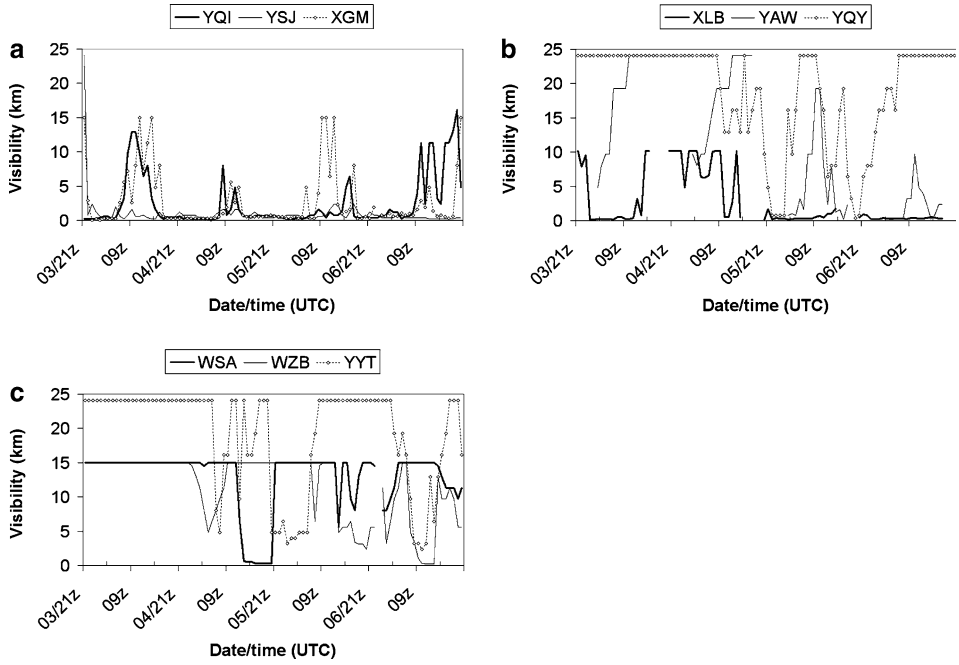

Figure 9
Time series data, 04–07 October, 2005: (a) Bay of Fundy, (b) Nova Scotia, (c) West Atlantic with WZB and YYT + 0.5 h.

while clearing breaks are indicated at 0700–1700 UTC on 04 October and 0900–1800 UTC on 06 October by YSJ and XGM. Fog episodes 2100–0400 UTC 05–06 October and 1400–1200 UTC 06–07 October may be inferred in the Nova Scotia area at XLB and YQY. Note that for this case study, data from a new visibility sensor recently installed at Cross Island in Lunenburg Bay replaces relative humidity from XLB. Determining contiguous fog banks is less clear in the West Atlantic area due in part to the distance separating the stations, and in this case the visibility time series seem uncorrelated at WSA, WZB, or YYT.

3.3.3. Horizontal fog distribution from satellite images and OA

The best cloud-free conditions over XLB occurred on 05 October, 2005, which was selected for further study. The main feature visible in Figure 10a appears to be a nonuniform bank of low clouds or fog running east northeast from the Bay of Fundy to just south of Newfoundland. Also shown in Figure 10b are plots of fog depth contours integrated from the surface where ES ≤ 2 C in the 1800 UTC OA as defined for Figure 6, and similar contours from the 1800 UTC GEM forecast in Figure 10c. Low ES areas in the OA plot generally agree with the outlines of the fog bank inferred from the satellite images, whereas the GEM forecast shows somewhat

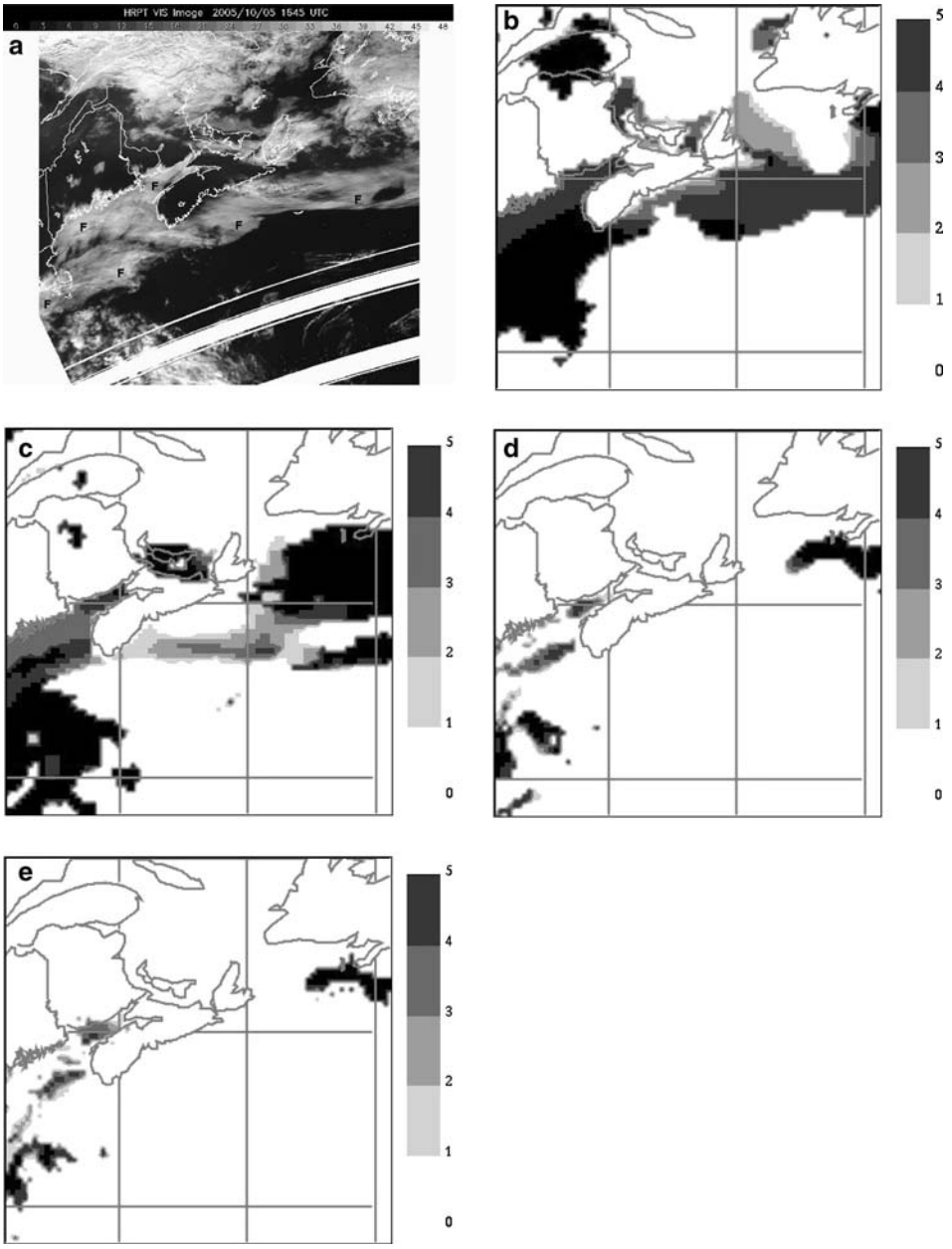

Figure 10
05 October, 2005: (a) 1645 UTC HRPT 0.6 μm visible image, (b) 1800 UTC OA moisture depth for ES $<$ 2 C, same levels as Figure 6, (c) GEM T_0 + 18h forecast moisture depth for ES $<$ 2 C, same levels as (b), (d) GEM T_0 + 18h forecast moisture depth for ES $<$ 0.5 C, same levels as (b), (e) GEM T_0 + 18h forecast moisture depth for QC $>$ 0 kg/kg, same levels as (b).

smaller low ES areas around Nova Scotia, and southward displacement of the middle section near XLB.

3.3.4. Vertical fog structure from radiosonde observations and OA

At the mandatory pressure levels in Figure 11 the OA TT compares well with the observed TT at both YQI and WSA, while OA ES and therefore TD varies significantly from observed ES at both locations. At YQI ES is saturated in the lowest 300 m, becoming much less humid above 500 m, consistent with low visibilities at 1200 UTC on 05 October in Figure 9. Except for the surface layer humidity not reaching saturation, similar behavior is observed at WSA, correlated with decreasing visibility in the time series from Figure 9.

Taking average values over four days for MB, OA TT appears to be generally warmer than observed TT with 0.29 C [0.21 C] for YQI and 0.2 C [−0.04 C] for WSA. OA ES appears generally drier than observed ES, −0.76 C [-1.7 C] at YQI and −0.83 C [−0.94 C] at WSA. The averaged TT RMS is 0.87 C [0.66 C] for YQI and 0.82 C [0.46 C] for WSA while the averaged ES RMS is 2.72 C [3.2 C] for YQI

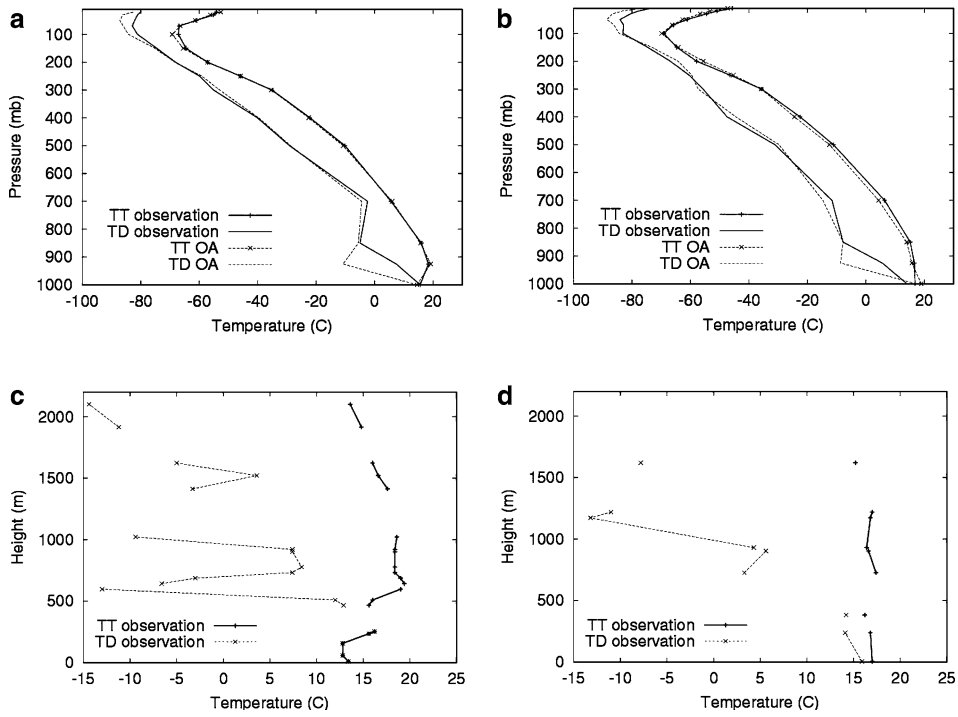

Figure 11
OA versus radiosonde data, 1200 UTC 05 October, 2005: (a) YQI, (b) WSA, (c) YQI lower troposphere (d) WSA lower troposphere.

and 2.97 C [3.03 C] for WSA, indicating similar differences at the two locations. As in the previous case, scores calculated for 1000, 925 and 850 mb in the boundary layer only are shown in brackets. One reason why the boundary layer scores are not significantly lower than those for 1000–100 mb is the extreme ES values from the OA exceeding observations by 11 C on 1200 UTC 05 October, 2005 at YQI for example.

3.3.5. Comparison and discussion of GEM forecast versus OA

The same observations for Figure 8 may be made for Figure 12, where the saturated layer up to eta 0.96 at YQI and XLB is represented with comparable errors by the GEM forecast, which also shows larger ES errors at higher levels. The most remarkable difference is at WSA where the profiles are fairly similar except that the GEM forecast shows a deeper humid layer up to eta 0.92, compared to eta 0.96 in the OA.

For comparisons between OA and GEM forecasts, the averaged TT MB for YQI is −0.16 C compared to −0.57 C for WSA, suggesting that GEM forecast TT is generally cooler than OA TT at those stations. In contrast the averaged TT MB at

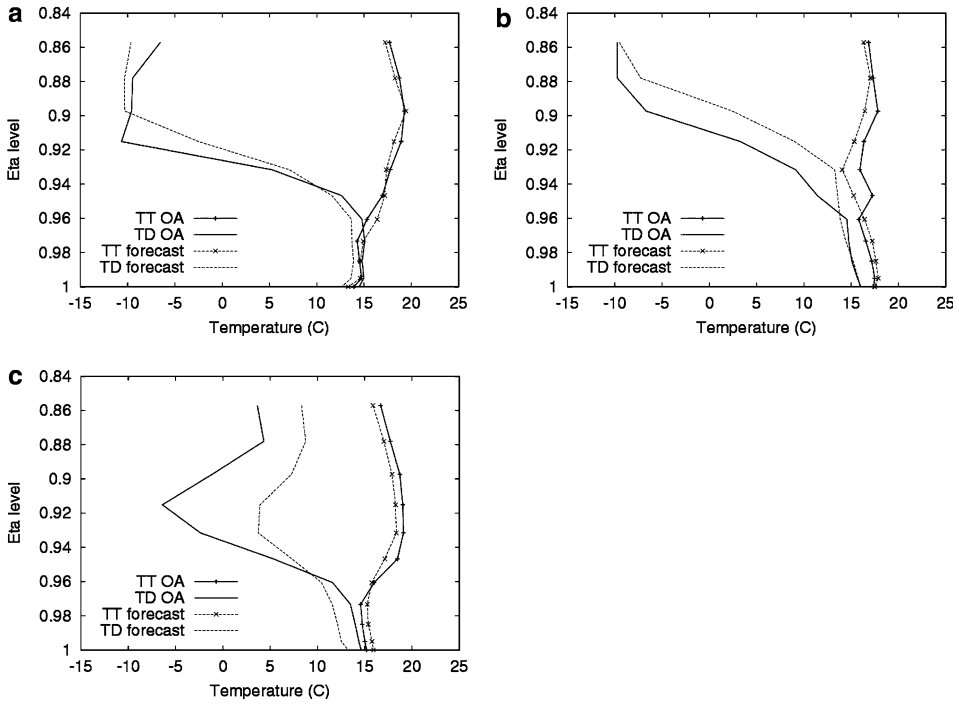

Figure 12
GEM forecast at T_0 + 12 h versus OA at 1200 UTC, 05 October, 2005: (a) YQI, (b) WSA, (c) XLB.

XLB is 0.14 C, suggesting the opposite. The corresponding averaged TT RMS of 0.56 C at YQI and 0.88 C at WSA suggest a smaller difference than 1.07 C at XLB. The averaged ES MB at YQI is 0.51 C, compared to −2.1 C at WSA and −0.83 C at XLB where the GEM forecast is generally moister than the OA. The averaged ES RMS of 3.48 C at WSA is comparable to 3.07 C at XLB, suggesting larger differences at those stations than YQI with 1.91 C. For the horizontal fields at eta level 1.0, the averaged MB of 0.36 C for ES suggests OA values generally greater than the GEM forecast values. The averaged RMS of 1.32 C for TT indicates higher horizontal than vertical differences between OA and GEM forecast value, but the opposite for ES with 1.99 C. Figure 10d shows integrated moisture depths where ES $\leq$ 0.5 C and Figure 10e shows QC $>$ 0.0 kg/kg using the same heights as defined for Figure 6. The contours look very similar in spite of differing parameters, but both underestimate the extent of the fog shown by the satellite images, OA and GEM forecast using ES $\leq$ 2.0 C. However this is consistent with similar plots for most days of the three case studies not shown here, except for Figure 6.

4. Summary and Conclusions

From all case studies there are notable differences between the OA and observations. This is compounded when the OA data are used to initiate and provide boundary conditions for the GEM forecast, leading to accumulated errors relative to the original measurements. This is especially relevant for fog forecasting where condensation thresholds are sensitive to temperature and humidity errors, and in these examples some errors have approached a substantial fraction of measured values. It must be noted that the vertical profile scores are for the atmosphere from 1000–100 mb, where deviations are generally larger in the upper atmosphere than near the surface. Scores calculated from 1000–850 mb are not consistent for all three cases, but seem to indicate less deviation in the boundary layer. Similarly, the horizontal scores include deviations from distant surface locations which may not affect Lunenburg Bay.

The integrated moisture depths in Figures 6b, 6c, 10b and 10c suggest that ES $\leq$ 2.0 C yields a reasonable match for the OA versus the horizontal distribution of fog in satellite images, but is less satisfactory when applied to the GEM forecast. Similar plots from the GEM forecast in Figures 6d, 6e, 10d and 10e indicate that while QC $>$ 0.0 kg/kg corresponds to a real physical threshold and corresponds well with ES $\leq$ 0.5 C, neither shows consistent improvement over the GEM forecasts where ES $\leq$ 2.0 C in Figures 6c and 10c. Figures 7 and 11 show vertical profiles typical for TT and ES at all locations, on all days with available GEM forecast data. In general the largest systematic deviations of the GEM forecast from the OA are at higher altitudes, but those occurring near the surface still suggest decreased accuracy of ES and to a lesser extent TT. The tendency for

Table 4

GEM forecast versus OA

Date	Averaged MB (C)	ES RMS (C)	Averaged MB (C)	TT RMS (C)
Eta 1.0 horizontal fields at 1800 UTC				
04–07 July 2003	−0.9	3.04	−0.81	1.78
29 June-02 July 2004	0.11	2.32	−0.96	1.68
04–07 October 2005	0.36	1.99	0.03	1.32
YQI 1200 UTC vertical profile				
29 June-02 July 2004	0.79	3.06	0.22	0.97
04–07 October 2005	0.51	1.91	−0.16	0.56
WSA 1200 UTC vertical profile				
29 June-02 July 2004	−1.39	2.59	−0.79	1.43
04–07 October 2005	−2.1	3.48	−0.57	0.88
XLB 1200 UTC vertical profile				
29 June-02 July 2004	1.09	2.33	0.25	0.91
04–07 October 2005	−0.83	3.07	0.14	1.07

cooler TD, and thus higher ES, in the GEM forecasts is also notable. Table 4 summarizes the averaged verification scores for all three cases and in general the RMS varies over a comparable range for vertical profiles and horizontal areas, larger for ES than TT. Near the surface the GEM forecast TT is cooler but ES is drier on average than the OA as indicated by the MB, while the vertical profile MB for YQI and XLB indicates the GEM forecast TT is warmer and ES drier on average than the OA. When combined these imply a net tendency for GEM to underpredict fog conditions except at WSA, modelled as an oceanic location, where the MB indicates cooler TT and moister ES in the GEM forecast. This tendency of GEM forecasts to become drier near the surface compared to the OA is due in part to the configuration of surface boundary physics submodels mentioned in Section 2.2. Thus for boundary layer phenomena in general and fog in particular, GEM should be reconfigured to accommodate the relevant surface physics, condensation thermodynamics plus spatial and temporal resolution.

ES and QC appear to be useful fog proxies, but might be improved when supplemented by other parameters.

In summary, the following conclusions have emerged from this study.

1. The CMC OA contain differences from vertical observations of TT and ES that could decrease forecast quality, although most occur above the boundary layer.
2. There is a consistent correspondence between fog satellite images and horizontal ES contours from the OA and operational GEM forecasts, at levels drier than the condensation threshold.
3. The operational GEM forecasts show limited correspondence with fog satellite images, due likely to a combination of poorly resolved moisture fields in the OA

and non-optimum boundary layer condensation physics leading to underprediction of TD and QC.

While sea fog formed and advected by mesoscale flow can in principle be represented in the operational GEM forecast, these conclusions indicate that modelling considerations specific to sea fog must be taken into account if reliable forecasts are required.

5. Future Work

It has been shown that the current operational 15 km regional GEM forecast is insufficient for forecasting fog. Approaches to address this deficiency by appropriately configuring the numerical model include GEM experiments to find optimum combinations of surface physics parameterizations for sea fog which are currently underway. This could also include modifying the surface scheme moisture options and the near-surface diagnostic extrapolation method mentioned in Section 2.2. A second approach would involve complementary experiments using similar model configurations with a different numerical weather prediction model like the Mesoscale Compressible Community model (MC2); this has already been done for 15, 9, 3 and 1km resolutions and will be presented in a forthcoming paper.

Other approaches that could address the poor representation of moisture in the model input data include numerical bogusing techniques to assimilate fog banks in satellite imagery into the OA. Development of satellite analogue advection fog model output products using techniques similar to satellite radiance analogues calculated from model output as developed by (GARAND and NADON, 1998) is a possibility. In the longer term we anticipate that increased model resolution, denser in situ and remotely sensed observations, and improved parameterizations of physical processes will lead to improved fog analysis and forecasting.

Acknowledgements

The authors would like to acknowledge the contributions of summer intern Olga Stachowiak and co-op student Victoria Whiffen, as well as assistance from Andrew Phillips, Teresa Canavan and Christopher Fogarty from the Meteorological Service of Canada at Dartmouth and Jocelyn Mailhot at Dorval. Financial support for Lorenzo de la Fuente was provided by the Canadian Foundation for Climate and Atmospheric Sciences.

We also wish to dedicate this paper to our late colleague Dr. Yves Delage, whose contributions will be sorely missed.

References

MURACA, G., MACIVER, D.C., URQUIZO, N., and AULD, H., *The climatology of fog in Canada*, Conf. *Fog and Fog Collection* (St. John's Canada, 2001).

WEBER, A. and BUCKLEY, R.L., *Visibility trends for coastal regions*, 14th Conf. *Applied Climatology* (Am. Meteor. Soc. 2004).

WHIFFEN, B., DELANNOY, P., and SIOK, S., *Fog: Impact on road transportation and mitigation options*, 10th World Congress and Exhibition on *Intelligent Transportation Systems and Services* (Madrid Spain, 2003).

RIORDAN, D. and HANSEN, B. K. (2002), *A fuzzy case-based system for weather prediction*, Eng. Int. Syst. *3*, 139–146.

ROACH, W.T. (1994), *Back to basics: Fog – Definitions and basic physics*, Weather *49*, 411–415.

ENVIRONMENT CANADA, *Where the wind blows* (Breakwater Books Ltd., St. John's Newfoundland 1995).

TELFORD, J.W. and CHAI, S.K. (1993), *Marine fog and its dissipation over warm water*, J. Atmos. Sci. *50*, 3336–3349.

LEWIS, J.M., KORACIN, D., and REDMOND K.T. (2004), *Sea fog research in the United Kingdom and United States: A historical essay including outlook*, Bull. Am. Meteor. Soc. *85*, 395–408.

OSBORNE, A.H. (1976), *Techniques for the prediction of sea fog over the Scotian shelf*, Technical Report TEC 825, Environment Canada.

LEIPPER, D.F. (1994), *Fog on the U.S. West Coast: A review*, Bull. Am. Meteor. Soc. 75, 229–240.

GEISZLER, D., COOK, J., TAG, P., THOMPSON, W., BANKERT, R., and SCHMIDT, J. (2000), *Evaluation of ceiling and visibility prediction: preliminary results over the California coast using COAMPS*, Sci. Appl. Internat. Corp.

RITCHIE, H., DESJARDINS, S., SHENG, J., and WANG, L., *Coupled atmosphere-ocean observations and modeling for Lunenburg Bay, Nova Scotia*, Sym. *Forecasting the Weather and Climate of the Atmosphere and Ocean* (American Meteorological Society 2004).

MAILHOT, J. (2006), Pers. corresp.

STULL, R.B., *Meteorology for Scientists and Engineers* (Brooks/Cole, Pacific Grove California 2000).

UNIVERSITY CORPORATION FOR ATMOSPHERIC RESEARCH, *COMET: Satellite Meteorology,* http://www.comet.ucar.edu/class/satmet/ellrod.html, 2006.

CÔTE, J., GRAVEL, S., MÉTHOT, A., PATOINE, A., ROCH, M., and STANIFORTH, A. (1998), *The Operational CMC-MRB Global Environmental Multiscale (GEM) Model. Part 1: Design considerations and formulation*, Mon. Wea. Rev. *126*, 1373–1395.

FOGARTY, C. (2004), pers. corresp.

GARAND, L. and NADON, S. (1998), *High-resolution satellite analysis and model evaluation of clouds and radiation over the Mackenzie Basin using AVHRR data*, J. Climate *11*, 1976–1996.

(Received June 15, 2006, accepted September 2, 2006)
Published Online First: May 16, 2007

Pure appl. geophys. 164 (2007) 1327–1345
0033–4553/07/071327–19
DOI 10.1007/s00024-007-0221-8

Pure and Applied Geophysics

Implementation of a Single-Column Model for Fog and Low Cloud Forecasting at Central-Spanish Airports

ENRIC TERRADELLAS[1] and DARÍO CANO[2]

Abstract—Operations at Central-Spanish airports are often, especially in winter, affected by visibility reduction. The *Instituto Nacional de Meteorología* (INM), the Spanish Weather Service, has developed a single-column model (SCM) in order to improve short-term forecasts of fog, visibility and low-clouds. The SCM, called H1D, is a one-dimensional version of the HIRLAM limited-area model. It is operationally run for three airports in the region: Madrid-Barajas, Almagro and Albacete-Los Llanos. Since SCMs cannot deal with horizontal heterogeneity, the terms that depend on the horizontal structure of the atmosphere are estimated from the outputs of the three-dimensional (3-D) model and introduced into the SCM as external forcings. The systematic analysis of the meteorological situations has evidenced the existence of a close relationship between fog formation and the presence of drainage winds in the region. Since the 3-D model docs not have the necessary resolution to correctly simulate the main features of the drainage flow caused by the complex topography in the proximity of Madrid-Barajas, it cannot provide the SCM with the correct forcings. This problem has been partially overcome through the introduction of a module that, under certain conditions, substitutes the values computed from the 3-D model outputs by others that are based on a conceptual model of the phenomenon and have been empirically derived from climatological knowledge. This module improves the H1D verification scores for the basic meteorological variables—wind, temperature and humidity—and reduces the false alarm rate in fog forecast.

Key words: Drainage winds, fog forecast, low clouds, single-column model, visibility.

1. Background

1.1. Introduction

There are several important effects of fog and low clouds on land and marine transport (see e.g., MUSK, 1991 or TALLEY, 1999), but they are especially remarkable in aeronautical activities, where visibility reduction affects both the safety and the efficiency in the air-traffic management (ALLAN *et al.*, 2001). The need for precise forecasts is highlighted in numerous documents issued by the World Meteorological

[1] Enric Terradellas, Instituto Nacional de Meteorología, Arquitecte Sert, 1. 08005, Barcelona, Spain. E-mail: enric@inm.es
[2] Instituto Nacional de Meteorología, Madrid, Spain.

Organisation Commission for Aeronautical Meteorology, but, in spite of the pressing demand, the production of precise fog and low clouds forecasts constitutes an unsolved issue for operational weather services.

The first problem of numerical weather prediction (NWP) models relative to fog and low clouds forecasting is the deficient parameterization of the exchanges both within the atmospheric boundary layer (ABL) and between the surface and the lowest layers of the ABL. These parameterizations are especially imprecise in the stable ABL, the atmospheric framework for the fog development. Deficiencies come from the incomplete knowledge and the small scale of the phenomenology that takes place there.

During recent years, several field campaigns have been carried out aiming at improving the knowledge of the structure and dynamics of the stable ABL and, consequently, their parameterization in NWP models. Examples of such campaigns are SABLES-98 (CUXART *et al*., 2000b) in Central Spain, CASES-99 (POULOS *et al*., 2002) and VTMX 2000 (DORAN *et al*., 2002) in North America. In addition, new mathematical tools have been used in the data analysis to estimate turbulent kinetic energy and fluxes (TERRADELLAS *et al*., 2005). Nevertheless, most of this work has been done in the absence of liquid water. The estimation of vertical fluxes requires high-frequency measurements, but getting in-cloud, or even close to saturation, fast measurements of humidity is not a trivial issue. Also, the large-eddy simulations (LES) have turned out to be problematic in a strongly stable ABL (SAIKI *et al*., 2000; HOLTSLAG, 2003). The small size of eddies renders the model incapable of maintaining the resolved turbulence.

Fog formation is also directly related to microphysical processes that are not represented accurately enough in the models. In particular, horizontal visibility, one of the magnitudes to be forecast, is not in the basic prognostic equations and, therefore, it has to be diagnosed from other variables. Some studies have shown a relationship of the visibility with the droplet number concentration (e.g., MEYER *et al.,* 1980). Nevertheless, many models (the one described in this paper being among them) estimate the visibility from the equation presented by KUNKEL (1984) that relates it with the liquid water content, which constitutes a prognostic magnitude in most models. GULTEPE *et al*. (2006) carried out an analysis of observations collected during the Radiation and Cloud Experiment held in 1995 in Canada: They have presented a promising parameterization of the visibility as a function of both, droplet number concentration and liquid water content. In models without a prognostic equation for the droplet number concentration, its application calls for a relationship between the droplet number concentration and other magnitudes such as air temperature (GULTEPE and ISAAC, 2004).

Other problems of NWP models lie in their scarce horizontal and vertical resolutions, which are not suitable to predict phenomena that sometimes fall well within the microscale domain. Moreover, models are usually committed to reject observations that are not representative of a relatively extended area or to modify

them in order to improve their representativeness. In addition, during the assimilation process, the initial fields of mass and wind are forced to evolve in order to fulfil some prescribed, but not always realistic, relationships aimed to avoid the numerical growth of spurious waves. Therefore, especially over inhomogeneous terrain, the state of the atmosphere at a specific location can be considerably different to that in the closest model grid-point achieved after completing the initialisation procedures.

One way to overcome these problems is the use of one-dimensional (single-column) models (SCMs), where the terms depending on the horizontal structure of the atmosphere are estimated from the outputs of operational three-dimensional (3-D) models. The SCMs have been operationally used in different places, mainly for fog and low clouds forecasting (see TEIXEIRA and MIRANDA, 2001; TARDIFF, 2002; BERGOT *et al.*, 2005). They have also been used, mainly because of their simplicity, in the study of the behaviour of the atmosphere in particular situations. For example, DUYNKERKE (1991), BERGOT and GUÉDALIA (1994), and GUÉDALIA and BERGOT (1994) used them to analyze different fog events.

The main advantages of SCMs are that their vertical resolution can be greatly improved without a significant computational cost: that the parameterization schemes can be adapted to the kind of phenomenon or situation that is being simulated, and that local observations can be assimilated without any constraint with respect to spatial representativeness. Finally, the fact that some kind of local adaptation can be introduced into the SCM, generally through the substitution of external forcings coming from 3-D models, either based on climatological knowledge, or just obtained through the comparison of different trials (tuning), opens new possibilities for improvement.

It is important to bear in mind that SCMs cannot estimate horizontal advections or horizontal mass divergences. Therefore, they will only be useful over relatively flat terrain and in meteorological situations with a relative horizontal homogeneity. When the terms that depend on horizontal heterogeneity become important and a 3-D model is not able to provide precise estimations of them, the only possibility is to turn to climatological values that are often only available after extensive research, as described later in this paper for Madrid-Barajas airport.

The present paper presents the H1D (pseudo-acronym of one-dimensional HIRLAM) model, a single-column model developed at the INM, and its application for fog and low-clouds forecast at Central-Spanish airports. In section 1.2, the geographical framework is presented together with the main climatological features of the region. Section 2 describes the main features of the model, its initialization, the estimation of terms depending on horizontal heterogeneity, the local adaptation for Madrid-Barajas and the operational set-up. Section 3 reports some verification results. Finally, conclusions, ongoing research and future work are summarized in Section 4.

1.2. Geographic Framework

The area under study (Fig. 1), covered by the Madrid and *Castilla-La-Mancha* administrative regions, is located in Central Spain, on the southern part of the Central Iberian Plateau. The western part is gently tilted towards the Atlantic Ocean without any remarkable orographic obstacle, but the rest of the region is surrounded by mountains, like an amphitheatre. The Central Range, with peaks over 2400 meters above sea level (ASL), the highest in the region, represents the northern boundary; the Iberian Range and *Sierra Morena,* the eastern and southern limits, respectively. Two main rivers, Tajo and Guadiana, cross the region flowing westwards, with their respective basins divided by the Toledo Mountains. On the eastern part, the Júcar River flows southwards and then eastwards, crossing the mountains through narrow passes on its way towards the Mediterranean.

Madrid-Barajas is the main airport in the region. It is located several tens of kms south of the Central Range, east of the city. Near it there are several smaller airports around Madrid, primarily entrusted with general aviation, cargo or military operations: Torrejón, Colmenar Viejo, Cuatro Vientos and Getafe. Also, there is a military heliport (Almagro) in the southern part of the region and a civil and military airport (Albacete-Los Llanos) in the southeast.

In winter fog is relatively common over the region. The systematic analysis of the meteorological conditions in Central Spain has evidenced the coexistence of two mesoscale mechanisms in most fog events: Cold drainage winds converging at the bottom of valleys and a southern advection produced by a relatively warm and wet air mass coming either from the Mediterranean or from the Atlantic, which is lifted over the cold mass. These conditions are frequent when the western part of an anticyclone is placed over the region. Since the prevalence and the characteristics of

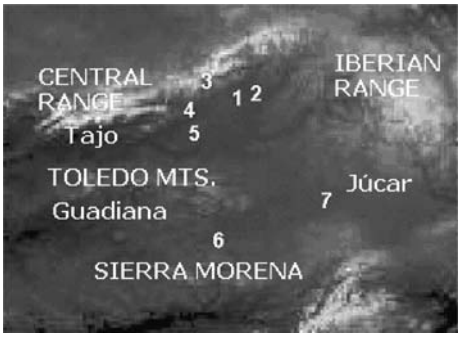

Figure 1
The main orographic features of the area under study: Central Range, Iberian Range and *Sierra Morena* surround the region. The Tajo and Guadiana rivers flow westwards, towards the Atlantic, and the Júcar River flows towards the Mediterranean. The numbers indicate the location of the airports in the region: Madrid-Barajas (1), the main international airport, Torrejón (2) Colmenar Viejo (3), Cuatro Vientos (4), Getafe (5), Almagro (6) and Albacete-Los Llanos (7).

the drainage winds considerably differ from place to place, as dictated by local topographic features, there are also important spatial variations in the frequency of fog occurrence.

2. Model Design and Implementation

2.1. The H1D Model

The H1D model is an SCM developed at the INM, a one-dimensional version of the HIRLAM model. The 3-D HIRLAM, widely described in UNDÉN *et al.* (2002) and references therein, is a limited-area model developed in collaboration between the National Meteorological Services of Denmark, Finland, Iceland, Ireland, the Netherlands, Norway, Spain and Sweden, and a cooperation agreement with *Météo-France*. The one-dimensional version is a hydrostatic model, with the resolution currently set to 60 levels in the vertical. The grid resolution increases towards the surface with the lowest full level, where temperature, specific humidity and wind are defined, located at about 30 meters above ground level (AGL). The model is integrated with a time-step of 10 seconds.

The physical package includes a tiled surface scheme, a turbulence parameterization based on the turbulent kinetic energy (TKE) prognostic equation, a radiation scheme and a parameterization of moist processes including large-scale and convective condensation.

The radiation scheme is based by SAVIJÄRVI (1990). Its first implementation in HIRLAM is documented in SASS (1994) and later improvements in WYSER *et al.* (1999). The scheme considers only two spectral parts: The solar or shortwave (SW) and the thermal or longwave (LW) bands, and only one vertical loop for each one.

The turbulence scheme is based on the combination of a prognostic TKE equation with a diagnostic mixing length (l), which is a so-called TKE-l scheme. It is based on the scheme described in CUXART *et al.* (2000a), but with important modifications. The main change is the substitution of the Bougeault-Lacarrière mixing length (BOUGEAULT and LACARRIÈRE, 1989) by a new formulation (LENDERINK and DE ROOY, 2000).

The surface scheme uses the so-called mosaic of tiles approach, first introduced by Avissar and Pielke (1989). Such an approach is especially important in SCMs because it is the only way to explicitly represent a horizontal heterogeneity. The surface fluxes of heat, moisture and momentum are independently calculated at every tile and then aggregated, thus allowing an independent evolution of different land-use patches, which are only coupled through the atmosphere. Five different surface types are considered: sea or inland water, ice, bare land, low vegetation and high vegetation. Surface fluxes and the soil and surface evolution are calculated using the ISBA scheme (NOILHAN and PLANTON, 1989; NOILHAN and MAHFOUF, 1996).

The STRACO—acronym of Soft TRAnsiton Condensation—scheme is based on a Kuo-type convection scheme (KUO, 1974). It emphasizes the gradual transitions between convective and stratiform regimes. The representation of microphysical processes follows SUNDQVIST (1993). The visibility is a diagnosed magnitude. It is estimated from the liquid water content (LWC), using the expression deduced by KUNKEL (1984) after the analysis of several fog episodes:

$$\text{Visibility} = 0.027(LWC)^{-0.88}, \tag{1}$$

where visibility is in meters and LWC in gm^{-3}.

2.2. Model Initialisation

The atmospheric column, as well as the soil magnitudes in H1D, can be initialised either from the 3-D model or from a 6-hour forecast of the model itself. In SCMs, the horizontal pressure gradient cannot be computed. Therefore, the concept of geostrophic balance completely loses its meaning and, as a consequence, there is no relationship between mass and dynamic fields to be fulfilled during the initialisation. It makes it possible to initialise the wind column totally independent of those of temperature, humidity and cloud condensate.

Ongoing work is addressed to combine both mentioned sources in a variational assimilation scheme. Nevertheless, the current version forces the selection of the best column through a decision based on the closeness of the screen value to the observation. In the case of the temperature, humidity and cloud condensate, the choice is based on the value of the expression $\Delta T + 2\Delta q$, where ΔT is the error in the screen temperature (in K) and Δq is the error in the screen specific humidity (in g/kg).

As it is explained in section 2.5, the model is actually run about four hours after the nominal run time. It makes possible the assimilation of observational data recorded at different times. In the operational setup, temperature, specific humidity and wind velocity from synoptic observations released at HH + 00 and HH + 03 are assimilated using a nudging scheme (HOKE and ANTHES, 1976). In addition, prescribed profiles of liquid water are introduced when the observations report a visibility reduction.

The H1D model needs several physiographic and climatic values. Default values are obtained from the HIRLAM Climate Data Base: Orographic roughness, land-class fraction and soil type are obtained from constant data sets; and soil moisture and land surface temperature from monthly changing data sets.

In particular, the definition of land-class fractions is made through the scheme described in WILSON and HENDERSON-SELLERS (1985), which contains 21 different land classes. These values are used in the estimation of other parameters: surface albedo, surface-vegetation roughness (monthly changing) and tile fractions. An orographic roughness derived from the sub-grid topography of the 3-D model is used

Table 1

Physiographic values used in the H1D runs for Madrid-Barajas, Almagro and Albacete-Los Llanos airports: Surface albedo, orographic roughness, tile fractions and dominant land use and soil type in the different tiles

	Madrid-Barajas	Almagro	Albacete-Los Llanos
Albedo	0.24	0.18	0.18
$z_{0,oro}$ (m)	0.11	0.04	0.05
Surface fraction of:			
bare ground	0.20	-	-
low vegetation	0.73	1.00	1.00
high vegetation	0.07	-	-
Dominant land use in:			
bare ground tile	Desert	-	-
low vegetation tile	Crops	Crops	Crops
high vegetation tile	Deciduous broadleaf	-	-
Dominant soil type in:			
bare ground tile	3% clay, 92% sand	-	-
low vegetation tile	18% clay, 43% sand	18% clay, 43% sand	18% clay, 43% sand
high vegetation tile	3% clay, 92% sand	-	-

in the estimation of the total surface roughness: the final value (z_0) is set according to TIBALDI and GELEYN (1981):

$$z_0 = \sqrt{{z_{0,oro}}^2 + {z_{0,veg}}^2} \tag{2}$$

where $z_{0,oro}$ and $z_{0,veg}$ are, respectively, the orographic and the surface-vegetation roughness. The soil type is defined through a scheme containing nine soil classes with different fractions of sand, clay and loam.

Table 1 shows the physiographic values used in the H1D runs for Madrid-Barajas, Almagro and Albacete-Los Llanos.

2.3. Estimation of Terms Depending on Horizontal Heterogeneity

The model equations include several terms that are dependent on the horizontal heterogeneity of the atmosphere and, therefore, cannot be computed by a SCM. The H1D model overcomes this problem through the estimation of different magnitudes from 3-D HIRLAM forecasts. It ingests hourly forecasts of the basic variables at the different levels of four grid-points surrounding the site, thus allowing estimation of both longitudinal and latitudinal gradients. The horizontal pressure gradient is computed from these values at levels below 1000 meters AGL. Nevertheless, above that height, the pressure force is derived from the wind forecast through the assumption of geostrophic balance. Finally, the vertical velocity profile and the surface pressure tendency are directly interpolated from the hourly forecasts at the surrounding grid-points.

Although this methodology has produced reasonably good results, individual runs generated significant errors. The first problem is that gradients from a single time-step in the 3-D model might not be temporally representative. Nevertheless, the main source of error seems to be the lack of spatial representativeness of gradients. These are computed at a fixed scale, defined by the grid-length of the 3-D HIRLAM, which is 0.16° latitude, that is, about 18 km. It is obvious that the ideal scale depends on the wind speed: the stronger the wind is the larger the scale should be. A discussion concerning the problem of retrieving estimations of horizontal gradients from 3-D models can be read in BERGOT *et al.* (2005).

The awareness that a correct estimation of the horizontal gradients is rather difficult has lead to the implementation of an artifice preventing the model from the introduction of excessive horizontal advections. Positive (negative) horizontal advections of any magnitude are stopped when the magnitude achieves a value in the SCM that is above (below) the maximum (minimum) value in the four grid-points surrounding the site in the 3-D model. This procedure notably improves the global verification scores, although under certain conditions, especially when wind blows from variable directions and non-negligible speed, it may represent a slow relaxation of the SCM simulation towards that of the 3-D model.

2.4. Local Adaptation: Drainage Winds at Madrid-Barajas Airport

As denoted in the first section of this paper, one of the main advantages of the SCMs is their flexibility, thus facilitating the introduction of local adaptations. Several different ways to introduce conceptual models into SCMs can be thought of. In the present case, under certain conditions, the horizontal gradients or the vertical velocity provided by 3-D HIRLAM are substituted by climatological values.

It is well known that drainage winds play an important role in the onset or inhibition of fog at Madrid-Barajas Airport (CANO *et al.*, 2001). Since the 3-D HIRLAM does not correctly simulate such flow, it cannot provide the H1D with accurate values for the external forcings. To overcome this problem, several studies have been undertaken aimed at achieving quantitative climatological estimations of the above-mentioned forcings, especially of the vertical velocity. Sensitivity tests carried out with H1D proved that vertical velocity has a strong influence in fog formation. It is obvious that the strong vertical stratification of potential temperature, specific humidity and wind velocity observed in very stable conditions yields important vertical advections, even with low vertical speed. Strong stability is usually associated with weak horizontal pressure gradients and, in these situations, the topographic features cause the development of circulations that are far from being non-divergent and that, therefore, produce non-negligible vertical velocities. The topography in the region is not especially sharp, but complex enough to produce these kinds of circulations.

The first observational evidence of a dominant upward motion in the area in the presence of a drainage flow was found by CANO *et al.* (2001) after the analysis of radar data using the velocity azimuth display (VAD) technique, first described by BROWNING and WEXLER (1968). An average vertical profile with upward velocity between 0.01 and 0.02 ms^{-1} was obtained at midnight between 1200 and 2000 m ASL from a selection of 40 nights with a clear drainage flow. The profile has to be viewed as a spatial average over several hundreds of km^2 around the radar and, therefore, can only be considered from a qualitative point of view. Nevertheless, the average upward velocity at midnight, when a mean downward motion due to nocturnal cooling could be expected, is already the symptom of a mass convergence in the lower part of the valleys that drain the Central Range.

Several simulations have been made with TAPM, a 3-D high-resolution non-hydrostatic model developed at the Commonwealth Scientific and Industrial Research Organisation (CSIRO) in Australia (HURLEY, 2005) in order to better characterize the drainage flow in the surroundings of Madrid-Barajas airport. The model has proved its ability to reproduce the known features of the flow in the area, with the wind blowing down-valley, following the riverbeds and finally converging and producing ascents (SORIANO *et al.*, 2004). The simulations have shown important day-to-day variations in some parameters, for example, the depth of the katabatic flow, which has shown values from 200 to almost 1000 meters, depending on the stability and the direction of the synoptic flow. Nevertheless, the nocturnal wind profiles over Madrid-Barajas usually present an upward vertical velocity increasing with height up to a maximum at about 400 m AGL. The mentioned maximum value tends to increase throughout the night reaching 0.04–0.05 ms^{-1} at sunrise.

Finally, the horizontal wind divergence at low levels has been computed from data gathered by an array of six anemometers set up on the Madrid-Barajas airport premises. With the assumption of a constant air density, the divergence is estimated by calculating the horizontal flux across the perimeter of the array (CANO *et al.*, 2005). The results totally agree with the conceptual model of a drainage flow producing upward motion. There is a clear diurnal cycle, with daytime divergence and nocturnal convergence. Figure 2 represents the mean diurnal variation in November between 2001 and 2005: There is a significant convergence during nighttime, but daytime divergence is only shown associated with the presence of mountain breeze. Although the value of the daytime divergence presents an important variation throughout the year, the nocturnal convergence remains almost constant, in agreement with TAPM simulations and radar estimations.

The analysis of satellite images has also confirmed some features of the conceptual model (CANO and TERRADELLAS, 2005). Figure 3 presents the average brightness temperature retrieved at 0300 UTC on clear nights of January 2003 from the infrared channel of the METEOSAT-7 satellite. Apart from the urban thermal island corresponding to the Madrid conurbation, which also seems to play a role in the overall circulation, a spot of relative high temperatures is clearly visible on the

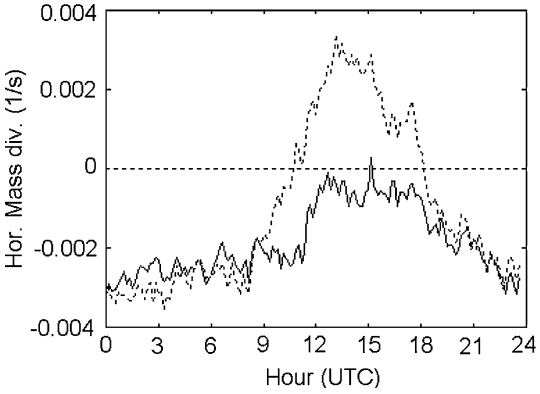

Figure 2
Horizontal mass divergence near surface computed from wind measurements recorded at Madrid-Barajas in November, from 2000 to 2005: mean value (full line), mean value for days with mountain breeze (dashed line).

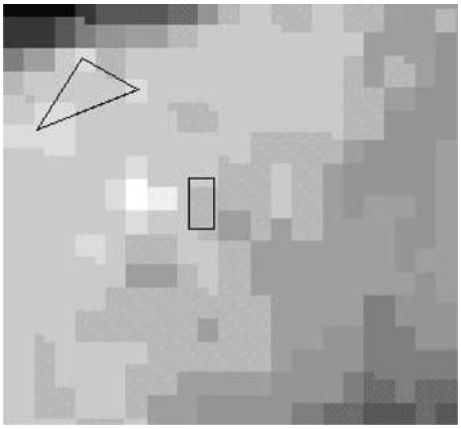

Figure 3
Average brightness temperature retrieved at 0300 on clear nights of January 2003 from the infrared channel of the METEOSAT-7 satellite (dark colors represent cold temperatures). The black box marks Madrid-Barajas airport. West from it, the white spot reflects the Madrid urban thermal island. Around the vertices of the triangle, the warm slope zones can be noticed.

western part, over terrain elevated about 800 m ASL. This spot may be identified as the interception by the terrain of a relatively warm air mass flowing over the drainage current: a returning flow. Such areas of relative high temperatures are well known by biologists (e.g., BOURQUE *et al.*, 2000) who sometimes call them warm slope zones.

After the data analysis and 3-D high-resolution numerical simulations of a drainage flow in the region, there were rough estimates of some climatological values such as horizontal mass divergence or horizontal advection of temperature and

humidity. A first estimate of these values was introduced into the H1D model, but further adjustments have been performed, adopting a tuning procedure. The current version of the module that simulates drainage winds implemented in H1D is described in the following paragraphs.

The module is activated when two conditions are fulfilled: There is a ground inversion and the wind speed up to a certain level is below a predefined threshold. In the current version, the threshold has been set to 8 ms^{-1} for winds below 700 m AGL. First versions of the module used to set the depth of the drainage flow as that of the ground inversion. As the drainage flow seemed to be too thin in the simulations, its depth has been increased in two model levels in later versions, with a maximum depth of 700 m.

In the first time-steps of a katabatic episode, the wind speed is set to zero at levels within the flow using the horizontal wind advection term. When the depth of the flow grows and reaches an upper level, the wind speed at this level is also set to zero. From this moment, the horizontal wind advection ceases acting until the end of the episode when the term is used again to set the wind speed to zero. The remaining of forcings are set to the following values, while the module is activated:

- Horizontal advections: The air mass advected by drainage winds is relatively cold and dry. Therefore, negative thermal and moisture advections are introduced into levels within the flow: In the current version, the values are:

$$-v\nabla T = -2.0 \cdot 10^{-4} \cdot \tau - 1.0 \cdot 10^{-4}, \tag{3}$$

$$-v\nabla q = -1.0 \cdot 10^{-7} \cdot \tau, \tag{4}$$

where the advections are in mKs^{-1} and ms^{-1}, and τ, the value of the ground inversion, in K.

- Horizontal pressure gradient: North or northeast winds are observed during drainage episodes. The local pressure gradient should be in accordance with it. It is represented in the model through the introduction into levels within the flow of a geostrophic wind with the following zonal (u_g) and meridional (v_g) components:

$$u_g = -1.2 \cdot \tau, \tag{5}$$

$$v_g = -0.2 \cdot \tau, \tag{6}$$

where u_g (positive for west winds) and v_g (positive for south winds) are in ms^{-1}.

- Horizontal mass divergence: The largest absolute values seem to be close to the ground. Therefore, a vertical profile with the strongest convergence close to the surface is introduced into H1D (Fig. 4). The actual values are scaled by τ.

The night 19 October, 2005 is presented as an example of the effect of the module. Although the 3-D HIRLAM predicted south winds during the night, north winds were reported at Madrid-Barajas and other nearby stations, an evidence of a well

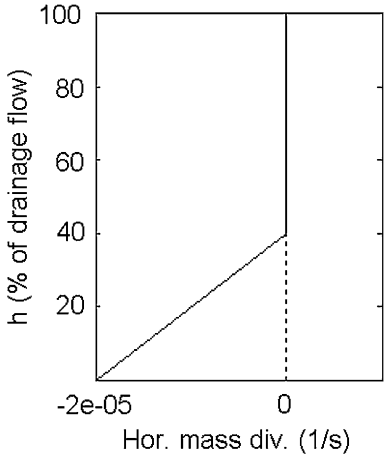

Figure 4
Shape of the vertical profile of horizontal mass divergence introduced into H1D by the module designed to simulate drainage flows. The actual values are scaled by the magnitude of the ground inversion (in K).

developed drainage flow. Since there was a strong ground inversion of about 150 m depth (Fig. 5) and light wind at low levels, the drainage module was automatically activated. The evolution of temperature was not substantially modified because the 3-D model already predicted upward motion and, therefore, a cold vertical advection at low levels. Nevertheless, the light horizontal dry advection that was introduced is enough to prevent the onset of fog that H1D would forecast if the drainage module had not been activated (Fig. 6).

Figure 7 compares verification scores of H1D with and without the drainage flow module during February and March 2006. It can be noticed that the introduction of the module improves the temperature forecasts during the night.

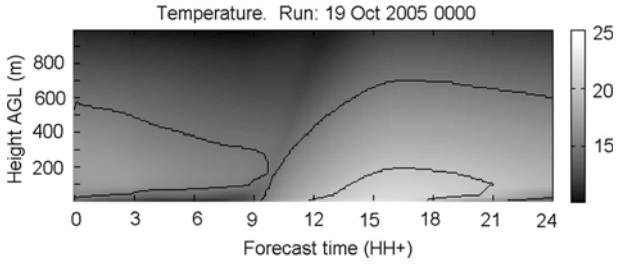

Figure 5
Evolution of the temperature at the lowest layers forecast by H1D for Madrid-Barajas on 19 October, 2005 (00 UTC run).

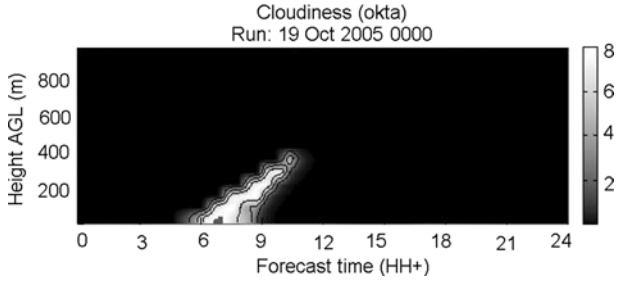

Figure 6
Cloudiness forecast by H1D for Madrid-Barajas on 19, October 2005 without the module that simulates the effect of drainage winds.

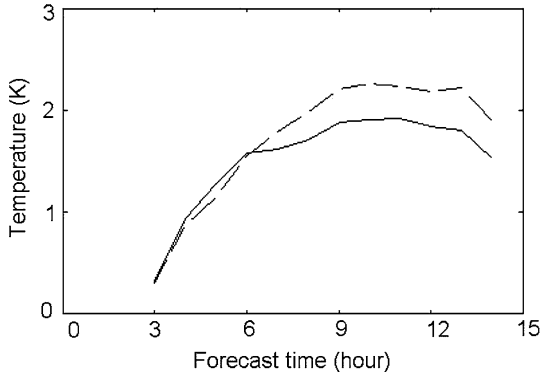

Figure 7
Verification of the screen temperature forecast for Madrid-Barajas by H1D (1800 run) during February and March 2006: rmse with the module that simulates the drainage flow (full line) and without it (dashed line).

2.5. Operational Set-up

The H1D model is operationally run at the INM Centre in Barcelona four times daily for the three airports in the region: Madrid-Barajas, Almagro and Albacete-Los Llanos. It is also run for several other sites: six domestic and three foreign airports. In the particular cases of Paris-Charles de Gaulle Airport in France, Casablanca-Nouasseur Airport in Morocco and Warsaw-Okecie Airport in Poland, the model is run with the aim of comparing it with other models or other forecasting methods. Nominal runtimes are 0000, 0600, 1200 and 1800 UTC. Nevertheless, actual runtimes are about four hours later, because runs start once the post-process of the 3-D HIRLAM is finished. The model is integrated for 24 hours.

The runs take a few minutes. Then the forecasts for domestic airports are uploaded to the INM intranet and those for foreign locations to the Internet. The

availability over the Internet may take several extra minutes, because the INM web pages are refreshed every 15 minutes. Summarizing, forecasts are available between 4 hours and 4 hours 30 minutes after the nominal runtime.

The model is not designed to produce automatic forecasts to the user, but to supply some extra information to the forecaster who will make the final decision.

3. Model Performance

Significant changes have been performed in the operational version of H1D during summer 2005. Primary among them is the introduction of the ISBA scheme to represent the atmosphere-biosphere-surface interactions. The updated version has only been run during the winter season 2005–2006. Therefore, verification results may not be definitive. In particular, statistically significant verifications of low ceiling and visibility (C&V) forecasts are not available yet.

Some verification results of the basic meteorological magnitudes are presented in Figures 8 and 9 for the 1800 UTC run, which, in general, is the most useful to forecast visibility reductions. The H1D forecasts are compared with conventional ground observations performed at the synoptic stations. Interpolations of the 3-D HIRLAM outputs to the selected sites are also verified against observations in order to obtain comparable scores.

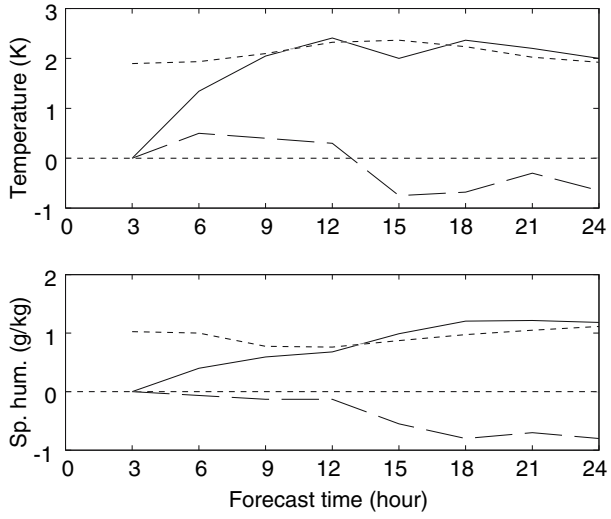

Figure 8
Verification of the screen temperature (up) and specific humidity (down) at Madrid-Barajas forecast by H1D (1800 UTC runs) between 1 October, 2005 and 31 January, 2006: bias (dashed line) and rmse (full line). The dotted line represents the rmse of 3-D HIRLAM.

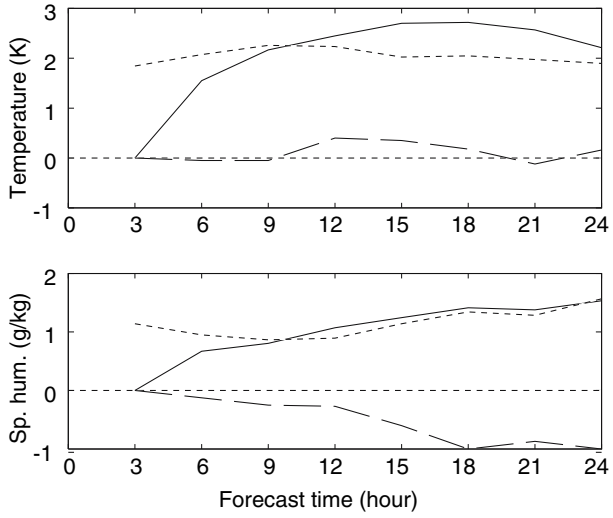

Figure 9
Verification of the screen temperature (up) and specific humidity (down) at Albacete-Los Llanos forecast by H1D (1800 UTC runs) between 1 October, 2005 and 28 February, 2006: bias (dashed line) and rmse (full line). The dotted line represents the rmse of 3-D HIRLAM.

In most cases, H1D achieves better scores than 3-D HIRLAM for the first forecast hours. Figure 8 shows the verification scores of the temperature and specific humidity forecast at screen level for Madrid-Barajas. H1D presents a lower root-

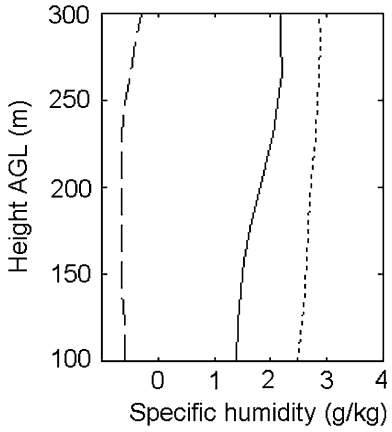

Figure 10
Verification of 6-hour forecasts of the vertical profile of specific humidity for Madrid-Barajas with radio sounding data from 0000 UTC releases between 1 October, 2005 and 31 January, 2006: bias (dashed line) and rmse (full line). The dotted line represents the rmse of 3-D HIRLAM.

mean-squares error (rmse) than 3-D HIRLAM during 10–11 hours for temperature and during 13–14 hours for specific humidity. Figure 9 shows that the forecast of temperature and specific humidity at screen level for Albacete-Los Llanos presents better verification scores than 3-D HIRLAM during about 10 hours. The scores of the 0000 UTC runs are even better in most cases: at Albacete-Los Llanos, H1D presents better scores than 3-D HIRLAM for screen-level specific humidity forecasts during 20 hours.

Notable results are also achieved at upper levels. Figure 10 shows the verification scores for 6-hour forecasts of the vertical profile of specific humidity for Madrid-Barajas. Forecasts are compared with radio sounding data from 0000 UTC releases. Balloons are launched about 5 km away and 51 m above the reference point of the H1D runs. For this reason, the lowest levels have been removed from the graph.

4. Conclusions

Modern commercial aircrafts can safely operate in conditions of reduced visibility, but problems arise with less sophisticated planes. The efficiency in the management of many aeronautical activities is rather sensitive to poor C&V conditions; however, better forecast skill would help to mitigate inconveniences. Therefore, there is a pressing demand for better forecast products related to C&V conditions. Nevertheless, fog and low clouds prediction proves to be an unsolved challenge for the weather services.

In this framework, the SCMs are probably not a definitive solution allowing release of automated predictions, nonetheless they may provide the operational forecaster with new products to be integrated with other sources of information. Following this idea, at the INM, the team responsible for the aeronautical weather forecasts in the region under study has successfully integrated the H1D outputs in a decision tree, notably improving the skill of fog and low clouds forecasts.

Mainly because of the assimilation of local observations, H1D has proved able to yield better local forecasts than traditional 3-D models at least up to 10–12 hours. Future work should probably be aimed at the design of specific observational systems, similar to that described in BERGOT *et al.* (2005), as well as to a more efficient use of the available information through a variational assimilation scheme. The availability of new observational data and a more efficient assimilation could reduce the dependence on the initial 3-D column, allowing three-hourly runs of H1D.

The flexibility of SCMs has permitted the introduction of a conceptual model of drainage flow into the forecasting model and, in turn, it substantially improved the forecasts for Madrid-Barajas airport. The need of such local adaptation arises from the fact that the 3-D HIRLAM does not have the necessary resolution to correctly simulate the phenomenon; therefore, it cannot provide the SCM with the correct

external forcings. Knowledge of regional circulations may improve this kind of local adaptation and correct some deficiencies related to the horizontal heterogeneity.

Ongoing research is aimed at improving knowledge of the behavior of water vapor within the mountain breeze cycle. Estimations of the integrated water vapor in the column are retrieved, using neural networks, from multispectral records of the SEVIRI radiometer on board the METEOSAT Second Generation satellite (MARTÍNEZ *et al.*, 2003). Results show a diurnal variation with minimum values during night (Cano et al., 2006). Its amplitude is too large to be explained by surface condensations and evaporations. A part of such variation is probably due to nocturnal dry advections and diurnal wet advections, not completely compensated by upper return circulations.

Acknowledgements

There are several people who we would like to thank: Javier Calvo, from the Numerical Weather Prediction staff at the INM in Madrid, for his help with the H1D model, Javier Casado, head of the INM office at Madrid-Barajas airport, for his assistance with aeronautical matters, and Beatriz Téllez and Thomas Cernocky from the INM staff in Barcelona for their aid with cartography.

The current work has been partially supported by the European Science Foundation, through the COST Action 722 on Short range forecasting methods of fog, visibility and low clouds.

REFERENCES

ALLAN, S. S., GADDY, S. G., EVANS, J. E. (2001), *Delay and Casualty Reduction at the New York City Airports Using Terminal Weather Information Systems*, Lincoln Laboratory Project Report ATC-291, Massachusetts Institute of Technology, Lexington, MA, 59 p.

AVISSAR, R., PIELKE, R. A. (1989), *A parameterization of heterogeneous land surfaces for atmospheric numerical models and its impact on regional meteorology*, Mon. Wea. Rev. *117*, 2113–2136.

BERGOT, T. and GUÉDALIA, D. (1994), *Numerical forecasting of radiation fog. Part I: Numerical model and sensitivity tests*, Mon. Wea. Rev. *122*, 1218–1230.

BERGOT, T., CARRER, D., NOILHAN, J., and BOUGEAULT, P. (2005), Improved site-specific numerical prediction of fog and low clouds: A feasibility study, Wea. Forecasting *20*, 627–646.

BOUGEAULT, P. and LACARRÈRE, P. (1989), *Parameterisation of orography induced turbulence in a meso-beta scale model*, Mon. Wea. Rev. *117*, 1872–1890.

BOURQUE, Ch. P.-A., MENG, F. R., GULLISON, J. J., and BRIDGLAND, J. (2000), *Biophysical and potential vegetation growth surfaces for a small watershed in northern Cape Breton Island, Nova Scotia, Canada*, Can. J. Forest Res. *30*, 1179–1195.

BROWNING, K.A. and WEXLER, R. (1968), *The determination of kinematic properties of a wind field using Doppler radar*, J. Appl. Meteor. *7*, 105–113.

CANO, D. and TERRADELLAS, E. (2005), *The use of conceptual models in fog forecasting, COST 722 Short-Range Forecasting Methods of Fog, Visibility and Low Clouds*, Workshop Proceedings, Larnaca, Cyprus, 67–71.

CANO, D., CASADO, J., PALACIO, I., TÉLLEZ, B., TERRADELLAS, E., and CUXART, J. (2001), *Importancia de los flujos catabáticos en las predicciones para el aeropuerto de Madrid-Barajas*, V Simposio Nacional de Predicción, INM, Madrid, Spain (CD) (in Spanish).

CANO, D., CASADO, J., TERRADELLAS, E., SORIANO, C., and PALACIOS, I. (2005), *Convergencia horizontal de masa y su influencia en la formación de nieblas en el aeropuerto de Madrid-Barajas*, 6.° Encontro Luso-Espanhol de Meteorología, Sesimbra, Portugal (CD).

CANO, D., CASADO, J., TERRADELLAS, E., PALACIOS, I., and MARTÍNEZ, M. A. (2006), *Comparison between different estimates of the precipitable water content and the mass divergence over the Madrid-Barajas airport*, V Asamblea Hispano-Lusa de Geodesia y Geofísica (Proceedings), Seville, Spain (in press) (in Spanish with abstract in English).

CUXART, J., BOUGEAULT, P., and REDELSBERGER, J. L. (2000a), *A turbulence scheme allowing for mesoscale and large-eddy simulations*, Quart. J. Roy. Met. Soc. 126, 1–30.

CUXART, J., YAGÜE, C., MORALES, G., TERRADELLAS, E., ORBE, J., CALVO, J., FERNÁNDEZ, A., SOLER, M. R., INFANTE, C., BUENESTADO, P., ESPINALT, A., JOERGENSEN, H. E., REES, J. M., VILA, J., REDONDO, J. M., RODRIGUEZ, I., and CONANGLA, L. (2000b), *Stable atmospheric boundary layer experiment in Spain (SABLES 98): A report, Boundary-Layer Meteorol. 96*, 337–370.

DORAN, J. C., FAST, J. D., and HOREL, J. (2002), *The VTMX 2000 campaign*, Bull. Am. Meteor. Soc. *83*, 537–551.

DUYNKERKE, P. G. (1991), *Radiation fog: A comparison of model simulations with detailed observations*, Mon. Wea. Rev. *119*, 324–341.

GUÉDALIA, D. and BERGOT, T. (1994), *Numerical forecasting of radiation fog. Part II: A comparison of model simulations with several observed fog events*, Mon. Wea. Rev. *122*, 1231–1246.

GULTEPE, I. and ISAAC, G. A. (2004), *Aircraft observations of cloud droplet number concentration: Implications for climate studies*, Quart. J. Roy. Met. Soc. *130*, 2377–2390.

GULTEPE, I., MÜLLER, M. D., and BOYBEYI, Z. (2006), *A new warm fog parameterization scheme for numerical weather prediction models,* J. Appl. Meteor. (in press).

HOKE, J. E. and ANTHES, R. A. (1976), *The initialization of numerical models by a dynamic initialization technique*, Mon. Wea. Rev. *104*, 1551–1556.

HOLTSLAG, A. A. M. (2003), *GABLS initiates intercomparison for stable boundary layer case*, GEWEX News *13*, 7–8.

HURLEY, P. J. (2005), *The air pollution model (TAPM) version 3. Part 1. Technical description*, CSIRO Atmospheric Research Technical Paper *71*, Aspendale Vic., Australia, 54 pp.

KUNKEL, B. A. (1984), *Parameterization of droplet terminal velocity and extinction coefficient in fog models*, J. Climate Appl. Meteor. *23*, 34–41.

KUO, H. L. (1974), *Further studies of the parameterization of the influence of cumulus convection on large-scale flow*, J. Atmos. Sci. *31*, 1232–1240.

LENDERINK, G. and DE ROOY, W. (2000), *A robust mixing length formulation for a TKE-l turbulence scheme*, Hirlam Newsletter *36*, 25–29.

MARTÍNEZ, M. A., VELÁZQUEZ, M., and MANSO, M. (2003), *Generalization of LPW and SAI SAFNWC/MSG Neural Network Algorithms to MODIS data: Impact on the MSG products validation*, Proc. 2003 EUMETSAT Meteor. Satellite Conf., Weimar, Germany, 462–469.

MEYER, M. B., JIUSTO, J. E., and LALA, G. G. (1980), *Measurements of visual range and radiation-fog (haze) microphysics*, J. Atmos. Sci. *37*, 622–629.

MUSK, L. F., *The fog hazard.* Chapter 6 in *Highway Meteorology* (Perry, A. H., and Symons, L. J., eds.) (E&FN Spon, London, UK 1991), pp. 91–130.

NOILHAN, J. and MAHFOUF, J.-F. (1996), *The ISBA land surface parameterization scheme*, Global and Planetary Change *13*, 145–149.

NOILHAN, J. and PLANTON, S. (1989), *A simple parameterization of land surface processes for meteorological models*, Mon. Wea. Rev. *117*, 536–549.

POULOS, G. S., BLUMEN, W., FRITTS, D. C., LUNDQUIST, J. L., SUN, J. L., BURNS, S. P., NAPPO, C., BANTA, R., NEWSOM, R., CUXART, J., TERRADELLAS, E., BALSLEY, B., and JENSEN, M. (2002), *CASES-99, A comprehensive investigation of the stable boundary layer*, Bull. Am. Meteor. Soc. *83*, 555–581.

SAIKI, E. M., MOENG, C.-H., and SULLIVAN, P. P. (2000), *Large-eddy simulation of the stably stratified planetary boundary layer*, Boundary-Layer Meteor. *95*, 1–30.

SASS, B. H., RONTU, L., and RÄISÄNEN, P. (1994), *HIRLAM-2 Radiation Scheme: Documentation and Tests*, HIRLAM-3 Project, Technical Report 16, Norrkoping, Sweden, 42 p.

SAVIJÄRVI, H. (1990), *Fast radiation parameterization schemes for mesoscale and short-range forecast models*, J. Appl. Meteor. *29*, 437–447.

SUNDQVIST, H. (1993), *Inclusion of ice phase of hydrometeors in cloud parameterization for mesoscale and large-scale models*, Contr. Atmos. Phys. *66*, 137–147.

SORIANO, C., CANO, D., TERRADELLAS, E., and PHYSICK, B. (2004), *Prediction of fog episodes at the airport of Madrid-Barajas using different modelling approaches*, 9th. Internat. Conf. on Harmonisation within Atmospheric Dispersion Modelling for Regulatory Purposes, Proc., vol. II, Garmisch-Partenkirchen, Germany, 315–319.

TALLEY, W. K. (1999), *The safety of sea transport: Determinants of crew injuries*, Appl. Economics *31*, 1365–1372.

TARDIFF, R. (2002), *Northeast Ceiling and Visibility Initiative*, NCAR-RAP 2001–2002 Annual Report, 38 p.

TEIXEIRA, J. and MIRANDA, P. M. A. (2001), *Fog prediction at Lisbon Airport using a one-dimensional boundary-layer model*, Meteorol. Appl. *8*, 497–505.

TERRADELLAS, E., SOLER, M. R., FERRERES, E., and BRAVO, M. (2005), *Analysis of oscillations in the stable atmospheric boundary layer using wavelet methods*, Boundary-Layer Meteor. *114*, 489–518.

TIBALDI, S. and GELEYN, J.-F. (1981), *The Production of a new Orography, Land-Sea Mask and associated Climatological Surface Fields for Operational Purposes*, ECMWF Tech. Memo. 40, Reading, UK, 93 p.

UNDÉN, P., RONTU, L., JARVINEN, H., LYNCH, P., CALVO, J., CATS, G., CUXART, J., EEROLA, K., FORTELIUS, C., GARCIA-MOYA, J. A., JONES, C., LENDERLINK, G., MCDONALD, A., MCGRATH, R., NAVASCUES, B., NIELSEN, N. W., ØDEGAARD, V., RODRIGUEZ, E., RUMMUKAINEN, M., RÖÖM, R., SATTLER, K., SASS, B. H., SAVIJARVI, H., SCHREUR, B. W., SIGG, R., THE, H., and TIJM, A. (2002), *HIRLAM-5 Scientific Documentation*, HIRLAM-5 Project, Norrkoping, Sweden, 144 pp.

WILSON, M. F. and HENDERSON-SELLERS, A. (1985), *A global archive of land cover and soils data sets for use in General Circulation Models*, J. Climatol. *5*, 119–143.

WYSER, K., RONTU, L., and SAVIJÄRVI, H. (1999), *Introducing the effective radius into a fast radiation scheme of a mesoscale model*, Contr. Atmos. Phys. *72*, 205–218.

(Received March 31, 2006, accepted November 15, 2006)
Published Online First: May 16, 2007

Pure appl. geophys. 164 (2007) 1347–1364
0033–4553/07/071347–18
DOI 10.1007/s00024-007-0222-7

Pure and Applied Geophysics

Synoptic Classification and Establishment of Analogues with Artificial Neural Networks

S. C. Michaelides,[1] F. Liassidou,[2] and C. N. Schizas[2]

Abstract—Weather charts depicting the spatial distribution of various meteorological parameters constitute an indispensable pictorial tool for meteorologists, in diagnosing and forecasting synoptic conditions and the associated weather. The purpose of the present research is to investigate whether training artificial neural networks can be employed in the objective identification of synoptic patterns on weather charts. In order to achieve this, the daily analyses at 0000UTC for 1996 were employed. The respective data consist of the grid-point values of the geopotential height of the 500 hPa isobaric level in the atmosphere. A uniform grid-point spacing of $2.5° \times 2.5°$ is used and the geographical area covered by the investigation lies between 25°N and 65°N and between 20°W and 50°E, covering Europe, the Middle East and the Northern African Coast. An unsupervised learning self-organizing feature map algorithm, namely the Kohonen's algorithm, was employed. The input consists of the grid-point data described above and the output is the synoptic class which each day belongs to. The results referred to in this study employ the generation of 15 and 20 synoptic classes (more classes have been investigated but the results are not reported here). The results indicate that the present technique produced a satisfactory classification of the synoptic patterns over the geographical region mentioned above. Also, it is revealed that the classification performed in this study exhibits a strong seasonal relationship.

Key words: Synoptic classification, self-organizing features map, artificial neural networks.

1. Introduction

The systematic use of synoptic weather charts dates back to the beginnings of modern meteorological practices. Scattered all over the world, synoptic meteorological stations have been established measuring and recording various meteorological parameters at fixed times. Surface observing stations report atmospheric pressure, temperature, wind direction and speed, cloud, etc., whereas stations for the upper atmosphere report geopotential height, temperature, humidity and wind direction and speed. In the past few decades, the above network of synoptic observing sites has been supplemented by several other observing platforms, operating both at synoptic and non-synoptic modes.

[1] Meteorological Service, Nicosia 1418, Cyprus. E-mail: silas@ucy.ac.cy
[2] Department of Computer Science, University of Cyprus, Cyprus.

Using the information collected from the above meteorological observing stations, meteorologists prepare various weather charts for analysis and study. These weather charts comprise one of the major tools used by meteorologists, both for the needs of their day-to-day operational practices (e.g., weather forecasting) and for the diagnostic study of the atmospheric behavior (e.g., study of the regional climatological characteristics). Usually, these weather charts are geographical maps representing the spatial distribution of the meteorological parameter in study.

Traditionally, professional meteorologists have analyzed weather charts by drawing the respective iso-lines of parameters by hand. Bearing in mind that the reporting positions on weather charts are irregularly located, the above procedure requires substantial practice and experience and, to a certain extent, personal (subjective) intuition based on predetermined "geometric" models.

More recently, the drawing of the iso-lines is carried out with the aid of computers and appropriate software packages. In this modern objective approach, the irregularly spaced primary observed data constitute again the database for the construction of the weather charts. Normally, with the proper mathematical treatment, these primary data are transformed from an irregularly to a regularly spaced set of values. The inferred regularly spaced values, known as grid-point values are subsequently utilized to draw the respective iso-lines. Through experience, meteorologists seek to identify specific "geometric" patterns resulting from the drawing of the above-mentioned iso-lines and relate them to a specific behavior of the atmosphere. These patterns are commonly referred to as synoptic patterns. An early attempt to manually classify such synoptic patterns is discussed by LAMB (1950). Such manual techniques have subsequently been followed by several automated approaches based on some form of correlation, clustering or eigenfunction analysis (see HEWITSON and CRANE, 2002).

The main objective of this work is to present a new methodology which can be used to identify and thereby classify synoptic patterns on weather maps, in an absolutely objective and automated manner. This novel approach is based on the utilization of Artificial Neural Networks (ANN). More specifically, the aim is to identify and classify similar synoptic patterns over the European continent, during a calendar year, by using an unsupervised ANN learning paradigm, based on the Kohonen's self-organizing feature maps algorithm (SOFM, see KOHONEN, 1990, 2001). As a result of this classification, a series of "synoptic analogues" will be established.

In climatology, a commonly used clustering method is the k-means approach. However, the k-means method suffers from two major deficiencies, namely the determination of the mean values for each cluster required to initialize the algorithm and the determination of the number of such means.

The SOFM approach was adopted by CAVAZOS (1999) to produce relationships between circulation and humidity fields on the one hand, and precipitation on the

other hand. In addition to these two fields, CAVAZOS (2000) explores the influence of teleconnections on extreme precipitation events, adopting the same approach. In many respects, SOFM are similar to traditional clustering approaches (the fact that the SOM algorithm reduces to the k-means clustering algorithm as the neighborhood distance is reduced to zero is pointed out by KOHONEN, 2001). Nevertheless, SOFM have advantages over such traditional approaches which are outlined by HEWITSON and CRANE (2002).

The nonlinearity is a prime characteristic of issues related to the atmospheric sciences. In this respect, ANN have been utilized in classifying clouds observed in satellite imagery (BANKERT, 1994; BANKERT and AHA, 1996; PEAK and TAG, 1992, 1994), tornado prediction (MARZBAN and STUMPF, 1996), rainfall run-off estimation (FURUNDZIC, 1998), agrometeorology (FRANCL and PANIGRAHI, 1997), sea-surface temperature forecasting (TANGANG *et al.*, 1998), spatial meteorological analysis (KALOGIROU *et al.*, 1998), completing time series of meteorological elements (KALOGIROU *et al.*, 1997), and in forecasting minimum temperature (SCHIZAS *et al.*, 1994). More recently the ANN methodology has been adopted in the classification of rainfall variability (MICHAELIDES *et al.*, 2001).

LORENZ (1969) has proposed that the analogue method for meteorological analysis can be employed in the non-deterministic search of weather states that closely resemble each other. However, the method did not find immediate application, mainly due to the lack of appropriate nonlinear mathematical tools. However, the artificial neural network method (which is actually a nonlinear analogue technique) has revived the idea of analogue weather analysis (ELSNER and TSONIS, 1992). The analogue method has been recently reconsidered and appears to be promising (VAN DEN DOOL, 1989; NICOLIS, 1998). The present research is an attempt to demonstrate that ANN can be utilized in the search of "synoptic analogues."

2. Data

The data used in the present research consist of the grid-point values of the geopotential height of the 500 hPa level at 0000UTC (Universal Time Coordinated) for each day in 1996, as archived by NCEP (National Centers for Environmental Prediction, United States of America). The geopotential height is measured in geopotential meters. The grid used in the NCEP analyses has a uniform $2.5° \times 2.5°$ spacing and the geographical area that was used for this investigation is bounded by parallel circles 25°N and 65°N and by meridians 20°W and 50°E. This area is covered by 493 grid points (17 lines and 29 columns) and covers the entire European continent, part of the Middle East and the Northern African Coast. Bearing in mind that the year 1996 includes 366 days, the number of data points that cover the whole year is 180,438.

3. ANN Methodology

Artificial Neural Networks are a branch of artificial intelligence. It is beyond the scope of this article to provide a detailed theoretical background on ANN; such information is widely available and described in detail in any standard textbook on ANN and will not be duplicated here. ANN have proven to be very effective in a large number of complex applications such as pattern recognition, classification, prediction, control systems, etc. It is for these abilities that ANN have been chosen in this research, in an effort to investigate their suitability in the area of synoptic pattern identification and classification and to suggest that they can be used as a basis for the construction of analogues of such patterns.

3.1. Method

In unsupervised learning there are no target values as in the case of other methods of ANN. Given a training set, $X^{(k)}$, $k = 1, 2, \ldots, p$, the objective is to discover significant features or regularities in the training data (input data). In our case the input data was 366 vectors, one for each day in year 1996. The neural network attempts to map the input feature vectors onto an array of neurons (usually one- or two-dimensional). By doing so, the input feature vectors can be clustered into c-clusters, where c is less or equal to the number of neurons used (CHARALAMBOUS *et al.*, 2001). Input vectors are presented sequentially in time without specifying the desired output (see SCHNORRENBERG *et al.*, 1996; MICHAELIDES *et al.*, 2001). The one-dimensional architecture of Kohonen's SOFM was adopted in the present research.

The input vector X is connected with each unit of the network through weights w_j, where $j = 1, 2, \ldots, M$. M equals to 493, for the area in study (493 grid points). The neuron whose weight vector is closest to the input vector X (in terms of Euclidean distance) is the winner. This neuron is represented with I and is the winner neuron to input X if $\|w_I - X\| = \min_i \|w_i - X\|$, $i = 1, \ldots, M$.

Note that $\|w_I - X\| = [(w_{i1} - x_1)^2 + (w_{i2} - x_2)^2 + \ldots + (w_{iM} - x_M)^2]^{\frac{1}{2}}$ is the Euclidean distance between weight vector w_i and input vector X (CHARALAMBOUS *et al.*, 2001). The number of the SOFM output nodes (possible classes) N in the present study was varied for values 15 and 20 (more experiments with more classes were also carried out but since the results from these lead to the same conclusions, they are not presented for brevity).

The weight vectors of the winner neuron, as well as its neighborhood neurons, are updated in such a way that they become closer to the input pattern. Learning follows the following rule:

$$w_i^{(\text{new})} = \begin{cases} w_i^{(\text{old})} + a(X - w_i^{(\text{old})}), & i \in N(I, R) \\ w_i^{(\text{old})}, & I \notin N(I, R) \end{cases}$$

where the neighborhood set $N(I,R)$ of neuron I of radius R consists of the neurons 1, $I \pm 1,\ldots, I \pm R$, assuming these neurons exist, with maximum value being around the winner I, in order for a larger number of neighborhood units to share the experience of learning with the winner unit, and it becomes zero as the distance between the neighborhood units and I increases. The coefficient a in the above relationship is called the learning factor and decreases to zero as the learning progresses. For simplicity, R is considered to have the shape of a geometric area, such as a rectangle or hexagon.

The radius of the neighborhood around the winner unit is relatively large to start with, to include all neurons. As the learning process continues, the neighborhood is consecutively shrunk down to the point where only the winner unit is updated (PATTERSON, 1995).

As more input vectors are represented to the network, the size of the neighborhood decreases until it includes only the winning unit or the winning unit and some of its neighbors. Initially, the values of the weights are selected at random.

The method which was used for the SOFM to work, is described as:

1. The initial value of the weights was set to small random numbers, as well as the learning rate and the neighborhood. Steps 2 to 4 were repeated until the weights of the network were stabilized.
2. One vector X was chosen from the dataset as an input to the network.
3. The table for unit I with weight vector closest to X was determined by calculating

$$\|w_I - X\| = \min_i \|w_i - X\|.$$

4. The weight vector in $(t + 1)$ iteration was updated according to:
   $w_i(t + 1) = w_i(t) + a(t)(X - w_i(t))$, for units that belong in set $N(I,R)$
   $w_i(t + 1) = w_i(t)$, for units that do not belong in set $N(I,R)$.
5. The neighborhood and the learning rate of the parameters were decreased (CHARALAMBOUS *et al.*, 2001).

When all vectors in the training set were presented once at the input, the procedure was repeated many times with the vectors presented in order each time. This part of the algorithm at the end organizes the weights of the one-dimensional map, such that topologically close nodes become sensitive to input that is physically similar. Nodes were ordered in a natural manner, reflecting the different classes of the training set (MICHAELIDES *et al.*, 2001).

The Kohonen self-organizing feature map algorithm in its unsupervised mode was chosen for building the neural network models, because neither the number of output classes (categories) nor the desired output are as *a priori*. This is a typical example where unsupervised learning is more appropriate, since the domain expert will be given the chance to see the results and then decide which model gives the best results and thus guided to decide the number of output classes that better represent the system (PATTICHIS *et al.*, 1995).

The Kohonen self-organizing features map network is a type of unsupervised network, which has the ability to learn without being shown correct outputs in the sample patterns. These networks are able to separate data into a specified number of categories with only two layers: An input layer and an output layer, the latter consisting of one neuron for each possible output category.

The training patterns are presented to the input layer, then propagated to the output layer and evaluated. One output neuron is the "winner" for each training pattern. The network weights are adjusted during training.

For the architecture, the number of inputs, outputs (classes), the learning rate, the initial weights, the size of neighborhood and the number of epochs are set. The training patterns are presented to the network using the rotation method (in order) and the distance metric used during the network's processing was Vanilla (or Euclidean as it is known).

The 366 files containing the data to be processed were merged into a single two-dimensional array, which was then fed as input to NeuroShell2. The array resulting from the merging of the 366 files has a dimension of 493 columns and 366 rows. This merging was achieved by placing the 17 rows in each day sequentially, thus transforming each of the two-dimensional arrays corresponding to each day (17 rows and 29 columns) into a single row having 493 columns. The 366 rows correspond to the 366 days in 1996.

3.2. Strategies for Classification

One of the major inherent problems in the endeavor to classify the synoptic patterns over any particular geographical region, is the *a priori* identification of the number of different classes that one can expect from such a classification. This is simply because the number of distinctive synoptic patterns over any particular geographical region is not *a priori* known. In the past, such a synoptic classification was performed by a qualitative inspection of synoptic maps. In other words, this was achieved by professional meteorologists who looked at a series of plotted synoptic maps and picked out "geometric" similarities (e.g., PREZERAKOS, VLASSI and MICHAELIDES, 1991). Nevertheless, it seems that in an attempt to perform a classification with an unknown number of classes, experimentation with various possibilities is a practical procedure which can lead to some useful results. For this reason, it was decided to run a number of experiments and build classification models with different numbers of output nodes (i.e., classes). In the present article, the results for 15 and 20 output nodes are presented.

Kohonen networks are trained for a fixed number of epochs. Small problems may train in as little as 50 epochs, but the number can be set to 10,000 for really large problems. In this case, it was decided that the network should be trained for 3000 epochs. The learning rate and neighborhood size are automatically reduced as training progresses. The neighborhood size should begin with a relatively high

number, such as 90 percent of the number of neurons in the output layer. The network's initial weights, as well as the learning rate, were set as a random value of 0.5 and the size of the neighborhood was determined each time from the number of outputs. The termination of the learning process (presentation of learning events) was determined when the neighborhood became zero.

The data for the days that are associated with each class were subsequently used to determine an average spatial distribution of the geopotential height of the 500 hPa isobaric surface, which corresponds to the respective ''synoptic analogue.'' The average spatial distribution was determined by calculating the average of the geopotential height at each grid point, considering all the individual days that were found to be members of each class. For the visualization of the analogues which are constructed as explained above, a graphics package is employed. The graphics software package Vis5d was used to draw the contour maps over the geographical area in study for each of the 15 and 20 classes. The iso-lines were drawn for every 60 geopotential meters.

In order to determine the degree of similarity between the different days represented by each analogue, the standard deviation of the geopotential height at each grid point was calculated. For each class, 493 values of the standard deviation were calculated.

4. Results

The results for the two classification strategies adopted, namely with 15 and 20 classes, are discussed and the respective synoptic analogues are presented.

4.1. Classification with 15 Classes

Firstly, the results for the classification assuming 15 classes are presented. For the respective ANN architecture, the output was set to 15 neurons and the size of the neighborhood was set to 14 (as 90% of the output neurons) and the learning process took 1098352 cycles to complete.

The results of the classification with 15 classes are shown in Table 1. Class 15 has the highest frequency of all the classes, followed closely by class 1. Class 6 is the least frequent, followed by classes 3 and 7. Graphically, the results are presented in Figure 1a, depicting the classification for each day in 1996. One immediate observation from the figure is that there is a strong seasonal dependency of the synoptic classes, recognized by the neural network model. This seasonal dependency is more clearly depicted in Figures 1b to 1d, each representing the classification results for the four seasons separately. The strong effect of seasonality on automated synoptic classifications is well known; the seasonal signal can effectively mask the synoptic scale signal if not removed from the gridded data prior to performing the classification (for details see YARNAL, 1993).

Table 1

Number of days in each class for 15 classes

Class	Number of days	Class	Number of days
1	37	9	24
2	20	10	22
3	17	11	27
4	28	12	26
5	25	13	21
6	13	14	29
7	17	15	40
8	20		

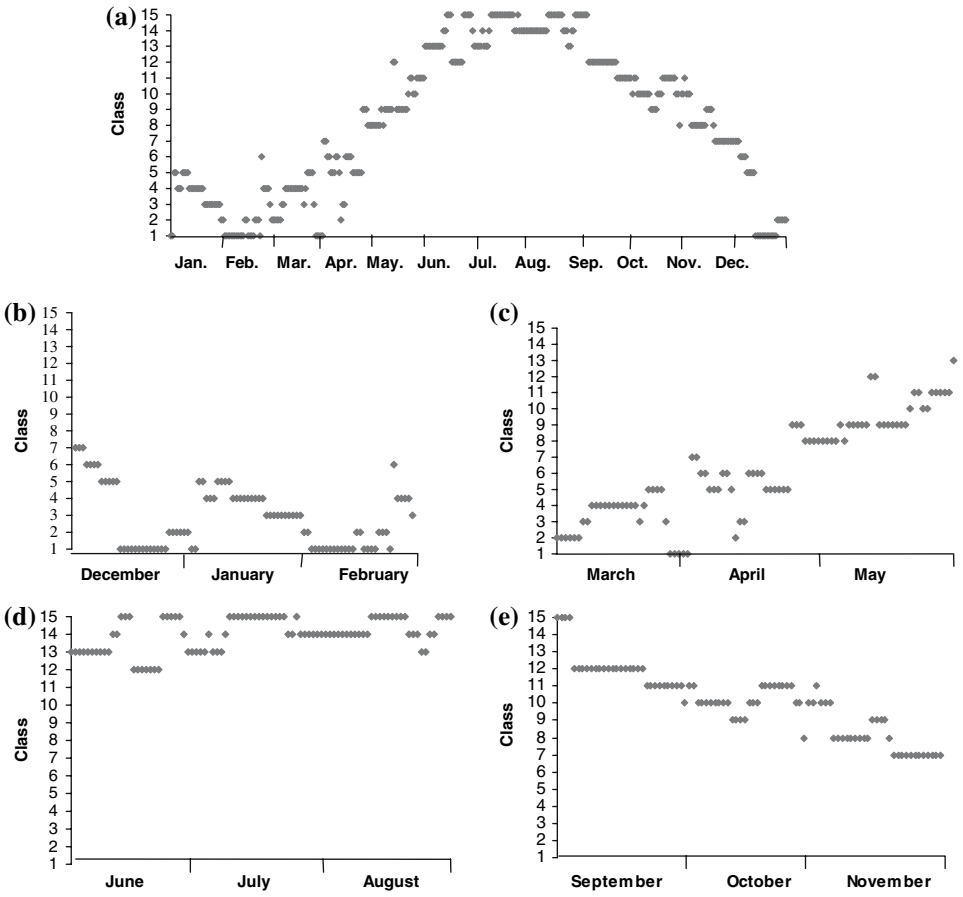

Figure 1
Daily synoptic classification with 15 classes for (a) the whole year 1996, (b) Winter, (c) Spring, (d) Summer and (e) Autumn.

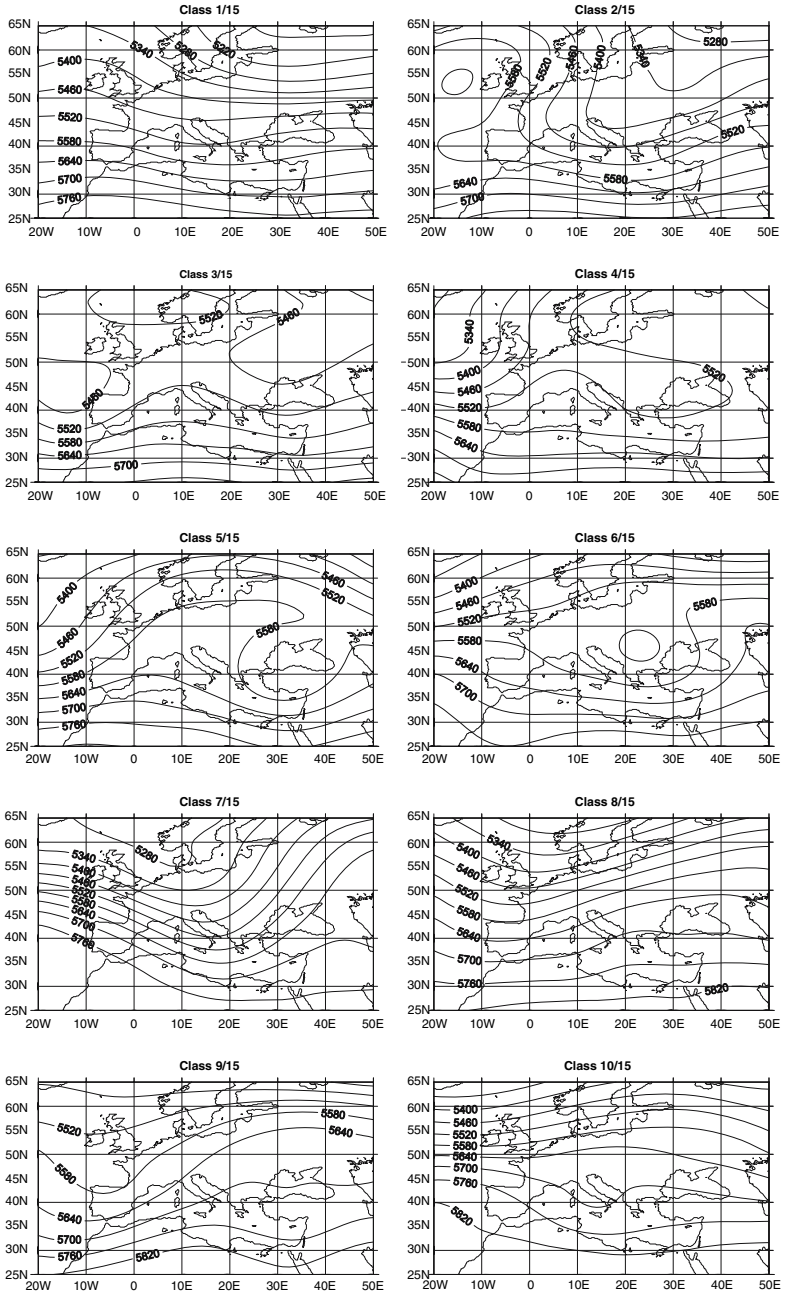

Figure 2
The 15 synoptic analogues established by considering 15 classes. Lines are 500 hPa contours drawn for every 60 geopotential meters.

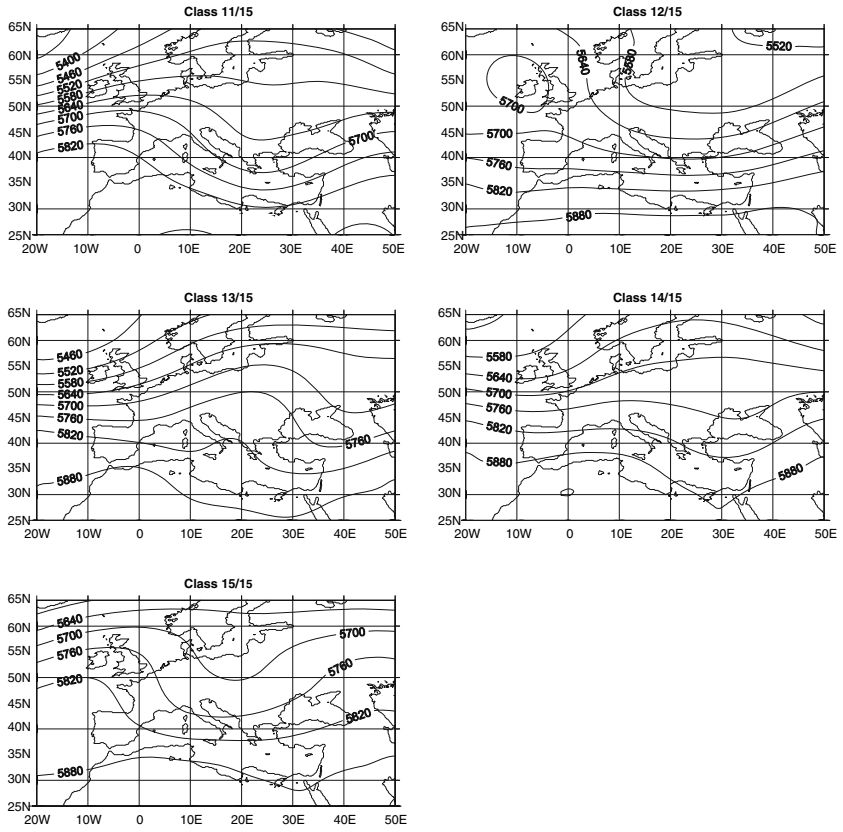

Figure 2
(Contd.)

The first obvious characteristic of the classification is the persistence of specific classes over a period of a few days, reflecting the life-cycle of the respective synoptic systems. There seems to be some kind of limitation imposed by season, as to which classes are observed in any particular period. During the Winter, only classes 1 to 7 are noted, the rest being excluded. Similarly, Summer is characterized only by a few classes namely from 12 to 15. The representation of Winter and Summer by just a few classes reflects the relatively stable Winter-time and Summer-time weather conditions, respectively.

On the contrary, the transitional seasons of Spring and Autumn are characterized by a large number of classes, reflecting exactly the unsettled character of these seasons, as regards the weather. Spring is characterized by a diversity of classes, being represented by classes from 1 to 13. As Spring progresses, there is a clear tendency for the classes to move towards the Summer-time patterns. Also, Autumn is quite diverse as regards its representation by different classes. This latter season is

represented by classes from 7 to 15 with a tendency to move towards Winter-time patterns by the end of the season.

It is beyond the scope of the present article to discuss the detailed spatial characteristics of each class separately. Definitely, from a meteorological point of view, the ANN was able to distinguish between different ''geometric'' patterns, each of which can be considered to correspond to a distinctive distribution of the 500 hPa isobaric field over the area.

For each class, the standard deviation at each grid-point was calculated, in order to get a measure of the dispersion of the grid-point values around the respective grid-point mean value, as established by the analogue. These standard deviation values were found to range from 7.5 and 23.36 meters.

4.2. Classification with 20 Classes

In the case of the classification assuming 20 classes, the output was 20 neurons and the size of the neighborhood was chosen to be 18 (as 90% of the output neurons, which is the same as in the case of 15 classes) and the learning process was terminated after it took 1098497 learning events. The results are summarized in Table 2.

Classes 1 and 20 had the highest frequency of all, followed closely by classes 14, 16 and 18. Class 8 is the least frequent, followed by class 17. More analytically, the results are graphically presented in Figure 3a, which shows the specific class that each day belongs to. As in the case of 15 classes, there is a strong seasonal dependency of the synoptic classes recognized by the neural network model. This observation is more clearly depicted in Figure 3b to 3e, each representing the classification results for the four seasons separately, as defined previously. The obvious characteristic of the classification is the persistence of specific classes over a period of a few days, reflecting the life cycle of the respective synoptic systems, over a period of a few days.

The limitation imposed by seasons as to which classes are observed in any particular period, is also observed in the case of 20 classes. During Winter, only classes 1 to 9 are noted, the rest being excluded. Similarly, Summer is characterized only by a few classes, namely from 16 to 20. The relatively stable Winter-time and

Table 2

Number of days in each class for 20 classes

Class	Number of days	Class	Number of days	Class	Number of days
1	31	8	6	15	11
2	9	9	18	16	26
3	20	10	12	17	8
4	14	11	17	18	26
5	24	12	15	19	24
6	11	13	12	20	31
7	25	14	26		

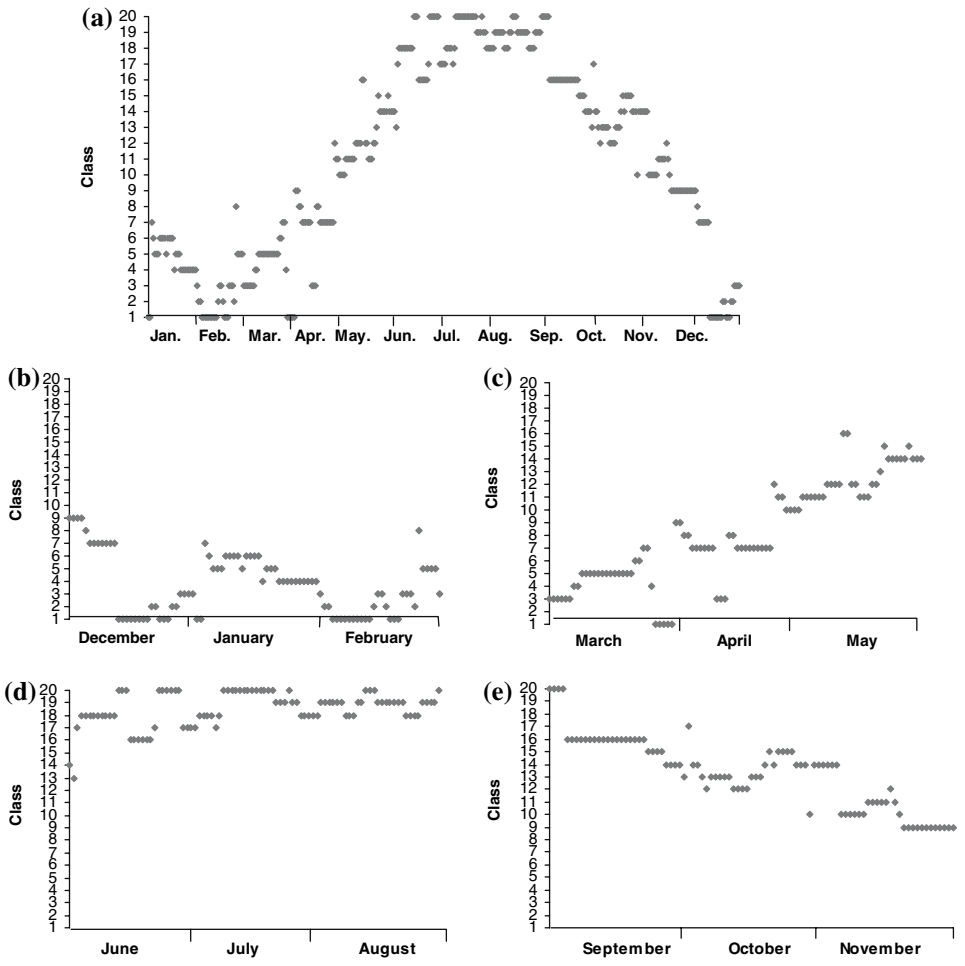

Figure 3
Daily synoptic classification with 20 classes for (a) the whole year 1996, (b) Winter, (c) Spring, (d) Summer and (e) Autumn.

Summer-time weather conditions are reflected by the representation of each of Winter and Summer by few classes.

On the contrary, the transitional seasons of Spring and Autumn are, as in the 15 classes results, characterized by a large number of classes, reflecting exactly the unsettled character of these seasons. Spring is characterized by a diversity of classes, being represented by classes from 1 to 16. As Spring progresses, there is a clear tendency for this season's classes to move towards those of Summer-time. Also, Autumn is quite diverse as regards its representation by different classes. This latter season is represented by classes 9 and from 17 to 20 with a tendency to move towards Winter-time classes by the end of the season.

Twenty average distributions of the geopotential height were calculated by using the members belonging to each class. These analogues corresponding to each class are depicted in Figure 4. From a meteorological point of view, the ANN was able to distinguish between different ''geometric'' patterns, each of which is considered to represent a distinctive distribution of the 500 hPa isobaric height over the area.

The values of the standard deviation calculated at each grid point were found to range from 8.78 and 29.25 meters. Both of these values were slightly higher than the respective minimum and maximum standard deviation values derived for the 15 classes.

5. Discussions and Conclusions

The research presented in this paper comprises an example of the application of SOFM as a useful and practical means in synoptic pattern classification. The adoption of automated synoptic classification systems based on SOFM has also been explored by other researchers who discuss the usefulness of the applicability of this technique (e.g., CAVAZOS, 1999; 2000; HEWITSON and CRANE, 2002). However, CANNON *et al*. (2002) argue that SOFM may exhibit some problems when applied to synoptic classification problems; it may be that small SOFM yield worse cluster solutions than k-means and offer little beyond existing methods in terms of interpretation and spatial ordering of results. They also refer to work outside synoptic climatology that has indicated relatively poor cluster separation for SOFM relative to methods such as the k-means algorithm; the strength of the SOFM method is most evident when large feature maps are used to describe atmospheric variability, however using large feature maps leads to problems with interpretation and defining subclassifications.

Another important issue in developing an automated synoptic classification system is the potential of such systems to recognize important links between the synoptic-scale patterns and weather conditions at the surface (e.g., CAVAZOS, 1999; 2000; HEWITSON and CRANE, 2002). However, as argued by CANNON *et al*. (2002), automated approaches for synoptic classification (including the SOFM method discussed above) define synoptic patterns based on synoptic-scale circulation data and as such may have little climatic significance.

The motivation behind the use of ANN lies in their capacity for making no assumptions about the underlying probability density functions, finding near-optimum solutions from different data sets and the fact that learning is accomplished through training. In addition to these characteristics, ANN has widely been used in modeling a large variety of dynamic systems that are characterized by nonlinearity. It appears that ANN may be utilized in tackling a large number of problems in Meteorology and Climatology.

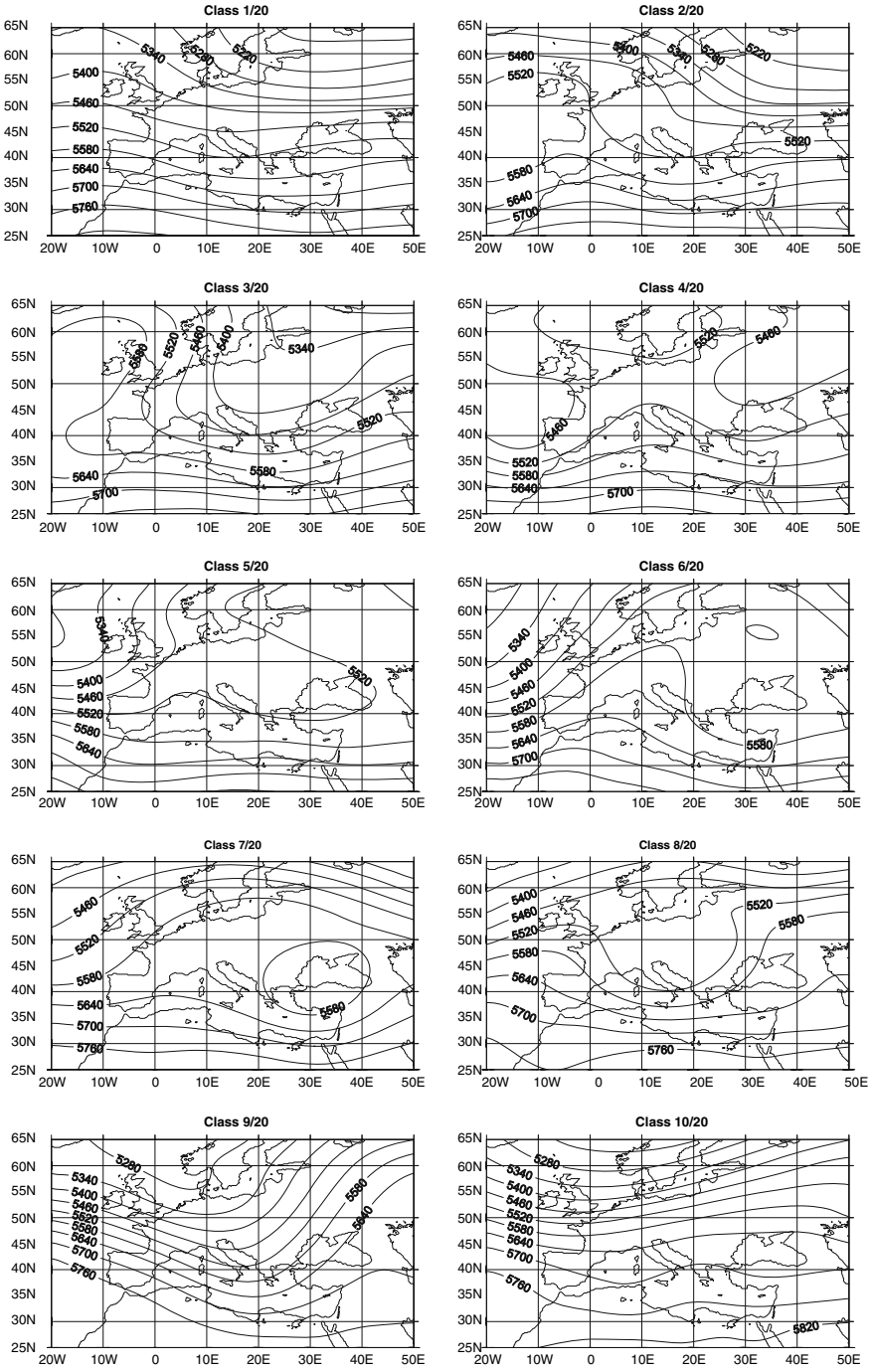

Figure 4
The 20 synoptic analogues established by considering 20 classes. Lines are 500 hPa contours drawn for every 60 geopotential meters.

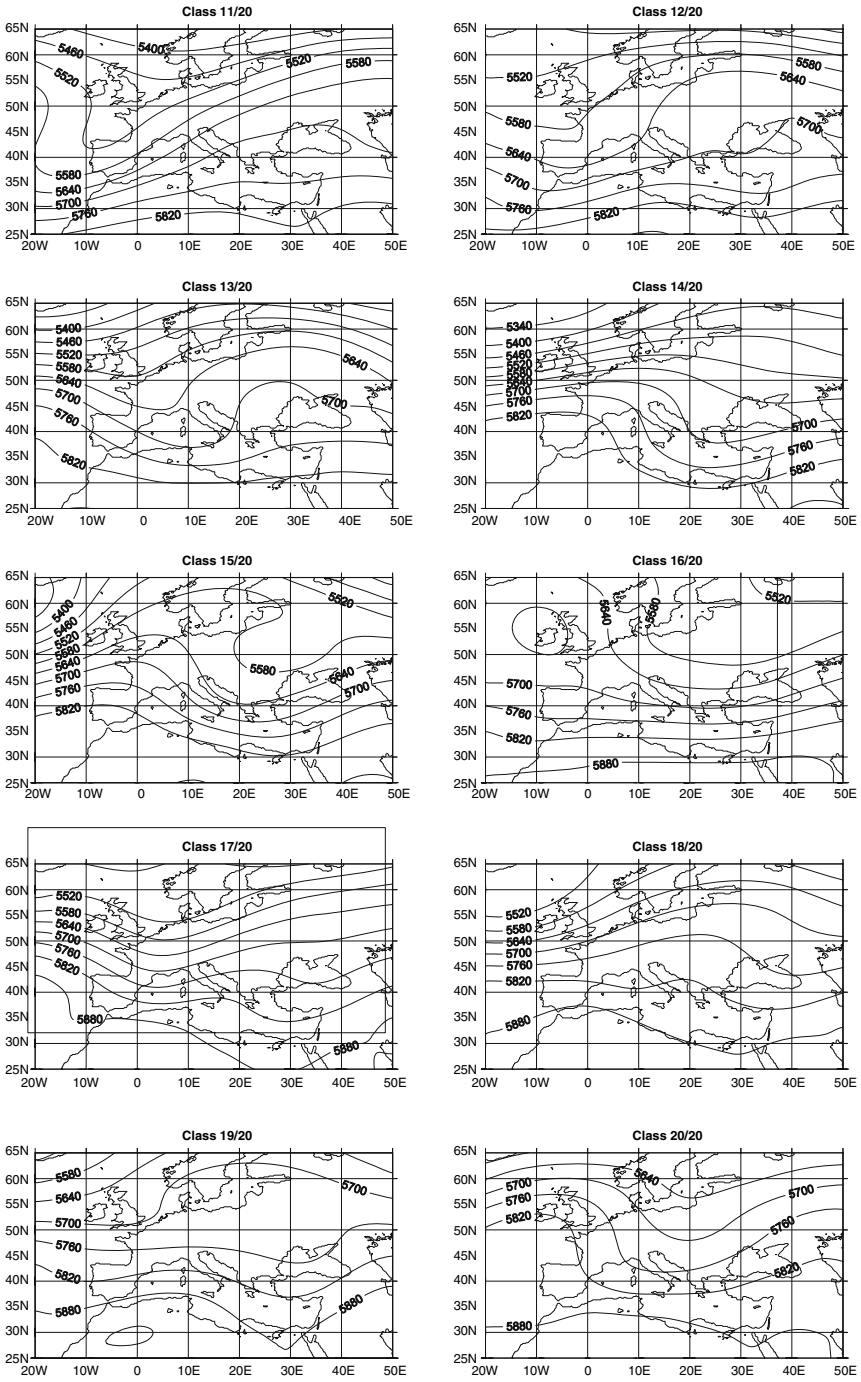

Figure 4
(Contd.)

The main outcomes of this research are:

- The analysis presented above has shown that ANN can successfully be used to identify and classify similar patterns resulting from the drawing of the iso-lines on weather charts and subsequently relate them to a specific behavior of the atmosphere. The ANN models trained were capable of detecting shared characteristics between the patterns and differentiate them in various classes.
- There is a strong seasonal dependency of the classification established by using the ANN methodology. Another characteristic of the ANN classification is the persistence of specific classes over a period of a few days, reflecting the life cycle of the respective synoptic systems over a period of a few days.
- Winter is characterized by only the first classes and Summer is characterized by only the last ones. The representation by few classes reflects the relatively settled weather conditions in these two seasons. On the contrary, Spring and Autumn are characterized by a larger number of classes, representing their unsettled synoptic character. By the end of Spring (Autumn), there seems to be a tendency for the respective classes to move towards the classes characterizing Summer (Winter).
- For each class, an average distribution is determined, each representing a synoptic analogue associated with the respective class. This analogue corresponds to a distinctive synoptic situation and is, roughly speaking, associated with a distinctive distribution of the weather over the area.
- Experiments carried out with more classes show that the findings with 15 and 20 classes are retained when the output nodes increases, showing that the technique's classification capabilities are independent of the number of classes considered.

A possible extension of the ANN classification discussed in this study can be in the classification of data that belong in more than one level and for any meteorological parameters, as the ones mentioned in the beginning. It must be emphasized however, that in such an endeavor it is essential that the input data comprise a sufficiently long time-series of the respective meteorological parameters.

In the analysis presented above, only one meteorological element (namely, the geopotential height) corresponding to a single isobaric level was studied. Obviously, a similar classification can be made for the same parameter corresponding to any isobaric level or even for any other meteorological parameter. In a more complex approach, the ANN methodology presented above can be used for similar synoptic pattern identification with combinations of meteorological parameters (e.g., geopotential height and temperature). In such an endeavor, the ANN will establish analogues that encompass the spatial distribution of two (or more) parameters, a function that will be extremely difficult for the human brain to accomplish.

There can be several potential applications which can make use of synoptic analogues in atmospheric sciences, derived with the technique described in this paper. There are numerous examples in which synoptic patterns have been used to diagnose or forecast specific weather conditions. The reader is referred to two recently

published research findings on this issue; in the first, synoptic patterns are related to understand the transfer of Saharan dust over the east Mediterranean (RETALIS and MICHAELIDES, 2006); the other refers to forecasting low visibilities due to fog formation in Poland (GLOWACKA *et al.*, 2005).

Ackowledgements

The authors wish to thank Dr. ISMAIL GULTEPE of Environment Canada and Université du Québec for reading a draft of this paper and for offering insightful comments for improving it. The comments by an anonymous reviewer are also appreciated.

REFERENCES

BANKERT, R.L. (1994), *Cloud classification of a AVHRR imagery in maritime regions using probabilistic neural network*, J. Appl. Meteorol. *33*, 909–918.

BANKERT, R.L. and AHA, D.W. (1996), *Improvement to a neural network cloud classifier*, J. Appl. Meteorol. *35*, 2036–2039.

CANNON, A.J., WHITFIELD, P.H., and LORD, E.R. (2002), *Synoptic map-pattern classification using recursive partitioning and principal component analysis*, Mon. Wea. Rev. *130*, 1187–1206.

CAVAZOS, T. (1999), *Large-scale circulation anomalies conducive to extreme precipitation events and derivation of daily rainfall in northeastern Mexico and southeastern Texas*, J. Climate *12*, 1506–1523.

CAVAZOS, T. (2000), *Using self-organizing maps to investigate extreme climate events: An application to wintertime precipitation in the Balkans*, J. Climate *13*, 1718–1732.

CHARALAMBOUS, C., CHARITOU, A., and KAOUROU, F. (2001), *Comparative analysis of neural network models: Application in bankruptcy prediction*, Annals of Operations Res. *99*, 403–425.

ELSNER, J.B. and TSONIS, A.A. (1992), *Nonlinear prediction, chaos and noise*, Bull. Am. Meteorol. Soc. *73*, 49–60.

FRANCL, L.J. and PANIGRAHI, S. (1997), *Artificial neural network models of wheat leaf wetness*, Agric. Forest Meteorol. *88*, 57–65.

FURUNDZIC, D. (1998), *Application example of neural networks for time series analysis: Rainfall-runoff modeling*, Signal Processing *64*, 383–396.

GLOWACKA, A., TERRADELLAS, E., CANO, D., BAKOWSKI, R., WIAZEWSKI, W., and PARADOWSKI, M. (2006), *A case study: Comparison between results of HIRLAM 1d and weather patterns method for fog prediction on 16th January 2005 at Warsaw-Okecie airport,* Proc. Workshop on *Short Range Forecasting Methods of Fog, Visibility and Low Clouds, Larnaca, Cyprus*, May 2005 (ed. S. Michaelides) (OPOEC), 98–105.

HEWITSON, B.C. and CRANE, R.G. (2002), *Self-organizing maps: Applications to synoptic climatology*, Climate Res. *22*, 13–26.

KALOGIROU, S., NEOCLEOUS, C., MICHAELIDES, S.C., and SCHIZAS, C.N. (1997), *A time series reconstruction of precipitation records using artificial neural networks,* Proc. Fifth European Congress on *Intelligent Techniques and Soft Computing*, EUFIT 97, Aachen, Germany (ed. H.J. Zimmermann), vol. *3*, 2409–2413.

KALOGIROU, S.A., NEOCLEOUS, C.C., MICHAELIDES, S.C., and SCHIZAS, C.N. (1998), *Regeneration of isohyets by considering landscape configuration using artificial neural networks,* Proc. Fourth International Conference on *Engineering Applications of Neural Networks*, EANN98, Gibraltar, June 1998 (eds. A.B. BULSARI, J. FERNADEZ DE CANETE, and S. KALLIO), 383–389.

KOHONEN, T. (1990), *The Self-Organizing Map*, Proc. of the IEEE, vol. *78*, no. 9, 1464–1480.

KOHONEN, T. (2001), *Self-Organizing Maps*, 3rd Ed. (Springer Series in Information Sciences).

LAMB, H.H. (1950), *Types and spells of weather around the year in the British Isles: Annual trends, seasonal structure of the year, singularities,* Q. J. Roy. Meteorol. Soc. *76*, 393–429.

LORENZ E.N. (1969), *Atmospheric predictability as revealed by naturally occurring analogues*, J. Atmos. Sci. *26*, 636–646.

MARZBAN, C. and STUMPF, G.J. (1996), *A neural network for tornado prediction based on Doppler radar-derived attributes*, J. Appl. Meteorol. *35*, 617–626.

MICHAELIDES, S.C., PATTICHIS, C.S., and KLEOVOULOU, G. (2001), *Classification of rainfall variability by using artificial neural networks*, Internat. J. Climatology *21*, 1401–1414.

NICOLIS, C. (1998), *Atmospheric analogues and recurrence time statistics: Toward a dynamical formulation*, J. Atmos. Sci. *55*, 465–475.

PATTERSON, D.W., *Artificial Neural Networks, Theory and Applications* (Prentice Hall 1995).

PATTICHIS, C.S., SCHIZAS, C.N., and MIDDLETON, T.M. (1995), *Neural Network Models in EMG Diagnosis*, IEEE Transactions on Biomedical Engineering, vol. *42*, no. 5, 486–495.

PEAK, J.E. and TAG, P.M. (1992), *Toward automated interpretation of satellite imagery for Navy shipboard applications*, Bull. Am. Meteorol. Soc. *73*, 995–1008.

PEAK, J.E. and TAG, P.M. (1994), *Segmentation of satellite imagery using hierarchical thresholding and neural networks*, J. Appl. Meteorol. *33*, 605–616.

PREZERAKOS, N.G., MICHAELIDES, S.C., and VLASSI, A.S. (1991), *Atmospheric synoptic conditions associated with the initiation of north-west African depressions*, Internat. J. Climatology *10*, 711–729.

RETALIS, A. and MICHAELIDES, S. (2006), *Synergetic use of Terra/Modis imagery and meteorological data for studying aerosol dust events in Cyprus*, Internat. J. Environ. and Pollution, in press.

SCHIZAS, C.N., PATTICHIS, C.S., and MICHAELIDES, S.C. (1994), *Forecasting minimum temperature with short time-length data using artificial neural networks*, Neural Network World *2*, 219–230.

SCHNORRENBERG, F., PATTICHIS, C.S., KYRIACOU, K., VASSILIOU, M., and SCHIZAS, C.N. (1996), *Computer-aided classification of breast cancer nuclei*, Technol. Health Care J. *4*, 147–161.

TANGANG, F.T., HSIEH, W.W., and TANG, B. (1998), *Forecasting regional sea-surface temperatures in the tropical Pacific by neural network models, with wind stress and sea-level pressure as predictors*, J. Geophys. Res. *103*, 7511–7522.

VAN DEN DOOL, H.M. (1989), *A new look at weather forecasting through analogues*, Mon. Wea. Rev. *117*, 2230–2247.

YARNAL, B., *Synoptic Climatology in Environmental Analysis* (Bellhaven Press, London, 1993).

(Received June 11, 2006, accepted October 29, 2006)
Published Online First: June 8, 2007

Pure appl. geophys. 164 (2007) 1365–1381
0033–4553/07/071365–17
DOI 10.1007/s00024-007-0223-6

Pure and Applied Geophysics

Probabilistic Visibility Forecasting Using Neural Networks

JOHN BJØRNAR BREMNES[1] and SILAS CHR. MICHAELIDES[2]

Abstract—Statistical methods are widely applied in visibility forecasting. In this article, further improvements are explored by extending the standard probabilistic neural network approach. The first approach is to use several models to obtain an averaged output, instead of just selecting the overall best one, while the second approach is to use deterministic neural networks to make input variables for the probabilistic neural network. These approaches are extensively tested at two sites and seen to improve upon the standard approach, although the improvements for one of the sites were not found to be of statistical significance.

Key words: Visibility forecasting, neural networks.

1. Introduction

Forecasting visibility is of considerable importance to several weather-dependent human activities and operations, it even has a direct life and property safety impact. In aviation, for example, aerodrome visibility forecasting can be crucial and, to a large extent, it plays a decisive role in smooth flight planning and operations. In order to provide the best possible guidance for meteorologists and other decision makers, forecasts should be formulated in probabilistic terms (e.g., MURPHY, 1991; ROULSTON *et al.*, 2006). In the present article the focus is restricted to forecasting probabilities for a set of visibility ranges or categories.

Probabilistic visibility forecasting using statistical methods was already described in early attempts such as by BOCCHIERI *et al.* (1974), who applied linear regression with both observations and output from atmospheric models as predictors. VISLOCKY and FRITSCH (1997) carried out a similar study and demonstrated improvements by using a network of stations. The use of observations was also the topic in LEYTON and FRITSCH (2003, 2004).

[1] Norwegian Meteorological Institute, Box 43 Blindern, NO-0313 Oslo, Norway. E-mail: j.b.bremnes@met.no
[2] Meteorological Service, Nicosia, 1418 Cyprus. E-mail: silas@ucy.ac.cy

Neural networks have extensively been used in atmospheric sciences, e.g., GARDNER and DORLING (1998) and HSIEH and TANG (1998), however, the adoption of neural networks for visibility forecasting is a rather recent endeavor. PASINI *et al.* (2001) focused on deterministic forecasting using weighted least squares estimation. Prediction of categorical events was the topic of NUGROHO *et al.* (2002), who proposed a combination of two types of neural networks to account for the strong imbalance often seen in categorized visibility data. MARZBAN *et al.* (2005) compared neural network with logistic and linear regression and concluded that the former presents superior quality.

In this article, the potential of further improvements in neural network modeling is explored by (i) simply averaging predictions from several neural network models and (ii) by using a two-stage approach, where deterministic neural networks are applied to form new input variables for the probabilistic neural networks. The paper is organized as follows: A review of neural networks considering their usage in this work is given in the next section. Section 3 concerns forecast validation, while section 4 describes the proposed approaches in more detail. Results from two case studies are presented in section 5 followed by some concluding remarks in section 6.

2. Neural Networks

A brief description of how neural networks are defined and applied is presented in this section. For a more comprehensive introduction to the topic, the reader is referred to BISHOP (1995). Estimation in the case studies of section 5, is carried out by means of the nnet package included in the statistical software R (R DEVELOPMENT CORE TEAM, 2005).

2.1. Description

Neural networks can be considered as very flexible functions that map predictive information $\boldsymbol{x}$ into visibility. The p-dimensional vector $\boldsymbol{x}$ is often referred to as a predictor or input variable and contains available information about the future visibility at the time the forecast is being made. Typically, the predictor is comprised of the latest measurements, output from atmospheric models, seasonal or diurnal information.

Only neural networks with a single hidden layer are considered, and in the case of K output variables, the neural nets are defined by the K functions

$$f_k(\mathbf{X}) = \beta_{0k} + \sum_{h=1}^{H} \beta_{hk} g\left(\alpha_{h0} + \boldsymbol{\alpha}_h^T \boldsymbol{x}\right), \; k = 1, 2, \ldots, K. \tag{1}$$

Here, H is the number of hidden units, the function $g(u) = (1 + e^{-u})^{-1}$, and the αs and βs unknown parameters to be estimated. For deterministic predictions of

visibility, the number of output variables K is equal to one and the function $f_k(\boldsymbol{x}) \equiv f(\boldsymbol{x})$ simply defines the visibility in the relevant unit. For probabilistic predictions, K is the number of visibility classes and the probability of class K is defined as

$$P_k(\boldsymbol{x}) = \frac{e^{f_k(\boldsymbol{x})}}{\sum_{j=1}^{K} e^{f_j(\boldsymbol{x})}}, \tag{2}$$

which ensures that the probabilities add up to one.

2.2. Estimation of Parameters

In order to estimate the unknown parameters of the neural network in (1), a set of historical data is needed. Let $\boldsymbol{x}_1, \boldsymbol{x}_2, \ldots, \boldsymbol{x}_n$ denote the predictor values and $\boldsymbol{y}_1, \boldsymbol{y}_2, \ldots, \boldsymbol{y}_n$ the corresponding observed visibility. In the probabilistic case, each observation $\boldsymbol{y}_i$ is of dimension K and is coded such that the component representing the observed class is one, while the remaining are zero. In other words, y_{ik} is one if the k-th class is observed (for the i-th case) and zero otherwise.

Estimation of parameters also requires a definition of a loss function. For deterministic neural networks optimization with respect to square errors is most common. A variant of this is chosen here:

$$\sum_{i=1}^{n} (y_i - f(\boldsymbol{x}_i))^2 + \lambda \left(\sum_{h=0}^{H} \beta_h^2 + \sum_{h=1}^{H} \sum_{l=0}^{p} \alpha_{hl}^2 \right), \tag{3}$$

which should be minimized with respect to the αs and βs. Note that these also appear in the function f and that the index k is left out since the neural net is defined by only one univariate function. The latter term of (3) is added in order to penalize non-smooth functions, which may reduce the predictive capabilities of the network in cases with many parameters. The degree of smoothness is controlled by the tuning parameter $\lambda \geq 0$, and a positive λ is often seen to improve predictions HASTIE *et al.* (2001, chapter 11.5.2).

In two of the modeling approaches described later, some of the training cases are defined to be of less importance than others. The degree of importance is specified by introducing a weight to each case, and in the loss function (3) these appear as factors in the least-squares term. Training cases with large weights will then have more influence on the fit than cases with small weights, and the estimated neural network will be drawn towards these.

For probabilistic neural networks the most frequently applied loss function

$$-\sum_{i=1}^{n} \sum_{k=1}^{K} y_{ik} \ln P_k(\boldsymbol{x}_i) + \lambda \left(\sum_{h=0}^{H} \sum_{k=1}^{K} \beta_{hk}^2 + \sum_{h=1}^{H} \sum_{l=0}^{p} \alpha_{hl}^2 \right) \tag{4}$$

is chosen, and neural networks are fitted by minimizing this with respect to the αs and βs. Note that these parameters also appear in the functions P_k, in equations (2) and (1). As above a penalizing term is added to control the degree of smoothness of the fitted neural networks.

It is not possible to solve the minimization problems (3) and (4) explicitly, so iterative numerical methods must be applied. An additional complicating factor is that there are usually many local minima and there is, consequently, no guarantee that the methods will find the global minimum. To deal with this, the minimizations are here repeated five times with random initial values resulting in equally many fitted neural networks. The predictions by these networks are then averaged before any further use.

2.3. Training Procedure

In the neural networks described above, there are two tuning parameters that need to be determined, the number of hidden units H and the regularization parameter λ. It is here decided to test predefined sets of these, $H \in \{1, 2, 4, 8, 16\}$ and $\lambda \in \{0.01, 0.1, 1, 5\}$, using cross-validation on the training data. The cross-validated predictions for all combinations of H and λ are then evaluated using either the ranked probability score (RPS), see section 3, or the root-mean-squares error (RMSE) depending on whether the predictions are probabilistic or deterministic. The best combination is then selected, and before making predictions for the test data, the neural networks are retrained using all the training cases.

2.4. Selection of Predictors

The selection of predictors is an important step in the modeling process in order to make good predictions. In the two case studies to follow, there are many predictors to choose from and even more when transformations of these are included. The selection is here based on a greedy forward search algorithm. At the first step, neural networks with one predictor variable are trained, as described above, for all possible predictor candidates. The predictor contributing to the best prediction with respect to either RPS or RMSE is chosen. At the second step, neural networks with two predictor variables (one of them selected at the previous step) are considered. The best predictor combination is then chosen. The process is repeated until addition of new predictor variables no longer improves the validation score. For more information about search algorithms see for example BISHOP (1995, chapter 8.5) or HAND *et al.* (2001, chapter 8.2).

3. Forecast Validation

Probabilistic forecasts for a set of ordered categories can be validated in various ways. Reliability diagrams and ROC curves are useful, but do not easily summarize

the quality in a single number. In order to rank models in an objective manner, a more suitable score is needed, and it is here proposed to use the ranked probability score (RPS). Let $\hat{p}_1, \hat{p}_2, \ldots, \hat{p}_K$ denote the predicted probabilities for each of the K categories and $y_1, y_2, \ldots, y_k$ corresponding binary variables, which are one for the observed class and zero for the others. The RPS for a single prediction is then defined by

$$\mathrm{RPS} = \sum_{k=1}^{K} \left(\sum_{j=1}^{k} \hat{p}_j - \sum_{j=1}^{k} y_j \right)^2 . \tag{5}$$

Note that the inner sums are the cumulative probabilities of the predictions and observations, respectively. Further, the optimal score is zero which is obtained when the probability mass is assigned to the observed class. The worst possible score is $K - 1$; so the lower the score is, the better the model. For several predictions, the RPS (5) is computed for each and then averaged. When averaging over many cases it is also possible to compute the contribution to the RPS for each observed class.

4. Modeling Approaches

In this section the models applied to the subsequent case studies are described.

4.1. Standard Probabilistic Approach (STD)

In the standard probabilistic approach (STD) a forward search for the best predictors is first carried out on the training data as described in section 2.4. A new probabilistic neural network based on the best predictors is then trained using all the training data and predictions are made for the test data. For the reasons mentioned in 2.2, note that there are actually five neural networks, but in principle they can be thought of as a single one.

4.2. Multi-Model Averaging (MMA)

Instead of using only the best model from the forward search, several neural network models can be trained, having one for each predictor combination. Predictions for each model are then made for the test data and the average of these applied. A weighted average could also have been applied, but since the best models usually will have quite similar scores and in addition be strongly correlated, it was decided prior to the experiments that there would not be much to gain. Experiments with the best three (MMA3) and five predictor combinations (MMA5) are carried out.

4.3. Two-Stage Neural Network Modeling

The basic idea in the two-stage modeling process is to apply deterministic neural networks to create new input variables for the probabilistic neural network. It is most natural to start with making a deterministic neural network whose output is predicted visibility (in meters). A forward search for predictors is then first carried out, followed by training and predictions on the test data. In order to train the probabilistic neural network, deterministic predictions are also needed for the training data. For this the cross-validated predictions already made in the training procedure are applied. A probabilistic neural net is then fitted using the predicted visibility as the only input variable. This approach is hereafter referred to as STD-1D.

In addition to have a deterministic prediction of visibility as an input variable, it may also be useful to have predictions of its error as a quantitative measure of uncertainty. Absolute errors are here applied, mainly because their range is less than those obtained using square errors. As usual, a forward search for predictors is first carried out, followed by training of the best model and then by making predictions of absolute errors on the test data. The cross-validated predictions from the training procedure are used to represent the absolute error on the training set. Finally, a probabilistic neural net is fitted using the predicted visibility and the predicted absolute error as input variables (STD-2D) and predictions made for the test data.

For most purposes, reduced visibility events are more important than good ones, and it may be of interest to put more weights on these cases. In probabilistic forecasting this is difficult to achieve without making biased probabilities. The two-stage approach, however, provides an option; in the deterministic neural nets used to create predictors, weights can be included to the loss function as described in 2.2. In the case studies discussed later, the weight for a given case is defined as one minus its empirical class probability. Although the deterministic predictions are biased, the output from the probabilistic neural network is not. The methodology is otherwise as explained above, and the approaches using weights are denoted by STD-1DW and STD-2DW, respectively.

5. Case Studies

The modeling approaches described above were applied to data from two sites one from Larnaka Airport in Cyprus and the other from Gardermoen in Norway. Variables have been selected and derived from the usual range of observational variables obtained at synoptic stations. Other relevant data for operational forecasting, such as output from numerical weather prediction models and remote sensing systems, have not been considered.

5.1. Larnaka Airport: One-Hour Forecasts

5.1.1. Data

The data applied in this case study are hourly observations from April to September, covering a two-year period (2003 and 2004); the data from the former year were used for training, while the latter were employed for testing and evaluation. The variables contained in the original data set were first reduced subjectively from about 50 to 8. In addition, a total of 10 derived variables were included, together with the month and the hour. A list of the variables is given in the first column of Table 1. In this context, tendency is defined as the increase during the last hour and log refers to a logarithmic transformation of the respective variable.

The definition of the visibility categories and the number of cases within each category is displayed in Table 2. As can be seen, the events with reduced visibility (0–1500 m) are rather rare: The percentage of reduced visibility cases adds up to 2.4% in the training set and only to 0.2% in the test set.

Table 1

List of available predictors for Larnaka Airport, the stage at which predictors were selected in the forward search and their rank (in parentheses) at the first stage of the search. The second and third most important predictors at the first stage are also specified

Predictor	Deterministic neural net				Probabilistic neural net	
	without weights		with weights			
	visibility	abs.error	visibility	abs.error		
Height of cloud base	1 (1)	(3)	(3)	(3)		(2)
Height of cloud base (log)				2 (7)		
Height of cloud base tendency						
Temperature	2 (12)					
Visibility						
Visibility (log)			2 (13)			(3)
Visibility tendency	(2)	1 (1)	(2)	(2)	1	(1)
Humidity						
Humidity (log)	(3)	(2)	1 (1)	1 (1)		
Humidity tendency						
Pressure						
Pressure tendency				3 (5)		
Dew point						
Dew point depression						
Dew point depression tendency						
Wind direction						
Wind speed						
Wind speed (log)						
Month						
Hour						

Table 2

Definition of visibility categories and the number of events within each for Larnaka Airport

Data set	Visibility categories (m)				
	[0, 200]	(200, 600]	(600, 800]	(800, 1500]	> 1500
Training set	14	19	14	48	3813
Testing set	4	4	1	0	4082

5.1.2. Results

In order to find suitable subsets of the twenty predictors for the various neural network models, a forward selection procedure was first carried out for each, as described in section 2.4. The selected predictors are marked in Table 1, with respect to the stage at which they were selected. In addition, the ranking at the first stage of the selected and initially most relevant predictors is shown. It is evident that important predictors at the first stage were not necessarily chosen at all and that initially less important predictors were selected at a later stage. For example, the temperature in the deterministic neural network for visibility without using weights was not so important at the first stage (ranked 12th), but turned out to be the most important at the second stage. Similar examples are in general quite common and just indications that some variables may only be influential when they interact with other variables.

The forward search for the standard probabilistic neural network was also the basis for choosing the best three and five models in the multi-model averaging approach. In decreasing order of quality, they were

- visibility tendency,
- visibility tendency and pressure tendency,
- visibility tendency and height of cloud base,
- visibility tendency and wind speed (log),
- visibility tendency and dew point depression tendency.

After the predictor combinations were selected, the modeling approaches described in section 4 were tested. Due to randomness in the parameter estimation as well as in assigning data to the cross-validation sets, it was decided to repeat the experiment ten times in order to make conclusions more robust.

It is not possible to show the fitted neural networks for all experiments, but the ones from the last replication are depicted in Figure 1. For simplicity, the categories representing reduced visibility (< 1500 m) are merged and only the predicted probability of reduced visibility is shown. For the STD model it can be noticed that the probability is at its minimum when visibility remains unchanged, relatively large with visibility deteriorations (about 65%) and moderate with visibility improvements

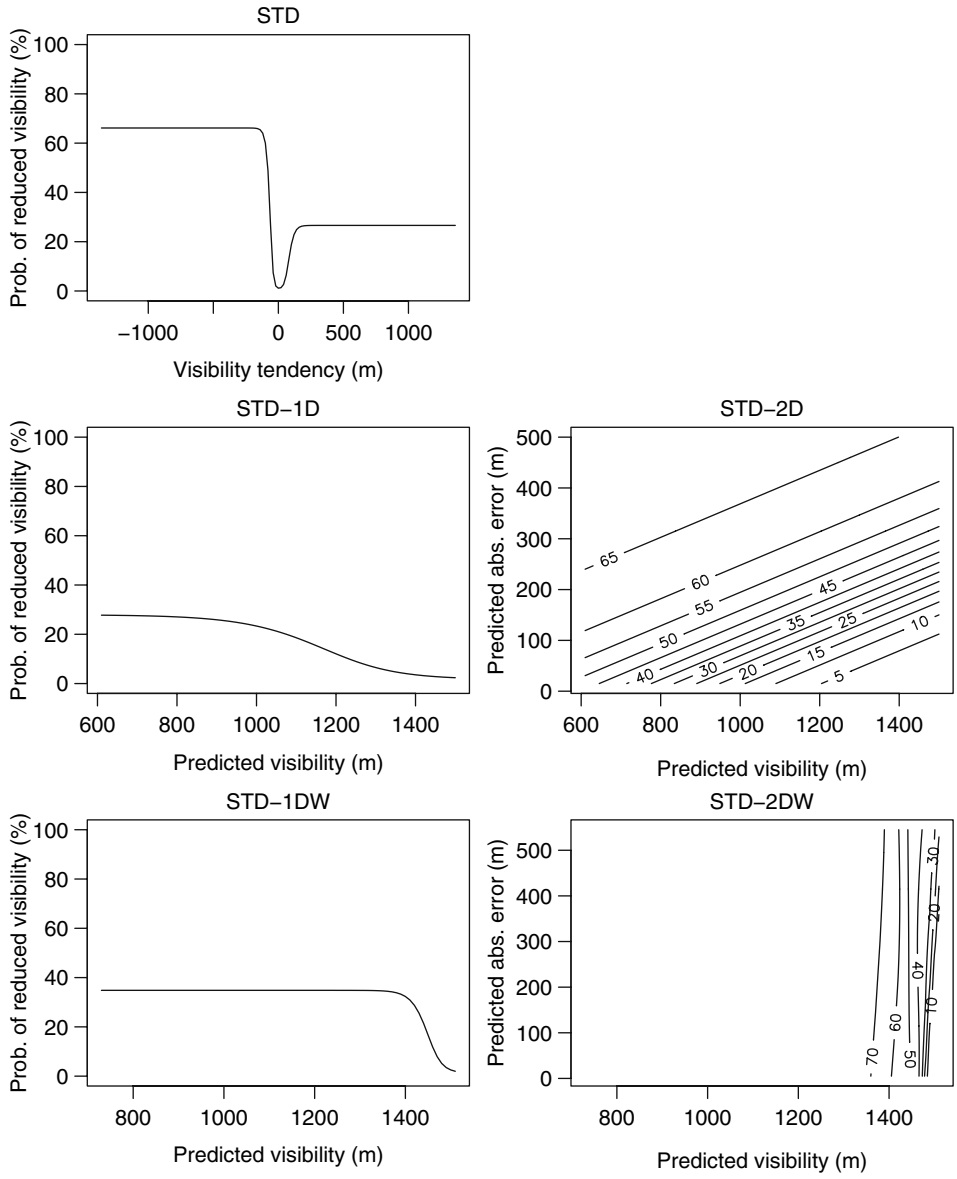

Figure 1
Predicted probability of reduced visibility for the various models for Larnaka Airport. The plots on the right side are contour plots.

(about 25%). The STD-1D and STD-2D models both suggest decreasing probabilities with increasing predicted visibility, as expected. By adding an extra predictor that quantifies the uncertainty (STD-2D), the probability of reduced visibility is

largest when the uncertainty is high. Taking into account that it is more difficult to predict reduced visibility than good, this is also reasonable. The approaches using weights, STD-1DW and STD-2DW, have similar interpretations.

The overall quality of the various models is summarized using the ranked probability score and shown in Figure 2 along with the average predicted probabilities of reduced visibility. The persistence, defined by assigning 100 percent probability to the current class, is included as a reference. The results are averaged over all the ten replications, except for the horizontal lines which show the range of the RPSs over the ten experiments. Further, the RPSs have been split into two parts: One part for cases when the observed visibility is reduced and the other when it is good.

The ranked probability scores show that the statistical models STD, MMA3, MMA5, and STD-2D all performed better than persistence, while the other three models were worse. Three of the statistical models were better than the standard model (STD), but only slightly. For all neural network models, the main contribution to the RPSs is due to the predictions of the 0.2% cases with observed visibility less than

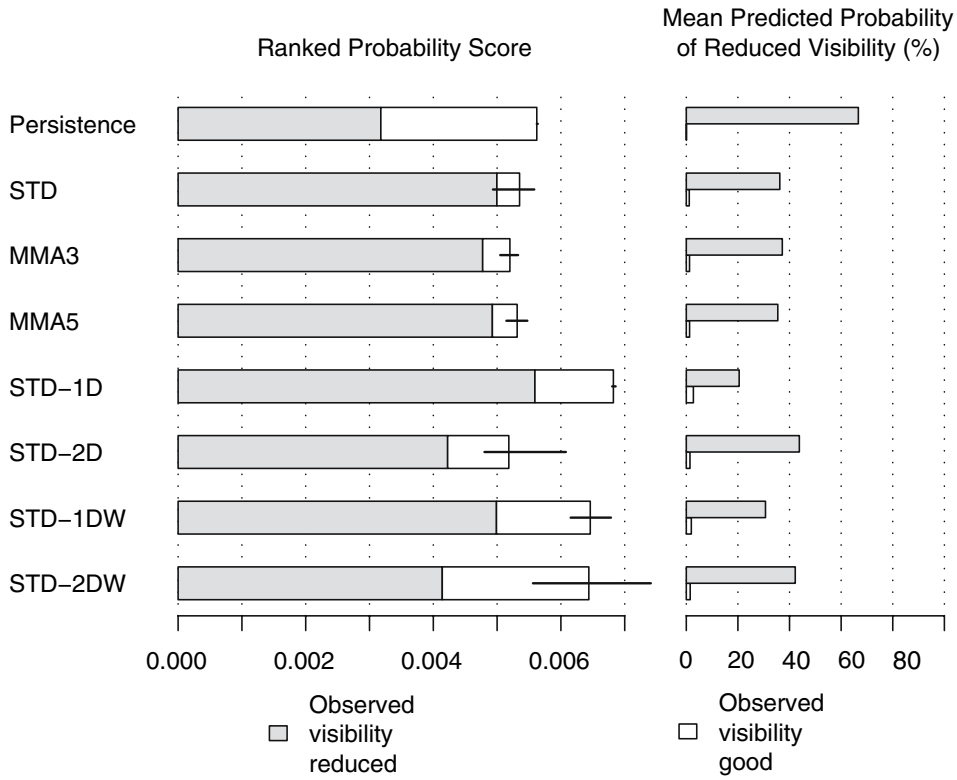

Figure 2
Ranked probability scores and average predicted probabilities of reduced visibility for Larnaka Airport. The horizontal lines represent the ranges of the ranked probability scores within the ten replications of the experiment.

1500 m, which is an indication of the difficulties in forecasting these events. From the bar plot of the average predicted probability of reduced visibility it can be noticed that the persistence had a quite good discrimination of good and reduced visibility. An explanation may be that the nine reduced visibility events are quite clustered in time.

In order to assess the significance of the findings, 95% bootstrap confidence intervals were made by re-sampling in the temporal dimension (not between experiments) with replacement, see DAVISON and HINKLEY (1997, chapter 3.8); the number of bootstrap replications were 2000. Table 3 shows 95% confidence intervals of pair-wise differences in expected RPS between various modeling alternatives. Although some of the models had better results than persistence on our test data, the confidence intervals shown in column one indicate that they are not significantly better. Further, there seems to be no evidence that any of the new proposed methodologies are better than the standard neural network approach (STD); STD-1D is even worse than STD. In addition to the highly imbalanced data, one reason may be the lack of predictive potential in the data and that one may expect better results for the proposed statistical models in easier forecasting problems. Lastly, it can be concluded that using both predicted visibility and its predicted absolute error (STD-2D) is better than using only the former (STD-1D).

5.2. Gardermoen: Six-Hour Forecasts

5.2.1. Data

The data from Gardermoen are six-hourly observations (the highest temporal resolution available) for the years 1985 to 2004; the 1985 to 1994 data were assigned for training and the remaining for testing and evaluation. In addition to the 9 basic variables contained in the data set, 9 derived variables together with the month and the hour were made available; these are listed in the first column of Table 4.

Using the same visibility categories as for Larnaka Airport, Table 5 summarizes the number of cases in each category for Gardermoen. In the training set, the percentage of events with reduced visibility (0–1500 m) is similar to Larnaka Airport, namely 2.8%, but the actual number of events in the data set is larger. In the test set, the percentage of events in Gardermoen amounts to 2.8%.

Table 3

95% basic bootstrap confidence intervals for difference in expected ranked probability score between models in first column and persistence, STD and STD-1D, respectively, for Larnaka Airport. Intervals not covering zero indicate statistical significant differences

Models	Persistence	STD	STD-1D
STD	(−0.0032, 0.0023)		
MMA3	(−0.0032, 0.0021)	(−0.00038, 0.000035)	
MMA5	(−0.0031, 0.0022)	(−0.00015, 0.000046)	
STD-1D	(−0.0020, 0.0040)	(0.00081, 0.0022)	
STD-2D	(−0.0027, 0.0015)	(−0.0012, 0.00072)	(−0.0028, −0.00061)

Table 4

List of available predictors for Gardermoen, the stage at which predictors were selected in the forward search and their rank (in parentheses) at the first stage of the search. The second and third most important predictors at the first stage are also specified

Predictor	Deterministic neural net								Probabilistic neural net	
	without weights				with weights					
	visibility		abs.error		visibility		abs.error			
Wind speed							5	(14)		
Wind speed (log)	1	(1)		(2)	1	(1)				(2)
Wind direction		(2)								
Humidity										
Humidity (log)	2	(11)	6	(19)	2	(15)	3	(13)		
Humidity tendency			1	(1)						
Visibility										
Visibility (log)										
Visibility tendency				(3)					1	(1)
Visibility 18h ago										
Visibility 18h ago (log)	3	(4)			3	(16)	4	(15)		
Snow cover			2	(6)			2	(6)		
Temperature			3	(4)		(2)				(3)
Temperature tendency						(3)				
Cloud cover			4	(20)			7	(8)		
Height of cloud base			5	(12)			6	(10)		
Pressure										
Pressure tendency		(3)			4	(8)		(3)		
Month			7	(16)				(2)		
Hour							1	(1)		

Table 5

Definition of visibility categories and the number of events within each for Gardermoen

Data set	Visibility categories (m)				
	[0, 200]	(200, 600]	(600, 800]	(800, 1500]	> 1500
Training set	83	195	60	36	12943
Testing set	62	204	92	33	13402

5.2.2. Results

The outcome of the variable selection processes for the Gardermoen data is summarized in Table 4. In contrast to the Larnaka case study, it can be noted that for most of the approaches more predictors were selected; in fact up to seven predictors were applied, while for the Larnaka data only three. It is reasonable to assume that this can be attributed to more cases with reduced visibility which allows for more complex dependencies to be fitted. As in the Larnaka case study, the second

and third best predictors at the first stage were not selected at all in any of modeling approaches.

The variable selection process for the standard probabilistic neural network resulted in these five models in decreasing order of quality:

- visibility tendency,
- wind speed (log),
- temperature,
- visibility tendency and pressure tendency,
- visibility tendency and height of cloud base.

The first three models were applied in MMA3 and all models in MMA5. Since using only temperature as predictor was one of the best model, it was evident already at this stage that the predictability could not be expected to be good.

The experiment was repeated ten times as in the first case study, and the fitted probabilistic neural networks for the last replication are shown in Figure 3. In the standard probabilistic approach (STD) it can be seen that the probability of reduced visibility is at its minimum when the hourly changes in visibility are small and somewhat larger in other situations. The probabilities are, however, low (less than 10%) in all cases indicating the difficulty of detecting reduced visibility six hours in advance. Further, the STD-1D and STD-2D models both show decreasing probability of reduced visibility with increasing predicted visibility, as expected. The inclusion of information about uncertainty (STD-2D) shows low probabilities when the uncertainty is also low. Introducing weights in the deterministic neural networks gives similar probabilistic neural nets (STD-1DW and STD-2DW) as those without weights with the exception of the STD-2DW model whose fit is more varied.

In Figure 4 the ranked probability score and the average predicted probability of reduced visibility is shown for each model. All statistical models have better RPSs, averaged over the 10 replications, than persistence, and all the new proposed statistical models are better than the standard probabilistic approach (STD). As for the Larnaka case study, the best model was STD-2D. Further, the variation in the ranked probability scores was quite modest compared to the case of Larnaka. The difficulty in predicting reduced visibility is again confirmed since the main contribution to the RPS is due to the 2.8% cases with reduced visibility. Similar interpretation can be obtained by assessing the average predicted probabilities of reduced visibility which are quite low for all models.

The significance of the results can be evaluated by considering the 95% basic bootstrap confidence intervals displayed in Table 6. From the first column all confidence intervals for the expected difference in RPS between the statistical models and persistence are all entirely negative. Hence, the statistical models have in general better performance than persistence (at this site and lead time). On basis of the confidence intervals in the second column it can also be concluded that

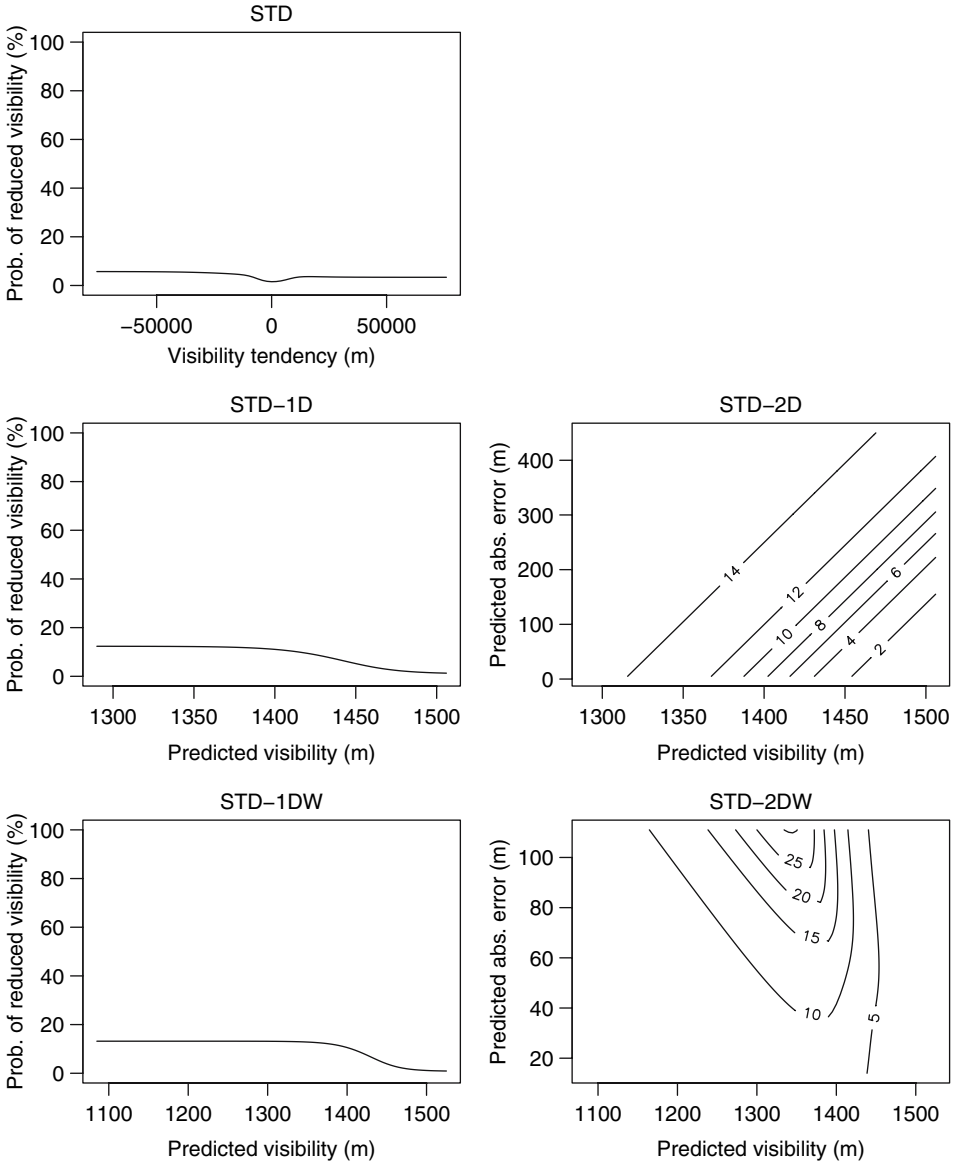

Figure 3
Predicted probability of reduced visibility for the various models for Gardermoen. The plots on the right side are contour plots.

multi-model averaging and the two-stage modelling approach are better than the standard probabilistic neural network (STD). Finally, using both deterministic predictions of visibility and its uncertainty (STD-2D) is better than just using the former (STD-1D).

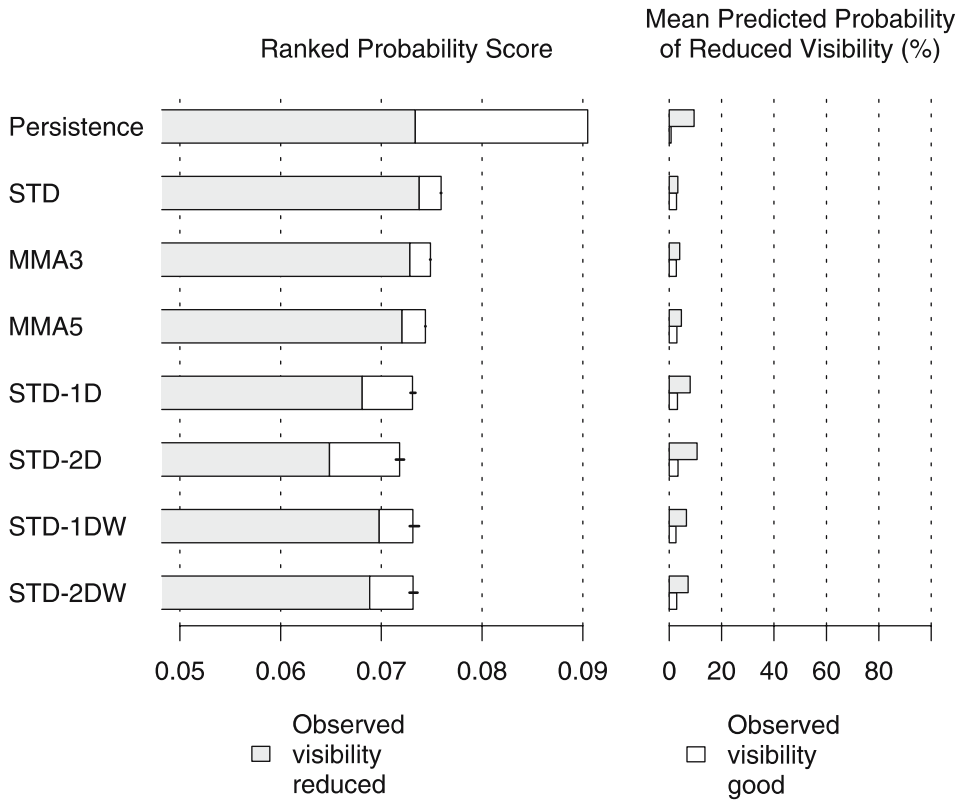

Figure 4
Ranked probability scores and average predicted probabilities of reduced visibility for Gardermoen. The horizontal lines represent the ranges of the ranked probability scores within the ten replications of the experiment.

6. Conclusions

Two alternatives to the standard probabilistic neural network modeling are proposed and tested on data for two sites. The outcome from the first site were not

Table 6

95% basic bootstrap confidence intervals for difference in expected ranked probability score between models in first column and persistence, STD and STD-1D, respectively, for Gardermoen. Intervals not covering zero indicate statistical significant differences

Models	Persistence	STD	STD-1D
STD	(−0.018, −0.011)		
MMA3	(−0.019, −0.012)	(−0.0013, −0.00087)	
MMA5	(−0.019, −0.013)	(−0.0018, −0.0014)	
STD-1D	(−0.021, −0.014)	(−0.0036, −0.0022)	
STD-2D	(−0.022, −0.015)	(−0.0050, −0.0031)	(−0.0017, −0.00089)

statistical significant, although the actual results were in favor of the proposed approaches. One might expect that more data would give stronger support to the latter (4073 out of 4082 cases were in the good visibility category). At the second site, however, the results were significant; in terms of ranked probability scores the best statistical model was about 5% better than the standard probabilistic neural network model. In both case studies, the use of visibility predictions and their predicted absolute error by two deterministic neural networks as input to a probabilistic neural network gave the best results. The use of case weights in the deterministic neural networks, however, did not have a positive effect on the quality of the probabilistic forecasts.

Although the improvements are modest, the proposed approaches could be recommended in operational forecasting. In particular, it is easy to implement multi-model averaging which also has the positive side-effect that the time-consuming search for the best predictor variables can to some extent be relaxed. Another possibility would be to combine the two proposed approaches. In the context of operational forecasting it should also be noted that all sources of data should be considered in order to provide the best possible forecasts, not only surface measurements at the respective site as in this article.

Finally, the highly imbalanced data in the two case studies have stimulated to new work on methods better dealing with rare events, and the outcome of that will be reported in another article. It would also be interesting to apply the present approaches to sites where the predictability is better and reduced visibility more common.

References

Bishop, C.M., Neural Networks for Pattern Recognition (Oxford University Press 1995).

Bocchieri, J. R., Crisci, R. L., Glahn, H. R., Lewis, F., and Globokar, F. T. (1974), *Recent developments in automated prediction of ceiling and visibility*, J. Appl. Meteor. *13*, 277–288.

Davison, A. C. and Hinkley, D. V., *Bootstrap Methods and their Applications* (Cambridge Univeristy Press 1997).

Gardner, M. W. and Dorling, S. R. (1998), *Artificial neural networks (the multilayer perceptron)—A review of applications in the atmospheric sciences*, Atmos. Environ. *32*, 2627–2636.

Hand, D. J., Mannila, H., and Smyth, P., *Principles of Data Mining* (MIT Press 2001).

Hastie, T., Tibshirani, R., and Friedman, J. (2001), T*he Elements of Statistical Learning* (Springer Verlag).

Hsieh, W. W. and Tang, B. (1998), *Applying neural network models to prediction and data analysis in meteorology and oceanography*, Bull. Am. Meteo. Soc. *79*, 1855–1870.

Leyton, S. M. and Fritsch, J. M. (2003), *Short-term probabilistic forecasts of ceiling and visibility utilizing high-density surface weather observations*, Wea. Forecasting *18*, 891–902.

Leyton, S. M. and Fritsch, J. M. (2004), *The impact of high-frequency surface weather observations on short-term probabilistic forecasts of ceiling and visibility*, J. Appl. Meteor. *43*, 145–156.

Marzban, C., Leyton, S. M., and Colman, B. (2005), *Ceiling and visibility forecasting via neural nets*. http://www.nhn.ou.edu/ marzban/comet.pdf.

Murphy, A.H. (1991), *Probabilities, odds, and forecasts of rare events*, Wea. Forecasting *6*, 302–307.

NUGROHO, A.S., KUROYANAGI, S., and IWATA, A. (2002), A *solution for imbalanced training sets problem by combnet-ii and its application on fog forecasting*, IEICE Trans. Inf. and Syst. E85-D, *7*, 1165–1174.

PASINI, A., PELINO, V., and POTESTÀ, S. (2001), *A neural network model for visibility nowcasting from surface observations: Results and sensitivity to physical input variables*, J. Geophys. Res. *106, D14*, 14951–14959.

R DEVELOPMENT CORE TEAM (2005), *R: A Language and Environment for Statistical Computing*, R Foundation for Statistical Computing, Vienna, Austria, ISBN 3-900051-07-0, http://www.R-project.org.

ROULSTON, M.S., BOLTON, G.E., KLEIT, A.N., and SEARS-COLLINS, A. L. (2006), *A laboratory study of the benefits of including uncertainty information in weather forecasts*, Wea. Forecasting *21*, 116–122.

VISLOCKY, R. L. and FRITSCH, J. M. (1997), *An automated, obeservation-based system for short-term prediction of ceiling and visibility*, Wea. Forecasting *12*, 31–43.

(Received April 12, 2006, accepted October 29, 2006)
Published Online First: June 11, 2007

Pure appl. geophys. 164 (2007) 1383–1396
0033–4553/07/071383–14
DOI 10.1007/s00024-007-0224-5

Pure and Applied Geophysics

Climatological Tools for Low Visibility Forecasting

Otto Hyvärinen,[1] Jukka Julkunen,[2] and Vesa Nietosvaara[3]

Abstract—Forecasters need climatological forecasting tools because of limitations of numerical weather prediction models. In this article, using Finnish SYNOP observations and ERA-40 model reanalysis data, low visibility cases are studied using subjective and objective analysis techniques. For the objective analysis, we used an AutoClass clustering algorithm, concentrating on three Finnish airports, namely, the Rovaniemi in northern Finland, Kauhava in western Finland, and Maarianhamina in southwest Finland. These airports represent different climatological conditions. Results suggested that combining of subjective analysis with an objective analysis, e.g., clustering algorithms such as the AutoClass method, can be used to construct climatological guides for forecasters. Some higher level subjective ''meta-clustering'' was used to make the results physically more reasonable and easier to interpret by the forecasters.

Key words: Low visibility, fog, clustering, forecast model reanalysis.

1. Introduction

Low visibility negatively affects flight operations. Especially small airports and airplanes without expensive approach equipment are greatly affected. In a case of low visibility, planes have to use an alternate airport which causes extra consumption of fuel. The threshold of poor visibility is set by convention to 1 kilometer. Visibility can decrease to less than 1 kilometer for a number of different physical reasons, e.g., by fog or by rain and snow showers. An experienced forecaster realizes which weather types are the most commonly associated with these events, and also becomes familiar with the climatological peculiarities of the areas within which he mostly has to work. This kind of climatological background is important because numerical weather prediction models are not always as useful as forecasters would like them to be. However, if a forecaster has 10 or even 20 airports under his responsibility, he cannot rely on personal experience alone. At the minimum, the forecaster needs

[1] Finnish Meteorological Institute, Remote Sensing for Weather Applications, Helsinki, Finland. E-mail: otto.hyvarinen@fmi.fi
[2] Finnish Meteorological Institute, Aviation and Military Weather Service, Rovaniemi, Finland. E-mail: jukka.julkunen@fmi.fi
[3] Finnish Meteorological Institute, Remote Sensing for Weather Applications, Turku, Finland. E-mail: vesa.nietosvaara@fmi.fi

distributions of some relevant parameters such as monthly distribution of wind direction and fog. Unfortunately, these classical distributions give only an approximation of low visibility weather parameters. More advanced statistical methods should be investigated.

Often only SYNOP observations (WMO, 1995) are available for low visibility forecasting. SYNOP observations have a rather coarse time scale (3 hours), which is not optimal for nowcasters. But sheer numbers of observations (about 80,000 observations from one airport for the period of 30 years) can be used to calculate distributions from these data. On the other hand, SYNOP observations are basically point measurements. To be able to visualize the synoptic situation of low visibility cases, some kind of spatial analysis is needed. Recently, various reanalyses of past observations with modern methods have been published. For example, TARDIF (2004) used NCEP-NCAR Reanalysis Project data to characterize the synoptic weather patterns associated with fog. In the present study, the ERA-40 reanalysis data (UPPALA *et al.*, 2005) generated by the European Centre for Medium-Range Weather Forecasts is used.

An objective method that shows the typical situations of low visibility can help forecasters to learn the climatology of new areas they are assigned to. Clustering algorithms are examples of such objective methods. In this method, a set of observations is divided into groups, so that members of the same group are more alike than the members of different groups (RIPLEY, 1996). Clustering methods can be divided into three main approaches: 1) Hierarchical methods, 2) partitioning methods, and 3) methods based on mixtures of parameterized densities (e.g., probability distribution). The first two approaches are commonly used in meteorological literature. Hierarchical methods result in trees or dendrograms, which can be easily visualized. A recent article for meteorological applications on this method was given by CHENG (2004). Partitioning methods include the well-known K-means algorithm. In K-means, samples are divided to a pre-assigned number of groups. Then, the group centers and memberships are chosen so that the sum of squared distances from each sample to the group center is minimized. However, this algorithm has some shortcomings. For example, the number of clusters has to be decided by the user, and discrete data cannot be used in this method. A recent article using partitioning method was by (GUTIÉRREZ *et al.*, 2004). The third approach of clustering assumes the samples come from the same mixture of sources and they can be parameterized. These sources are usually probability distributions but fuzzy logic technique can also be used. In this study, the AutoClass classifier (CHEESEMAN *et al.*, 1988) is used, handling both continuous and discrete observations, and automatically selecting the best number of clusters. AutoClass fits probability distributions to the data and searches for the clusters with the highest probability. Probability distributions can be either discrete nominal or continuous (real-valued). Distributions for continuous data are assumed to be either single normal or multinormal. If continuous data have a clear lower bound, then the log-normal distribution can be used for the analysis.

2. Observations and Methods

Present data consist of SYNOP observations obtained from the sixteen Finnish weather stations and main airports (Fig. 1) at every three hours for about 30 years from 1970 to 2000. Minimally, the SYNOP observations consist of various observations, including pressure, clouds, temperature at 2 meters height, relative humidity, wind, and weather situations. The geopotential and temperature information from the ERA-40 reanalysis data were analyzed at the pressure levels used in opearational forecasting such as 1000 hPa, 850 hPa, and 500 hPa. It is worth noting that the ERA-40 reanalysis data are available every six hours, not every three hours

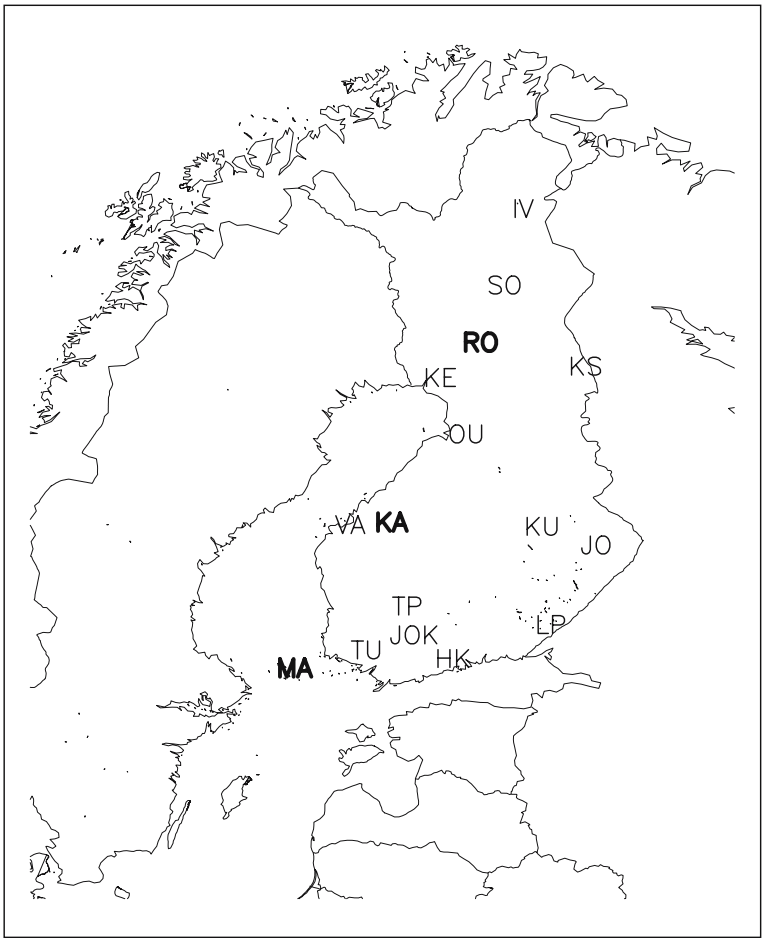

Figure 1
Finnish weather stations used in the study. Rovaniemi (RO), Maarianhamina (MA) and Kauhava (KA) were investigated in more detail.

as for the SYNOP observations. The analysis of data is performed using the R software (R DEVELOPMENT CORE TEAM, 2005).

2.1. Subjective Approach for Fog Climatology

In the analysis, in order to get classical distributions of visibility, wind speed and direction, and other related parameters, three airports are chosen to apply a subjective analysis of the synoptical observations. The airports, representing three different climatological regions, are: 1) Rovaniemi (RO) airport from northern Finland, 2) Maarianhamina (MA) airport from southwest Finland, and 3) Kauhava (KA) airport from western Finland (Fig. 1). The Rovaniemi airport is an elevated airport, and its altitude is approximately 195 m above sea level (ASL). It is well-known for its heavy fog periods, which often cause difficulties to aviation. The Kauhava airport represents a small airport in western Finland which is located at low altitude (42 m ASL) just at an intermediate zone between the lowlands of the coastal western Finland and slightly more elevated terrain in the east. The Maarianhamina airport is located in the inner parts of a relatively large island on the Northern Baltic Sea and represents a marine station. Its height is 2 m ASL and it is in the lower part of the island.

Weather forecasting in the above-mentioned airports is quite difficult. After a subjective analysis, the results are compared to the results of an objective analysis, and then an evaluation is made.

2.2. Objective Approach with AutoClass

The AutoClass uses a Bayesian approach, and its goal is to find the most probable set of class descriptions for a given data set and prior expectations. The use of priors automatically includes the Occam's razor to the model and prevents overfitting of the models. Other methods based on the maximum likelihood (e.g., K-means) determine classification that best predicts the data. The skill of these models to classify new data is often poor because they try to fit the learning set exactly. Full Bayesian solution is in practice too costly, and maximum *a posteriori* (MAP) parameter values are searched in the parameter space. The search has two levels. The model level search (the first level), is for the best number of clusters and the cluster probabilities of an individual case. In the second level, the MAP parameter values for probability distributions for each cluster are computed. Models are first rated by their best posterior probabilities, and then the best models and their MAP parameter values are reported. The AutoClass does not assign cases to clusters, but for each case it provides the probabilities of belonging to a cluster. These probabilities are not manipulated further and they are assigned to the clusters of highest probability.

In the present study, the AutoClass for 500 cycles took about one hour of the CPU time for each station and this 500 cycles is considered to be enough for the best classification was found much earlier.

Clustering was performed for all sixteen stations. Then, only low visibility observations were performed, i.e., when the visibility was less than 1 km. This means that we did not try to predict fog at this stage but we only wanted to see the existence of the fog type or other low visibility situations.

Before running AutoClass, the features for clustering and their probability distributions are chosen. The selection of features has a significant impact on the clustering, so great care is needed. For the present study, the amounts of low and total cloudiness, 2 m temperature, relative humidity, wind speed and direction, and the codes for present and past weather are chosen. This was based on empirical climatological knowledge of Nordic fog events and their dependence on weather. Temperatures near zero degrees Celsius usually favor certain fog types e.g., freezing fog. Cloudiness and wind were also expected to be good classifiers, since fog events on rather calm and clear conditions typically represent radiation fog events, while advective fog types are often observed in relation to certain large-scale weather patters. The probability models for these features are rather straightforward: Present and past weather have discrete nominal models and others have continuous models. In these calculations some conversions of data were needed. For example, present weather values from 00 to 99 are considered too detailed, so only the first digit is used. The wind u and v components with multinormal distributions are then used. This is a reasonable choice under the constraints of the AutoClass because richer selection of distributions is not available. Cloudiness and relative humidity in our study have a clear upper bound and are they are inverted so that their distribution is considered as log-normal. Note that, in the more general case, cloudiness and relative humidity have both lower and upper bounds; therefore, a simple log-normal or normal distribution can be quite inappropriate for many applications.

The rounding of the SYNOP messages can result in some uncertainties. This can cause some problems because any clustering method can find spurious clusters caused by rounding. This can be especially problematic with wind observations where limited resolution of wind direction might suggest false finger-like distributions of observations. We tried to remedy this by adding the Gaussian noise with standard deviation of half the bin to the wind observations, as suggested in AutoClass documentation.

After the clustering, ERA-40 data were used to visualize the average synoptic situations of all clusters for selected pressure and temperature levels. Then, the mean and standard deviation were computed for the ERA levels nearest in time to each occurrence. From the images of average conditions, an indication of the synoptic conditions associated with each cluster is then obtained.

The significance of the patterns that can be seen in the average synoptic images for the ERA data set is also explored. The 850 hPa temperature field in a geographic location for any single cluster is compared to the mean and standard deviation of the same field for the entire ERA data set. For the tests of statistical significance, a

simple bootstrap system (WILKS, 1995) is used. As a metric for the distance between different distribution, the Bhattacharyya distance (BHATTACHARYYA, 1943) is used, because it uses information from both the mean and the standard deviation of any parameter. Then, for each grid point of every cluster, the following procedure was performed: First, the Bhattacharyya distance between the entire ERA data set and the cluster under investigation was calculated. Second, a distribution of the Bhattacharyya distances between the entire ERA data set and random data sets of the cluster under investigation was constructed. Third, the Bhattacharyya distance of original cluster was compared to the constructed distribution. If the Bhattacharyya distance of original cluster was larger than a certain percentage of the values in the distribution (depending on the rejection level), it is concluded what is seen in the average synoptic images is not just random fluctuations of data.

3. Results and Discussion

3.1. Subjective Approach

Results showed that the occurrence of low visibility values at Rovaniemi airport was very high. On the other hand, low visibility observations associated with calm conditions are rare. That indicates that radiative fog at the Rovaniemi airport was not very common and the fog occurrence is likely due to weather patterns and advection. The reason for this is likely that Rovaniemi airport is located on top of a hill therefore, orographical effects are likely to influence the air flow resulting in foggy weather. Most foggy weather events which occur at this airport are during southwesterly moist air flow. Additionally, because of its northern location, some of the very low visibility observations may be caused by snowfall.

At the Kauhava airport, observations suggest that there are many low visibility observations during calm conditions. Particularly in autumn morning hours low visibilities may occur due to fog occurring as a result of radiative cooling. Because most low visibility observations are during almost windless situations, it is suggested that advection fog type occurrence is quite rare. It is obvious that Kauhava airport lies in the area where radiative cooling is intense during autumn.

The Maarianhamina airport has a quite different seasonal distribution of very low visibilities compared to the other airports. The main difference is that most of the low visibility observations are in springtime, and they likely occur because of radiative cooling and advection.

3.2. Objective Approach

The number of clusters given by the AutoClass for each station varied from 12 to 23 clusters, while most of the stations had less than 16 clusters. This variation seems quite reasonable. The station that had most of the clusters (the Kauhava airport) has

the reputation of being difficult to forecast for low visibilities. In all cases, the smallest clusters were substantially smaller than the largest ones. These clusters are ignored in many cases, because it is quite likely that these clusters are artifacts as a result of the result of the inability of AutoClass to model all the details of data with its inherent probability distributions. Thus small clusters probably do not give new insights to the climatology of low visibility.

There are areas of statistical significance in ERA-40 images (not shown), except for the very small clusters that are suspicious anyway. In some cases, these areas encompassed the whole area from which ERA-data were used; in most cases they covered most of the area. Therefore, weather patterns seen in ERA-40 images have statistical significance, and cannot be dismissed as random fluctuations.

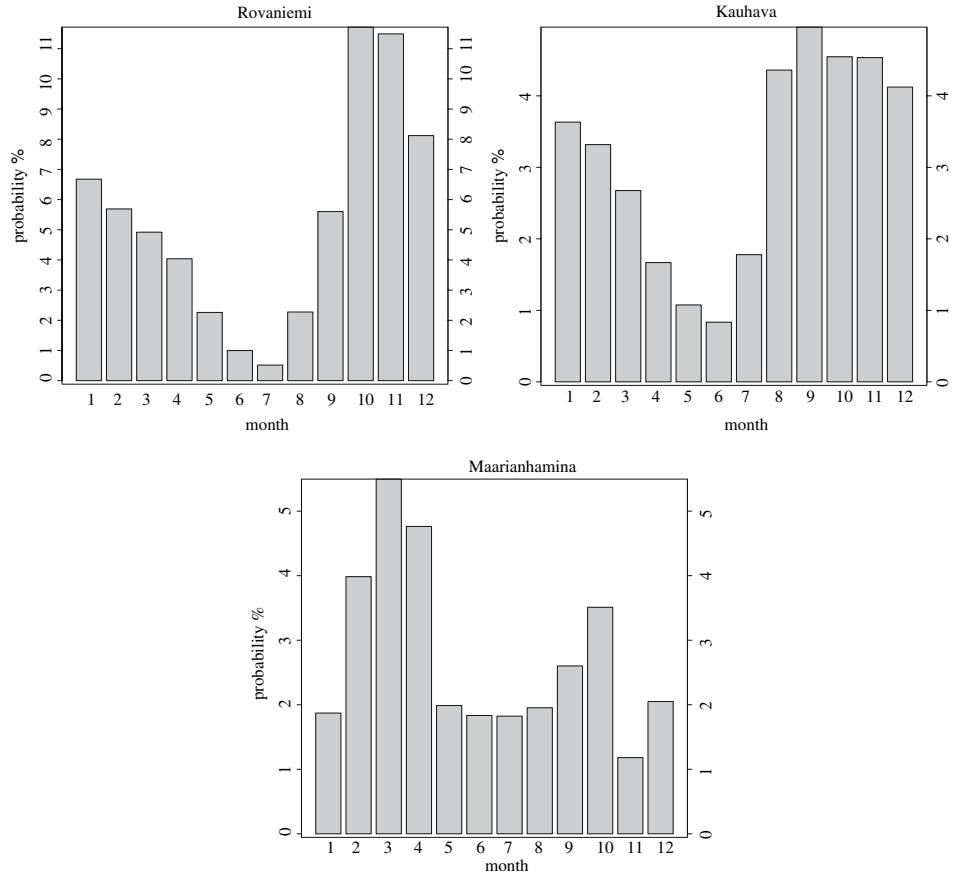

Figure 2
Monthly frequency of low visibility at the Rovaniemi, Kauhava and Maarianhamina airports.

3.3. Interpretation of the Results

Both the subjective and objective methods used in this study help us to interpret the nature of fog events at the three airports.

The simple monthly probability diagrams for low visibility already show some basic characteristics of fog occurrence at each individual station (Fig. 2). Both at Rovaniemi and Kauhava, fog occurrence is high in autumn (from October to November) and also in winter (from December to March), but at the Kauhava airport, fog is likely to occur in late summer (August). At the Maarianhamina airport, fog occurrence is at its peak in February, March and April.

A more detailed subjective analysis can be made with the help of low visibility frequency charts (Fig. 3). These charts reveal not only the monthly distribution already shown in Figure 2, but also the preferred time for fog occurrence. For the Rovaniemi airport, the autumn maximum for fog shows low visibilities occurring at any time of day, though the maximum occurrence does not change significantly during the morning hours. On the contrary, during spring months, fog normally occurs only at night and in the morning. At the Kauhava airport, the figure shows other characteristics of the fog: morning fog likely occurs from late summer to early

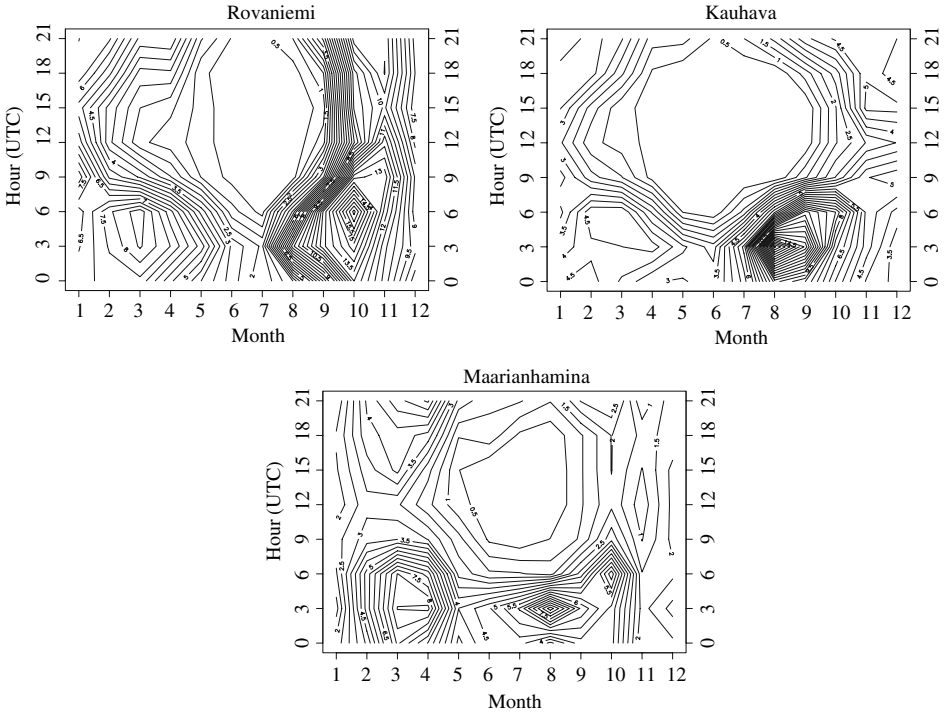

Figure 3
Annual frequency of low visibility at the Rovaniemi, Kauhava and Maarianhamina airports.

autumn. A secondary maximum can also be seen from February to April. At the Maarianhamina airport, the low visibilities are highly concentrated for late night and early morning hours throughout the year. Day time fog occurrence for this location is remarkably low.

The above results suggest some speculations on how many of the fog occurrences are explained by classifying them as radiative or advective fogs, and how much of the variability is due to the different topography and environmental factors. It is also important to know if these features can be determined by using the objective classification methods, e.g., clustering techniques.

The objective interpretation by ''eyeballing'' cluster characteristics is used in the analysis. We especially considered wind, cloudiness, and SYNOP code distributions, temperature, and temporal distribution of occurrence. As it turned out, it was reasonably easy to classify clusters to three ''meta-clusters'': advection fog, radiation fog and non-fog cases. The distinction between advection and radiation fog clusters was in fact surprisingly clear: while radiation fog cases typically reflect calm or weak wind conditions at surface with mostly clear skies, the advective fog cases show an association with moderate winds (4–7 m/s or even more) with overcast skies and a tendency to be independent of the time of day. Non-fog cases were typically differentiated very well by the clustering: the non-fog cases (such as low visibilities caused by snowfall) were concentrated in the clusters representing only a small percentage of all cases. An example from the Maarianhamina airport is shown in Figure 4. As with the choice of features for the clustering, we constructed the meta-clusters reflecting our knowledge of Nordic fog occurrences. It is conceivable that some of the details would change if this procedure was adopted in a vastly different climate, but essential parts of the procedure would remain the same.

Clearly, at these three stations, radiation fog dominates during summer, while the advection fog is more dominant during winter. Radiation fog is also highly dependent on the time of day, being most likely to occur at dawn, while advection fog has not such a strong dependency on the time of day. The Kauhava airport shows a remarkable exception in this respect: Purely advective fogs decrease and a vast majority of cases represent radiation fog.

The ERA-40 reanalysis data proved to be extremely useful in meta-clustering: The mean synoptic conditions for each cluster helped us to decide whether the cluster belonged to an advection or radiation fog meta-cluster. As an example of mean synoptic conditions with ERA-40 reanalysis data, images for an advection fog cluster representing the Maarianhamina airport are shown in Figure 5. This example illustrates typical conditions for the occurrence of advection fog/stratus. The following characteristic properties can be found:

— A relatively warm airmass at the lower troposphere, which can be seen as a local ridge of temperature at 850 hPa over the area of interest.
— Upper level ridge to the east of the area, indicating warm air advection over the area.

For each station then an objective evaluation is done. Of particular interest were the clusters with some systematic fog occurrence patterns for individual stations. These systematic patterns could be either a specific fog type bound to a particular

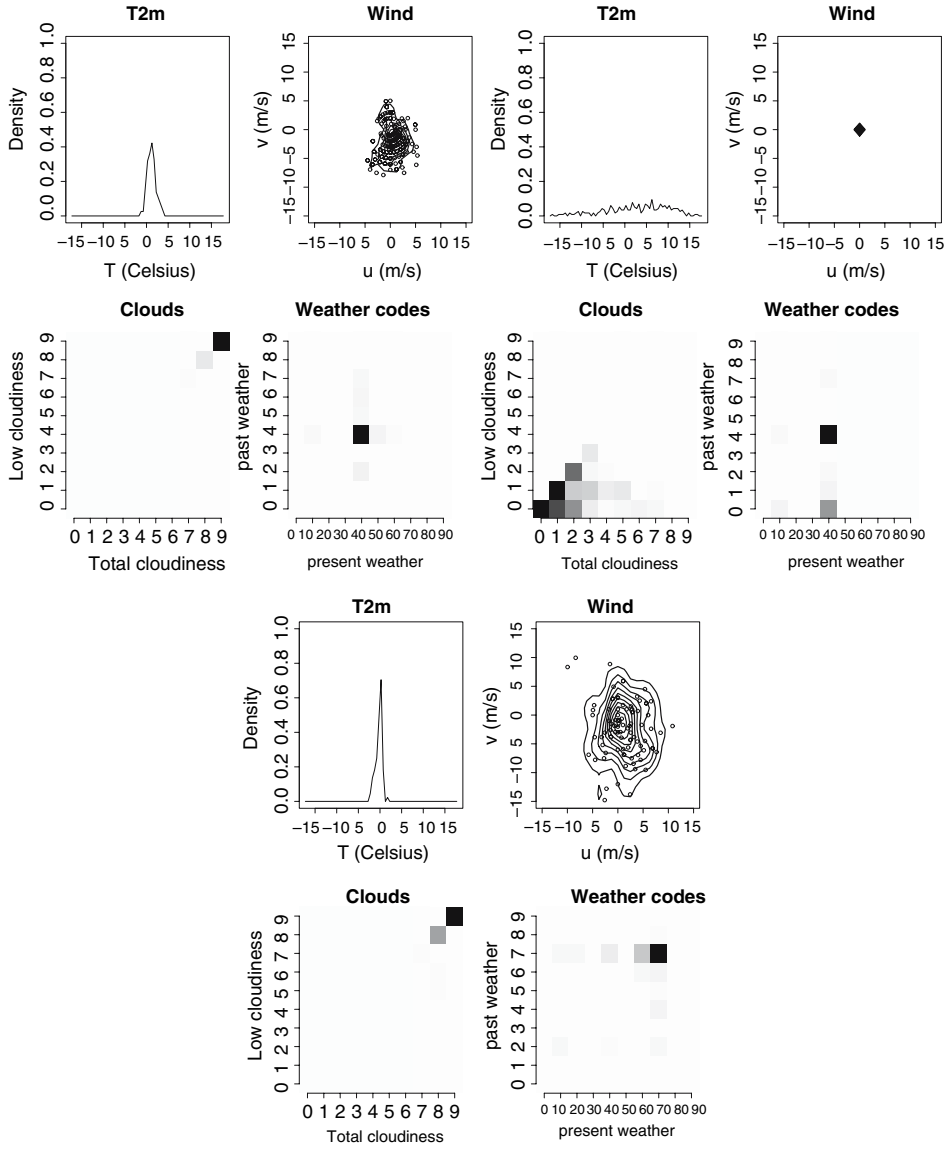

Figure 4
Three typical representatives of ''advection fog'', ''radiation fog'' and ''non-fog'' (snowfall) clusters for the Maarianhamina airport. Roughly, SYNOP codes of present weather are for fog from 40 to 49, and for snowfall are from 70 to 79. The SYNOP code of past weather for fog is 4 and for snow 7. For SYNOP codes, dark color indicates high density, light color low density.

season of the year or a fog-type associated with specific synoptic situations (as shown by ERA-40 data).

At the Rovaniemi airport, three major fog types are found: (1) Advective late autumn-wintertime fog (represents roughly 60% of all fog occurrences), (2) an early autumn radiation fog (20% of the total number of fog occurrences) and (3) a wintertime rime fog associated with weak flow and high pressure ridge or high pressure center in or to the south of northern Finland (also 20% of the total number of fog occurrences). These fog types truly represent the fog ''archetypes'' for this particular airport. An example of surface pressure pattern for type 3 fog is shown in Figure 6a.

Another example for the radiation fog at the Kauhava airport is considered as a sub-type for a radiation fog, which is the most typical fog type at Kauhava (FRISK, pers. Comm., 2005). This fog type can be identified as ''a radiation fog associated with a secondary low formation in the Bay of Bothnia.'' This meta-cluster consists, in fact, of three clusters, and for each of them a distinct flow pattern is clearly seen in ERA-40 mean synoptic charts. The flow pattern suggests that when there is a less intense low pressure centered over the Bay of Bothnia (Fig. 6b), morning radiation fog is often observed. This pattern and its connection to the morning fog events has also been verified and described by the operational forecasters making daily forecasts for the Kauhava airport.

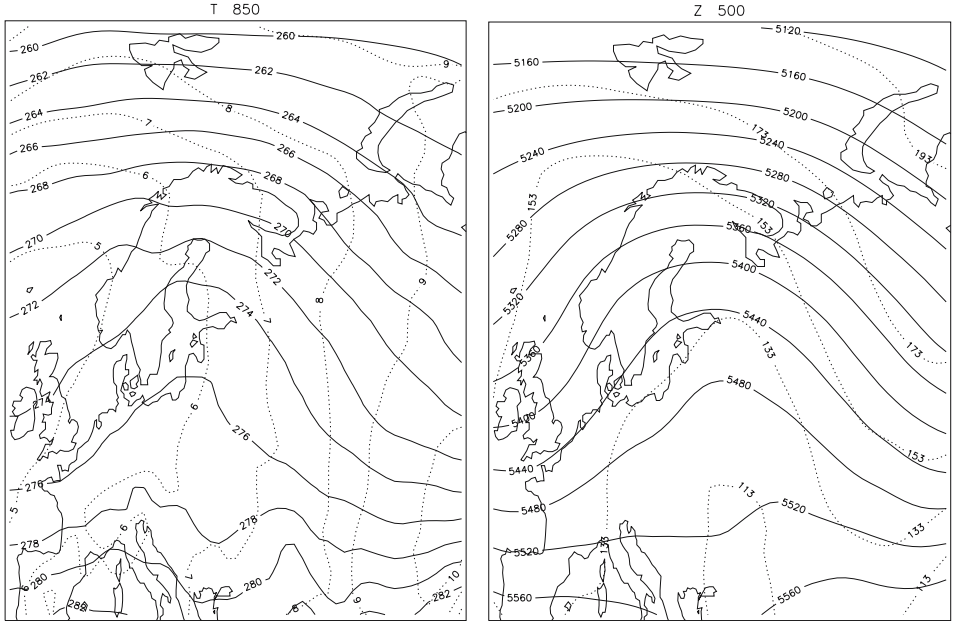

Figure 5
Synoptic conditions for one arbitrary advection fog cluster of the Maarianhamina airport. Solid lines indicate mean values, dotted lines standard deviation.

The clustering results can be combined with the other diagrams for improved results. An example is shown in Figure 7, where we have combined clustering results with the monthly probability diagram. The resulting image shows when the low visibilities likely occur, and what kind of low visibility cases exist.

4. Summary and Conclusion

Aviation forecasters need to know the low visibility and fog climatologies of each airport for safe aircraft landing and take-off. The purpose of this study was to investigate possible new tools that use clustering methods and ERA-40 reanalysis fields. In this study, both subjective and objective methods are used, helping us to interpret the nature of fog events at several airports. Three Finnish airports are used in the analysis, representing different climatological regions.

The results suggest that the combination of the subjective analysis and a clustering algorithm (e.g., a AutoClass method) could be used to construct climatological guidelines for forecasters. It is also found that results were in

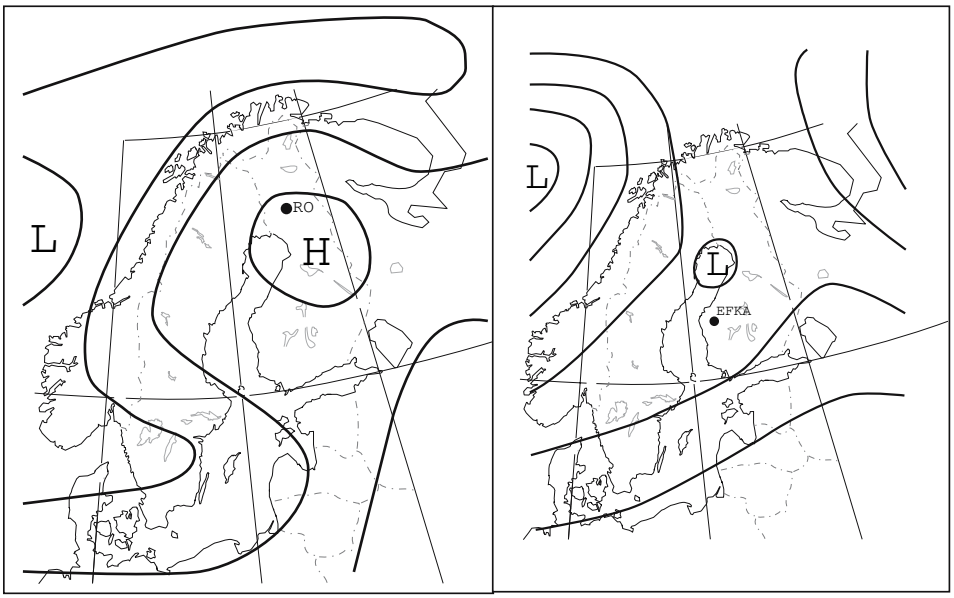

Figure 6
Schematic images showing the mean surface pressure conditions in Scandinavia for two fog types: a) Fog type at the Rovaniemi airport ''A wintertime rime fog within a high pressure ridge''. b) Fog type at the Kauhava airport ''An autumn morning radiation fog associated with a secondary low pressure on the Bay of Bothnia''. Isobars are in solid black contours. Locations of the Rovaniemi (RO) and Kauhava (KA) airports are shown with a black dot.

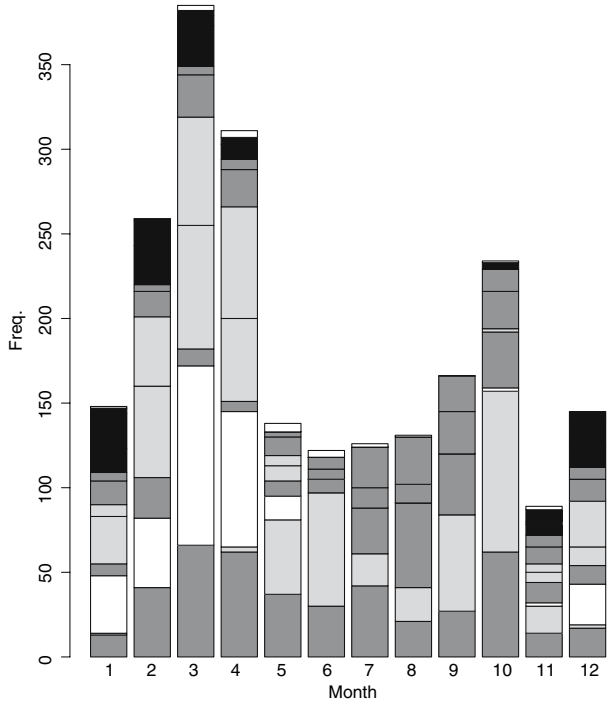

Figure 7
Monthly frequency of low visibility at the Maarianhamina airport augmented with the clustering information. Every bar segment represents a cluster. Clusters have been subjectively classified to "meta-clusters" and colored accordingly: light gray clusters represent occurrences of advection fog, dark gray clusters represent occurrences of radiative fog, black clusters represent non-fog events and white clusters are left unclassified.

agreement with forecasters' decisions. This supports our idea to use the integrated (combined) methods in training the forecasters.

It must be emphasized that the clustering results depend on the method used. AutoClass has a rich family of distributions, as mentioned above, but real distributions of some parameters can still be quite different. In the present work, some higher level subjective "meta-clustering" is performed in order to make the results more physically reasonable and easier to interpret by the forecaster.

Our future plans can be divided into three parts: 1) The method refinement, 2) broadening the scope, and 3) applying the method to the operational environments. Selection of features for clustering is quite *ad hoc* and should be revisited for future applications. For example, pressure information in the current clustering analysis is not used. It will also be interesting to widen the scope of the present investigations and apply the new methods to other airports in Finland and use more detailed observations (e.g., METAR) over the orographic environments. The quantitative way of justifying the choice of our clustering method also needs to be researched, and

a detailed comparison methodology with different clustering techniques (e.g., K-means) needs to be developed.

References

Bhattacharya, A. (1943), *On a measure of divergence between two statistical populations defined by their probability distributions*, Bull. Calcutta Math. Soc. *35*, 99–110.

Cheeseman, P., Kelly, J., Self, M., Stutz, J., Taylor, W., and Freeman, D. (1988), *AutoClass: A Bayesian Classification System*. In Proc. Fifth Internat. Conf. on *Machine Learning*, Ann Arbor, MI. June 12–14 1988. Morgan Kaufmann Publishers, San Francisco, pp. 54–64.

Cheng, C.S., Auld, H., Li, G., Klaassen, J., Tugwood, B., and Li, Q. (2004), *An automated synoptic typing procedure to predict freezing rain: An application to Ottawa, Ontario, Canada*, Weather and Forecasting *19*, 4, 751–768.

Gutiérrez, J. M., Cofiño, A. S., and Cano, R. (2004), *Clustering methods for statistical downscaling in short-range weather forecasts*, Mon. Wea. Rev. *132*, 9, 2169–2183.

R. Development Core Team (2005), *R: A language and environment for statistical computing*. R Foundation for Statistical Computing, Vienna, Austria. ISBN 3-900051-07-0, URL http://www.R-project.org.

Ripley, B.D. *Pattern Recognition and Neural Networks* (Cambridge University Press, Cambridge 1996).

Tardif, R. (2004), *Characterizing fog occurrences in the Northeastern United States using historical data*, 11th Conf. Aviation, Range and Aerospace Meteorology, Hyannis Port.

Uppala, S.M., Kållberg, P.W., Simmons, A.J., Andrae, U., da Costa Bechtold, V., Fiorino, M., Gibson, J.K., Haseler, J., Hernandez, A., Kelly, G.A., Li, X., Onogi, K., Saarinen, S., Sokka, N., Allan, R.P., Andersson, E., Arpe, K., Balmaseda, M.A., Beljaars, A.C.M., van de Berg, L., Bidlot, J., Bormann, N., Caires, S., Chevallier, F., Dethof, A., Dragosavac, M., Fisher, M., Fuentes, M., Hagemann, S., Hólm, E., Hoskins, B.J., Isaksen, L., Janssen, P.A.E.M., Jenne, R., McNally, A.P., Mahfouf, J.-F., Morcrette, J.-J., Rayner, N.A., Saunders, R.W., Simon, P., Sterl, A., Trenberth, K.E., Untch, A., Vasiljevic, D., Viterbo, P., and Woollen, J. (2005), The ERA-40 re-analysis., Quart. J. Roy. Meteorol. Soc., *131*, 2961–3012.

Wilks, D.S. *Statistical Methods in the Atmospheric Sciences: an Introduction* (Academic Press, San Diego, 1995).

World Meteorological Organization (1995), *WMO-No 306, Manual on Codes, International Codes*, Volume I.1, Geneva.

(Received April 27, 2006, accepted November 1, 2006)
Published Online First: May 16, 2007

Pure appl. geophys. 164 (2007) 1397–1421
0033–4553/07/071397–25
DOI 10.1007/s00024-007-0225-4

Pure and Applied Geophysics

Marine Layer Stratus Study

LEONARD A. WELLS

Abstract—The intent of this study is to develop a better understanding of the behavior of late spring through early fall marine layer stratus and fog at Vandenberg Air Force Base, which accounts for a majority of aviation forecasting difficulties. The main objective was to use LEIPPER (1995) study as a starting point to evaluate synoptic and mesoscale processes involved, and identify specific meteorological parameters that affected the behavior of marine layer stratus and fog. After identifying those parameters, the study evaluates how well the various weather models forecast them. The main conclusion of this study is that weak upper-air dynamic features work with boundary layer motions to influence marine layer behavior. It highlights the importance of correctly forecasting the surface temperature by showing how it ties directly to the wind field. That wind field, modified by the local terrain, establishes the low-level convergence and divergence pattern and the resulting marine layer cloud thicknesses and visibilities.

Key words: Marine layer, sky cover, temperature, precipitation, visibility, winds.

1. Introduction

The intent of this study was to develop a better understanding of the behavior of late spring through early fall marine layer stratus and fog at Vandenberg Air Force Base (AFB), which accounts for a majority of aviation forecasting difficulties. The study looked at Vandenberg AFB weather forecasting methodologies, validated them and determined if any new methods could be developed. This study also focused on determining what parameters influence the rise and fall of the marine layer inversion which affects the cloud thickness and ceilings heights.

In preparation for the current study over a hundred articles and theses were reviewed. The studies that pertain to forecasting the marine layer stratus and drizzle are listed in the reference section of this study. A brief review of three studies is discussed next.

The best description of the synoptic pattern required for the marine layer stratus/fog development process at Vandenberg Air Force Base is LEIPPER's (1995) four phases of the marine layer fog, which are: First phase offshore breeze which

Vandenberg Air Force Base, 30th Weather Squadron, California. E-mail: Leonard.wells@afccc.af.mil

strengthens the subsidence inversion; second phase marine layer inversion established up to 200 meters (650 feet); third phase marine layer inversion is established between 200–400 meters (650–1,300 feet), and the fourth phase lifting of the marine layer inversion to the subsidence inversion which provides drier air aloft, therefore allowing the stratus to dissipate. LEIPPER (1995) states that ''Other than LIBS (Leipper Inversion Base Statistics), the author believes there is no west coast fog forecasting that can be used with as much confidence''. The LEIPPER (1995) phases are not refined enough to assist the Air Force weather forecaster. For instance the second phase occurs when the marine layer inversion is less than 200 meters. The Air Force weather forecaster is required to specify within the Terminal Aerodrome Forecast (TAF) three separate ceiling categories (100 ft, 200 ft, and 500 ft). The third phase occurs when the marine layer inversion is between 200 to 400 meters, the Air Force weather forecaster is required to specify within the TAF two separate ceiling categories (700 ft and 1000 ft). The fourth phase occurs when the marine layer inversion is less than 400 meters, the Air Force weather forecaster is required to specify within the TAF two separate ceiling categories (1500 ft and 3000 ft). The current author will provide evidence so that the Air Force operational forecaster can develop a TAF for both stratus and fog with high confidence by using LEIPPER (1995) four development phases of the marine layer fog by using additional meteorological parameters.

Peter FELSCH's article (1990) ''Stratus Surge Prediction along the Central California Coast'' best describes the weather phenomenon known as the stratus surge from the south. In his article he defines the stratus surge ''as a narrow (mesocale) band of marine layer stratus that progresses northward along the coastline''. Stratus surge events are considered anomalies because summer season coastal winds are predominately northwesterly and act as mesocale weather fronts as they progress along the coast. The article's research was on the climatological and development of a conceptual model that keyed on the fact that the marine layer inversion in the south was rising, therefore creating ageostrophic flow for the stratus to move northward. FELSCH (1990) took the conceptual model and developed a forecast model that forecasted surge or no surge events and provided test results for the forecast model which had a skill score of 0.58 for forecasting the development of surge events. His conclusion was the following: The conditions allow the marine layer to the south to rise, while the marine layer to the north remains shallow resulting in a weakening or reversal of the normal pressure gradient. He also mentioned that ''model output 500mb vorticity advection patterns may also have a predictor value for forecasting the marine layer depth in response to changes in upper-level dynamics.'' This study examines the relationship of 500mb temperature advection and the relative position of 500mb ridge to Vandenberg Air Force Base with the rise and fall of the marine layer inversion. The current study will refer to the stratus surge as a southerly surge.

Greg IRETON's thesis (2001) ''Classification of Summertime West Coast Fog and Stratus Events and the Development of Fog and Stratus Forecast Techniques''

examined a possible link of the stratus behavior to a synoptic pattern, then verified whether the Navy's Coupled Ocean/Atmosphere Mesoscale Predication System (COAMPS) model correctly forecast the development of the marine layer stratus. The thesis research mainly concentrated on the marine boundary layer (MBL) and the following parameters: Trajectory analysis and forecasting using Vis5d, moisture fluxes, low-level Q vectors to examine forced vertical motions, and thermal wind relationships. In the current study a slightly different approach is taken and the entire column of air from surface to 500mb (18,000 ft) is examined.

The current study covers three major areas. The first section describes the actual marine layer conditions from 16 August, 2005 to 17 September, 2005. The second section describes different weather parameters that affect the marine layer. The third section discusses how well the three different operational forecast models handled the weather parameters outlined by the previous two sections. The study also reviews three distinct weather events that occurred at Vandenberg AFB during the collection period; a southerly surge, an extreme maximum temperature event, and drizzle occurring with clouds less than 2,000 feet thick.

The values for all the illustrations within the study are: Ceilings are in feet (ft), cloud thickness are in feet, the visibilities are in statute miles (SM), all wind speed are in knots, upper air temperature are in degree Celsius and surface temperature are in Fahrenheit.

2. Observations and Data Analysis

The data collection period was 16 Aug 04–17 Sep 04. The data included 778 surface observations, 84 upper air soundings, 128 sea-surface temperature observations, three different forecast models and one analysis model. The normal daily synoptic Upper Air Sounding (00Z and 12Z) were used during the entire study period plus two additional Upper Air Soundings (15Z and 18Z Mon–Fri) only requiring the data up to 60,000 feet. Data were used to compare the cloud ceiling heights, cloud thickness, 500mb temperature and heights, 850mb temperature and heights, 925mb temperature and heights to the model data, and the height of the marine layer and subsidence inversion.

Model data were collected for the first 24 hours after the initial hour using the sampling feature on the Advance Weather Interactive Processing System (AWIPS). The following forecast model hours were collected: Global Forecast System (GFS) Model, 00 hour, 06 hour, 12 hour, 18 hour and 24 hours; mesoscale ETA data were collected and verified every three hours starting from initial hour up through the 24 hour point; and the Pennsylvania State and National Center for Atmospheric Research Mesoscale Model (MM5) collected and verified every hour starting from initial hour up through the 24 hour point. The Local Area Prediction System (LAPS) model pulls together the Vandenberg Air Force Base local data suite that contain 59

temperature and humidity sets, 79 ultrasonic anemometers, six 915 Mhz Boundary Wind profilers, six mini-SODAR profilers, a 50 Mhz Tropospheric Doppler Radar wind profiler and three automated surface observing system (ASOS). The LAPS data is then pushed to the 1 Km MM5 and used in the initialization process. Model surface data (temperature, relative humidity, and surface wind speed and direction) were verified using the ASOS located at Vandenberg's Airfield. The LAPS model was used to verify whether surface convergence or divergence was occurring over the airfield's location.

Sea-surface temperature data were collected for two different times (00Z and 12Z) from two different buoys (46023 and 40611). These data were used to determine the actual land-sea breeze interaction.

3. Results and Discussion

3.1. Marine Boundary Layer Conditions

At Vandenberg AFB terrain is a key player in marine layer and fog behavior (see Fig. 1). If conditions are right for the marine layer to develop, low-level convergence and divergence play an important role in the severity of the event. There were a total of 778 observations recorded with 160 observations associated with a southerly surge. A total of 427 observations contain ceilings less than 3500 feet or visibilities less than 7 SM.

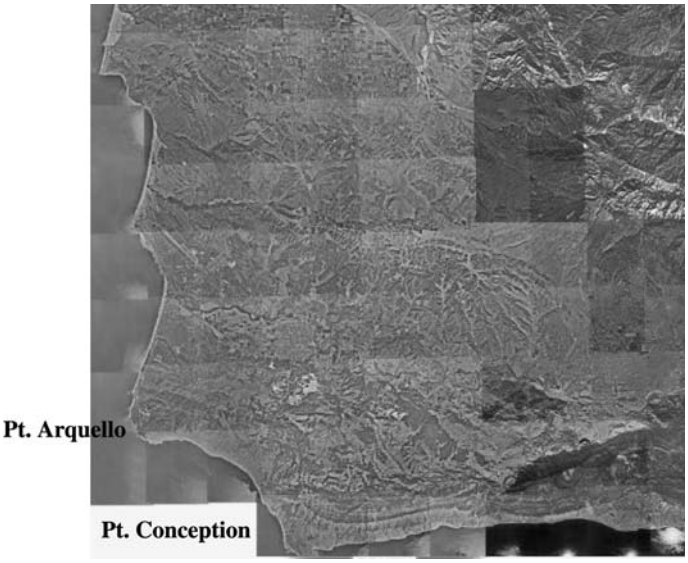

Figure 1
Topography surrounding Vandenberg AFB, courtesy of USGS TerraServer USA.

Table 1

Visibility less than 3 SM

Visibility less than 3 SM Non-Southerly Surge Event			
	Wind Direction	Calm	
Convergence	Northwest to East		All Obs
Obs	15	4	23
Divergence	East to Northwest		
Obs	28	13	49
Visibility less than 3 SM Southerly Surge			
	Wind Direction	Calm	
Convergence	Southwest to North		All Obs
Obs	13	21	37
Divergence	Southeast to Northwest		
Obs	19	12	34

A correlation exists between convergence, divergence, wind direction and low visibility for the marine layer stratus and fog (see Table 1). A total of 72 observations contained visibility values less than 3 SM, with calm winds recorded in 17 observations. Visibility less than 3 SM occurs most frequently with surface convergence when the wind direction is from northwest to east or under calm wind conditions (19/23 observations). Visibility less than 3 SM occurs most frequently with surface divergence or neutral conditions when the wind direction is from east to northwest (41/49 observations).

During a southerly surge event, a different correlation exists between the convergence, divergence, wind direction and low visibility. A total of 71 observations contained visibility values less than 3 SM, with calm winds recorded in 33 observations. When the wind direction is from southwest to north, visibility less than 3 statue miles occurs most frequently under convergent conditions or calm wind conditions (34/37 observations). When the wind direction is from southeast to northwest, visibility less than 3 SM occurs most frequently under divergent conditions or calm wind condition (31/34 observations).

It appears a correlation exists between convergence, divergence, wind direction and ceiling heights (see Table 2). A total of 121 observations contained ceiling values less than 3,000 feet under divergent conditions. During marine layer stratus events, ceiling heights below 500 feet most often occurred with surface convergence when the wind direction was northwest through east or calm wind condition (54/63 observations). Ceilings from 500 feet to 1,000 feet occurred with surface convergence when the wind direction was from west to north (39/43). Ceilings 1,000 feet to 1,500 feet occurred with surface convergence when the wind direction was from southwest to north or under calm wind conditions (9/9 observations). Ceilings

Table 2

Ceilings Non-Southerly Surge Event

Ceilings less than 500 feet			
	Wind Direction	Calm	
Convergence	Northwest to East		All Obs
Obs	43	11	63
Divergence	Northeast to Northwest		
Obs	37	21	86
	Ceilings between 500 feet to 1000 feet		
	Wind Direction	Calm	
Convergence	West to North		All Obs
Obs	39	1	43
Divergence	North to Southeast		
Obs	14	9	34
	Ceilings between 1000 feet to 1500 feet		
	Wind Direction	Calm	
Convergence	Southwest to North		All Obs
Obs	6	3	9
Divergence	Northwest to Southeast	Calm	
Obs	13	3	19
	Ceilings between 1500 feet to 2400 feet		
	Wind Direction	Calm	
Convergence	East to West		All Obs
Obs	2	3	5
Divergence	Southeast to Southwest		
Obs	4	3	7
	Ceilings greater than 2500 feet		
	Wind Direction	Calm	
Convergence	Southwest		All Obs
Obs	1	0	1
Divergence	Southwest to Northeast		
Obs	4	1	5

1,500 feet to 2,400 feet occurred with surface convergence when the wind direction was from east to west or under calm wind conditions (5/5 observations). Ceilings above 2,500 feet occurred with surface convergence when the wind direction was from southwest (1/1 observation).

A total of 151 observations contained ceiling values less than 3,000 feet under divergence conditions. Ceiling heights below 500 feet occurred with surface divergence when the wind direction was from northeast to northwest or when the wind speed was calm (58/86 observations). Vertical visibility conditions are often associated with ceilings equal to 100 feet (22/38 observations). Ceilings between 500 feet to 1000 feet occurred with surface divergence when the wind direction was from north to southeast or under calm conditions (23/34 observations). Ceilings 1,000 feet to 1,500 feet occurred with surface convergence when the wind direction

was from northwest to southeast or under calm wind conditions (16/19 observations). Ceilings between 1,500 feet and 2,400 feet occurred with surface divergence when the wind direction was from southeast to southwest or under calm wind conditions (7/7 observations). Ceilings above 2,400 feet occurred with surface divergence when the wind direction was from southwest to northeast or under calm wind conditions (5/5 observations).

During southerly surge events the relationship between wind direction, convergence, divergence and ceiling heights shifted, becoming simpler (see Table 3). A total of 62 observations contained ceiling values less than 900 feet under convergent conditions. Ceilings heights below 200 feet occurred with surface convergence when the wind direction was from southwest to north or under calm wind conditions (31/34 observations). Vertical visibility conditions are often associated with ceilings equal to 100 feet (18/34 observations). Ceilings heights below 500 feet occurred with surface convergence when the wind direction was from west to north or under calm wind conditions (43/50 observations). Ceilings 500 feet to 900 feet occurred with surface convergence when the wind direction was from southwest to north (9/12 observations). No ceilings were recorded above 800 feet under convergent conditions.

A total of 75 observations contained ceiling values less than 1,300 feet under divergent conditions. No ceilings were recorded above 1,200 feet. Ceilings below 200 feet occurred with surface divergence when the wind direction was from

Table 3

Ceilings Southerly Surge Event

Ceilings Southerly Surge Event			
Ceilings less than 500 feet			
	Wind Direction	Calm	
Convergence	West to North		All Obs
Obs	17	26	50
Divergence	Northeast to Northwest		
Obs	25	13	42
Ceilings between 500 feet to 900 feet			
	Wind Direction	Calm	
Convergence	Southwest to North		All Obs
Obs	8	1	12
Divergence	North to Southeast		
Obs	22	0	28
Ceilings greater than 900 feet			
	Wind Direction	Calm	
Convergence			All Obs
Obs	0	0	0
Divergence	West		
Obs	13	3	5

southeast to northwest or under calm wind conditions (25/28 observations). Ceilings between 200 feet and 500 feet occurred with surface divergence when the wind direction was from southeast to northwest or under calm wind conditions (13/14 observations). Ceilings between 500 feet and 900 feet occurred with surface divergence when the wind direction was from southwest to northwest (22/28 observations). Ceilings above 900 feet occurred with surface divergence from west (5/5 observations).

There is a strong correlation between the height of the marine layer inversion and the restriction to visibility. There were only two observations out of 169 where visibility was lower than 3 SM and the ceilings where equal to or greater than 500 feet.

a) Wind direction

There appears to be three dominate wind directions at Vandenberg AFB during the summer: land breeze (southeasterly), sea breeze (northwesterly) and gradient flow (northeasterly). See Figure 2 for wind direction versus 925mb temperatures.

The surface gradient wind flow for Vandenberg AFB during the summer is controlled by the interaction of the thermal trough in the central California valley and the position of the Pacific Ridge (see Fig. 3). If the thermal trough is the dominant feature, the flow will be northeasterly. If the Pacific Ridge is the dominant feature, the surface gradient flow will be northwesterly to northerly.

The basics about the land-sea breeze interaction are: Sea breezes blow perpendicular to the coastline from sea to land, while the reverse happens with the land breeze. Sea breeze begins to develop 3 to 4 hours after sunrise with peak gusts occurring in the afternoon. The best conditions for land and sea breezes to develop are weak surface pressure gradients and clear skies, which allow for strong heating

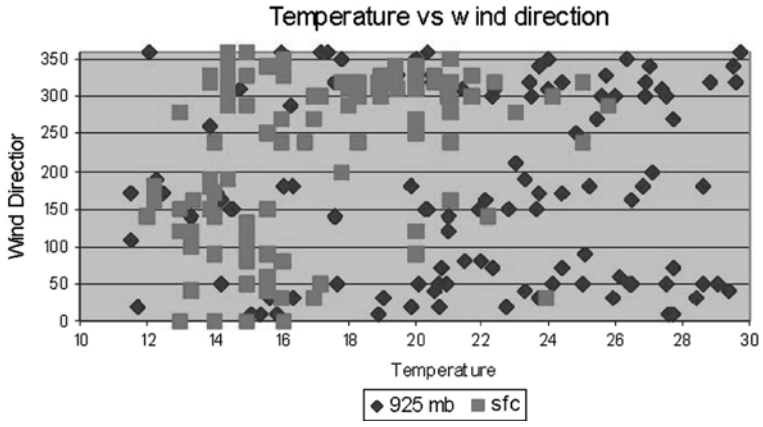

Figure 2
Wind direction versus surface and 925-mb temperatures.

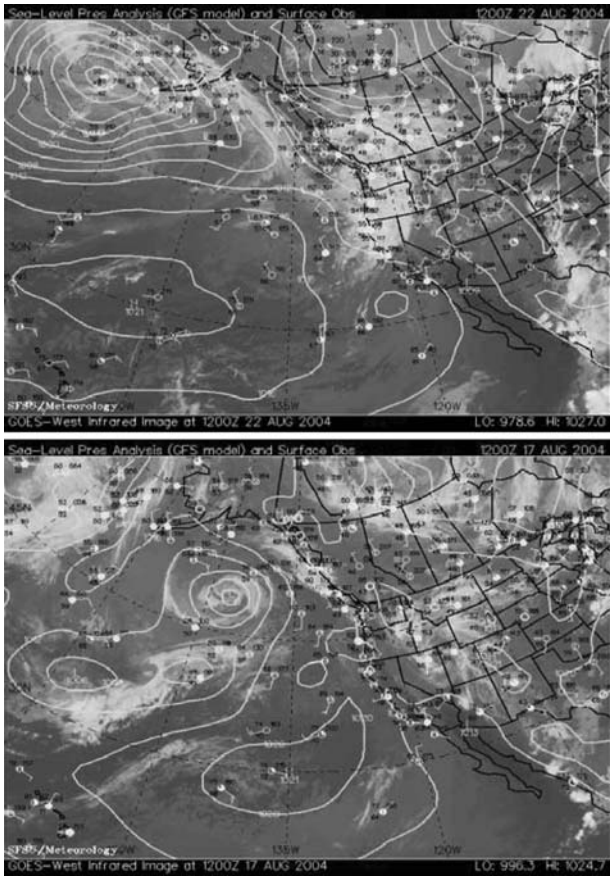

Figure 3
Surface circulation overlaid on satellite images for 17 and 22 Aug. 05.

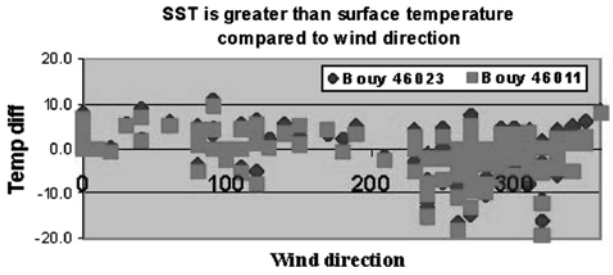

Figure 4
Difference between the sea-surface and land-surface temperatures compared to wind direction.

and radiational cooling. The land breeze generally develops shortly after midnight and peaks near sunrise.

It can be seen in Figure 4, when the land and sea temperatures are the same, the wind direction can be from any direction. When sea-surface temperatures (SST) are greater than 2° F above the surface temperature, winds are mainly from the northeast to southeast direction (except for days when a strong offshore wind develops and the direction remains out of east to southeast). When surface temperatures are between +1° F to −5° F of the sea-surface temperature, then the wind direction is based on the surface gradient flow.

Figure 5 shows the sea breeze as the dominant feature after 18Z. Winds between south and west were associated with southerly surges. Sunrise during this study was from 1323Z–1346Z. The largest SST and land temperature difference occur around 12Z and begins to decrease by 15Z, which correlates the establishment of a land breeze.

During offshore wind events the surface temperature rapidly climbs during the morning hours reaching the maximum temperature by 18Z (during this study the maximum surface temperature reached was 30° C). Even with weak-to-moderate offshore gradient flow, the sea breeze eventually predominates and progresses past the airfield (see Fig. 5). The largest SST and land temperature difference occurred when the wind speeds were less than five knots with northerly to southeasterly wind directions.

The dynamics that occur during sea and land breezes must be incorporated into the forecast process at Vandenberg AFB. In addition, forecasters rely on the mesoscale models, so initialization and verification remain a very important part of the process of recognizing slight shifts in the weather pattern.

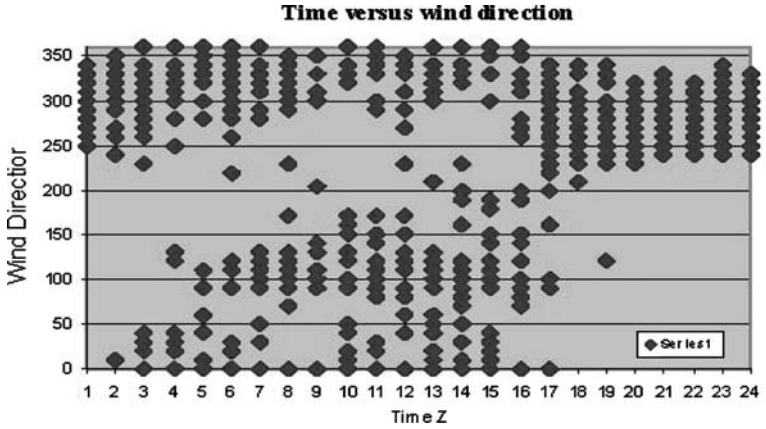

Figure 5
Time of day versus the wind direction.

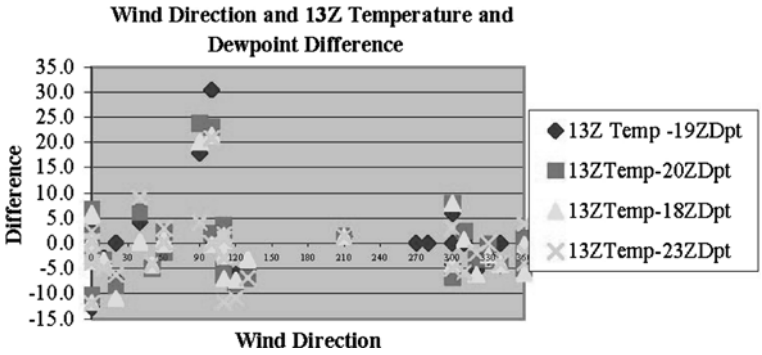

Figure 6
The difference between the previous day afternoon dewpoint temperature and next day's 13Z dry bulb temperature with the addition of wind direction.

b) Temperature

Surface temperature is also an important factor in the marine layer forecasting process. Correctly forecasting minimum surface temperature is the key to forecasting the wind direction. When one looks solely at dewpoint temperature no trends were indicated on the chart; however, when wind direction is added, a pattern did emerge (see Fig. 6). If the observed wind direction was west to northeast, the 19Z dewpoint temperature was a good indicator for minimum temperature. If the observed wind direction was east to southeast, then use the 23Z dewpoint temperature minus 6° F to forecast the minimum surface temperature.

The only two exceptions were a result of dry adiabatic heating and strong offshore winds associated with a Great Basin high. The general forecasting rule of using the surface dewpoint temperature that is associated with the surface maximum temperature in the afternoon to forecast the next morning low needs to be adjusted for Vandenberg AFB. This rule works only as long as the airmass has not been modified.

Normally the maximum temperature occurs between 20Z to 21Z with an exception occurring during an offshore wind event when the maximum temperature occurred at 23Z.

Figure 7 indicates there are actually three small dips (04Z, 08Z and 13Z) for lower temperatures during the night. There are two higher temperature peaks occurring at 17Z and 21Z. Later in this study it will be shown that the marine layer undergoes a cyclic pattern of increasing and decreasing ceilings heights.

c) Marine layer ceiling heights

It becomes evident that no simple correlation exists between surface relative humidity and ceiling heights. The relative humidity values must be influenced by

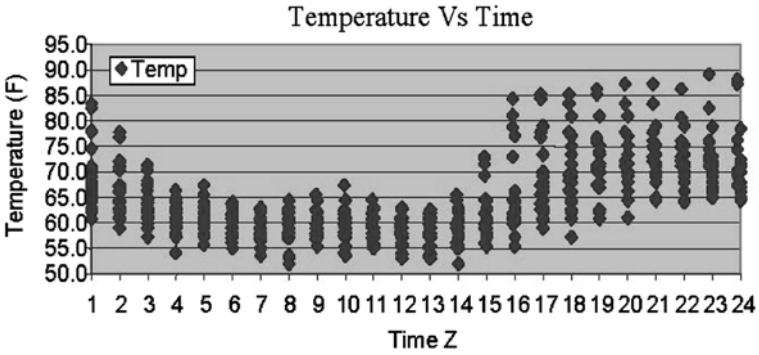

Figure 7
Temperature versus time (Z) of day.

other mechanisms. During the night the ceilings are routinely rising and falling in a cyclic pattern. Ceilings return or develop around 22Z–23Z and then gradually lower until 02–03Z. They rise a couple hundred feet by 06Z, and then lower again by 200 to 300 feet, with the minimum ceilings being reached during the hours of 12Z to 14Z. The ceilings begin to rise or break out by 17Z. Ceilings above 1,000 feet indicate a similar pattern, except the lowest ceilings occur around 14Z. There is a weak dip in the ceiling heights when they are around 1,200 feet, decreasing to 900 feet after 18Z.

Some correlations exist between ceiling heights, surface temperature and time of day. If the surface temperature is between 56° F to 59° F the ceilings roll in around 02Z (predominately below 500 feet). A cyclic pattern then drops the ceilings to 100 feet with breakout occurring between 17 to 19Z. If the surface temperature is between 54° F to 56° F, the clouds roll in after 08Z at 200 feet. The ceiling slowly increases through the night to 600 feet. It then decreases to 200 feet around 15Z before the ceiling breaks out by 17Z. If the surface temperature is 52° F to 54° F then the ceiling quickly breaks by 14Z. During the southerly surge events, 100-foot ceilings developed with a surface temperature of 60° F after 15Z, and the ceilings lasted until 17Z. Ceiling heights are predominately 300 feet during the night when temperatures are 60° F and below.

It was mentioned in a previous section that there are three basic wind directions that influence the weather pattern at Vandenberg AFB. Wind directions from 280 to 360 degrees are from the dying sea breeze or gradient flow as the temperature of the land and sea difference decrease. The ceiling gradually move in at 500 ft and lower, reaching 100 feet after 11Z (remaining until 15Z). When the wind direction is between 200 and 270 degrees, the ceiling decreases to 100 feet after 03Z and then fall under the cyclic pattern mention earlier. When the wind direction is 80 to 190 degrees, the clouds roll in above 500 feet and then decrease to 100 feet by 10Z, increasing after 15Z. When the wind direction was between 360 to 80 degrees, generally due to the surface gradient flow, the clouds roll in around 03Z with ceiling

heights around 700 feet and go through the cyclic pattern with short periods of ceilings at 100 feet, finally breaking out between 16Z to 17Z.

During a southerly surge event, there is more of a gradual change in ceilings with respect to wind direction and time. The ceiling will not totally break out if the wind direction is from the west through north. As the wind direction shifts in a clockwise direction, the ceilings delay lowering to less than 200 feet. When the winds are from west to north they go through the cyclic pattern mentioned earlier and rise after 16Z. When the winds are northeast to south, the ceilings increase to around 800 feet then lower back down to 500 feet, with break-out around 20Z.

This shows there is no significant correlation between the surface relative humidity values and ceiling heights. A correlation does exist between surface temperatures, winds, time of day and ceiling heights. Therefore, forecasting the surface temperature is important.

3.2. Weather Parameters Affecting the Marine Boundary Layer

A correlation exists between the marine layer thickness, 500mb height advection and 500mb temperature advection.

It appears the marine layer depth is greatest when the 500mb heights are increasing ($+10$m to $+20$m) and weak or no 500mb warm air advection (0° C to $+1$° C) occur's within the past three hours. This situation normally occurs when either the atmosphere is stabilizing or the 500mb contour and thermal ridges are approaching. The increasing cloud thickness can occur in two ways. First, the cloud tops remain the same while ceiling bases are lower. Secondly, the ceiling base remains the same while the cloud top increases.

During the morning hours, the combined effect of 500mb cold air advection (-0.5° C to -1.2° C) and 500mb heights change (-5 m to $+12$ m) within the past 3 hours increases cloud thickness and opposes the normal solar insolation burn-off. In other words, if at 12Z the clouds are 800 feet thick, then by 15Z the cloud depth will increase to 1200 feet. This affects the burn-off time by delaying scattered conditions for another 1 to 2 hours. When a weak 500mb shortwave moved through Vandenberg AFB during the early morning hours on 23 Aug 04, atmospheric destabilization increased cloud thickness. It was also observed during the study period that even very weak short waves, only seen in the water vapor imagery, can still affect the cloud dynamics.

3.3. 500mb Heights Affecting Marine Boundary Layer

This study refutes the following two Vandenberg Air Force rules of thumb: As 500mb heights decrease the marine layer ceiling will raise, and as 500mb heights increase the marine layer ceilings will decrease. The 500mb height changes alone do not predicate the ceiling height changes of cloud bases. It is more important to determine whether the area is on the front side of an upper-level ridge axis (downward vertical

Table 4

12HR-500-mb height change (m) and height values (m) in relation to ceiling heights

24hr 500mb	500mb Heights at 1200GMT																						
Hgt Chg	5800	5805	5810	5815	5820	5825	5830	5835	5840	5845	5850	5855	5860	5865	5870	5875	5880	5885	5890	5895	5900	5905	5910	5915
60	NO	NO	NO	NO	NO	NO	NO	NO	NO	NO	NO	NO	NO	NO	NO	NO	<600	NO	NO	NO	NO	NO	NO	NO
55	NO	NO	NO	NO	NO	NO	NO	NO	NO	NO	NO	NO	NO	NO	<600	<600	<400	NO	NO	NO	NO	NO	NO	NO
50	NO	NO	NO	NO	NO	NO	NO	NO	NO	NO	NO	NO	NO	<600	<600	<400	<400	<400	NO	NO	NO	NO	NO	NO
45	NO	NO	NO	NO	NO	NO	NO	NO	NO	NO	NO	NO	<800	<600	<400	<400	<400	<400	<400	NO	NO	NO	NO	NO
40	NO	NO	NO	NO	NO	NO	NO	NO	NO	NO	NO	<800	<600	<600	<400	<400	<400	<200	<200	NO	NO	NO	NO	NO
35	NO	NO	NO	NO	NO	NO	NO	NO	NO	NO	<900	<800	<600	<400	<400	<400	<400	<200	<200	<400	NO	NO	NO	NO
30	NO	NO	NO	NO	NO	NO	NO	NO	NO	<900	<900	<800	<400	<400	<400	<400	<400	<200	<200	<200	<400	NO	NO	NO
25	NO	NO	NO	NO	NO	NO	NO	NO	<1100	<900	<800	<600	<400	<400	<400	<400	<400	<200	<200	<200	<200	<400	NO	NO
20	NO	NO	NO	NO	NO	NO	NO	<1100	<900	<800	<600	<600	<400	<200	<200	<200	<400	<200	<200	<200	<200	<400	<400	NO
15	NO	NO	NO	NO	NO	NO	<1100	<900	<900	<600	<600	<400	<200	<200	<200	<400	<400	<200	<200	<200	<200	<200	<400	NO
10	NO	NO	NO	NO	NO	<600	<900	<900	<900	<600	<400	<400	<200	<200	<200	<400	<400	<200	<200	<200	<200	<200	<400	<400
5	NO	NO	NO	NO	<800	<600	<900	<900	<800	<400	<400	<200	<200	<400	<400	<400	<200	<200	<200	<200	<200	<400	<400	NO
0	NO	NO	NO	<900	<900	<600	<900	<800	<600	<400	<200	<200	<200	<400	<400	<400	<200	<400	<200	<200	<400	<400	NO	NO
-5	NO	NO	NO	<900	<900	<800	<800	<800	<600	<200	<200	<200	<400	<400	<200	<200	<200	<200	<200	<200	<400	<400	NO	NO
-10	NO	NO	NO	<1100	<1100	<900	<800	<600	<400	<200	<200	<200	<400	<400	<400	<400	<200	<200	<200	<200	<400	<200	NO	NO
-15	NO	NO	NO	<1500	<1500	<1100	<800	<600	<400	<200	<200	<200	<400	<400	<400	<400	<200	<200	<200	<200	NO	NO	NO	NO
-20	NO	NO	NO	<1500	>1500	>1500	<900	<1100	<400	<200	<200	<200	<400	<400	<400	<200	<200	<400	<200	<200	NO	NO	NO	NO
-25	NO	NO	NO	>1500	<1500	>1500	<1100	<1100	<900	<900	<400	<200	<400	<200	<200	<400	<400	<200	<200	NO	NO	NO	NO	NO
-30	NO	NO	<900	>1500	>1500	>1500	>1500	<1100	<900	<600	<200	<200	<200	<200	<200	<400	<200	<200	NO	NO	NO	NO	NO	NO
-35	NO	NO	<900	>1500	>1500	>1500	>1500	<1100	<900	<800	<200	<200	<200	<200	<200	<200	<200	NO	NO	NO	NO	NO	NO	NO
-40	NO	NO	<200	<1100	<1100	<1100	<900	<900	<200	<200	<200	<200	<200	<200	<200	NO	NO	NO	NO	NO	NO	NO	NO	NO
-45	NO	NO	<200	<1100	<800	<900	<800	<600	<200	<200	<200	<200	<200	<200	NO	NO	NO	NO	NO	NO	NO	NO	NO	NO
-50	NO	NO	<900	<900	<800	<900	<600	<200	<200	<200	<200	<200	NO	NO	NO	NO	NO	NO	NO	NO	NO	NO	NO	NO
-55	NO	NO	<900	<900	<800	<600	<200	<200	<200	<200	<200	NO	NO	NO	NO	NO	NO	NO	NO	NO	NO	NO	NO	NO
-60	NO	<400	<900	<800	<800	<400	<400	<400	<200	<400	NO	NO	NO	NO	NO	NO	NO	NO	NO	NO	NO	NO	NO	NO
65	NO	<800	<900	<600	<600	<400	<400	<400	<400	NO	NO	NO	NO	NO	NO	NO	NO	NO	NO	NO	NO	NO	NO	NO

motion) or the front side of an upper level trough axis (upward vertical motion). There was no direct correlation between cloud heights and 500mb height changes.

Table 4 shows the relationship between the 500mb height change in the previous 12 hours, the 12Z 500mb height values and the ceilings that occurred at 12Z. ''NO'' means no ceilings were observed in the combination. Tables 4 and 5 indicate the possibility of developing definitive guidance to determine expected ceilings. They

Table 5

24HR 500-mb height change (m) and height values (m) in relation to ceiling heights

24hr 500mb	500mb Heights at 1200GMT																						
Hgt Chg	5800	5805	5810	5815	5820	5825	5830	5835	5840	5845	5850	5855	5860	5865	5870	5875	5880	5885	5890	5895	5900	5905	5910	5915
60	NO	NO	NO	NO	NO	NO	NO	NO	NO	NO	NO	NO	NO	NO	NO	NO	<600	NO	NO	NO	NO	NO	NO	NO
55	NO	NO	NO	NO	NO	NO	NO	NO	NO	NO	NO	NO	NO	NO	<600	<600	<400	NO	NO	NO	NO	NO	NO	NO
50	NO	NO	NO	NO	NO	NO	NO	NO	NO	NO	NO	NO	NO	<600	<600	<400	<400	<400	NO	NO	NO	NO	NO	NO
45	NO	NO	NO	NO	NO	NO	NO	NO	NO	NO	NO	NO	<800	<600	<400	<400	<400	<400	<400	NO	NO	NO	NO	NO
40	NO	NO	NO	NO	NO	NO	NO	NO	NO	NO	NO	<800	<600	<600	<400	<400	<400	<200	<200	NO	NO	NO	NO	NO
35	NO	NO	NO	NO	NO	NO	NO	NO	NO	NO	<900	<800	<600	<400	<400	<400	<400	<200	<200	<400	NO	NO	NO	NO
30	NO	NO	NO	NO	NO	NO	NO	NO	NO	<900	<900	<800	<400	<400	<400	<400	<400	<200	<200	<200	<400	NO	NO	NO
25	NO	NO	NO	NO	NO	NO	NO	NO	<1100	<900	<800	<600	<400	<400	<400	<400	<400	<200	<200	<200	<200	<400	NO	NO
20	NO	NO	NO	NO	NO	NO	NO	<1100	<900	<800	<600	<600	<400	<200	<200	<200	<400	<200	<200	<200	<200	<400	<400	NO
15	NO	NO	NO	NO	NO	NO	<1100	<900	<900	<600	<600	<400	<200	<200	<200	<400	<400	<200	<200	<200	<200	<200	<400	NO
10	NO	NO	NO	NO	NO	<600	<900	<900	<900	<600	<400	<400	<200	<200	<200	<400	<400	<200	<200	<200	<200	<200	<400	<400
5	NO	NO	NO	NO	<800	<600	<900	<900	<800	<400	<400	<200	<200	<400	<400	<400	<200	<200	<200	<200	<200	<400	<400	NO
0	NO	NO	NO	<900	<900	<600	<900	<800	<600	<400	<200	<200	<200	<400	<400	<400	<200	<400	<200	<200	<400	<400	NO	NO
-5	NO	NO	NO	<900	<900	<800	<800	<800	<600	<200	<200	<200	<400	<400	<200	<200	<200	<200	<200	<200	<400	<400	NO	NO
-10	NO	NO	NO	<1100	<1100	<900	<800	<600	<400	<200	<200	<200	<400	<400	<400	<400	<200	<200	<200	<200	<400	<200	NO	NO
-15	NO	NO	NO	<1500	<1500	<1100	<800	<600	<400	<200	<200	<200	<400	<400	<400	<400	<200	<200	<200	<200	NO	NO	NO	NO
-20	NO	NO	NO	<1500	>1500	>1500	<900	<1100	<400	<200	<200	<200	<400	<400	<400	<200	<200	<400	<200	<200	NO	NO	NO	NO
-25	NO	NO	NO	>1500	<1500	>1500	<1100	<1100	<900	<900	<400	<200	<400	<200	<200	<400	<400	<200	<200	NO	NO	NO	NO	NO
-30	NO	NO	<900	>1500	>1500	>1500	>1500	<1100	<900	<600	<200	<200	<200	<200	<200	<400	<200	<200	NO	NO	NO	NO	NO	NO
-35	NO	NO	<900	>1500	>1500	>1500	<1100	<900	<800	<200	<200	<200	<200	<200	<200	<200	<200	NO	NO	NO	NO	NO	NO	NO
-40	NO	NO	<200	<1100	<1100	<1100	<900	<900	<200	<200	<200	<200	<200	<200	<200	NO	NO	NO	NO	NO	NO	NO	NO	NO
-45	NO	NO	<200	<1100	<800	<900	<800	<600	<200	<200	<200	<200	<200	<200	NO	NO	NO	NO	NO	NO	NO	NO	NO	NO
-50	NO	NO	<900	<900	<800	<900	<600	<200	<200	<200	<200	<200	NO	NO	NO	NO	NO	NO	NO	NO	NO	NO	NO	NO
-55	NO	NO	<900	<900	<800	<600	<200	<200	<200	<200	<200	NO	NO	NO	NO	NO	NO	NO	NO	NO	NO	NO	NO	NO
-60	NO	<400	<900	<800	<800	<400	<400	<400	<200	<400	NO	NO	NO	NO	NO	NO	NO	NO	NO	NO	NO	NO	NO	NO
65	NO	<800	<900	<600	<600	<400	<400	<400	<400	NO	NO	NO	NO	NO	NO	NO	NO	NO	NO	NO	NO	NO	NO	NO

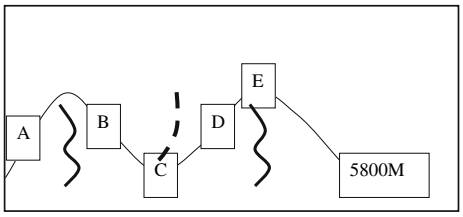

Figure 8
Points A-E represents Vandenberg AFB location in relation to the 500-mb height value 580DM.

show it is more important to combine the 500mb height rate of change with the 500mb height values when forecasting ceilings. The tools we have available to determine the 500mb height changes and current height values (within 5 meters) are the AWIPS charts (using the sampling feature) and SKEW-Ts. The forecast model alphanumeric (MOS and Grid) products only report values in decameters and have less resolution.

Figure 8 demonstrates the upper level stability can change even though the 500mb height stayed the same. Given any forecast period, if the upper air pattern changes position from points E to D, that station would experience upward vertical motion, therefore lifting the marine layer inversion. If the upper air pattern changed position over a station from points D to C, the station would continue to experience upward vertical motion, therefore lifting the marine layer inversion. If the upper air pattern changed position over a station from points C to B, the station would experience downward vertical motion, therefore lowering the marine layer inversion. If the upper air pattern changed position over a station from points B to A, the station would experience more upward vertical motion, therefore lifting the marine layer inversion. The amount of the height rise or fall within the marine layer inversion averages 300ft during this scenario which can make a difference of an hour in the break-out time.

There also appears to be a relationship between the 500mb temperature and the 850mb temperature changes. If the 500mb or 850mb temperature changes 1° C within a 24-hour period the marine layer inversion will change by 700 feet. For instance, if the 500mb temperature decreases 1° C the inversion 700 feet, and if the 500mb temperature increases the marine layer inversion lowers. If the 500mb temperature decreases by 0.5° C and the 850mb increases by 0.5° C and all the other parameters remain the same, there will be no change with marine layer inversion height.

During the first half and the last two days of the study period Vandenberg AFB was under the eastern side of the 500mb ridge, with weak short waves moving through the upper-level pattern. During the middle period the ridge shifted and Vandenberg AFB was on the backside of the upper-level ridge (unstable side). This was important

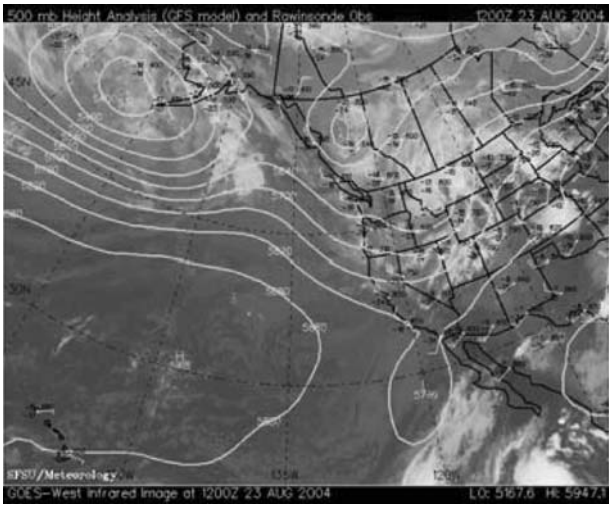

Figure 9
500-mb heights and satellite image at 23 Aug., 04 12Z.

because it affected the height of the subsidence inversion and the downward vertical motion strength. The pattern shifts affected Vandenberg in the following manner: on 23 August, Vandenberg AFB experienced a normal marine layer; on 30 August, a short episode of southerly surge developed (less than 48 hours in duration) northward just past Vandenberg AFB; and on 8 September, Vandenberg AFB was located on the unstable side of the ridge, no marine layer developed.

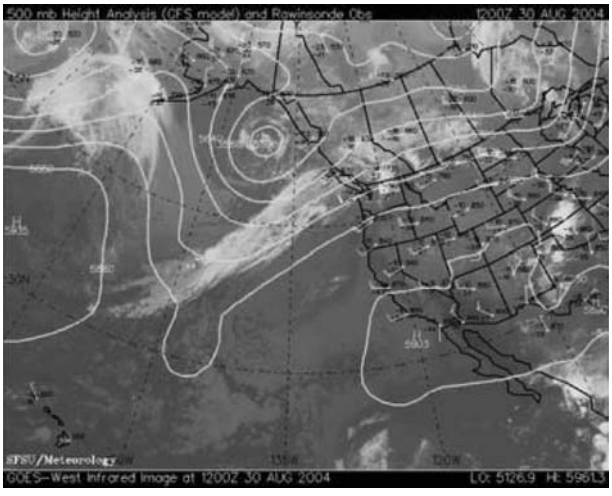

Figure 10
500-mb heights and satellite image at 30 Aug., 04 12Z.

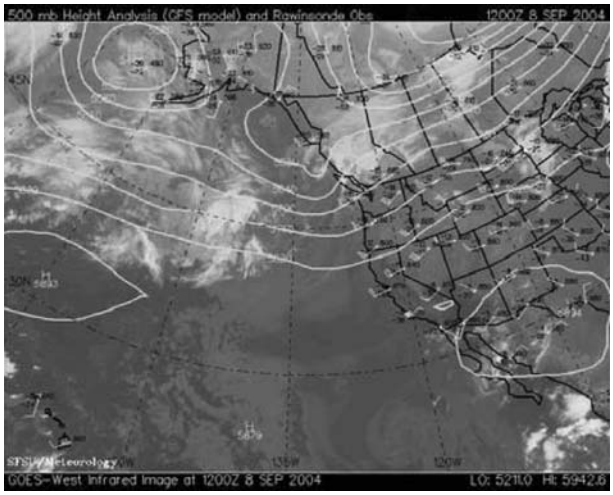

Figure 11
500-mb heights and satellite image at 8 Sep., 04 12Z.

It is critical to know where Vandenberg AFB is located in relation to the subsidence side compared to the more unstable side of the upper-level ridge. See Figures 9–11. This supports the conclusion about the relationship between 500mb heights, 500mb temperatures and marine layer ceilings.

3.4. Observed Cloud Burn-off Rates

The average burn-off rate is 320 feet per hour except during southerly stratus surge events and weak short wave passages. During southerly surge events the burn-off rate decreased to an average of 173 feet per hour. No correlation exists when you compare the 500mb temperature between -0.3° C to $+3^\circ$ C per 3 hour changes (20 out of 28 cases) and the burn-off rate ranges. This is evidence that some other mechanism is involved.

However, there is some relationship between the 500mb temperature plus height changes with the burn-off rate. Maximum burn-off rates occurs when the heights increase while temperatures decrease. There is a three-hour delay in the burn-out rate in response to a combined thermal and contour trough moving through Vandenberg AFB.

3.5. Drizzle Forecasting

During the study period, six cases of drizzle occurred. Three cases of drizzle occurred during periods dominated by a southerly surge, while the other three occurred after stratus advected southward from northern California. The article written by Paluch and Lenschow, *Stratiform Cloud Formation in the Marine Layer*,

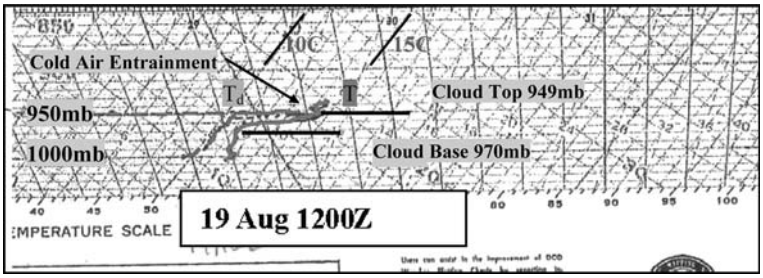

Figure 12
A sample skew-T when drizzle was observed. Red solid line is temperature. Green dashed line is dewpoint temperature.

demonstrates how small baroclinic circulations can set up within the marine layer. They state "an airmass will seek a stable condition such as warm air over colder air."

Cold air over warm air creates an unstable environment. Normally cold air in the boundary layer (below 2,000 feet AGL) infers stable conditions, while warm air infers unstable conditions. Generally for drizzle to develop the clouds must be at least 2,000 feet thick with some type of weak vertical motion. However, in all six cases the Skew-T cloud thicknesses were observed between 1,000 feet to 1,700 feet (using 88 percent relative humidity as the cut-off for cloud tops) and yet drizzle still occurred at Vandenberg AFB (see Fig. 12). Basic mesoscale meteorology for afternoon thunderstorm development is warm air below 600mb, cold air above 600mb and dry air entrainment at 700mb. This provides a mechanism for the air molecules to start moving in the vertical, with sinking cold air replacing the rising warm air. The same concept works on the microscale level and can be applied within the boundary layer.

All the drizzle events were associated with cold air entrainment. The reason drizzle may not occur with clouds thicker than 1,400 feet is because the microscale processes are not strong enough for the water droplets to reach the surface. Three of the six instances of drizzle occurred when the 925mb wind flow was predominately southeasterly. Due to radiational cooling, the air just above the higher terrain is allowed to become cooler than the marine layer cloud tops. The cooler air is advected over the marine layer, creating an atmosphere with dry air entrainment. This is most likely how the cooler, drier air is being trapped in the microscale processes. The other three cases developed when a high-pressure ridge moved into Washington and Oregon, providing an easterly flow over northern California and southern Oregon. Clouds then developed off the coast of California and advected southward, reaching Vandenberg AFB within 12 hours of development. Although it appears to be now casting, the idea of watching the Mini-SODAR's prospective graph (advection processes across the range) may assist in a short-term forecast, in addition to using

the temperature on the weather towers located at Oak Mountain (elevation is near 1,400 feet). Additional tools to use to forecast this type of drizzle is cloud top temperatures from infrared satellite pictures using the AWIPS sampling feature.

3.6. Verification of Three Operational Forecast Models

This section of the study looks at three different models (GFS, Meso ETA, local MM5) that are locally available to the forecaster at Vandenberg Air Force Base. The parameters were selected based on local forecasting rules of thumb, and on the initial analysis of the observational data for this study. The list of parameters that were compared are: surface temperature, surface relative humidity, surface wind direction and speed, 500mb temperature and height, 850mb temperature, and 925mb temperature. This section is broken into three parts that compares the different models parameters data under all conditions, during a southerly surge event and with the southerly surge data removed.

Table 6 shows model verification for the following parameters during non-southerly surge conditions. The forecast surface temperature for all models was too high through the different forecast periods. The best model was the MM5, which was just over 1° C too high at the 07Z and 23Z, and 1° C too low at 15Z. The forecast surface relative humidity for all models was too dry, with the MM5 doing the best with an average of one to three percent off for all forecast periods. The surface wind direction parameter showed mixed results. The GFS performed the best at the 07Z forecast period, while the MM5 performed the worst. MM5 performed the best for the 15Z forecast period while the Meso ETA performed the best for the 23Z forecast period. The wide direction differences were due to the fact that winds speeds were recorded as calm or forecasted to be calm (created high direction variability). The surface wind speed parameter the ETA did the best for two out of three forecast periods with wind speed difference of less than two knots. The forecast 500mb temperature parameter the GFS did the best in this category during all three forecast periods with a mean temperature difference of 0.13° C. The forecast 500mb heights parameter the GFS did the best two out of three forecast periods (07 and 15Z), while the MM5 did the best at 23Z. Mean difference was only three meters. During the study period, 925mb forecast temperatures were not available for the GFS. Local MM5 did very well with a mean difference of +0.02° C while Meso ETA maintained a −2° C to −3° C difference. The GFS was best model two of three forecast periods (07 and 15Z) for the 850mb temperature difference, while Meso Eta did the best at 23Z with a mean difference of only 0.5° C.

a) Southerly surge conditions

Table 7 shows model verification for the following parameters during southerly surge conditions. The GFS did the best forecasting the 500mb heights parameter for all three forecast periods with a mean difference of only 1.5 meters. The GFS did the best

Table 6

Model verification for all conditions. The term "all conditions" means all the collected data were used for the comparison

All Conditions	Mean			Std Dev			Std Err Mean		
	07Z	15Z	23Z	07Z	15Z	23Z	07Z	15Z	23Z
				500mb Temperature Diff (C)					
AVN	−0.1	−0.06	−0.124	0.959	1.223	1.054	0.105	0.133	0.12
Meso ETA	−0.31	−0.31	−0.332	1.266	1.485	1.42	0.121	0.142	0.14
Local MM5	−0.48	−0.3	−0.229	0.881	0.896	0.998	0.108	0.104	0.12
				500mb Hgt Diff (m)					
AVN	3.069	3.03	4.248	20.092	19.98	21.11	2.205	2.18	2.33
Meso ETA	−11.2	−14.1	−4.242	26.128	29.24	32.53	2.503	2.801	32.5
Local MM5	3.855	8.19	4.09	13.639	12.74	19.09	1.678	1.481	2.24
				850mb Temperature Diff (C)					
AVN	0.523	0.49	0.486	1.25	1.186	1.088	0.136	0.129	0.12
Meso ETA	−0.6	−1.11	−0.274	1.931	1.944	2.051	0.184	0.182	0.19
Local MM5	1.051	0.73	0.897	1.296	1.293	1.509	0.157	0.145	0.18
AVN				925mb Temperature Diff (C)					
Meso ETA	−2.73	−3.02	−2.454	3.684	3.711	3.752	0.35	0.348	0.35
Local MM5	0.219	0.03	0.118	2.61	2.62	2.586	0.317	0.618	0.3
				SFC Temperatures Diff (F)					
AVN	−5.21	−4.99	−4.592	10.647	10.67	10.73	0.984	0.958	0.98
Meso ETA	−3.72	−3.05	−3.063	8.583	7.447	9.116	0.548	0.465	0.57
Local MM5	−1.3	1.38	−0.392	6.052	4.988	4.425	0.283	0.219	0.2
				SFC RH Diff (%)					
AVN	34.69	33.5	32.03	25.035	24.6	23.51	25.03	24.6	23.5
Meso ETA	12.86	11.9	12.25	21.248	19.42	21.61	1.343	1.235	1.37
Local MM5	3.298	1.16	0.905	15.61	15.01	13.86	0.733	0.656	0.62
				SFC Wind Dir Diff (°)					
AVN	−6.41	−30.5	−40.87	152	151.3	141.3	13.82	13.82	12.8
Meso ETA	−18.1	−23.5	−19.29	105.88	104.2	109.3	6.764	6.498	6.83
Local MM5	−18.5	−14.2	−28.23	143.66	91.96	133.7	−1.429	−0.86	−1.7
				SFC Wind Spd Diff (kts)					
AVN	−2.07	−2.21	−2.623	6.237	5.63	5.596	0.567	0.514	0.51
Meso ETA	−1.33	−1.75	−1.333	4.068	3.823	3.462	0.26	0.238	0.22
Local MM5	−1.43	−0.86	−1.66	3.802	3.065	3.513	0.181	0.135	0.16

forecasting the 500mb temperature for two out of three forecast periods (07 and 15Z) with MM5 doing the best at 23Z. Both models had a mean temperature difference less than 0.41° C. The Meso ETA did well forecasting 850mb temperature difference category for the 07Z and 15Z forecast periods, with the GFS doing the best at 23Z. Both models had a mean temperature difference of only 0.5° C. During the study period 925mb temperature was not available for the GFS. Local MM5 did very well forecasting the 925mb temperature with a mean temperature difference of – 0.68° C to

Table 7

Model verification during southerly surge conditions

Southerly Surge	Mean			Std Dev			Std Err Mean		
	07Z	15Z	23Z	07Z	15Z	23Z	07Z	15Z	23Z
				500mb Temperature Diff (C)					
AVN	1.59	1.43	0.23	10.47	10.2	13.5	2.402	2.3	3.18
Meso ETA	−17.9	−23	−15	15.88	16	19.3	3.311	3.3	4.03
Local MM5	−5.46	2.02	-4.9	16.86	15.6	22.4	4.353	3.9	5.78
				500mb Hgt Diff (m)					
AVN	−0.42	−0.2	−0.4	0.983	1.14	1.32	0.225	0.3	0.31
Meso ETA	−1.09	−1.2	−1.1	1.606	1.73	1.7	0.335	0.4	0.36
Local MM5	−0.66	−0.4	−0.4	0.617	0.82	0.86	0.159	0.2	0.22
				850mb Temperature Diff (C)					
AVN	0.54	0.7	0.32	1.377	1.6	1.14	0.316	0.4	0.29
Meso ETA	0.43	−0.1	0.91	1.072	1.04	0.82	0.219	0.2	0.17
Local MM5	1.31	1.34	1.29	1.094	0.96	0.96	0.273	0.2	0.26
				925mb Temperature Diff (C) AVN					
Meso ETA	−4.35	−3.9	−3.6	4.902	4.75	4.13	1.01	1	0.84
Local MM5	−0.68	−1.2	−0.8	3.567	3.54	3.98	0.892	0.9	1.06
				SFC Temperatures Diff (F)					
AVN	−6.7	−7.7	−5.8	9.219	9.3	10.1	2.061	2	2.21
Meso ETA	−5.73	−4	−3.6	9.134	7	7.82	1.232	0.9	1.05
Local MM5	−2.76	−1.5	−0.9	3.767	4.1	2.86	0.379	0.4	0.28
				SFC RH Diff (%)					
AVN	42.4	40.2	36.2	16.19	16.3	17.5	3.62	3.5	3.82
Meso ETA	15.3	13.7	13.5	19.46	18.5	19.1	2.672	2.4	2.85
Local MM5	7.52	7.4	4.23	8.635	12.2	10	0.868	1.2	0.94
				SFC Wind Dir Diff (°)					
AVN	9.09	8.57	−23	154.4	164	144	32.92	36	30.7
Meso ETA	6.6	−24	−25	129.5	124	134	18.9	17	18.1
Local MM5	−19.2	−32	−70	159.4	120	142	16.1	11	13.3
				SFC Wind Spd Diff (kts)					
AVN	−1.46	−3.8	−2.5	5.449	5.79	3.81	1.162	1.3	0.81
Meso ETA	−1.85	−3	−1.6	3.27	−3	−1.6	0.477	0.4	0.36
Local MM5	−1.03	−1.5	−1.8	2.655	2.5	2.67	0.267	0.2	0.25

−1.2° C while Meso ETA maintained a negative –3° C to −4° C difference. All the models forecasted the surface temperatures too high through the different forecast periods. The MM5 was the best model and was off by less than 2° C at the three forecast periods. All the models forecasted the surface relative humidity were too dry with the MM5 doing the best with an average of 7 percent difference for all forecast periods. The forecasted surface wind direction parameter showed mixed results. Meso Eta performed the best at the 07Z forecast period, while the GFS performed the best

Table 8

Model verification for all conditions without the southerly surge.

W/O Southerly Surge	Mean			Std Dev			Std Err Mean		
	07Z	15Z	23Z	07Z	15Z	23Z	07Z	15Z	23Z
				500mb Hgt Diff (m)					
AVN	3.232	3.2	5	22.33	22.3	23	2.84	2.84	2.92
Meso ETA	−9.37	−12	−1.4	28.05	31.6	34.7	3.03	3.4	3.72
Local MM5	6.596	9.9	6.4	11.34	11.4	17.6	1.59	1.5	2.31
				500mb Temperature Diff (C)					
AVN	0.013	0.1	−0	0.933	0.86	0.98	0.12	0.11	0.12
Meso ETA	−0.1	0.1	−0.1	1.078	1.33	1.27	0.12	0.14	0.14
Local MM5	−0.43	−0.3	−0.2	0.943	0.92	−0.2	0.13	0.12	0.13
				850mb Temperature Diff (C)					
AVN	0.552	0.5	0.5	1.245	1.18	1.08	0.15	0.15	0.14
Meso ETA	−0.88	−1.4	−0.6	2.023	2.04	2.17	0.22	0.22	0.23
Local MM5	0.973	0.6	0.8	1.353	1.33	1.61	0.19	0.17	0.21
				925mb Temperature Diff (C)					
AVN	0.552	0.5	0.5	1.244	1.18	1.08	0.15	0.15	1.08
Meso ETA	−2.28	−2.8	−2.1	3.162	3.38	3.6	0.34	0.36	0.38
Local MM5	0.496	0.4	0.3	2.209	2.25	2.12	0.31	0.27	0.28
				SFC Temperatures Diff (F)					
AVN	−4.9	−4.4	−4.3	10.94	10.9	10.9	1.11	1.08	1.1
Meso ETA	−3.14	−2.8	−2.9	8.351	7.56	9.45	0.61	0.53	0.67
Local MM5	−0.9	2.2	−0.2	6.49	4.91	4.76	0.34	0.24	0.24
				SFC RH Diff (%)					
AVN	33.12	32	31	26.27	25.9	24.6	2.65	2.56	2.56
Meso ETA	12.2	11	12	21.7	20	22.3	1.55	1.41	1.58
Local MM5	2.122	−0.5	−0.1	18.88	15.3	14.7	0.9	0.75	0.75
				SFC Wind Dir Diff (°)					
AVN	−9.86	−39	−45	152	148	141	15.3	14.9	14.1
Meso ETA	−24	−23	−18	98.92	98.6	102	7.03	6.94	7.18
Local MM5	−18.3	−9.5	−16	139.1	82.4	129	7.52	4.07	6.58
				SFC Wind Spd Diff (kts)					
AVN	−2.2	−1.9	−2.6	6.416	5.57	5.93	0.65	0.56	0.59
Meso ETA	−1.2	−1.4	−1.3	4.233	3.97	3.85	0.3	0.28	0.26
Local MM5	−1.54	−0.7	−1.8	4.07	3.16	3.73	0.22	0.16	0.19

at the 15Z and 23Z forecast periods. The MM5 did the best for two out of the three forecast periods for surface wind speed with a difference of less than 1.5 knots.

b) Without southerly surge conditions

Table 8 shows the results of model verification without southerly surge conditions. The GFS did the best for two out of three forecast periods (07Z and 15Z) for the 500mb heights parameters, with Meso Eta doing the best at 23Z. Both models had a

mean height difference of three meters. The GFS took a complete sweep of the 850mb temperature category with a mean difference of only 0.5° C. MM5 took the honors for the 925mb temperature difference category, maintaining less than a 0.5° C difference. During the study period 925mb temperatures were not available for the GFS. The forecast surface temperature for all models was too high through the different forecast periods. The MM5 was the best with a surface temperature difference less than 2° C for all three forecast periods. The forecast surface relative humidity temperature for all models was too dry with the MM5 doing the best (an average of two percent difference for all forecast periods). The surface winds forecast area really showed mixed results. The GFS performed the best at the 07Z forecast period, while the MM5 performed the best at the 15Z and 23Z forecast periods. The surface wind direction forecast area really showed mixed results. The GFS performed the best at the 07Z forecast period, while the MM5 performed the best at the 15Z and 23Z forecast periods. The Meso Eta did the best for two out of the three forecast periods for the wind speed parameter with wind speed difference of less than one knot.

Three different forecast models were compared in three different situations and they indicated no single forecast model can be used alone to forecast the marine layer stratus. It appears the proper combination is to use the GFS to forecast the upper level features at and above 850mb and then use the local MM5 to forecast the parameters below 850mb.

4. Conclusion

Marine layer stratus is a feature that occurs entirely below the 925mb level but is also influenced by the weak upper level dynamics that move over Vandenberg Air Force Base. As the study indicated, no one parameter can be used by itself to determine the marine layer behavior. The current study was an attempt to take LEIPPER (1995) four phases of the marine layer fog and develop an operational forecast method that would assist the forecaster in forecasting both ceilings and visibilities. LEIPPER (1995) mentioned that two inversions have to exist for the marine layer stratus to develop. The subsidence inversion develops due the offshore breeze. The marine layer inversion then develops underneath the subsidence inversion and eventually it is lifted into the subsidence inversion which provides drier air aloft, therefore allowing the stratus to dissipate. IRETON (2001) states as a mesoscale indicator the following: "during the convergent pattern, the base of which is considered a hard boundary, i.e. the ocean, the flow is turned upward. The air, which is lifted cools and condenses resulting in the formation of clouds. The divergent pattern is in response to descending air running into a hard boundary and flowing outward. The descending air warms adiabatically and becomes drier since the warmer air has the ability to hold more moisture." The author summarizes from LEIPPER (1995) and IRETON (2001) statements, the key to forecasting the marine layer

stratus and fog behavior is, you must understand what atmospheric processes makes the subsidence inversion rise and lower.

The subsidence inversion will lift when the atmosphere becomes more unstable and the reverse is true, the atmosphere must become more stable in order for the inversion to lower. The current study pointed out two points that definitely affect the marine layer behavior: The position of the 500mb high and 500mb thermal advection that move over Vandenberg AFB. The marine layer inversion height is affected by the relationship between the 500mb temperature and the 850mb temperature changes. LEIPPER's (1995) study contained a diagram that showed when the marine layer inversion established up to 250 meters (820 feet) the visibility will be below 3 SM 94 percent of the time. The current study had similar results. There were only two observations out of 169 where visibility was lower than 3 SM and the ceilings where equal to or greater than 500 feet. The dynamics that occur during sea and land breezes must be incorporated into the forecast process at Vandenberg AFB.

Cold air entrainment drizzle should be forecasted at Vandenberg AFB, when a surface high-pressure ridge moves into Washington and Oregon providing an easterly flow over northern California and southern Oregon and the marine layer stratus exits. The cold air entrainment drizzle can reach Vandenberg AFB within 12 hours of development.

Following rules for forecasting are recommended to forecast the minimum temperature at Vandenberg AFB:

—If the observed wind direction was west to northeast; the 19Z dewpoint temperature was a good indicator for minimum temperature.
—If the observed wind direction was east to southeast, then use the 23Z dewpoint temperature minus 6° F to forecast the minimum surface temperature.

The overall conclusion for the model verification section is that the GFS does consistently better than the mesoscale models when dealing with the atmosphere at 850mb and above. The MM5 does best with the surface relative humidity, 925mb temperature and surface wind speed. There is a slight shift in how the models handle situations such as the southerly surge, with reliance on the MM5 for all forecast parameters. The exception to this is the 500mb level where it is best to use the GFS for guidance.

The marine layer behavior is influenced by weak upper-air dynamic features in combination with surface features that can often be missed by the forecaster. The forecaster has to keep the mesoscale features in perspective with the microscale processes that are occurring locally. For instance, this study highlights the importance of correctly forecasting the surface temperature, which ties directly to the wind field. This, in turn, controls the low-level convergence and divergence due to the local terrain and the resulting clouds and visibility.

Acknowledgements

I am grateful to all the weather forecasters at 30th Weather Squadron who assisted in collecting the data. I would also like to thank Philip Poyner and Mike Schmeiser for taking the time to provide assistance in proof reading and editing this article.

References

Detachment 30 (1969), *Forecasting Stratus/Fog Daytime Breaking*, 6th Weather Wing, 1–7.

Evermann, G.S. (1976), *Marine fog development along the West Coast during 1973 using transient ship and coastal station observations*, Naval Post Graduate School Thesis, 1–96.

Felsch, Peter (1990), *Stratus surge prediction along the Central California Coast*, NOAA Technical Memorandum NWS WR-209, 1–17.

Ireton, Greg, S. (2001), *Classification of summertime West Coast fog and stratus forecast techniques*, Naval Post Graduate School Thesis, 1–131.

Leipper, D.F. (1994), *Fog on the U.S. West Coast: A Review,* BAMS, *72* (2), 229–240.

Leipper, D.F. (1995), *Fog forecasting objectively in the California Coastal area using LIBS*, AMS Weather and Forecasting, *10* (2), 741–761.

Mack, E.J. *et al.* (1975), *Marine fog studies off the California Coast*, Third Annual Summary Report Project Sea Fog, Calspan Corporation, Naval Air System Command, 1–87.

McConnell, M.C. (1975), *Forecasting marine layer on the West Coast of the United States using the linear discriminant analysis approach*, Naval Post Graduate School Thesis, 1–69.

Naval Electronics Laboratory Center (1976), *Fog Related to Stratus Clouds in Southern California*, Naval Air Systems Command.

Noonkester, V.R. (1979), *Coastal marine fog in southern California*, Mon. Wea. Rev. *107*, 830–850.

Nuss, W.A. (1996), *Coastal meteorology science plan*, Naval Post Graduate School Thesis, 1–29.

Paluch, I.R. and Lenschow, D.H. (1991), *Stratiform cloud formation in the marine boundary layer,* J. Atmos. Sci. *48* 19, 2141–2158.

Peterson, C. A. (1975), *Fog sequences on the Central California Coast with examples*, Naval Post Graduate School Thesis, 1–84.

Pilie, R.J., Mack, E.J., Rogers, C.W., Katz, U., and Kocmond, W.C. (1979), The formation of marine fog and the development of fog-stratus systems along the California Coast, J. Appl. Meteor. *18* 1276–1286.

Rogers, C. W. (1974), *The Life Cycle of California Coastal Fog Onshore*, Calspan Corporation, Air Force Systems Command, pp. 1–93.

(Received August 1, 2006, accepted November 28, 2006)
Published Online First: June 8, 2007